# RELIABILITY-BASE MONITORING AND

# MAINTENANCE OF URBAN RAILWAY TURNOUT

# USING ACOUSTIC EMISSION

By

# MANWIKA KONGPUANG

A thesis submitted to the University of Birmingham for the degree of

**DOCTOR OF PHILOSOPHY**

School of Metallurgy and materials

College of Engineering and Physical Sciences

University of Birmingham

July 2021

**UNIVERSITY**OF
**BIRMINGHAM**

**University of Birmingham Research Archive**

**e-theses repository**

# ACKNOWLEDGEMENTS

# PUBLICATIONS

## Conference Papers and Oral Presentations

Papaelias, M., Amini, A., Culwick, R., Heesom, J., Huang, Z., Jantara Junior, V.L., Kaewwunruen, S., Kerkyras, S., **Kongpuang, M**., Shi, S., Upton, A., Vallely, P., García Márquez, Fausto Pedro "Advanced remote condition monitoring of railway infrastructure and rolling stock" the 1$^{st}$ International Conference on Welding & Non-Destructive Testing, Greece, 22-23 October 2018. *(Conference paper)*

**Kongpuang, M**., Culwick, R., Marsh, A., Jantara Junior, V.L., Vallely, P., Papaelias, M., and Kaewunruen, S "Quantitative evaluation of damage evolution in austenitic cast manganese steel crossings using acoustic emission." the 58$^{th}$ Annual British Conference on Non-Destructive Testing, The International Centre in Telford, UK, 3-5 September 2019. *(Oral presentation)*

**Kongpuang, M**., Papaelias, M., Kaewunruen, S., "Advanced Non-Destructive Evaluation for Remote Condition Monitoring of Urban Railway Turnout in Thailand" the 12$^{th}$ Samaggi Academic Conference and Careers Fair (SACC) 2020, London, UK, 15-16 February 2020. (Qualified to the finalists in the abstract competition in Engineering and Technology discipline). *(Oral presentation)*

**Kongpuang, M**., Jantara Junior, V.L., P., Papaelias, M., and Kaewunruen, S " Advanced Non-Destructive Technique for Remote Condition Monitoring of Urban Railway Track" the 10$^{th}$ Thai Student Academic Conference (TSAC2021), 8-9 May 2021. *(Oral presentation)*

**Kongpuang, M**., Culwick, R., Cheputeh, N., Marsh, A., Jantara Junior, V.L., Vallely, P., Papaelias, M., and Kaewunruen, S "Quantitative Analysis of the Structural Health of Railway Turnout Using Acoustic Emission Technique" the 17th International Conference on Condition Monitoring and Asset Management (CM2021), 14-18 June 2021. *(Oral presentation and conference paper)*

## Poster Presentations

**Kongpuang, M**., Papaelias, M., Kaewunruen, S., "Advanced NDT evaluation for remote monitoring of railway " JSPS UK Japan Symposium on Highspeed Rail Program, University of Birmingham, UK, 21 September 2018.

## Publication in preparation

**Kongpuang, M**., Jantara Junior, V.L. Papaelias, M., Kaewunruen, S., "Evaluation of damage evolution in austenitic cast manganese steel crossings compare to pearlitic rail steel using acoustic emission"

# TABLE OF CONTENTS

# LIST OF FIGURES

# LIST OF TABLES

# ABBREVIATIONS

| | |
|---|---|
| AE | Acoustic Emission |
| AEP | Acoustic Emission Pulsing |
| ASL | Average Signal Level |
| BCC | Body-Centered Cubic |
| BHN | Brinell Hardness Testing |
| BSE | Backscattered Electrons |
| CBM | Condition-Based Maintenance |
| CLSM | Confocal Laser Scanning Microscope |
| CM | Corrective Maintenance |
| CP | Crack Propagation zone |
| dB | Decibel |
| DCPD | Direct Current Potential Drop |
| EDS/EDX | Energy Dispersive Spectroscopy/ X-ray |
| EMAT | Electromagnetic Acoustic Transducer |
| FCC | Face-Centred Cubic |
| FF | Final Fracture zone |
| FGI | Field Gradient Imaging |
| ICDD | The International Centre for Diffraction Data |
| $K_{IC}$ | Stress Intensity Factor |
| LRUT | Long-Range Ultrasonic |
| MAD | Magnetic Anomaly Distortion |
| MARSE | Measured Area under the Rectified Signal Envelope |

| | |
|---|---|
| MFL | Magnetic Flux Leakage |
| MMA | Manual Metal Arc Welding |
| MT | Magnetic Particle Inspection Testing |
| NDT | Non-Destructive Testing |
| PEC | Pulsed Eddy Current |
| PM | Preventive maintenance |
| PRA | Probabilistic Risk Assessment |
| RAMS | Reliability, Availability, Maintainability, and Safety |
| RBM | Rail Bound Manganese |
| RCF | Rolling Contact Fatigue |
| RMS | Root Mean Square |
| RT | Radiographic Testing |
| S&C | Switch and Crossing |
| SED | Secondary Electron |
| SEM | Scanning Electron Microscope |
| SFE | Stacking Fault Energy |
| SHM | Structure Health Monitoring |
| SIF | Stress Intensity Factor |
| TWIP | Twinning-Induced Plasticity |
| UT | Ultrasonic Testing |
| VT | Visual Testing |
| XRPD | X-ray Powder Diffraction |

*"Impossible only means that you haven't found the solution yet."*

*---Anonymous*

# CHAPTER 1

# INTRODUCTION

**CHAPTER 1: INTRODUCTION**

This chapter gives a general overview of the research study. The structure of the Thesis describes the chapter introduction includes a description of the methodology, and the last section in this chapter is where the author used to conduct the experiment.

## 1.1 BACKGROUND

Shortly, the railway network in Thailand will expand rapidly to meet people's increasing transport needs. This has required the introduction of rolling stock with higher axle loads and operational speeds to be gradually introduced, especially in urban areas where the higher population density and infrastructure of the built environment railways will play a critical role in enabling sustainable long-term transport. Although the railway network in Thailand is small compared with road transport, almost 40 million people travel on intercity railways and 200 million on urban railways each year. The current Thai railway network has about 4,507 km of meter gauge lines, 90% of which are still single track. There are also issues associated with outdated facilities, poor management, insufficient servicing, and low operational speeds in the majority of the railway network. Thailand high-speed rail construction will start involved in the first phase of the project, a 250-km (155 miles) line, which is expected to be operational in 2021. The emphasis has shifted away from high-speed railways and onto dual-track services, with new 1.435 km of meter-wide tracks capable of accommodating trains at speeds of 160 km per hour being planned on two routes. Over 100 derailment accidents and more than 150 accidents involving personal vehicles in level crossings each year [1].

Figure 1. A high-speed train project is planned to operate in Thailand, which consists of 4 main lines. Starting from Bangkok to Chiangmai, Nong Khai, Rayong and Padang Besar (Malaysia) with a 250 km/hr speed for a distance of 1,039 km.

With the expansion of the railway network in order to satisfy the increasing demands of urban transport, rail structures are being put under increasing high cyclic loads leading to increased wear and fatigue damage initiation to occur more and more regularly. Rolling contact fatigue (RCF) is a kind of surface fatigue damage produced by interactions at the wheel-rail interface. It is primarily related to contact stresses, although impact loads from

wheel flats and bending stresses also play a significant role. Regular inspection operations must occur at night to avoid disruption in normal operations or when rail traffic is reduced. Thus, the use of conventional inspection methods is not optimised to support high traffic densities. The limitations of state-of-the-art inspection methodologies have led to an increasing interest in using the Acoustic Emission (AE) technique to monitor and maintain reliable railway tracks, especially urban railway turnouts, which are more challenging to inspect and form bottlenecks in the network. Turnout component structural deterioration has been seen regularly, resulting in increased railway maintenance costs and downtime.

## 1.2 STATEMENT OF THE PROBLEMS

Defects such as fatigue cracks have been historically one of the leading root causes of many derailments due to broken rail sections. Structural damage in rails and crossings can develop with time due to the complex bending and contact stresses they are exposed to. Besides, manufacturing defects during the casting or welding process (e.g., porosity, segregation, and inclusions) can also arise occasionally, resulting in structural failure at a much earlier stage. Cracks initiating and propagating below the surface are difficult to detect using conventional Non-Destructive Testing (NDT) techniques. A more appropriate method for crack growth monitoring in real-time is AE. When a load is applied to a solid structure, it begins to deform elastically. Associated with this elastic deformation are changes in the structure's stress distribution and elastic strain energy storage. As the load increases further, some permanent microscopic deformation or crack growth may occur, accompanied by a sudden release of the stored strain energy, partly in the form of propagating elastic waves termed acoustic emissions. If these acoustic

emissions are above a certain threshold level, they can be detected and converted to electric signals by sensitive piezoelectric transducers mounted on the structure's surface.

## 1.3  AIMS AND OBJECTIVES

Although AE testing is widely used in many industries, it is relatively new and limited trials have been found in the railway industry. Most studies have focused on proving empirical correlations alone rather than examining the reliability of AE applications to quantify defects. They also neglected to study the effects of background interference with sensors, variables such as frequency or load used, and the study of microstructure nature. As a result, this thesis aims to fill some of these gaps. It is essential to develop reliable correlations to quantify damage propagation, guarantee that relevant information can be obtained from AE data, and increase our understanding of crack propagation and the associated AE in conventional rail steel and Hadfield manganese crossings. The following are the four aims presented in this thesis:

(1) To study the applicability of the AE monitoring technique to acquire reliable quantitative relationships for a variety of AE parameters in conventional rail steel grades R220 and R260 compared to Hadfield manganese steel in order to quantify their damage propagation.

(2) To further understand the link between microstructural features and AE signals generated from crack growth, fractography was conducted to investigate the characteristics of the samples crack surfaces.

(3) To confirm that the customised AE techniques developed as part of this project will be possible to use in the field to detect any crack growth or impact damage that may occur on rails and crossings.

(4) To study the feasibility of using a 3D image analyzer (Laser Confocal Scanning Microscopy) to examine crack surfaces.

This study will be used to support Thailand's transport infrastructure, which will be set to transform over the next eight years.

## 1.4    SCOPE OF THE STUDY

Fatigue and fracture behaviour of rail steel grades and cast manganese steel used for manufacturing crossings have been studied. The fatigue test and crack growth monitoring were carried out using Direct Current Potential Drop (DCPD), and AE whilst the failed samples were also evaluated using fractography to support the correlation of the Acoustic Emission data with actual features observed on the fractured surface of the samples. The research primarily focuses on Acoustic Emission applicability and reliability for monitoring pearlitic rail materials grade R260 and austenitic cast manganese steel or Hadfield manganese steel for quantifying damage evolution occurring due to fatigue under laboratory.

## 1.5    THESIS STRUCTURE

This thesis has been divided into eight chapters. The following is the thesis's detailed structure:

**Chapter 1**: presents the background, statement of the problem, aims and objectives, structure of the thesis, and location of the study. It gives a general overview of the research study.

**Chapter 2**: gives a review of the type of railway turnout and their components, failure mechanism in rail, and explains rail fatigue with emphasis on rolling contact fatigue and crack growth model.

**Chapter 3**: gives a review of general information on the AE technique and uses AE as an NDT method in rail and crossing. Pearson correlation and linear regression analysis were used statistically for quantitative AE analysis. Signal processing under field conditions was reviewed to study the feasibility of future field trials.

**Chapter 4**: presents results and characterization of the materials used in the experiment. The experiment used three methods: scanning electron microscopy with energy dispersive x-ray spectroscopy (SEM+EDS), X-ray diffraction (XRD), and micro vicker hardness test. The result gained will be used as the fundamental data for the fractography study in Chapter 7. This chapter also provides information on defects and micro-mechanisms of fracture in metals.

**Chapter 5**: performed three-point bending fatigue testing on pre-cracked materials under laboratory conditions to investigate the feasibility of using AE quantity crack propagation in samples. The methodology for the thesis has summarised the steps below;

> Step 1: preparation of samples for fatigue testing.

> Step 2: a pre-fatigue cracking test is used to initiate the fatigue crack before the primary fatigue test and the initial crack size measurement.

> Step 3: the three-point fatigue bending tests under laboratory conditions.

> Step 4: the fracture surface analysis

**Chapter 6**: presents fatigue testing results and discussion of R260 rail steel and Hadfield manganese steel. The results of the two major materials were analyzed together with the R220 rail steel tested in the past. The result will be explained using quantitative evaluation by analyzing the AE signal occurring in each parameter.

**Chapter 7**: presents fractography of R260 rail steel and Hadfield manganese steel in 2D analysis using SEM and 3D analysis using Laser Confocal Scanning Microscopy

(LCSM). Non-metallic inclusions were examined to confirm the results of the surface analysis against the AE signal.

**Chapter 8**: presents the conclusion, major contribution and suggests further research.

## 1.6 LOCATION OF THE STUDY

The present study was carried out at the following locations:

Metallurgy and Materials Department, University of Birmingham, Birmingham, United Kingdom

Thailand National Metal and Materials Technology Centre (MTEC), Bangkok, Thailand

State Railway of Thailand, Bangkok, Thailand

EVOLEO Technologies, Porto, Portugal.

# CHAPTER 2

# RAILWAY TURNOUT AND INSPECTION

# TECHNIQUES

**CHAPTER 2: RAILWAY TURNOUT AND INSPECTION TECHNIQUES**

In this chapter, the author reviews articles and literature related to physical characteristics of railway turnout and damage mechanisms were reviewed as a basis for analysing experimental fracture surfaces.

## 2.1    TYPES OF RAILWAY TURNOUTS AND THEIR COMPONENTS

Turnouts are the railway equivalent of railway network junctions, allowing rolling stock to be transferred from one track to another. They are important elements of the railway network since they make traffic operations more flexible and more complex. Turnout derailments are those that occur at the turnout area. Nearly 572 derailments have been recorded in the EU from 2010 to 2015, while losses amount to EUR 200 million per year [2]. Railway turnouts are typically subjected to impact wheel loading, which necessitates the use of cast manganese steel instead of plain rail steel grades [3-5]. Plastic deformation, wear, and rolling contact fatigue can generally arise from loading the rail and turnout structure during the rolling stock passage. All these mechanisms can result in deterioration of the profile geometry requiring maintenance action.

### 2.1.1   Turnout components

A standard turnout consists of several parts, as shown in Figure 2. The single turnout is the most popular type compared to others. This type of turnout consists of three main parts, as shown in Figure 3, including the switch panel or point panel, which includes the movable rail parts used to control the direction of the train passage. A closing panel or intermediate track consists of the straight or curved rails required to link the switch blades to the crossing and crossing areas. It is a vital aspect of the turnout since it is the only point where the line continuity is interrupted.
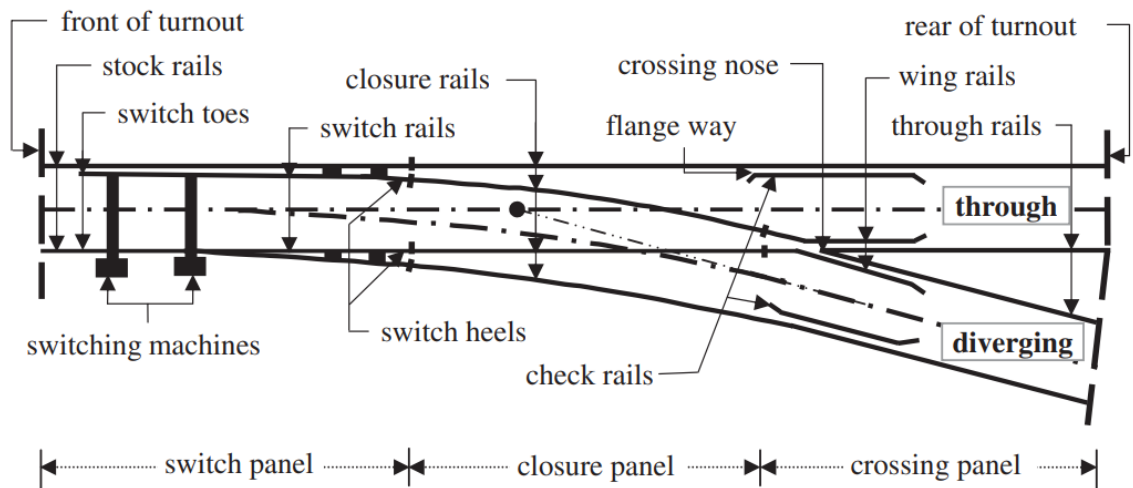
Figure 2. The geometry of a simple turnout [6].
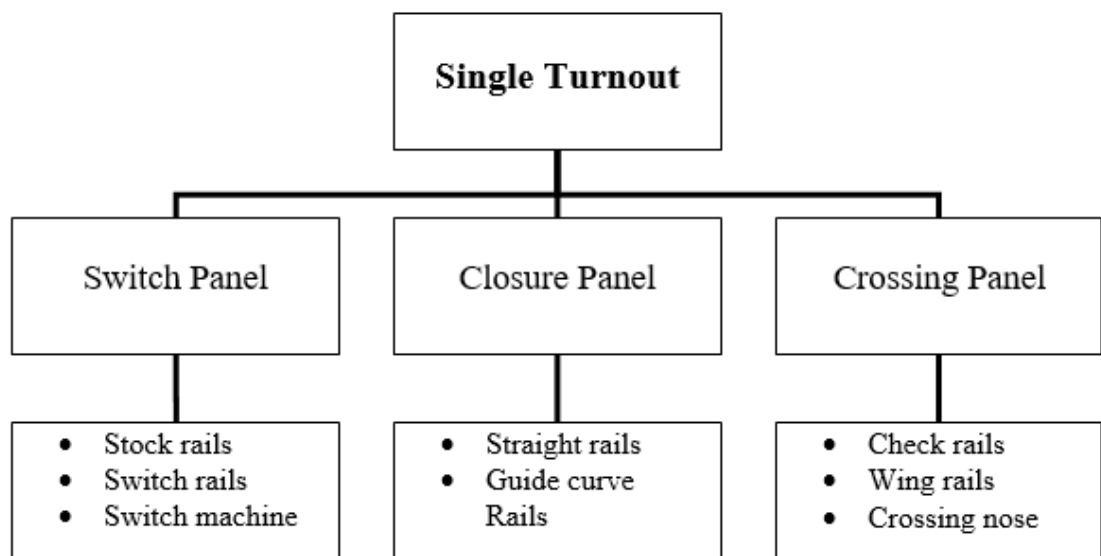


Figure 3. Diagram showing the major components of a standard turnout or set of points.

A crossing panel consists of a crossing nose, wing rail, and check rail. It helps trains to move in both directions. The panel's crossing is the place where two rails intersect. It is made up of two wing rails and a nose. Crossings may be either fixed type or movable. The three separate components are either bolted together (pearlite crossing) or cast together (Austenitic manganese steel crossing). When heavy axle load or high speeds are required, they are generally made of cast manganese steel. The guard rails run parallel to

the rails on both sides of the crossing. The railway wheels' lateral movements are limited by the check rails. As it involves combinations and discontinuities, switches and crossings are some of the most complex components of the rail network, resulting in increased dynamic loading and higher levels of degradation of these components relative to the in plain rails. In the crossing area, the wheel travels from the nose to the wing rail or from the wing rail to the nose, depending on the traffic direction. Damage in the crossing arises due to excessive impact loads at the nose area due to the discontinuity between the wing rail and nose. Due to the crossing design, there is a significant difference in the in-service conditions at the nose and wing rails. Because the nose of the crossing withstands contact stresses generated by in-service train wheels, the failure mechanism is spalling due to fatigue, but the wing rails exhibit wear due to the train wheels' rolling contact stress [7]. The typical damage mechanisms reported at crossings are defects such as rolling contact fatigue, wear, plastic deformation, breakage of parts in the railroad tracks, and other defects.
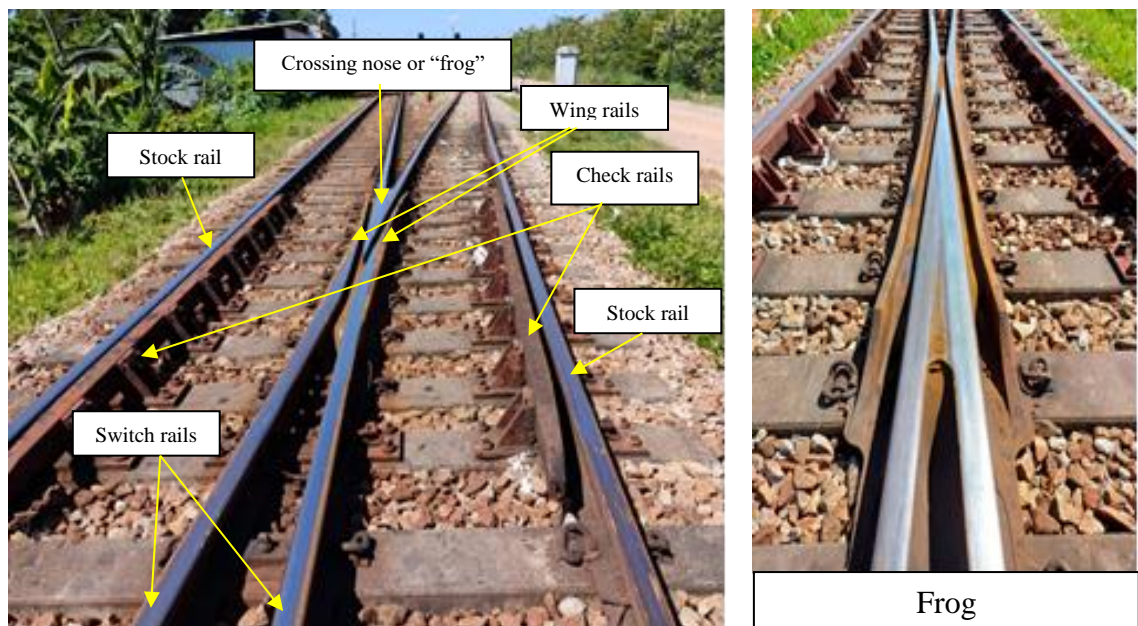


Figure 4. The various constituent components of a turnout, the pictures were taken at Bangsaphanyai railway station located in Prachuap Khiri Khan, Thailand.

Steel rails built from a standard rail profile with one side straight and the other curved are **stock rails**. Rail bracing is installed on the outside of the stock rail to keep it from shifting. To increase wear resistance and surface hardness, the tops of stock rails are always quenched.

**Switch rails** are moveable rails between diverging rails and guide trains from the rails to either the straight or diverging track.

The rail turnout control system's executive component is the **switch machine**. The turnout can be adjusted using electrical or pneumatic systems.

**Straight rails and Guide curve rails**, connection components are made up of two straight rails and two curve guide rails that link the switch rail to the frog and guard rail as a whole railway turnout.

A **check rail** is a small section of rail running parallel to the main rail on the opposite side of the frog. They exist to guarantee that the train does not derail by following the correct flangeway through the frog.

**Crossing nose** consists of a frog, wing rail, and connecting components used as the crossing part of two tracks. Multiple cutting and bending rail components or a single casting steel component can make a crossing nose.

### 2.1.2 Common types of railway turnouts

There are many types of turnouts. Figure 5 illustrates many major turnouts. Standard turnouts, also known as single turnouts, have a single through track and a diverging track. The right-hand turnout has shown in Figure 5(a), is where the diverging track departs the mainline to the right. Figure 5(b) shows an asymmetrical turnout to divert the track symmetrically from its regular route. The diamond crossing with double slips depicted in Figure 5(c) features two curves that connect two diagonal intersections,

bringing the total number of possible routes to four. In contrast, the diamond crossing with a single slip illustrated in Figure 5(d) features three possible routes due to the low number of intersections. Finally, the non-slip diamond crossing, as seen in Figure 5(e).
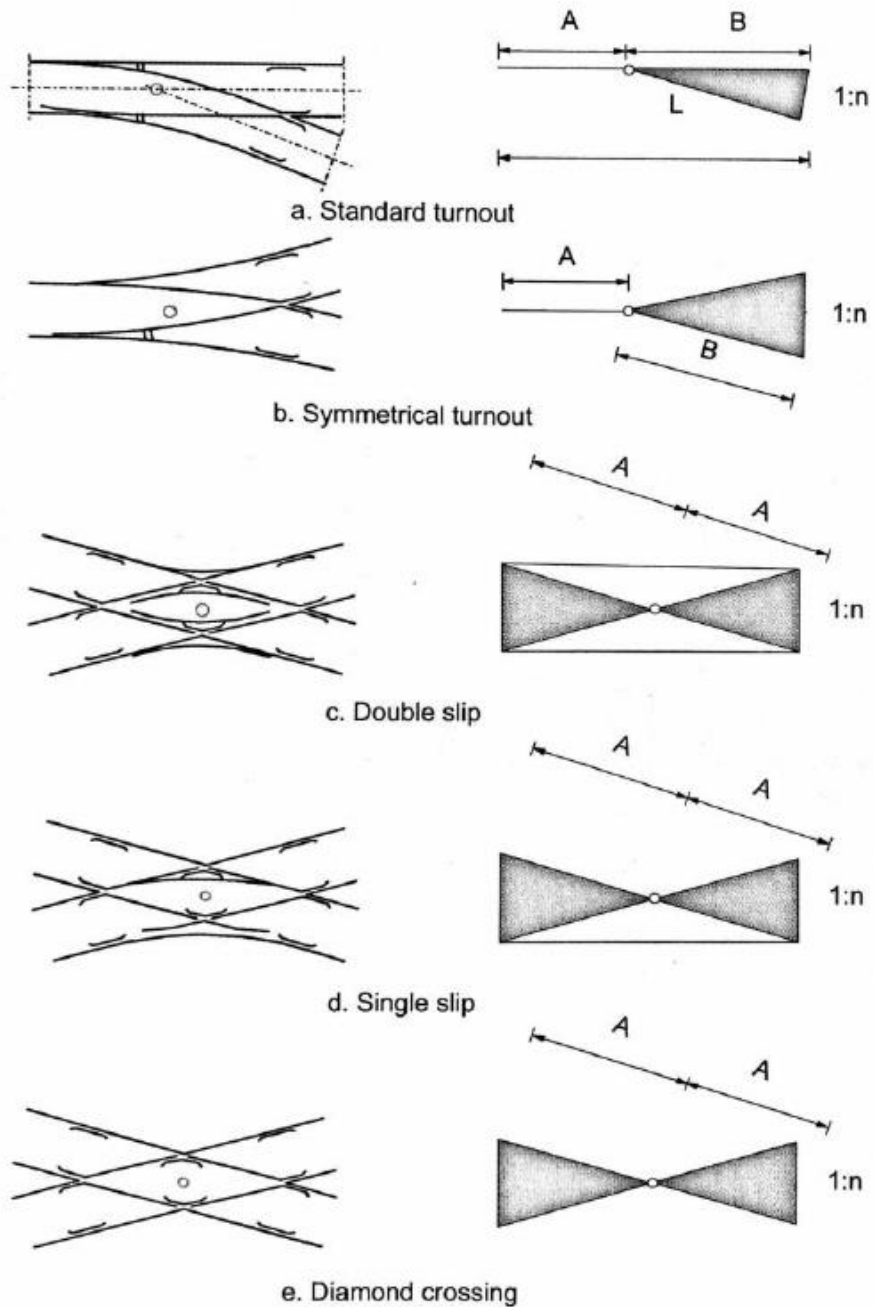


Figure 5. Common types of railway turnouts; standard turnout, symmetrical turnout, double slip, single slip, and diamond crossing [8].

As for the crossings, the typical diamond crossing consists of two straight tracks. There are two acute angle crosses and two obtuse angle crosses. On both sides, the crossover angle of the regular diamond crossing is the same. This crossing type is the junction between a straight track and a curved track or between two curved tracks compared to a curved diamond crossing. Thus, the angle of the angled diamond crossing at both ends is different. The right-angled crossing has a severe effect on the joint as the train passes, while the oblique crossing has less damage to the joints. If the angle of the intersection is smaller, the incidence of unguided sections becomes greater. As for the angle of intersection less than 1:12, the movable switch blades are given on the side of the obtuse cross-section. The swing noses are used on the typical side of the cross-section as outlined.
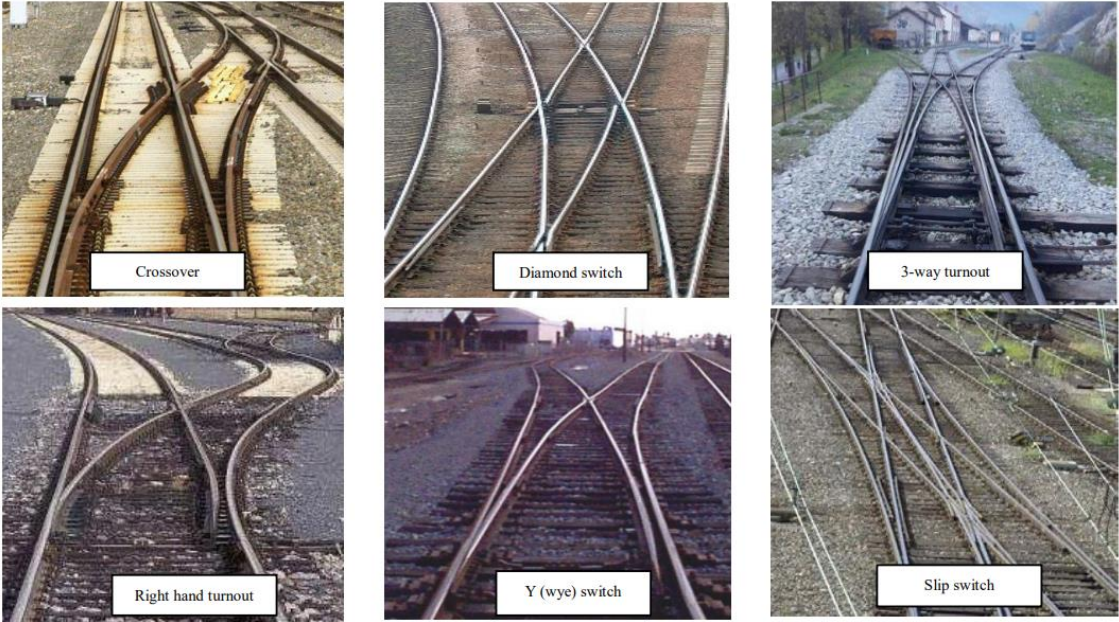


Figure 6. The most common types of turnouts are used in railway operations [9].

### 2.1.3 Railway Frog

The railway frog is a two-rail crossing point that is extremely important to the rail turnout's general functioning and the junction of two railway lines. As a result, passengers on the train will not feel uncomfortable owing to unexpected bumps. On the other hand, if the rail frog innovation is unreliable or if the rail frog is configured and geometrized incorrectly, irregularity will occur throughout the train's passage. As a result, selecting high-quality railway frogs is critical to the switch's safety and dependability and the overall reliability of the rail line. The rail frog can be divided into the fixed frog and the movable point frog (swing nose crossing) according to the structure type.
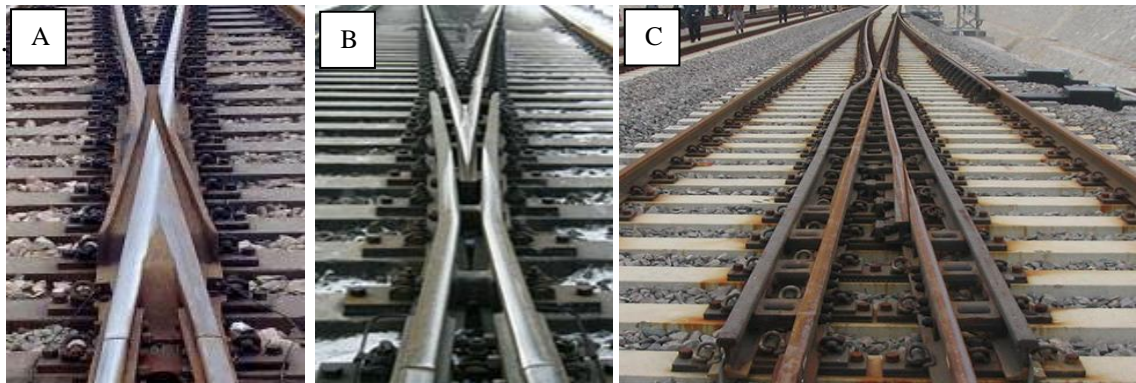


Figure 7. Fixed frog or Rail bound manganese frog (A), combined type rail frog (B), and movable point frog (C).

**Rail bound manganese frog (RBM)** is a kind of one-piece cast frog with austenitic cast manganese steel or, as it is also known, Hadfield steel. RBM rail frog is recommended for mainline turnouts and crossovers subject to high speed and heavy traffic. The RBM frog's integrity and stability are better because the crossing nose and wing rail were simultaneously cast. High cast manganese steel is a type of alloy steel that consists of an austenite-grain matrix. It contains 11 to 15 wt% Mn, with 0.8 to 1.25 wt% C (roughly a ratio 1:10 between C and Mn content), non-metallic inclusions, alloyed cementite, and phosphorus eutectic. With high manganese alloy, the cast railway frog exhibits high levels of wear resistance, greater strength, longer service life, and more convenient maintenance.

**The combined type of rail frog** contains the crossing nose, the wing rail, and other parts. The combined type of rail frog is not challenging to use because it does not involve any special process requirements. Therefore, the process and manufacturing technology are not complicated. However, the combined type of rail frog has more individual parts and thus, requires more maintenance.

**The movable point frog** refers to the structure of a railroad frog with movable components. As the railway frog is partly movable, the undesirable space in a fixed frog is removed, making the transition smoother. There are three types of movable point frogs: mobile nose style crossing, mobile wing rail type, and other mobile railway frogs.

### 2.1.4 Rail Materials

In terms of the railway infrastructure, the rails are the most important component. High fatigue strength, High wear resistance, high deformation resistance, high toughness, excellent weldability, and low residual stresses after manufacture and maintenance are the most important structural requirements for rails. Some of the requirements are in competition with each other. Thus, choosing the most suitable rail steel grade is vital to improve the railway system's reliability and safety. The most common rail materials used are medium and high carbon steel heat treated to give a fully pearlitic microstructure. Rails in Europe were traditionally built to UIC standards, according to UIC leaflet 860-0. For infrastructure managers, however, the European standard EN13674 has been in place since 2001. The Brinell hardness (BHN) indicates the new standard's steel grade instead of the tensile strength. The Brinell hardness can designate the modern rail grades in Europe and America as R200, R260, R260 Mn, R350 HT, and R320 Cr. Tensile strength must be between 650 and 1100 N/mm$^2$. Carbon, manganese, and chromium are the main

constituents of R320 Cr, a high strength steel grade. The chemical composition and mechanical characteristics of these steels are listed in Table 1.

Table 1. UK rail steel - chemical composition and mechanical properties of pearlitic rail steel [8].

| Rail steel grade | Carbon content (%) | Mechanical properties | | | Description | Specification |
|---|---|---|---|---|---|---|
| | | Hardness (BHN) | $R_m$ (N/mm$^2$) | Elongation (%) | | |
| R200 | 0.40-0.60 | 200-240 | >680 | 14 | Non- heat treated | |
| R220 | 0.50-0.60 | 220-260 | >770 | 12 | Non- heat treated | |
| R260 | 0.62-0.80 | 260-300 | >880 | 10 | Non- heat treated | EN |
| R260Mn | 0.55-0.75 | 260-300 | >880 | 10 | Non- heat treated | 13674-1 |
| R350HT | 0.72-0.80 | 350-390 | >1175 | 9 | Heat treated | |
| R350LHT | 0.72-0.80 | 400-440 | >1175 | 9 | Heat treated | |
| 700 | 0.40-0.60 | | 680-830 | 14 | | |
| 900A | 0.60-0.80 | | 880-1030 | 10 | | UIC |
| 900B | 0.55-0.75 | | 880-1030 | 10 | | 860-O |
| 1100 | 0.60-0.82 | | >1080 | 9 | | |

At turnouts, the railhead is exposed to compressive rolling and sliding loads, as well as a significant dynamic impact load. The standard rail grade is incapable of withstanding the impact loads imposed on the turnout component. Therefore, Hadfield steel is used instead of plain rail steel grades. Hadfield steel is the best choice for this component because it has a good mix of toughness, hardness, flexibility, and abrasion resistance, as shown in Table 2. This material has a higher level of toughness than the pearlitic rail steels. It has a high work hardening rate due to deformation twinning, instability in the plastic flow of materials, and the interactions between stacking faults and dislocations [163]. However, brittle carbide particles tend to form on cooling in these austenitic steels, which must be reduced to reach the ultimate toughness required. Besides, Hadfield manganese steel thermal expansion is 60 percent higher than pearlitic grades. Because of the formation of undesirable carbides after welding, these factors cause

problems in the welding. Using a low-carbide version will reduce the risk of carbide formation [10].

Hadfield manganese steel has characteristics that make it more adapted to repeated hits at the crossing than standard pearlitic steel. Manganese steel has a higher threshold stress intensity factor ($\Delta K_{th}$) than common structural steel, resulting in a lower crack growth rate [11]. Manganese steel's high work hardening ability and exceptional wear resistance are two key characteristics. As a result, fractures may go undetected during regular ultrasonic rail inspection. It is also important to plan out the welding process in advance for manganese steels since it is very sensitive to carbide precipitation and pearlite production during reheating, particularly at 260°C, resulting in embrittlement and toughness loss [12].

Table 2. UK austenitic grades for rail crossings (wt%) [10].

| Steel | C | Si | Mn | S | P | Cr | Mo | Ni | Cu | Al | N | O | V | Ti | Comment |
|---|---|---|---|---|---|---|---|---|---|---|---|---|---|---|---|
| Hadfield | 0.90 1.20 | 0.40 max | 11.0 14.0 | Both 0.050 max. but target as low as possible. | | – | – | – | – | – | – | – | – | – | – | Sawley, 1989; Hodgson, 1985 |
| Low-carbon grade | 0.70 0.90 | 0.40 max. | 12.0 16.0 | | | – | – | – | – | – | – | – | – | – | – | Sawley, 1989, Hodgson, 1985 |

Ossberger et al. studied Hadfield manganese steel's performance compared with other frog material, tool steel, and bainitic railway steel by measuring the transition shape every 3-5 months. Although the experimental results found that the Hadfield manganese steel had the highest rate of degradation concerning plastic deformation significantly in the run-in phase owing to the frog material's lower yield strength than the wheel, this steel's great advantage is its high rate of adaptation. As a result, it makes the frog less sensitive to loads arising from wheel profiles deviating from the standard [13].
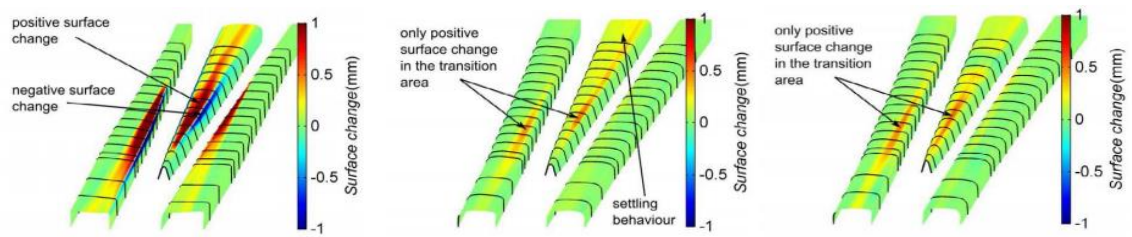
Figure 8. Shows the 3D contour plot for the surface change of explosion depth hardened cast manganese (left), tool steel (middle), and bainitic railway steel (right) [13].

### 2.1.5    Turnout Maintenance

One of the most critical aspects of the turnout life cycle is maintenance. It is powered by the efficiency of the system and dramatically affects the required costs and resources. A combination of corrective and preventive maintenance is the most widely used method for maintenance. The industry is attempting to move toward predictive maintenance using condition-based monitoring, but engineering safety reasons for changing current techniques will take time to develop. The use of predictive maintenance based on appropriate condition monitoring methods should improve the overall performance, reliability, safety, and maintainability of railways. Nonetheless, there will always be some problems that cannot be forecast and for which corrective and/or preventive maintenance actions will be required.

Maintenance strategies are divided into two categories: unplanned and planned, as shown in Figure 9.
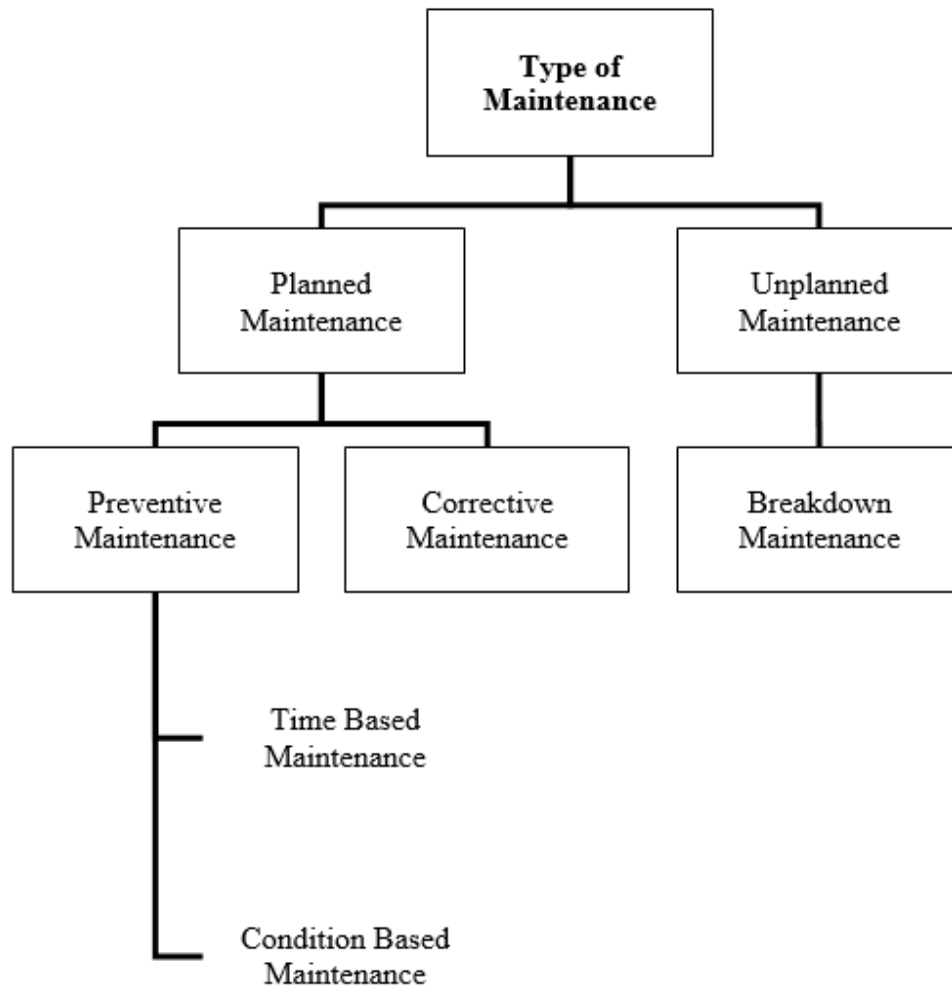


Figure 9. Maintenance strategy type (Sources: Adapted from BS 3811).

**Corrective maintenance (CM)**

Corrective maintenance focuses on taking a specific action after a problem has occurred to resolve it. The goal is to restore the damaged component to its original state as soon as feasible. The kind of damage and the time required to complete maintenance operations are reported by the CM. Some tasks may be postponed until the maintenance season starts. This kind of procedure is often referred to as programmed. However, since it overlaps

with characteristics associated with other maintenance methods, this term will be avoided in this thesis. On the other hand, different tasks cannot wait and must be completed immediately (these activities are known as not programmed). When it comes to the core of maintenance actions, they may be temporary if they are not conclusive and are employed to get the service back up and run as quickly as possible, or definitive if the problem is addressed on a more permanent basis intervention.

**Preventive maintenance (PM)**

Preventive maintenance (PM) must be carried out according to previously defined guidelines to eliminate or reduce the risk of failure or minimise the system components' wear. These criteria may be based on; systematic and periodic working preparation or subject to integrating the parameters that describe the system's state. The reliability of the components, their features, the functioning of the components, and their predicted degree of degradation (estimated from theoretical and/or empirical data) are all factors that go into task planning in a systematic approach. The definition of inspection takes on further relevance when the performance criteria are based on the importance of the relevant metrics and their practical limitations (this aspect will be detailed in the following sections). However, as previously mentioned, it is common practice to mix the two approaches in maintenance contracts.

**Predictive maintenance or Condition-based maintenance (CBM)**

This type of maintenance is similar to the condition-based monitoring method. This method uses sensors such as infrared thermography, vibration monitoring, and ultrasonic detection to evaluate the health of the equipment, which provides inspections of the working conditions of the equipment and during periods of stoppage [14]. In addition,

this maintenance method is based on calculating (or detecting early) the real failure causes in order to determine the best time to do maintenance and reduce failures and downtime. Predictive maintenance is correlated to the inspection and monitoring of certain parameters that must be calculated and evaluated on a regular basis (based on a predetermined frequency). The choice of parameters to control and describe the resources required to track these parameters are possibly two of the most critical points.

The turnouts are included in the general inspection of the railway track since they are considered a superstructure component.

### 2.1.6    Reliability, Availability, Maintainability, and Safety (RAMS)

The data analysed for the various types of railway lines were gathered to compare the RAMS parameters. Additionally, the researchers used three additional high-speed trains, conventional lines, tram lines, and metro lines (underground). A RAMS assessment was conducted to determine the reliability, availability, maintenance, and safety of these lines for Switch and crossing performance.

**Reliability** analysis determines the probability that a system will perform the required operation within a specified time. The reliability predictions are used to estimate the likelihood of failure estimate the probability of failure of individual components, taking into account their operating and environmental circumstances. The reliability of a device or service is critical in determining if it is functioning properly. As a result, the component's reliability can be calculated, and its analysis can determine the probability of a system element failing.

**Availability** refers to a commodity's ability to perform the specified function under such circumstances at a particular point in time or during a specified time, assuming the necessary external services are accessible. This factor quantifies the willingness of the

machine's user to ensure the system's continuity and advantages. However, in this analysis, availability will be determined by delays. Additionally, this availability would take into account the effect on the economic operation of the facility and the system's malfunction characteristics.

**Maintainability** is defined as the probability of completing a particular active maintenance activity within a specified time frame when performed under specified circumstances and with specified methods and resources. On the other hand, maintainability parameters reflect the subsystem's ability to be preserved and returned to operational status, taking into account specific requirements, methods, and resources.

The lack of unfavourable risks is defined as **Safety**. A probabilistic risk assessment may be used to estimate the cumulative risk by multiplying the severity of possible negative outcomes and the likelihood of such consequences. However, the PRA will not be carried out in this analysis due to a lack of data. Instead, risks and unsafe conditions have been identified, and any events or accidents involving investigation related to fatalities or serious injury have been analysed.

## 2.2   FAILURE MECHANISM IN RAIL

### 2.2.1   Wheel-Rail Contact Mechanisms

The wheel-rail contact mechanism is too complicated. The contact patch usually is elliptical with a radius of approximately 1 cm$^2$. If the wheel is worn, the contact patch becomes more oval. The wheel and rail determine the exact location of the wheel-rail contact; the bogie model factor includes the curvature of the track. The wheel tread and railhead seem to be in contact on the straight track, but in the curve, Contact occurs between the wheel flange and the corner of the rail gauge.

The possible region for interaction with the wheel-rail is shown in Figure 10. Region A is the contact between the wheel tread and the railhead, Region B is the contact between the flange and the rail gauge corner, and Region C is the contact between the field side of the wheel and the rail. In Region A, a contact patch is most likely to occur when a railway vehicle travels on a straight track or at extremely large radius curves. In this region, lateral force and contact stress are the lowest. In Region B, contact with a smaller contact area is also even more intense. Usually, contact stress and wear rate in Area B are much higher. If the wheel substance is worn at the critical point, the contact patch may be changed to two-point contacts at the wheel and flange. As for Region C, there is rarely a contact patch at this location. This area is subjected to a very high degree of contact stress and wear, however. The unexpected wear might cause the wheelset to have a steering problem [15].
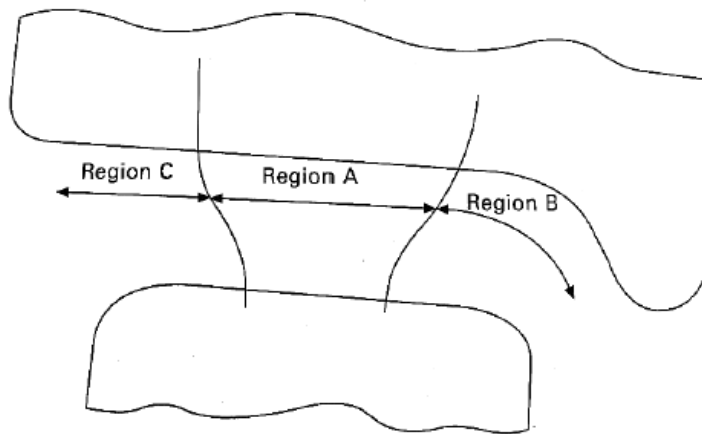


Figure 10. Wheel-rail contact zones [15].

Many factors may influence the estimated lifetime of the rail service. Service life is mainly affected by the rail's chemical composition, maintenance programs for the track, speed, and tonnage. These parameters include vertical and lateral head wear, railhead plastic flow or deformation, and rail defects development.

The production of rail faults in modern steel would be impaired by a robust maintenance program that will extend the amount of time before the rail is exposed to extreme wear and plastic flow effects. This would include strategies for friction control and a healthy profile of the rail. However, it is challenging to predict rail service life or the development of defects reliably.
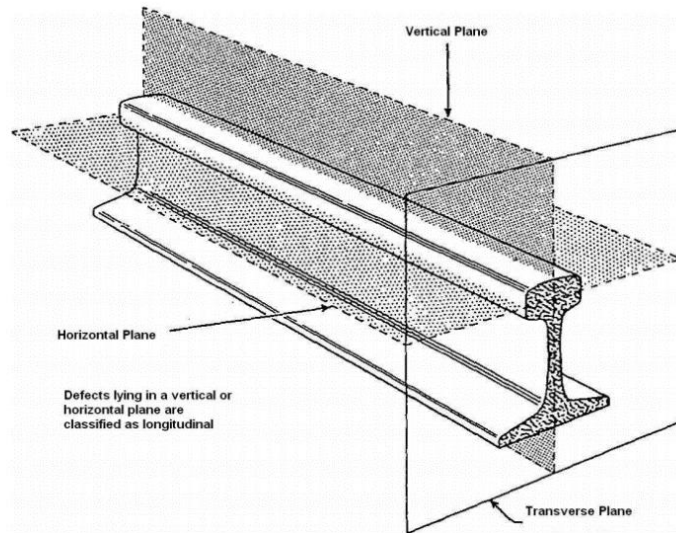


Figure 11. Terminology Used to Identify Defect Planes with Rail Section [16].

Rail Loads and Stresses: Internal rail faults often begin with certain rail stress types and evolve to a detectable size defect. A terminology that can be used to identify the planes of rail stresses is given below.

i.  Vertical Plane: stresses that progress in a longitudinal plane parallel to the rail's length.

ii.  Horizontal Plane: stresses that move along the rail horizontally.

iii.  Transverse Plane: stresses that transversely progress along the rail cross-section.

### 2.2.2        Failure Mode in Rail and Crossing

At the turnout point, components of the railhead included inside switches and crossings are subjected to significant dynamic impact loads. Because of their low impact

fracture toughness, standard rail grades are unacceptable. As a result, turnout-related derailments account for almost half of all railway derailments in the United Kingdom [17]. Although some conventional pearlitic steels, bainitic steels, and premium steel grades (e.g., 350 HT) are used, Hadfield manganese steel, with its high toughness and work-hardening rate, is chosen. In addition, Hadfield manganese steel has an austenitic microstructure. Due to the Mg alloy, the austenitic microstructure leads to a much higher strength than pearlitic rail steels [157]. Therefore, Hadfield manganese steel has become the preferred material for railway crossing construction [18].

In the last 20 years, there has been increased interest in the research of fatigue cracks, as well as the development of efficient monitoring and detecting fatigue growth in the Hadfield manganese steel crossings [7]. Studies have investigated the formation of the fatigue cracks in Hadfield manganese steel crossing (Fe–1.2% C–13% Mn) by exploring the atomic size of elements mixed in metals. Harzallah et al. [19] studied the effect of rolling contact fatigue on the mechanical behaviour of Hadfield manganese steel X120Mn12 by using different parameters. The hardness of manganese steel increases with increasing rolling speed and decreases with decreasing applied load. Simultaneously, the number of cycles directly affects the initiation and propagation of the crack, leading to the micro-spalling initiation. Guo et al. [20] studied the effect of wheel speed, at four different wheel speeds, i.e., 50 km/h, 100 km/h, 150 km/h, and 200 km/h in Hadfield manganese steel crossing by finite element (FE) model simulation to predict fatigue and wear of railway crossings. The test results clearly show that the wheel speed directly affects the von Mises stress and strain in the crossing nose. As a result, the speed limit of trains running through the Hadfield manganese steel crossing must be considered to prevent possible damage.

An analysis of typical rail damage mechanisms in turnouts was carried out [21]. Mechanical contact damage, such as plastic deformation, wear, fracture, and rolling contact fatigue, has been reported in turnouts. Furthermore, the rail discontinuities in the switch and cross-section panels increase the wheel-rail contact forces compared to conventional rails, even though the rail cross-sections carrying the load are weaker. As a result, rails near switches and crossings are likely to sustain more severe damage and degradation. Examples of rail turnout damage can be seen in Figures 12.



Figure 12. The worn switch rail, where the crack had formed from the railhead down to the metal, propagated longitudinally and gradually turned upwards again, causing a large part of the switch rail to be removed (A), Spalling (loss of material chips) on a manganese crossing nose (B), the nose is worn as shown by the vertical distance between the template and the nose (C) [21].

Wheels may be severely worn and damaged as a result of crossing changes [22]. As the geometry of the turnout deteriorates, the passing wheels' contact conditions may worsen, and the rate of deterioration may increase. A self-reinforcing spiral with an accelerating rate of deterioration may be created by installing an accelerometer on a crossing and a sensor to detect passing wheels alongside it. The wheel's location may be calculated in relation to the crossing's greatest vertical acceleration.

### 2.2.3    Rail Defects

Rail defects are often non-metallic inclusion or metallurgical origin flaws that occur during production as a result of poor local steel component mixtures. Later, these flaws cause a localised concentration of stresses under operational loads, resulting in rail failure. During the production process, faults are classified as external and internal flaws. In addition, the parts of the rail track can develop defects in the in-service rails. Most rail defects are found on the railhead, but several are still on the web and the rail foot. The following is an overview of the type of rail defect that is most common.

**Head checks**: Small parallel fractures at the gauge's corner characterise this common RCF defect. The distance between fractures varies based on the steel rail grade and local circumstances (typically smaller distances on head hardened rails). Cracks are placed at an angle of 35° - 70° to the longitudinal rail axis and more than 90° for high traction, depending on the wheel-rail contact condition. Shelling or spalling may result from cracks in the railhead that begin at an angle of between 10° and 15° and then spread parallel to the running surface, 2-3 millimetres below surface level, and finally in the gauge corner. Additionally, cracks can develop transversely and, in rare cases, cause the rail to fracture.
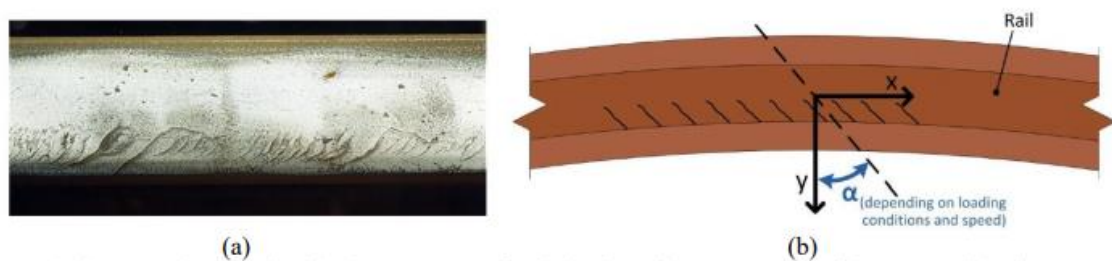


Figure 13. (a) severe head checks (b) illustrate head checks on the outer rail's gauge corner [23].

**Short-pitch corrugation:** On the running surface of short pitch corrugation, there is a pseudo-periodic pattern of sparkling ridges and dark hollows. The pitch ranges are from 20 to 100 mm, with a depth ranging from 0.01 to 0.4 mm in most cases, and the pitching depth is variable.

**Long-pitch corrugation:** Depressions in the running surface characterise long pitch corrugation ("waves"). With a depth of up to 1 mm, the pitch is typically between 30 and 300 mm. In this kind of corrugation, no apparent contrast between hollows and ridges.



Figure 14. Showing (A) Long-pitch corrugation defect [24], (B) Short-pitch corrugation defect [25], and (C) Short-pitch and long-pitch corrugation [26].

**Squats:** This RCF defect appears as a spreading and localised depression of the wheel-rail contact surface on the running surface, followed by a dark area comprising circular arc or V-shaped fractures. Within the head, the cracks develop at first at a shallow angle to the surface. The cracks develop transversely and lead to a rail break when they reach a depth of around 3-5 mm.
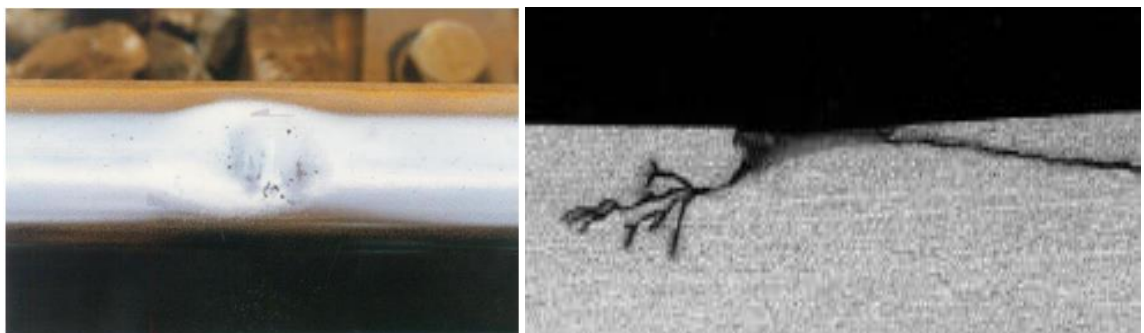


Figure 15. Showing (a) RCF-related squats in railway tracks (Kaewunruen, Freimanis and Ishida) and (b) Propagation of a squat [27].

**Progressive transverse cracking:** This issue may be caused by a defect within the railhead, a horizontal fracture inside the railhead, or a deep shelling of the gauge corner. The distinctive form of this progressive fracture gives rise to the name "kidney-shaped." This significant problem would reoccur on the same rail, resulting in large gaps if several failures occurred (risk of derailment). The non-destructive inspection technique can only detect transverse defects until the defect has progressed to the rail running surface and has broken out.



(a)  (b)
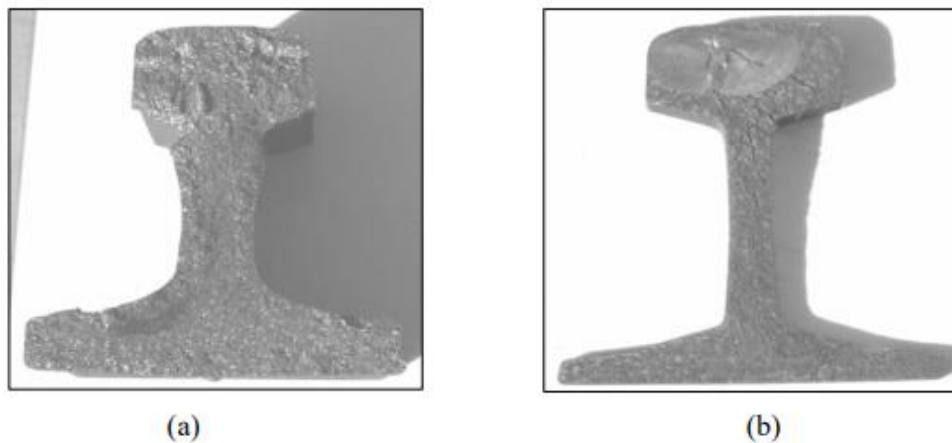
Figure 16. Transverse crack defects [28].

**Transverse fracture from corrosion pit:** Small sharp cracks in the corrosion at the foot base may offer a location for fatigue beginning. Cycled loading causes them to expand to critical size. This occurs in a transverse fracture at a fatigued area that is a little larger than a thumbnail, owing to the external fibre stresses experienced by the rail and the strength of the pearlitic rail grades presently in use.

Figure 17. Showing a transverse fracture from corrosion pit defect [158].

**Shelling:** an internal flaw that originates 2 to 8 mm below the gauge corner of the usually high rails on a curved track. Dark spots form in the gauge corner during the early stages of development, indicating shelling defects. On a horizontal or longitudinal axis, shelling cracks grow consistent with the gauge's corner's rail shape. The cracks may start in a longitudinal direction at an angle of approximately $10^o$ - $30^o$ to the rail surface, turn down and create transverse defects which, if not detected in time, may develop across a transverse plane and eventually result in rail failure. However, without the need for a previous shelling defect, transverse defects may also be caused directly by steel defects (inclusions) and grow in a transverse plane. Transverse defects are not visible visually because of their inner existence and may depend on regular ultrasonic rail inspection.
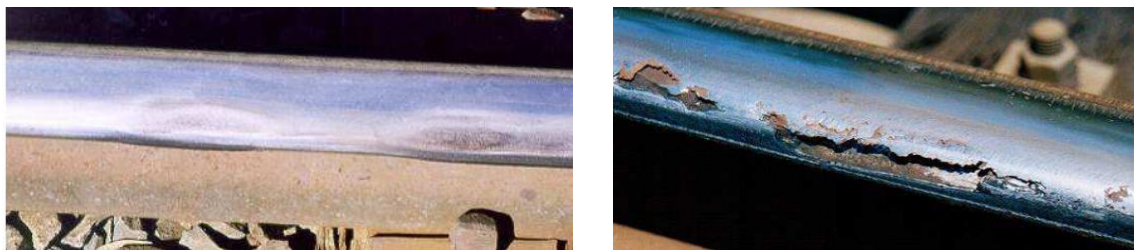


Figure 18. Showing (left) rail grinding can control moderate shelling defect, and (right) very severe shelling defect at Rail closure [158].

**Sub-surface-initiated fatigue:** During the track walking inspection or eddy current testing, no apparent surface fractures were found. When such defects have developed to a large enough size, as in the typical "Tache Ovale" defect, ultrasonic testing can identify defects.
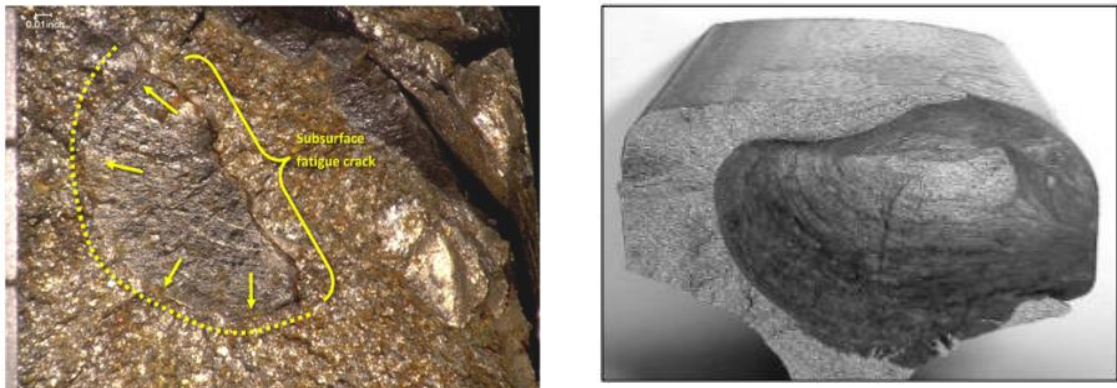
Figure 19. Tache Ovale and a subsurface fatigue fracture on the gauge side of the head [28-29].

**Fatigue from weld repair:** During the track walking inspection or eddy current testing, no apparent surface fractures were found. It is possible to detect signs of welded-in repair or plastic deformation on the running surface; however, this is not usually a reliable indicator of subsurface fatigue.

**Fatigue from machining stress raisers:** These defects are not readily apparent on the running surface near the fast fracture point. It involves machining the rail's foot, which is subject to the highest amount of tensile stress. Because of this, the design of turnouts must take into account the onset of fatigue from improperly machined stress elevators. Because the tired region is often small, it is impossible to identify unless it is precisely in line with the ultrasonic technique.
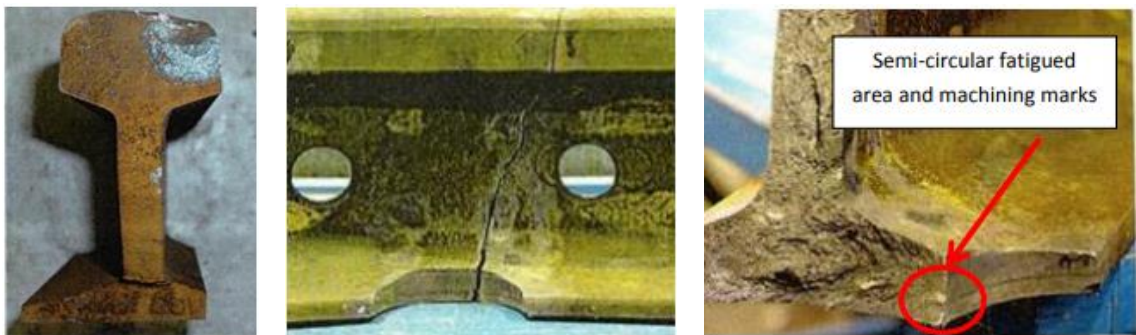


Figure 20. Showing (a) Weld-repair-related fatigue, (b) and (c) Defects are caused by fatigue from machining stress raisers [158].

**Wheel burn:** A elliptical-shaped self-hardened layer may form when a driving axle slips. This layer may either vanish or develop horizontally into a shell or transversely into the head, leading to an internal fracture leading to a break. On both track rails, there are wheel burn problems. Untreated wheel burns may lead to a squatting deformity.



Figure 21. Showing multiple wheel burn defects [30].

**Imprints:** This defect can be found on a variety of straight tracks at regular intervals, maybe over a long distance. A notch may form when an imprint has a sharp profile, leading to cracks and rail failures in the worst-case situation.



Figure 22. Showing imprints defects [158].

### 2.2.4 Cast Manganese Crossing Defects

The presence of structural damage in turnout components has been reported on a regular basis, resulting in increased railway costs of maintenance and downtime. High wear rates, plastic flow, broken crossing webs, cracked, loosened fasteners, and damaged components are examples of common damage types, as shown in Figure 23 [31][159].
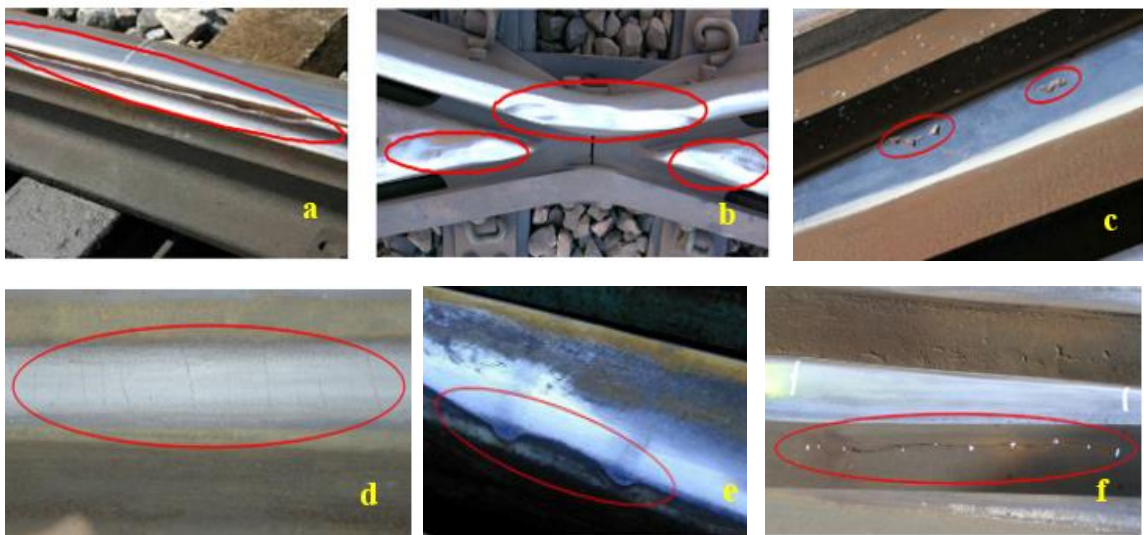


Figure 23. Example of damage on components: (a) part of the switch rail is detached, (b) plastic deformation and wear, (c) Spalling, (d) head checks, (e) squashing, and (f) cracks [31][159].

**Cracks on the crossing:** Subsurface defects such as bending fatigue and stress rising are caused by cracks in the crossing base. Microstructures with a harder surface are more prone to cracking in the case of Hadfield manganese steel crossings. Fatigue cracks may develop in the front and rear areas of the crossing nose. Inadequate wheel profile control, high dynamic forces, weak support, and manufacturing defects are possible reasons.

**Transverse cracking:** Cracking may occur under cyclic loads and result in a transverse break in the rail due to a geometric characteristic of corrosion pit or stress increase. Current NDT techniques cannot detect small corrosion pits. Visual inspection may also detect this failure process based on the defect's position.

Figure 24. Cracks running transversely over the crossing nose (left), Cracks running transversely over the crossing foot (right) [32].

**Cracking due to a defect in the casting:** Casting a large object, like a crossing, poses many challenges and often leads to casting problems, including shrinkage voids and porosity. If these defects are situated deep inside the casting body, they are invisible from the surface and have no impact on the life of the crossing. However, these defects may become stress boosters when the casting wears, resulting in spalling and collapse. At the moment, it is detected visually.
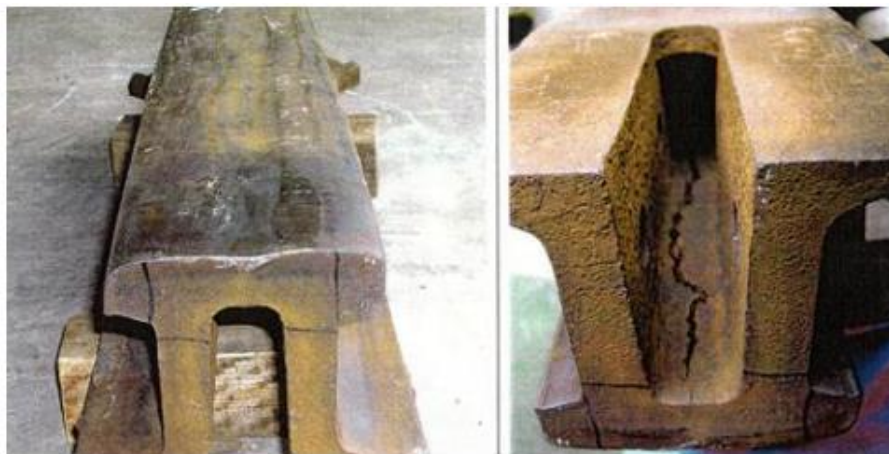


Figure 25. Longitudinal cracking from a shrinkage cavity [32].

**Spalling of the crossing:** A subsurface initiation with a subsequent fatigue failure merging causes spalling in the wheel transfer area. High dynamic forces produced by a non-wheel transfer zone and poor support conditions, as well as a wheel flange that does

not match the wheel transfer zone configuration and insufficient wheel profile control, are the main causes of this problem. Visual inspection is used to detect it at the moment.

**Crossing nose plastic deformation:** Only fixed-crossing turnouts have this defect. Plastic deformation is characterised by crossing yielding caused by strong lateral contact loads caused by improper geometry. Visual inspection and rail track inspections are usually used to identify this failure process.
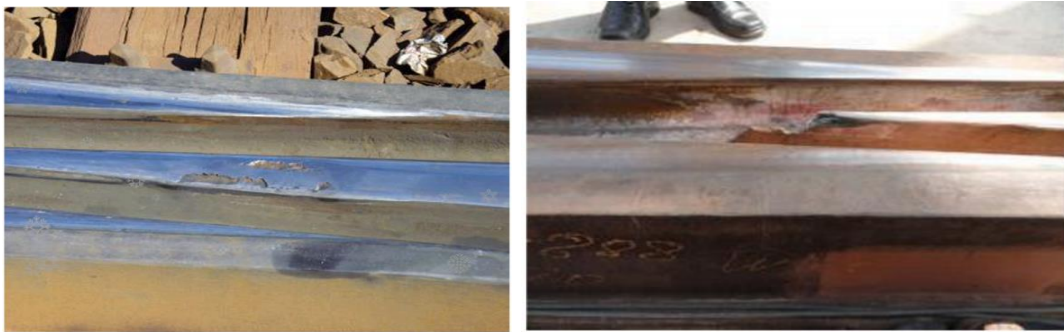


Figure 26. Spalling of the crossing (left) and the crossing nose has been deformed due to plastic deformation. (right) [32].

While it is reasonably straightforward to inspect conventional rails, this is not the case for cast manganese crossings with a mainly large-grain austenitic microstructure that induces ultrasonic beam scattering and attenuation. Flaws such as fatigue cracks and impact damage in cast manganese crossings occur mainly in the crossing's nose and wings. It will cause the section of the crossing to fail structurally. One key disadvantage of conventional ultrasonic inspection is that cracks initiating and propagating below the surface cannot be detected due to scattering and attenuation of the interrogating ultrasonic beam, resulting in the acoustic emission method becoming a more suitable technique for crack growth monitoring.

### 2.2.5 Rail Inclusions

Large brittle inclusions may cause initiation of cracks below the surface of the railhead, including those containing Ca, Al, Si, and O. Brittle inclusions allow fatigue to propagate in two ways so that cracks can nucleate immediately because there is little room for any deformation due to the surrounding matrix and induce microcracks at the matrix-inclusion interface [33]. These cracks will propagate and fail during operation. As such, the railway industry has been looking for ways to make these inclusions smaller and denser. As the challenges associated with brittle inclusions become less of a concern, emphasis has changed to soft, ductile inclusions, specifically MnS.

MnS, $Al_2O_3$, and $SiO_2$ are the most common types of inclusions. Inclusions found in the steel on solidification can have different shapes included elongated in the case of MnS or square like in the case of $Al_2O_3$, whilst carbides can be spherical with different diameters. After deformation, four different pearlitic rail steels were examined. MnS inclusions became elongated, while Al inclusions remained tiny and circular. $Al_2O_3$ stringers and hard angular $SiO_2$ were among the other inclusions in the deformed steel [34]. These alumina and silica inclusions are prone to start fractures because they are brittle and may shear in a brittle manner when loaded. Attempts are made throughout the rail steel production process to prevent the development of these impurities. Lui et al. found that steels with a high sulphur content had greater MnS inclusion densities [34]. Table 1 shows the R260 rail steels grade composition that appears to have less but more extensive inclusions than those of the R220 rail steels grade. These inclusions are oriented longitudinally [35].

Table 3. The chemical composition (in weight percent) of R220 and R260 rail steels grade, as published by the Institute of Rail Welding [36].

| Specification | Grade | Chemical composition | | | | | | | | | Mechanical properties | | |
| | | % by mass | | | | | | | | | Rm (Mpa) | Elongation (%) | BHN Hardness |
| | | C | Si | Mn | P | S | Cr | Al | V | H2 (ppm) | | | |
| EN 136741 | R220 | 0.50-0.60 | 0.20-0.60 | 1.00-1.25 | ≤ 0.025 | 0.008-0.025 | ≤ 0.15 | ≤ 0.004 | ≤ 0.03 | ≤ 3.0 | ≥ 770 | ≥ 12 | 220/260 |
| | R260 | 0.62-0.80 | 0.15-0.58 | 0.70-1.20 | ≤ 0.025 | 0.008-0.025 | ≤ 0.15 | ≤ 0.004 | ≤ 0.03 | ≤ 2.5 | ≥ 880 | ≥ 10 | 260/300 |

After that, the steel is rolled to produce the rail profile, which lengthens the impurities in the rolling direction, transforming them from spherical to oval. In rail steel, the majority of inclusions are longitudinally oriented and occur in a range of sizes. The rails are subsequently placed into service, and the rail surface and the inclusions deform further in service. Longitudinal loads exceed transverse loads, leading to a flattened inclusion at the surface, which serves as a crack initiation site [10]. This significant inclusion deformation is more consistent with MnS inclusions than $SiO_2$ or $Al_2O_3$ inclusions because MnS inclusions are very ductile.

## 2.3    RAIL FATIGUE

When a material is exposed to cyclic stresses, a crack may occur at loads considerably below the yield strengths under a static load of the material. Even in ordinarily ductile materials, fatigue failure is brittle, with minimal plastic deformation. Axial, flexural, or torsional stress may be applied to cause fatigue. In the initiation of cracking in stress concentration areas, fatigue failure phases increase crack propagation and eventually catastrophic failure.

Fatigue cracks have three phases of behaviour: (1) nucleation, (2) steady growth, and (3) unstable propagation leading to final failure [37]. RCF crack initiation and propagation are necessary to study three-dimensional to evaluate the severity [38]. Fatigue cracks should be detected early to minimize propagation and severe degradation of the rail system's structural stability [39].
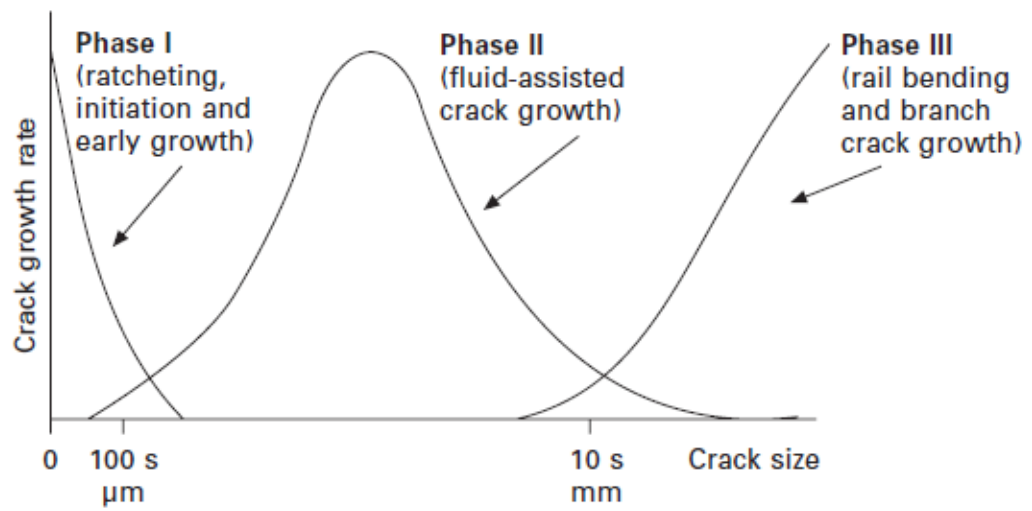


Figure 27. Three stages of fatigue crack [40].

Currently, pearlitic steels (e.g., R220 and R260 rail grades) are primarily used in rail manufacturing because of their low cost and reasonable wear and fatigue performance. Many researchers have studied RCF in the pearlitic rail steel to optimise rail steel grades [41-42]. Smallman investigated the impact of loads on three pearlitic rail steels using an Eddy Current probe to identify a fracture during the early stages of RCF [43]. The results indicated that the best resistance to rolling contact fatigue was found in head-hardened grade eutectoid steel. Comparing pearlite and bainitic rail steels, it was discovered that bainitic rail steels had a better rolling contact fatigue resistance but a poorer wear resistance [44].

### 2.3.1 Rolling Contact Fatigue (RCF)

Rolling contact fatigue (RCF) in rails is one of the most significant mechanisms of rail damage since it is hard to predict when this is going to happen. Because cracks and defects can develop in materials even under safe loading conditions, it was found that approximately 80-90% of all service failures are caused by fatigue. RCF cracks may originate on the surface or underneath it, as shown in Figure 28. Fatigue failures can occur under cyclic stress, which is well below the ultimate tensile strength (UTS) and, often, below the yield stress. There are two types of cracks that develop on rails as a result of rolling contact fatigue. Cracks develop both underneath and on top of the surface. Severe vertical stress combined with material defects causes cracks to form under the surface. Cracks used to be produced mostly as subsurface cracks. Rolling contact fatigue failures related to material defects have decreased as steel manufacturing methods have advanced [166]. Following the Hatfield rail accident in October 2000, which killed four passengers and wounded more than 70 of the train's 182 passengers, the railway industry was compelled to take RCF issues seriously [45].



Figure 28. A high-speed train had a catastrophic fatigue breakdown south of Hatfield station in the United Kingdom (October 2000) [27].

As shown in Figure 29, the difference in load conditions causes a variance in the rail and wheel contact patch, which leads to various kinds of rail defects. Figure 29 (a) shows how vertical stress causes surface and subsurface cracks in the contact area. Figure 29 (b) illustrates the beginning of surface cracks resulting from both vertical and lateral stress. Figure 29 (c) illustrates the development of RCF fractures started from the subsurface because of the vertical loading of a rolling material. If interfacial shear and slip follow the rolling contact, as shown in Figure 29 (d), the contact surface's plastic deformation leads to crack beginning and growth. Surface irregularities and surface cracking may occur as a result of material defects and inhomogeneities under such loading (Figure 29 (e)) [46].
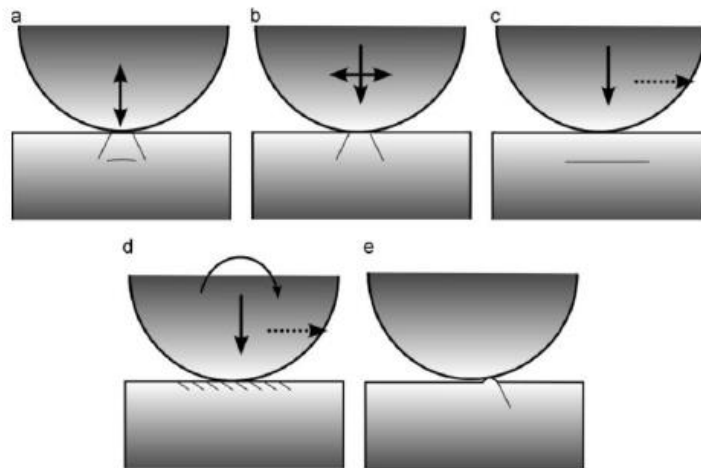


Figure 29. Different kinds of loading of contacts and corresponding crack formation (a) vertical loading results in the development of surface and subsurface cracks, (b) vertical and lateral loading results in the formation of surface cracks, (c) Subsurface cracks are caused by vertical loading of rolling material, (d) contact between rolling and interfacial shear and slip results in surface cracks, (e) irregularities in the surface cracking [46].

In the loading scenario, the wheel-rail contact induces plastic deformation of the rails, as described above. Depending on the loading and material, shear loads result in thinner plastically deformed layers with a larger material strain and a greater hardness gradient, whereas increased normal loads result in larger plastically deformed layers and

decreased hardness ranges [160-161]. Hadfield manganese steel's intense strain hardening ability, higher hardening depths are indicated for Hadfield manganese steel than a pearlitic grade, where the hardness increase would be three times more than the base material [162]. Pearlitic rail steel is subjected to significant plastic deformation, aligning the microstructure in the shear strain direction. No grain shearing is found for Hadfield manganese steel (See Figure 30).
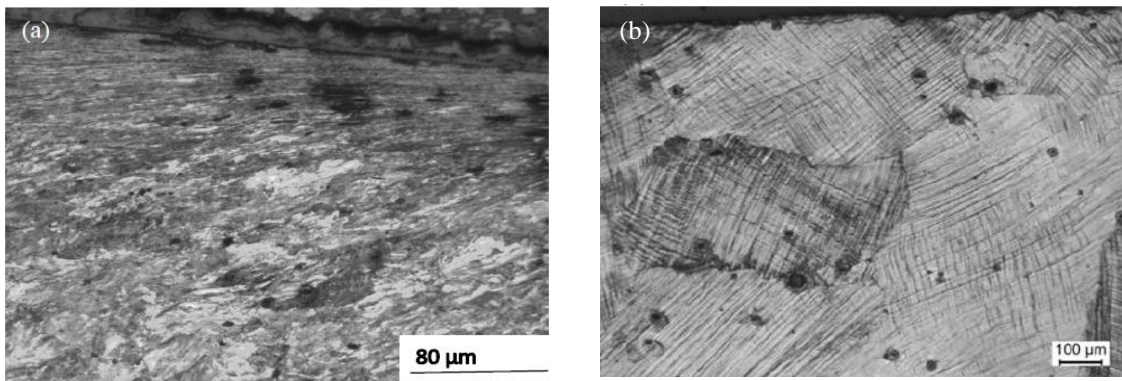


Figure 30. Wheel-rail contact surface microstructure deformation: (a) pearlitic steel and (b) Hadfield manganese steel [47].

### 2.3.2 Crack Growth Models

Material defects, such as those found in rail steels in the UK, may serve as stress concentrators and crack nucleation supports. However, it is unclear to what degree the inclusions impede fatigue cracking initiation. Even yet, cracks are more likely to develop on the rail's surface under extreme pressure and extremely thin ferrite layers that may act as planes of weakness [48]. MnS inclusions of vigorously strained flattened may also be initiated by cracks [49]. It is believed that inclusions may function as crack initiators in three different methods. The first is that localised deformation bands before inclusion may initiate microcracks. Two further possibilities are that they may induce interfacial debonding owing to high-stress concentration within elongated inclusions or that they could cause cracking by fracturing brittle inclusions [34]. Upon reaching a particular

depth, which depends on the material and applied load, a crack was shown to have propagated. This is the phase at which the crack progresses. The speed at which the crack is growing is accelerating at this point. Due to the loading of the passing trains, fatigue cracks are still propagating at this time [27]. It was originally believed that pro-eutectoid limits were satisfied by cracks less than 50 µm in length in 220-grade rail steel. Figure 31 shows that cracks tend to grow along the direction of the strain field in general, although they may also follow the grain boundaries of ferrite [49].
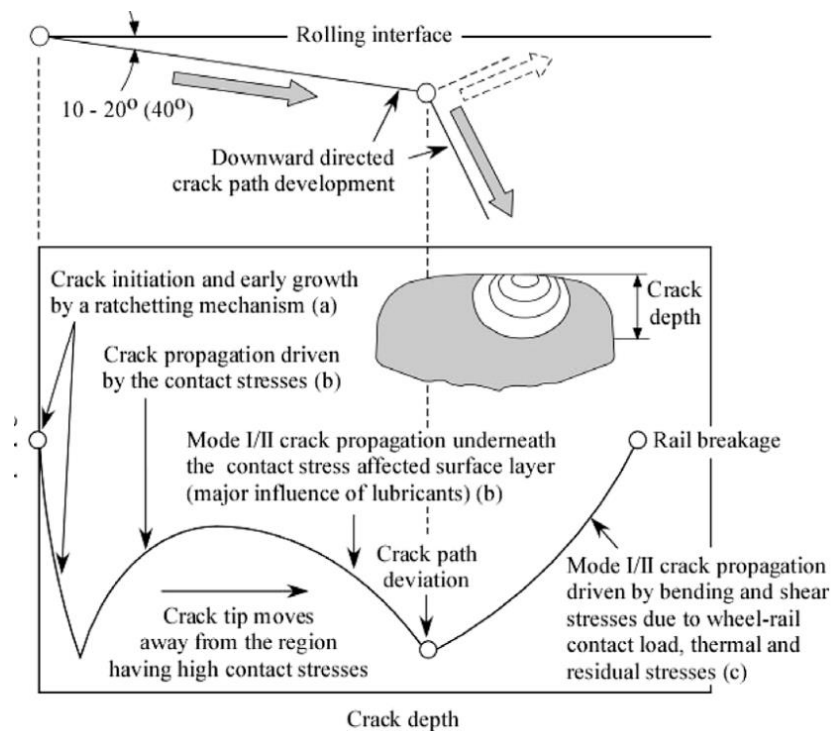


Figure 31. Cracks grow in the direction of the strain field [49].

Additionally, MnS inclusions in the steel act as crack propagation pathways (see Figure 30), the pearlite grain boundary, and the orientation of the strain field. Due to the absence of preferential pro-eutectoid ferrite straining, MnS inclusions were shown to have a greater role in crack initiation and distribution [49]. After cracking, the crack develops at a 60-80 degree angle to the rail surface. The crack will eventually get larger, causing failure of the rail.

Various models have been used to study the initiation and propagation of cracks. Figure 32 shows a crack propagation model in which the crack is divided into three phases [50].
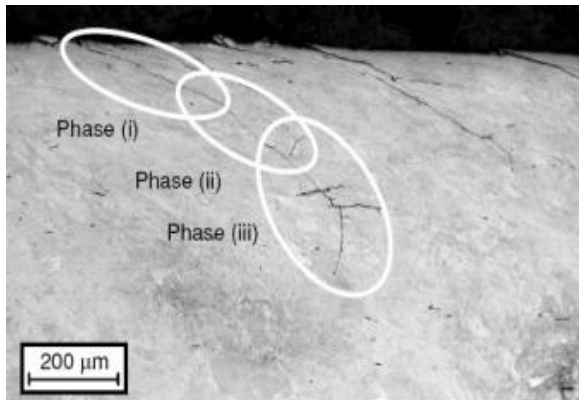


Phase (i) - Shear stress has induced surface initiation.

Phase (ii) - Crack development is characterised by transient behaviour.

Phase (iii) - subsequent crack growth caused by tension and/or shear forces.

Figure 32. The three stages of RCF accelerated the crack propagation on a railhead. [50].

Stage I: The crack propagates in conjunction with persistent slip bands. Before spreading to stage II, crack expansion in polycrystalline metals occurs in a few grain diameters. The crack propagation rate in stage I is extremely slow, approximately nm per cycle; however, in stage II, it may reach µm per cycle. A pattern of striations shows the fracturing surface of stage II of crack propagation. Figure 33 shows that each striation is created by a single stress cycle (See Figure 33-34).
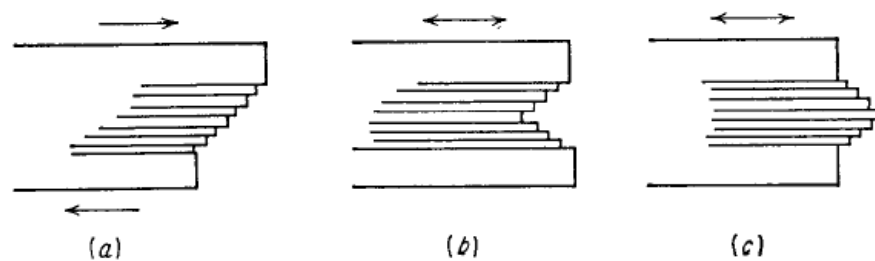


Figure 33. Model for crack initiation by Wood [51].
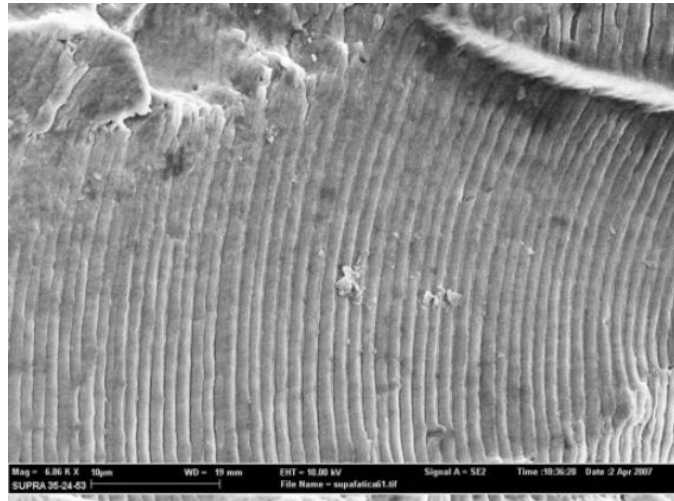
Figure 34. Fatigue fracture striation [52].

Fletcher and Beynon (2000) created a three-mechanism model of RCF-initiated crack development as a crack propagation prediction model. The tensile and shear stress intensity factors ($\Delta K\sigma,\tau$) for three different modes, consisting of ratchetting and ductility exhaustion, shear mode crack growth, and tensile mode crack growth, are compared in this model. Following that, a decision is made about whether crack growth can occur in a given loading situation (see Figure 35).
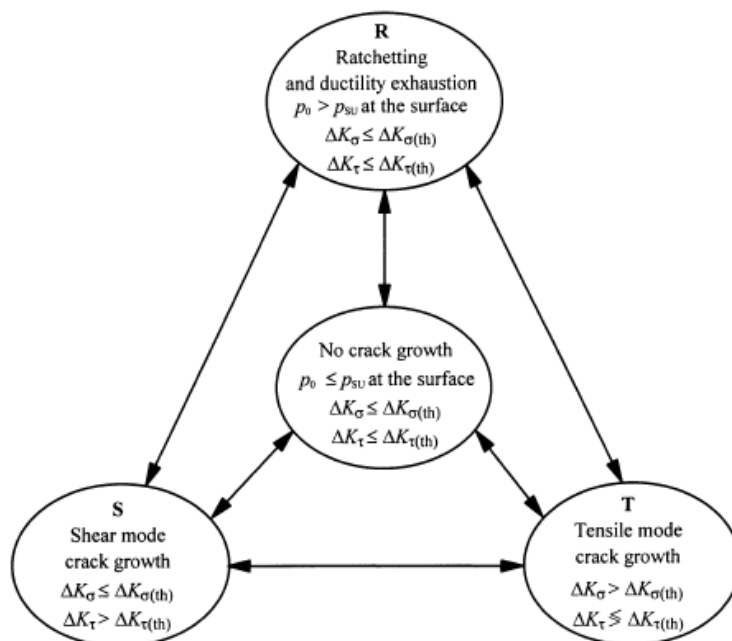


Figure 35. RCF's three-mechanism model initiated crack propagation [53].

# CHAPTER 3

# ACOUSTIC EMISSION AND OTHER NDT

# METHODS

# CHAPTER 3: ACOUSTIC EMISSION AND OTHER NDT METHODS

In this chapter, the author reviews articles and literature related to the AE technique. General knowledge of AE testing, the use of AE testing as an NDT technique in rail and emphasizes a literature review on quantitative analysis to find knowledge gaps are presented in this chapter. To enhance knowledge for research in the field, a review of the signal processing under field conditions is therefore included at the end of the chapter.

## 3.1    FUNDAMENTAL OF ACOUSTIC EMISSION

In the 1950s, Josef Kaiser discovered the Kaiser Effect in acoustic emission response during tensile testing of metals. The Kaiser effect relates to the amount of AE activity a metallic structure generates if the previous maximum load is not exceeded after initial loading and unloading have been performed [54]. The AE method is a condition monitoring technique developed to evaluate various structures, including metallic ones continuously. AE is widely recognised and used in a wide variety of industries to monitor various types of materials, including steel, reinforced concrete, composites, etc. [55].
 AE involves the generation of elastic stress waves, with a frequency content typically between 20 kHz and 1 MHz during crack growth. AE can be used to monitor damage in structural components in real-time by detecting using piezoelectric sensors the energy released in the form of elastic stress waves from the crack tip as it propagates under load. Detection, location, and assessment of the type of defects in materials made of metal, concrete, or composites are all possible with the use of AE.
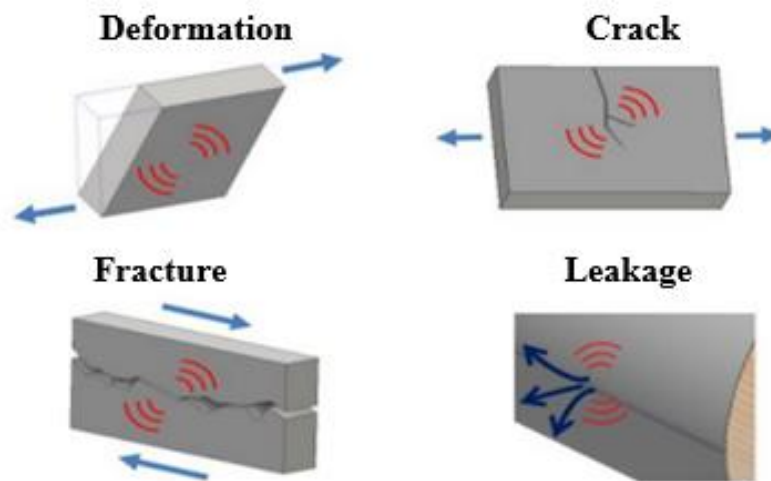
Figure 36. Damage patterns using acoustic emission examination.

The detection can be done by mounting the piezoelectric sensors in contact with the surface of the material to be monitored using an appropriate couplant such as grease or Araldite®. The elastic energy released is transferred through the material as transient elastic stress waves, which piezoelectric sensors placed on the surface can detect. Although most of the stress waves produced are elastic, inelastic stress waves may occur when stress exceeds the yield limit [56].

### 3.1.1 Acoustic Emission System and Parameters

AE sensors are capable of detecting very small signals involving surface displacements as low as 25 picometres. A typical commercial AE system consists of one or more AE piezoelectric sensors used to detect AE signals, a pre-amplifier that amplifies the initial signal (typical amplification gains are 20, 40 or 60 dB with the most commonly used amplification being 40 dB), main amplification which also provides the required phantom voltage for the AE sensors to operate (typical 28 VDC although more recently 5 VDC sensors have been made available also), digital data acquisition with a sampling rate up to 20 MS/s, and an industrial computer where the AE signals are recorded,

displayed and analysed. The Data acquisition card performs the analogue-to-digital conversion of the AE signals before they are logged in the computer for further processing using a dedicated software package. The measured AE signals are stored as data files for later signal processing and evaluation. Figure 37 shows the basic working principle of the AE condition monitoring technique. The typical AE waveform arising from crack growth and the key AE parameters of interest are shown in Figure 38.
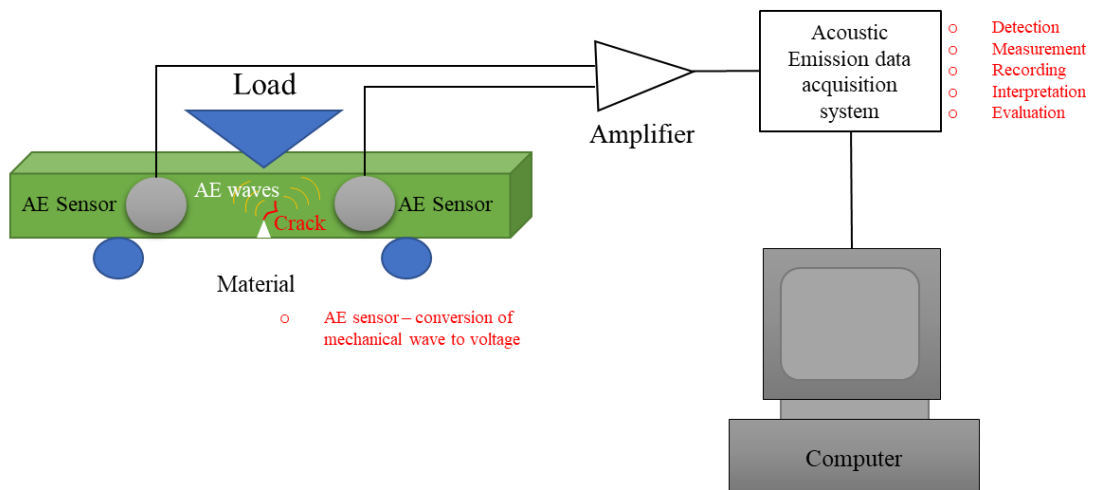


Figure 37. Scheme of the acoustic emission system for the identification of damage.
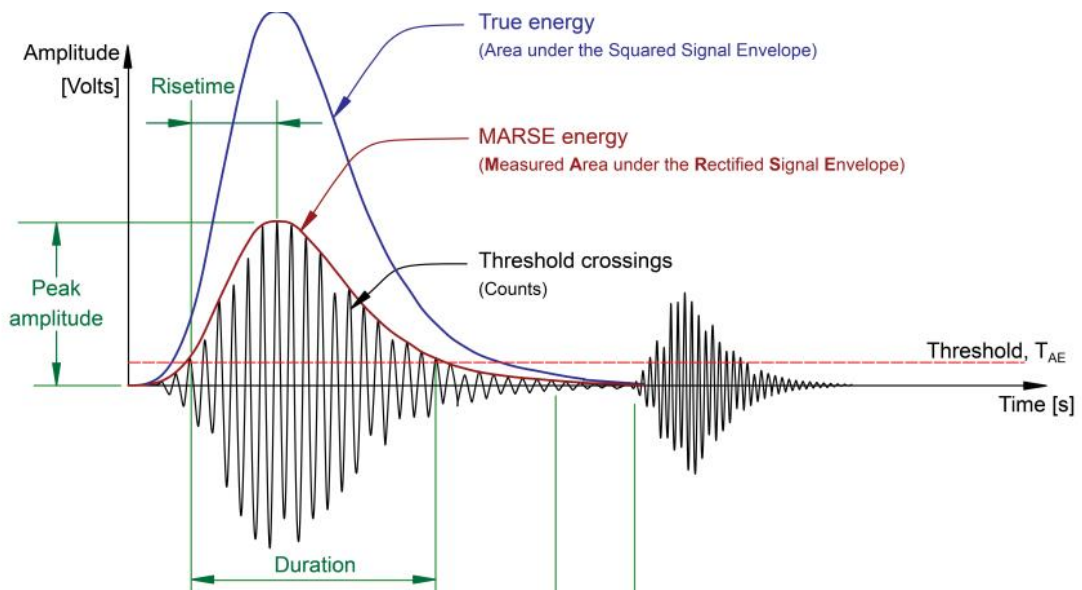


Figure 38. Acoustic emission waveform and important parameters [57].

An AE event is defined as a single dynamic process that releases elastic energy detected by the AE piezoelectric sensors. As the AE source is identified, the local mechanism that causes the AE event is detected. The electric signal observed at the transducer's output is called the AE signal. In continuous background noise, the AE measurements are generally carried out using an appropriate filtering method. The most typical type of filter is the definition of an appropriate threshold level above the background noise and below the AE signals generated during damage propagation. Typical AE parameters of interest include amplitude, duration, rise time, etc., as discussed in more detail [58].

**Amplitude (A)** is one of the most significant parameters associated with the measured voltage of a detected waveform. It is typically presented in decibels (dB) rather than V. It is a critical parameter for AE data analysis since it is inversely proportional to the degree of the damage mechanism that resulted in the recorded AE activity. Therefore, AE signals with amplitudes below the minimum threshold specified by the operator are not recorded during measurement and are automatically discarded.

$$dB = 20\log(\frac{V_{max}}{1\mu Volt}) \text{ - Pre-amplifier Gain (dB)}$$

**Duration (D)** is the period between the signal's initial and final threshold crossings. The length of an AE signal may be used to distinguish between various kinds of sources and screen out noise.

**Rise time (R)** is the time period between the initial threshold and the maximum amplitude, hence the time that the AE signal has been rising before it attained its maximum amplitude. This parameter is linked to the propagation of waves between the

AE event's source and the sensor. As a result, the rise time is utilised to discriminate between signals and additional criteria for noise filtering.

**MARSE, Measured Area under the Rectified Signal Envelope (E)**, is the AE signal's rectified voltage measured throughout an AE hit. MARSE is a parameter that is frequently used for data analysis purposes.

**Counts (N)** is the total number of times the amplitude of the AE signal exceeds the defined threshold throughout its duration. Thus, a single hit may result in one or many counts based on the size of the AE event and the material characteristics.

**Threshold** is the signal level below which no AE signals will be recorded. This is often used as the simplest of all filtering methods in order to discard unwanted background noise. However, when higher noise levels are involved more complex filtering methods are available and can be used.

### 3.1.2 Acoustic Emission Sources

Material plastic deformation or crack propagation are the two most common AE events. The more brittle materials produce more intense AE activity in comparison with the more ductile ones. The movement of dislocations causes atomic planes to slip past one another, while plastic deformation occurs at the microscopic level. Deformations on an atomic scale result in the release of energy as elastic stress waves that may be thought of as spontaneously produced ultrasounds that move through the structure. Cracks in the metal may cause stress levels to be several times higher in the area immediately around the crack tip than in the surrounding region when cracks are present. Therefore, AE behaviour can also be detected as the material undergoes plastic deformation at the crack tip.

Two kinds of fatigue cracks cause the generation of AE activity. The first type involves brittle particles (e.g., non-metallic inclusions such as $Al_2O_3$) near the initiation

point of the crack tip. Cracking these particles generates more intense AE activity because of their lower ductility, resulting in higher amplitude and energetic AE signals. The second type is the crack tip distribution caused by dislocation movement and small-scale cleavage produced by triaxial stress. The magnitude and velocity of the source case are linked to the total energy generated by AE and the amplitude of the waveform. The AE signal's amplitude is related to the crack propagation velocity and surface region. There are greater AE signals from large, discreet crack leaps compared to small, steady crack propagation. In the AE test, these elastic waves are identified and converted into electrical signals.

Detailed examination and analysis of these AE signals give useful knowledge on the origin and significance of the damage evolving in the material. As described in the following section, sophisticated equipment is required to detect AE signal energy and distinguish which signals are of interest and related to actual damage propagation and are not the result of background noise.

The list of materials in Table 4 shows where AE can be employed along with the different types of potential AE sources.

| Materials where AE has been evaluated |
| --- |
| Metals<br>Ceramics<br>Polymers<br>Composites (including those with metal, ceramic and polymer matrices and a wide variety of reinforcement materials)<br>Wood<br>Concrete<br>Rocks and geologic materials |
| **Potential AE sources** |
| Microcrack sources such as intergranular cracking<br>Macrocrack sources such as fatigue crack growth<br>Slip and dislocation movement<br>Phase transformations<br>Fracture of reinforcement particles or fibres<br>Debonding of inclusions of reinforcements<br>Realignment of magnetic domains<br>Delamination in layered media<br>Rockbursts<br>Fault slip (Earthquakes) |

Table 4. Materials that have been measured by AE and the source mechanism that produces AE [59].

### 3.1.3   Signal Processing

The term AE describes transient elastic waves caused by the sudden release of energy from localised damage evolution sources. Solid materials generate these acoustic waves when they are deformed or damaged. AE is related to a long-term change in the material's microstructure. AE is linked to the ultrasounds generated when the material is broken according to a more straightforward explanation.

Reported AE signals can be classified into three main categories: burst, continuous, and mixed signals. Burst signals are a form of AE activity associated with distinct AE signals linked to individual events occurring in a material, as seen in Figure 39a, e.g. crack growth. The burst AE signal can be caused by an unstable mode of plastic deformation or material degradation and is associated with short-duration and high-amplitude signal characteristics. Sometimes the form of a burst waveform is approximated by an exponentially diminishing sinusoid. The continuous AE signal consists of a low amplitude signal produced by a large number of sources simultaneously. As shown in Figure 39b, the AE signal has a random character, which is the product of alternating several burst type signals of indistinguishable amplitude.

A typical example is a noise resulting, for example, from fluid flow. Usually, general dislocation movement is found during the plastic deformation of metallic materials. In most realistic cases, both burst and continuous signals are detected (Figure 39c), where both components may be of concern or where one or the other may represent noise. Many AE technique applications detect, distinguish, and analyse signals resulting from both AE signal types. Most of the energy spent on fracture processes in ductile metals, for example, goes to the development of plastic deformation, which typically results in the generation of continuous AE signals. This is why defects can usually be observed in ductile metals at their early stages, taking advantage of the continuous AE signals detected. Reliable detection of certain defects, such as stress corrosion cracking and creep, is also based on the detection of continuous AE signals and their analysis. Burst acoustic emission may detect defects or conditions such as non-metallic inclusion fracture, corrosion material fracture, crack jumps in a brittle material, advanced stages in ductile metals, and others. The parameters commonly used to analyse burst waveforms

include amplitude or counts, whilst the parameters commonly used in data analysis with continuous signals are AE-RMS.
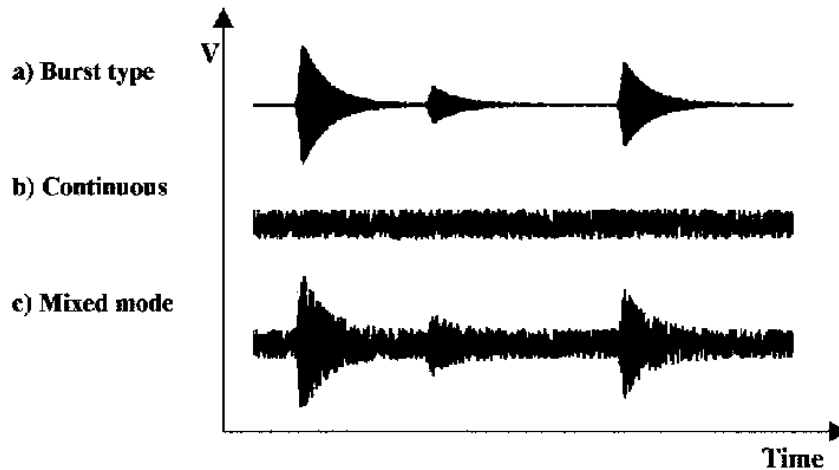


Figure 39. Schematic representation of different AE signal types [60].

AE activity can be generated due to a variety of mechanisms including, dislocation movement, phase transformation, crack initiation and propagation due to the application of stress, fibre fracture, twinning, and debonding.

During the data acquisition process, it is essential to filter out as much unnecessary noise as possible. After discussing a hit-based AE system, it will be addressed to determine an acceptable threshold before testing is needed. Any hits whose amplitude goes below the threshold are eliminated. The hit definition time (HDT), peak definition time (PDT), and hit lockout time (HLT) are three essential factors that the user specifies to identify a hit. High-Definition Time (HDT) is the greatest amount of time between the first and final threshold crossing. HLT specifies when the system is locked out after a hit has been captured before a new hit can be detected. As long as the HLT value is not too low, the AE hit reflections that were originally recorded may be logged as well.

On the other hand, the system may omit some important signals if the HLT value is too high. The PDT allows for accurate signal peak determination and should be set as low as feasible. True peaks may not be detected if it is set too low [180]. The sample rate is another important AE acquisition parameter. The real frequency included in the original data cannot be shown in the sample rate is too low. In order to sample a continuous signal adequately, it must be sampled at a rate higher than half its maximum frequency.

### 3.1.4   Intensity of acoustic emission signal

The intensity and level of activity of the AE source need to be determined to evaluate the damage severity accumulated with time. Post-test analysis may be required for a more accurate interpretation of the AE activity detected. Statistical evaluation of the AE signals obtained by each piezoelectric sensor, such as AE signal amplitude distribution, hit duration and hit density, are particularly useful. Other useful parameters include the Felicity ratio, which measures the damage level accumulated in a structural component under loading, unloading, and re-loading pattern [61]. During plastic deformation, various processes can generate AE. Their effect on the level of AE signal generation is summarised in Table 5.

Table 5. The AE signal's intensity is caused by a variety of plastic deformation processes [38].

| Mechanism of plastic deformation | Strength of AE signal |
|---|---|
| Frank-Read source | strong |
| Twin nucleation | strong |
| Yield phenomenon | strong |
| Cutting of coherent precipitates by dislocations | strong |
| Orowan bowing | weak |
| Twin growth and thickening | negligible |
| Grain boundary sliding without cracking | negligible |

The AE generation behaviour in a structure is influenced by microstructural variation. The AE behaviour is suppressed when a metal or alloy is subjected to cold

work. Due to high dislocation density that results in reduced glide distances. AE intensity tends to increase along with material strength as grain size is decreased. The grain size effect can be overridden by other factors, however. AE intensity declines with ageing in most precipitation-hardened alloys. The mean free path of mobile dislocations is decreased as dislocations or hard precipitates strengthen alloys. However, the median frequency rises even while AE intensity reduces when the gliding motion of individual mobile dislocations is constrained, even as the number of mobile dislocations increases [62-63].

Twinning happens when a crystal part is sheared in a new location and becomes a replica of the original crystal lattice. As a result, in specific directions, the crystal shears through specific lattice planes. Schmid and Wassermann's study focused on understanding the twinning mechanism during plastic deformation in metals [64]. Since then, many twin formation models have been suggested. Another significant origin of AE activity during deformation is related to second phase particles and inclusions. Inclusions are responsible for significant AE activity while cracking in steels loaded in the highest strength aluminium alloys. As a result of MnS inclusions decohesion, AE is produced in steels in large quantities. It produces signals similar to bursts in quantity, and their number is related to the number of inclusions present in the sample. Short-transverse-direction AE activity is highest, and longest-direction AE activity is lowest in inclusion-induced AE. Most of the AE observed in many Al alloys is caused by the fracture of Al-Si-Fe and other non-metallic inclusions, which frequently masks the AE activity near the yield point. Because numerous small particles contribute to the total activity, inclusion-induced AE produces continuous AE signals. In the last phase of the fracture, most materials and structures generate powerful, audible sounds. During cracking in high strength materials,

strong elastic stress waves are produced. Long before the final fracture, AE may be diagnosed, preventing catastrophic brittle failure in engineered structures. The primary driving force of AE technology development has been and continues to be structural health monitoring [65]. Only a tiny number (less than 100) of AE signals are generated immediately before the final fracture of brittle materials, such as ultra-high-strength steels and ceramics [62].

There is minimal subcritical crack growth, limiting AE activity generation. This behaviour is unfortunate because it is most likely that these materials will exhibit unexpected failure, and the need to avoid those failures is greatest. Even so, because a significant proportion of AE events have peak amplitudes above 60 dB or 1 mV, about 1V at the sensor before amplification, all the micro-fracture processes involved in these materials, for example, quasi-cleavage, cleavage, and intergranular crack, are all involved in these materials, can be easily detected. Non-metallic inclusions exert a significant effect on AE behaviour in moderate to high fracture toughness materials. The decohesion of MnS inclusions is the primary cause of excessive AE signals in ductile steels emitting relatively strong AE signals (peak amplitude <55 dB), starting with the early stages of elastic loading. Plastic flow and inclusion fracture can also cause AE events, especially in Al alloys. Materials with low toughness have inclusions that produce the highest peak AE intensity, lower than brittle fracture. The inclusion effect is highest when samples are stressed transversely. Maximum load counts are 20–50 times higher for short-transverse samples than for long-transverse samples.

### 3.1.5   Kaiser Effect and Felicity Effect

Phenomena in acoustic emission testing have a permanent effect. Until the previously implemented load is reached, a sample produces no AE activity when deformed, unloaded, and reloaded. The Kaiser effect refers to this kind of behaviour. The primary source of AE in loaded metal structures is plastic deformation, and the Kaiser Effect causes AE activity during further material deformation. AE generation occurs only as stress levels surpass the previous stress level in Kaiser Effect [66]. In the Kaiser effect, no AE activity will be generated when the load is released and applied again before the maximum of the previous load is reached. The Kaiser effect is useful, though not irreversible, for deciding a prior loading stage. Extended holding and annealing will minimize the load at which AE begins to be generated again before the previous loading is exceeded [67].

The Felicity Effect is an AE-related effect that decreases the Kaiser effect under high load materials. The Felicity effect enables AE to continue to be emitted before exceeding the previous maximum load.
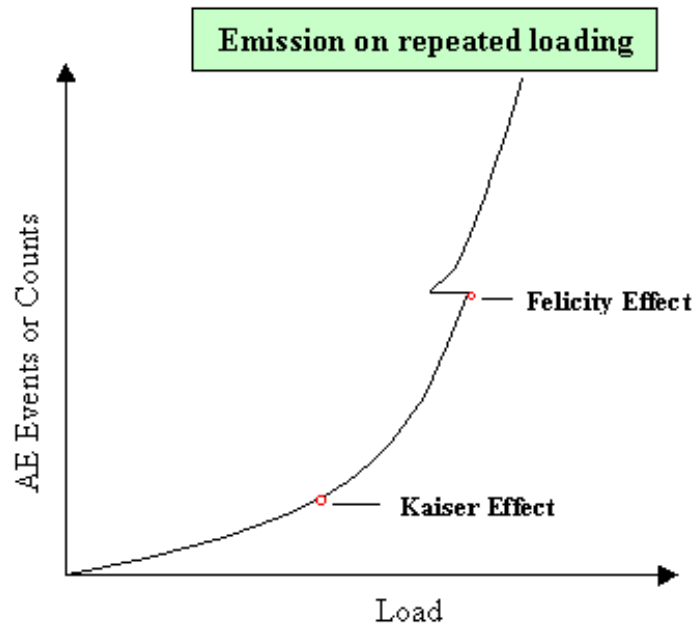
Figure 40. The effects of Kaiser and Felicity on the plot of AE vs Load [68].
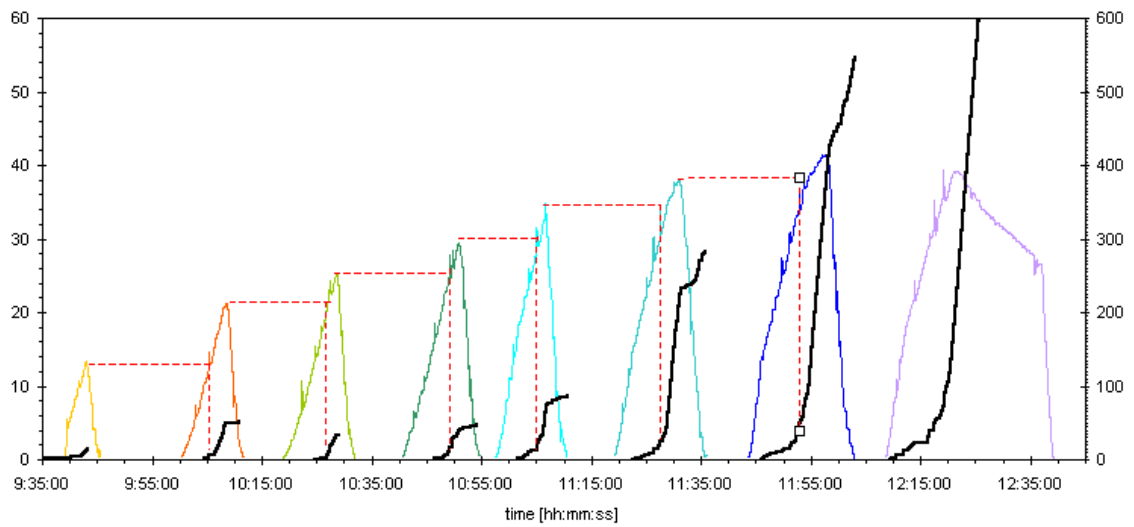


Figure 41. In a concrete specimen that has been cyclically loaded, the Kaiser effect is shown. Thick black lines show the AE activity, thin lines represent the load., and dotted lines represent the Kaiser effect [69].

## 3.2    QUANTITATIVE ACOUSTIC EMISSION ANALYSIS

The study of full quantitative acoustic emission analysis was largely neglected for rail steel evaluation until recently. The connection between AE count rate and ΔK for steel and welded steel specimens beyond the rail industry context has been examined in several papers, showing a roughly linear relationship on a logarithmic scale [70]. Based on short-term AE monitoring and supporting assumptions that crack propagation events are happening near peak load. Talebzadeh [71] found that the connections between AE crack propagation rates and count rates indicate the feasibility of predicting the remaining fatigue life of a structure. However, the correlation increases when the AE data is limited to the top 5% and 10% of the load range. A clear power-law correlation becomes evident when plotting the count rate against the stress intensity factor (ΔK) for many steel grades. Strong correlations were observed between the peak load AE rate per cycle and the energy emitted by crack growth. The ratio R of the minimum to maximum applied stress was also shown to improve the count rate. An important correlation for crack growth under variable load was reported by [72]. The power-law relationship between the AE count rate and ΔK was used to detect early crack propagation in rail steels, where ΔK values are lower. Fatigue testing was carried out, stopping the test when ΔK reached a significant value. Using optical and SEM microscopy during fractography of tested samples, cracking characteristics were evaluated. A sudden increase in AE activity was observed to coincide with crack growth onset [73]. A quantitative method for calculating the frequency-dependent media attenuation of AE source parameters was considered. The current method is designed to find certain typical values in frequency and time domains that are least sensitive to absorption without becoming interested in the whole medium attenuation computation [74].

In three-point bending tests, the link between the crack propagation mechanism and AE signals was investigated, and the impending fracture was detected by analysing the amplitude distribution, total AE energy, and AE event count [75]. Other AE parameters, as well as AE hit rate and duration damage characterisation, are addressed by Aggelis et al. They found a cracking mode from tensile to shear as the duration and rise time rose [76]. The earliest attempt to detect crack initiation in samples under a four-point bending test is the quantitative AE study for rail steels. By estimating crack growth in an aluminium alloy under cyclic loading and comparing AE count rate with fracture mechanics parameters, Bassim, Lawrence, and Lui [73] investigated the hypothesis that the count rate was caused by either crack growth rate (da/dN) or change in $\Delta K$. The AE count rate had a weak connection with da/dN, while the correlation with $\Delta K$ was stronger, indicating a definite power-law relationship compared to the Paris-Erdogan crack growth rate law. Shi et al. [77] observed both cumulative signal amplitude and duration when measured against loading cycles in rail steel inspection, similar to crack length. Both the energy duration rates of AE showed a dependence on $\Delta K$ through a Paris-Erdogan type power law. Variations were, however, present throughout the results obtained, which was related to a sudden rise in the rate of crack growth. A long-term forecast for AE testing can rule out this inherent uncertainty, but constant monitoring still seems feasible, given a clear relationship.

Rather than investigating the reliability of AE applications to measure defects, most research has concentrated only on proving empirical relationships. They also ignored to investigate the impacts of background, as well as the effects of variable, and the microstructure nature. This thesis aims to fill in the gaps that many researchers have

missed. It is imperative to develop a reliable relationship to quantify the damage and ensure that relevant information can be obtained from the AE data.

### 3.2.1 Pearson Correlation and Linear Regression Analysis

A correlation or simple linear regression may decide a relevant linear relationship between two numerical variables. The degree and direction of a linear connection between two variables may be determined using correlation analysis. In comparison, in a linear equation, simple linear regression analysis predicts parameters that estimate one variable's values that are dependent on the other [78].

- **Pearson correlation coefficient (r)**

The Pearson coefficient of correlation, r, assumes values between -1 and 1. The greater the linear correlation between the two variables, the farther r is from 0. The sign of r corresponds to the relationship's direction. Achieving a value of +1 or -1 shows that all data points are included in the best fit line. No data points show any variation besides this line. Pearson's R-value describes the relationship between two variables with a straight line or linear relationship. The more significant the difference along the best fit line, the closer the r to 0 value. Various relationships and their coefficients of correlation can be seen in the illustration below.
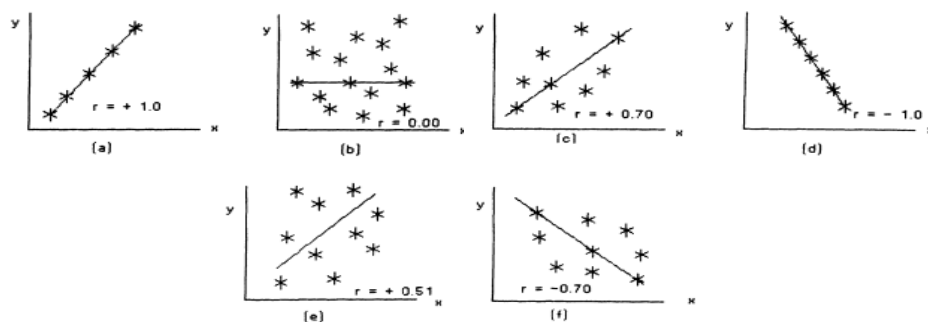


Figure 42. Illustrate what the interactions would look like with different r values at different strength levels [79].

Pearson's correlation coefficient can be interpreted as the following guidance:

Table 6. Correlation coefficient interpretation using a conventional approach [80]

| Guidelines for interpreting Pearson's correlation coefficient | Interpretation |
|---|---|
| 0.00 - 0.10 | Negligible correlation |
| 0.10 – 0.39 | Weak correlation |
| 0.40 – 0.69 | Moderate correlation |
| 0.70 – 0.89 | Strong correlation |
| 0.90 – 1.00 | Very strong correlation |
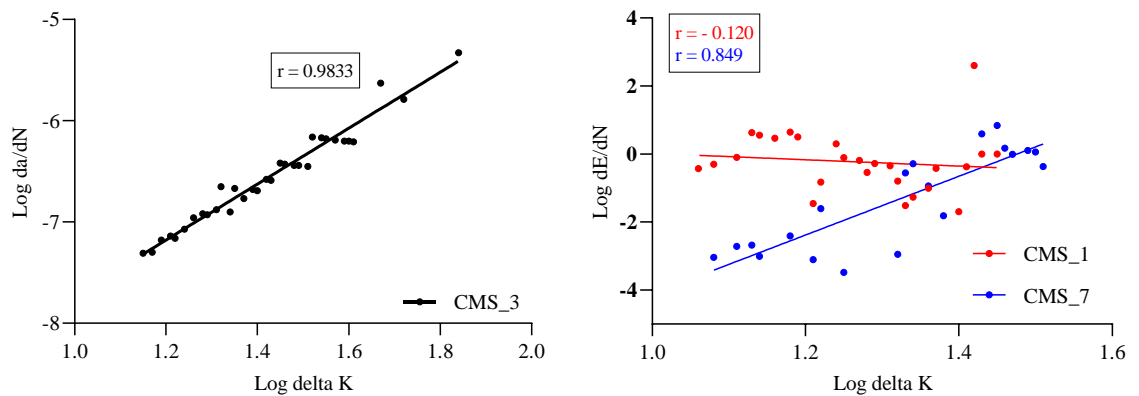


Figure 43. Illustrate what the interactions would look like with different r values at different strength levels.

These standards are guidelines, and whether or not an entity is strong may also depend on what is evaluated.

- **Linear Regression**

Analysis of linear regression produces slope and intercept predictions for the linear equation forecasting an outcome variable, Y, dependent on predictor variable values, X. Below, a general form of this equation is shown:

$$\hat{y} = b_0 + b_1 x$$

When X=0.0, the intercept ($b_0$) is the predicted value of Y. The slope ($b_1$) is the average change in Y for each rise in X by one unit. As a result, in addition to expressing the strength and direction of the linear connection between X and Y, slope estimation also

shows how Y varies as X increases. This equation may also be used to predict Y values for a given X value [81].

The testing methods used to verify quantitative reliability are shown in **Chapter 5,** and a discussion of the results are analyzed statistically according to **section 3.2.1** is shown in **Chapter 6**.

## 3.3    NON-DESTRUCTIVE TECHNIQUE USING IN RAILS

The detection of defects in crossings presently relies on visual inspection. This activity is labour-intensive and inefficient. Consequently, as damage reaches severe levels of degradation, most affected crossings are currently replaced reactively. The shortcomings of manual inspection are driving the advancement of technology for onboard monitoring. Ultrasonic testing (UT) shows the best results in detecting cracks, though it is not optimised for detecting surface defects unless they propagate further inwards [82-83]. Eddy current testing can detect surface defects. The eddy current system probe, on the other hand, must be kept at a constant distance from the railhead, making it impossible to be used in crossings passed at speed and due to its high sensitivity to lift-off variations [84]. The magnetic flux leakage (MFL) technique, which may be used for transverse surface defects or near-surface, often suffers from constant distance restrictions between the sensors and rail surfaces. Hadfield manganese steel itself is paramagnetic and cannot be subjected to MFL. Even if radiography application for the inspection of Hadfield manganese steel in the field was straightforward, internal cracks could be easily missed due to this technique's limitations in detecting relatively small cracks.

Nonetheless, new crossings prior to being installed are fully inspected radiographically using very powerful X-ray sources. In addition, inspections must be

performed at night or when train traffic is at a minimum. As a result, RCF detection using conventional inspection techniques remains a problem.

Table 7. Defect of the rail and recommended NDT technique [85].

| NDT technique | Performance | Rail defects detected |
|---|---|---|
| **Ultrasonic (UT)** | Manual inspection is reliable, although it may overlook rail foot defects. Surface defects smaller than 4 mm, as well as internal flaws, may be missed at high speeds, especially near the rail foot | Surface defects, railhead internal defects, rail web defect, and foot defects |
| **Long-range ultrasonic (LRUT)** | Large transverse defects are reliably detected (>5% of the total cross-section) | Surface defects, railhead internal defects, rail web defect, and foot defects |
| **Laser ultrasonic** | Internal defects are reliably detected. It is susceptible to sensor lift-off changes and is difficult to operate at high speeds. | Railhead, rail web defect, and foot defects |
| **Magnetic flux leakage (MFL)** | Surface flaws and shallow internal railhead deficiencies are reliably detected. Cracks smaller than 4 mm are not detectable. At greater speeds, MFL performance degrades | Surface defects and near-surface internal railhead defects |
| **Radiography (RT)** | Internal defects in welds that are hard to observe by other methods are reliably detected. Certain transversal defects may be missed. | Welds and known defects |
| **Automated visual inspection (VT)** | It is capable of detecting corrugation, missing railhead profile components, and defective ballast at high speeds. At speeds greater than 4 km/h, it is impossible to identify surface-breaking defects accurately | Surface breaking defects, railhead profile, corrugation, defective ballast |
| **Electromagnetic Acoustic Transducer (EMAT)** | Reliable for both external and internal defects. Rail foot problems are easy to overlook. Variations in lift-off have a negative impact. | Surface defects, railhead, rail web defect, and foot defects |
| **Acoustic Emission (AE)** | Limited experiments. It is impossible to identify any internal defects. | Rail breaks, squats, wheel burns wet spots, worn rail profiles |
| **Pulsed Eddy Current (PEC) including Field Gradient Imaging (FGI)** | Surface-breaking defects are reliably detected. Grinding marks and lift-off variations have a negative impact. | Surface and near-surface internal defects |
| **Acoustic Emission Pulsing (AEP)** | Experiments are limited. It can only be used in specific locations. Can overlook non-transverse or minor transverse defects | Surface defects, railhead internal defects, rail web and foot defects |
| **Magnetic Anomaly Distortion or Detection (MAD)** | Experiments are limited. Large internal or surface-breaking defects greater than 50 percent of a cross-sectional area may be detectable | Broken rails, rail gaps |

## 3.4    AE TESTING AS NDT TECHNIQUE USING IN RAIL

The difference between AE and another non-destructive testing (NDT) techniques is that AE identifies the material's damage behaviour as it develops in real-time, whereas other NDE methods aim to analyse its internal structure. Besides, AE allows only the input of one or more relatively small piezoelectric sensors mounted on the surface of the structure. At the same time, evolving damage is continuously tracked by the AE system. Other NDE techniques can evaluate the whole structure or specimen, such as ultrasound and X-ray radiography for validation purposes. In addition, the specimen's structure can be studied in more depth and taken to the laboratory for fractographic analysis [86]. Conventional models for fatigue may provide components with an estimated life cycle. However, Zhu and Olofsson [87] demonstrated that these models frequently overestimate the service life of components in order to be reliable; such forecasts must be combined with appropriate assessment techniques and monitoring.

AE is monitoring or measuring the method that begins at the micro level up to final failure, which allows the inspection of the operation before the machine or material is seriously damaged. Since these conventional techniques are used after discontinuities develop and grow in a material, the AE approach can detect discontinuities during the initial phases and growth of any crack at the microstructure and macrostructure level. AE is typically applied during loading to verify AE's occurrence, whereas most others are applied before or after structural loading. A propagating crack is an expanding discontinuity that generates AE energy in the form of elastic stress waves. Compared to other traditional inspection techniques, the benefit of the AE approach is that real-time monitoring can be used to avoid damage in advance.

Additionally, this test may be conducted without interrupting the production or operation of the equipment, and it can cover a large area in a single test. Experimental findings based on the application of AE to identify fatigue crack initiation and propagation in different kinds of materials (e.g., steel, aluminium, reinforced concrete, and so on) indicate that cracks may be identified in their earliest stages [76]. Danyuk et al. investigated the use of AE in operating equipment and discovered that, despite the noise generated by the surroundings, the AE sensor could still detect crack initiation [88].

Recently, AE technology has been applied for monitoring cracks in turnouts while in service at the Changzhou North Railway Station in the Shanghai-Nanjing line [89]. Thus, China is devoting considerable effort to pursuing a railroad track monitoring system and focusing on safety monitoring rather than condition monitoring. Simultaneously, German and French turnout monitoring systems are used to verify the switch machines' functioning to avoid transformation failure. Currently, the turnout is being monitored for cracks, switching force, turnout split during shunting, closure between the switch rail and the point rail, indication of the switch machine's gap, switching current, and voltage.

### 3.4.1 AE Signals during Fatigue Testing

Typically, fatigue studies are long-term experiments. Many signals, including noise from the loading machine, are observed using sensitive AE sensors during fatigue testing. Hence, to remove unnecessary noise signals, appropriate filters should be used. During a fatigue test, AE signals can be caused by different factors, such as cyclic loading, dislocation movement, crack initiation, and crack closure. Cracks during subcritical crack growth should be observed and monitored to ensure the safety of steel structures undergoing fatigue loading. There has been an analysis of the AE activity behaviour arising from propagating fatigue cracks. The AE activity started with the crack's initiation

and then continued closely linked with the crack's measured length. Cyclic loading and fixed load amplitude were used; the primary emission from active crack growth was found to occur only at peak load levels. Two sources may result in the primary emission from the growing fatigue crack. Firstly, there may be emissive particles in the concentrated stress area near the crack tip, usually non-metallic inclusions. The local stress level increases as the crack advance into all these particles, and their cracking will produce a primary emission. The other source is the crack tip movement itself. In a mixed-mode, crack tip movement usually occurs. Some of the new surfaces are produced by dislocation movement, and some of them are created by small-scale cleavage in an area of local weakness, abrupt fragmentation of the material. Crack tip displacement usually is not detected by dislocation activity, but cleavage is a sudden and relatively gross process that generates plenty of AE energy in the generally detectable range. In AE monitoring of fatigue cracks, secondary action from crack face friction is often frequently detected. This operation also induces only the same signal in continuous cycle fatigue, cycle after cycle, at intermediate load levels. This secondary emission may proceed for hundreds of thousands of cycles, then die out only to begin again later in the test. The leading hypothesis is that this is created by rubbing rough spots on the crack surface, as stated. It has also been proposed that, as the crack tip opens and closes, the recently formed surfaces at the crack tip may attach and then break apart again. Theoretical relationships have been developed between AE and crack propagation levels. Extensive research work on AE from constant cycle fatigue has been carried out. In the event of constant cycle fatigue, distinguishing between primary and secondary emissions is straightforward.

|  (a) | (b) | (c) |
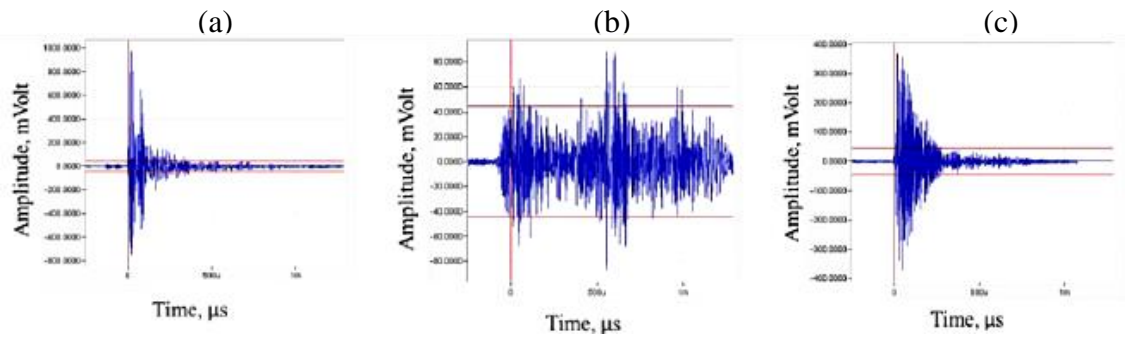
Figure 44. Different types of signalling patterns from detections (a) AE signals expected of iron oxide fracture (b) Plastic deformation caused by internal stresses in the probe area (c) Signals of a tiny crack [90].

### 3.4.2    The advantages and limitations of the AE technique

Sensitivity to environmental noise and mechanical noise is a significant disadvantage of this method. If the ultrasonic wave frequency is in the same region as the sound wave released from the discontinuity, it may make the test difficult or impossible if the noise cannot be eliminated. Thus, an essential aspect of AE testing is signal processing when the AE is applied to track inspection. A need to separate genuine stress-wave AE activity originating from the material and external signals, such as environmental noise, mechanical noise, and electric noise, is achieved by careful electronic filtering of the received AE data. The AE technique is unique because it allows access to information about defects in solids under load. AE reflects changes in internal structure caused by stress relaxations in solids. The AE response is directly related to the size and speed of the emitting defect, such as cracking [91]. Because the signal generated from propagating cracks is low and difficult to detect in the background of excessive environmental noise, appropriate filtering should be used to detect small fatigue cracks propagating very slowly [92-93]. Another disadvantage of using the AE method is that no further tests can be performed once the damage has already occurred. Also, newly detected data will be the data of new discontinuities or the old crack expanding.

73

One of AE's limitations is that commercial AE systems can provide only qualitative or semi-quantitative information regarding the amount of damage accumulating. Thus, an additional inspection may be required using appropriate methods to quantify the amount of damage accumulated in the structure. In most service environments, noise is prevalent, and AE signals are frequently poor. As a result, signal selection and noise removal are difficult but essential for effective AE applications [94]. Summarizing the advantages and limitations of the Acoustic Emission technique is shown in Table 8.

Table 8. Advantages and Limitations of Acoustic Emission Techniques.

| Advantages of AE | Limitations of AE |
|---|---|
| 1. This allows for early identification of problems to be repaired before they become major problems. | 1. It is only capable of producing qualitative rather than quantitative results. |
| 2. High sensitivity. | 2. Identified problem areas can be inspected using conventional NDT methods. |
| 3. Global, simultaneous inspection: 100% Inspection of the structure. | 3. Loud environments present challenges. |
| 4. There is no need to scan the whole structural surface, which reduces plant downtime for inspection. | 4. Can only locate active defects: in certain situations, may also need to locate dormant problems. AET, once again, would be ineffective in this situation. |
| 4. Only functional defects are identified, whereas stable fractures and previous manufacturing defects are not. Allows the company to concentrate on the most important issues, saving time and money. | 5. It is necessary to have an operator that is knowledgeable, experienced, and skilled. |
| 5. Optimize inspection budgets with real-time condition data | 6. This involves the employment of technology and software that is both complex and costly. |
| 6. Only microscopic holes in the insulation are needed to attach sensors, causing less insulation disruption. | |
| 7. Compliance assistance: A range of guidelines accept AET and comply with local, state, and federal regulations. | |

## 3.5    SIGNAL PROCESSING UNDER FIELD CONDITIONS

The potential of deploying AE RCM for railway infrastructure monitoring has been explored in several studies. However, just a few field experiments have been conducted, with most studies focused on laboratory experiments. Murav'ev et al. investigate the potential of using AE to track the rails on a bridge in Novosibirsk that spans the Ob River. When the defect size was small, they found that AE could identify the defects that the ultrasound sensor never could [95]. Bollas et al. [96] researched AE monitoring of railway wheelsets on moving trains and trams using AE sensors to explore the application of AE for online monitoring of wheel defects. As seen in Figure 45, the defects they found are displayed as periodic peaks in the ASL versus time plots.
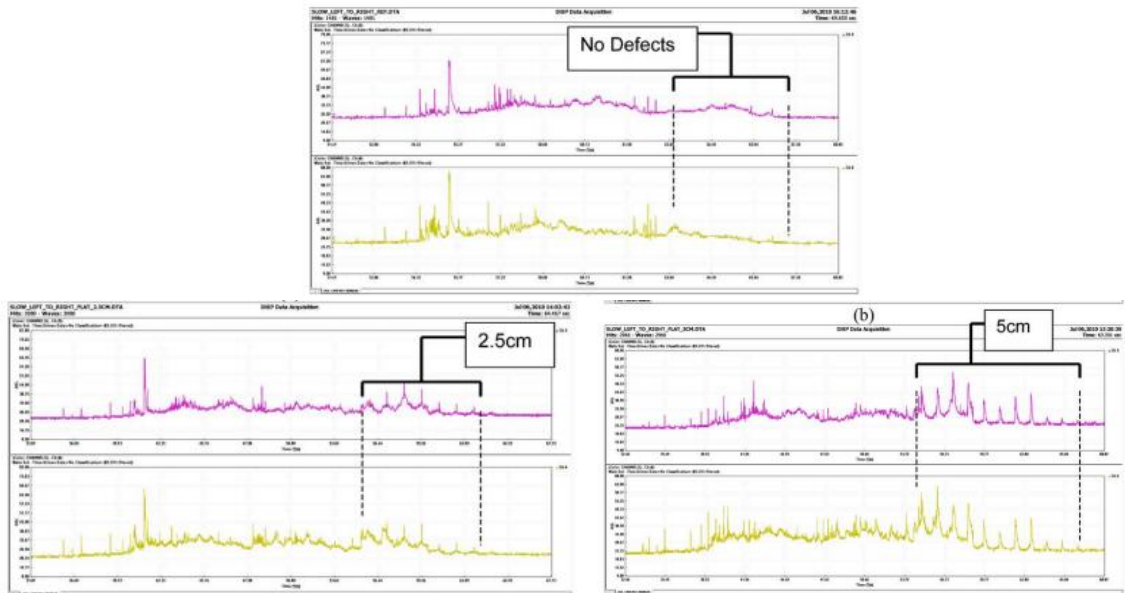


Figure 45. Movement of the reference train (a), a flat defect surface of 2.5 cm (b), and 5 cm (c) [96].

Bruzelius et al. report the frequencies of the relevant AE signals. The signals' frequency range was set to be between 20kHz and 1 MHz [97]. Zhang et al. produced 100-150 kHz, whereas. Shi et al. recommended 100 kHz-500 kHz to maximise crack-related occurrences [85][98]. When considering AE field measurements, the background

noise has to be filtered out. In order to classify damage-related signals, further study of the AE waveforms is needed. By comparing generated signals with other monitoring techniques, such as changes in sample resistance with an applied potential difference, it is possible to establish a correlation between the AE data, crack size, and crack growth rate [99].
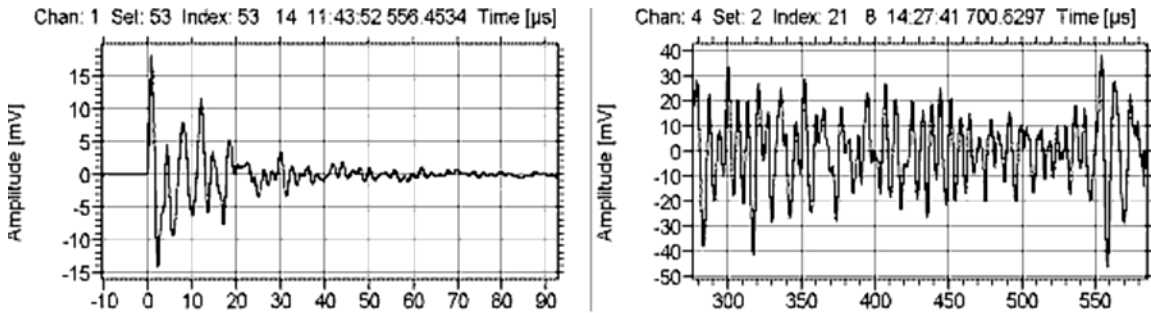


Figure 46. Types of AE signals (Left) showing the transient AE signals (bursts), background noise is clearly deviated from at the beginning and ending points, (Right) showing the signal peak correlated with the signal connected to the crack following signal filtering [99].

These peaks in the results can be found in the experiment of Vallely using the same equipment as used in this study. The peaks due to crack growth are readily distinguishable from the background noise. Graphs of the raw AE emission data are shown in Figure 47.
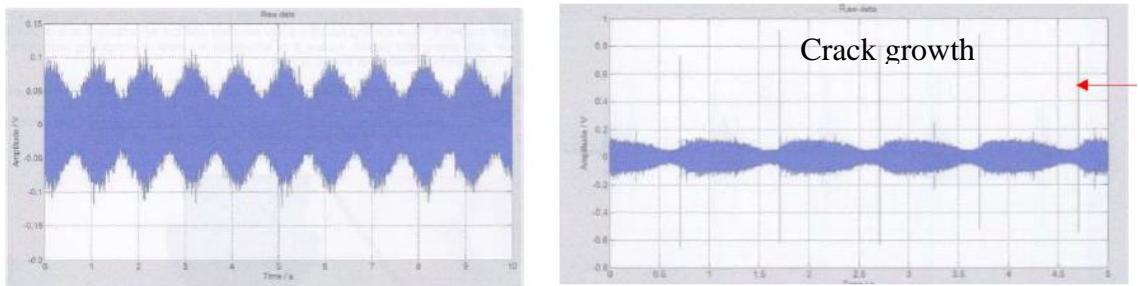


Figure 47. (Left) Upon loading, the background noise of an uncracked reference sample and (Right) crack growth are shown as peaks in the graph much greater than those found in the background noise sampled under the same loading conditions [100].

# CHAPTER 4

# MATERIALS CHARACTERISATION

# CHAPTER 4: MATERIALS CHARACTERISATION

This chapter describes the characteristics of materials used in experiments using SEM to analyse the physical characteristics, XRD to evaluate the crystal structure, and microhardness testing to evaluate the hardness of the tested material at the microstructural level. This chapter also reviews the types of defects as well as the microscopic fracture mechanisms.

## 4.1 METAL DEFORMATION AND RELATED PROPERTIES

### 4.1.1 Defects in solids

Imperfections in crystalline solids can be broadly classified into four groups, zero-dimensional (point defects), one-dimensional (line defects or dislocation), two-dimensional (surface defects or planar defects), three-dimensional (volumetric defects or bulk defects) [101].
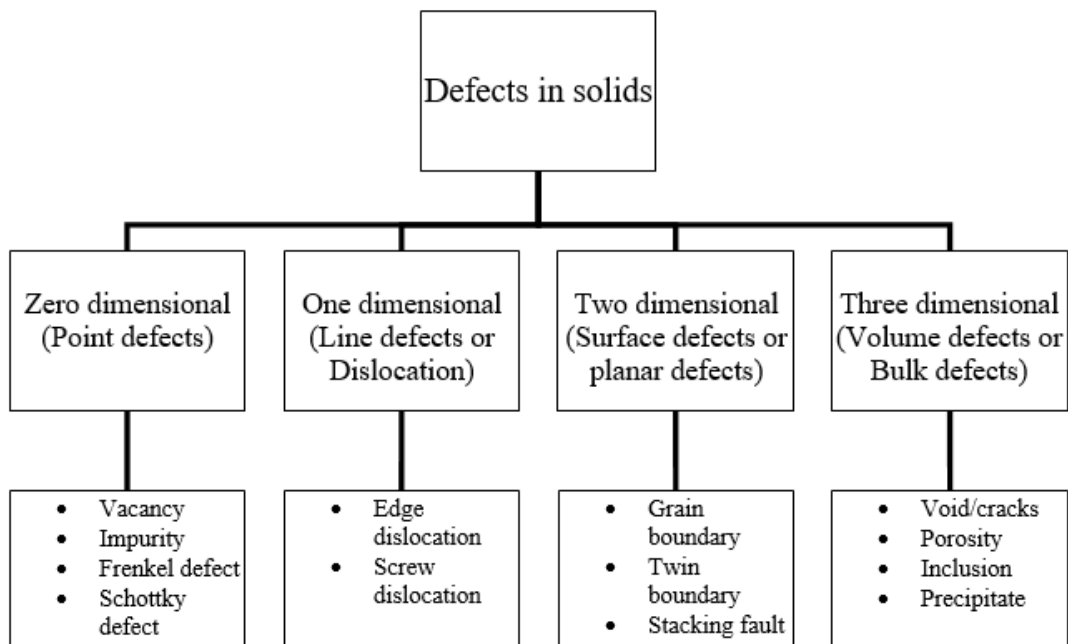


Figure 48. Classification of the crystalline defect [181].
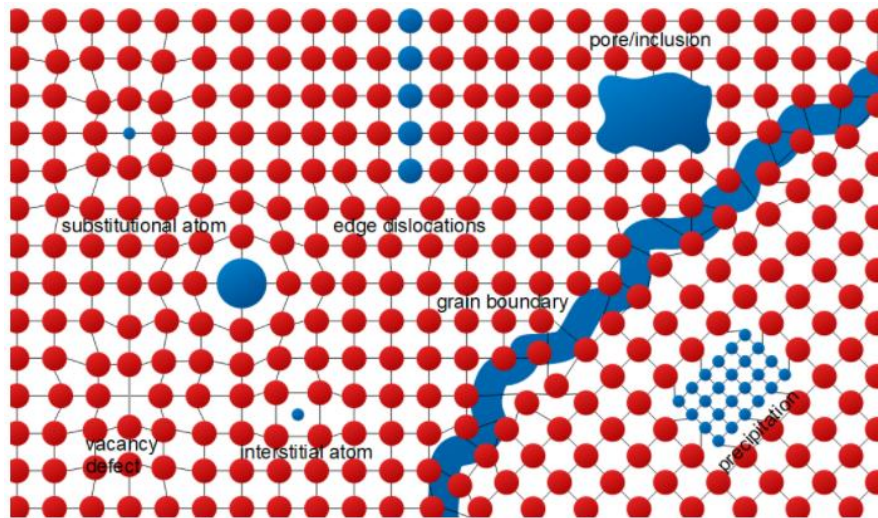
Figure 49. Various crystallographic defects may be further classified based on their effect on the surrounding structure [102].

### 4.2.1.1 Point defects

Point defects are the smallest of all flaws that can occur in any material. The less complicated point defects consist of vacancies (missing atoms at a specific crystal lattice positions), interstitial impurity atoms (extra impurity atoms in interstitial positions), self-interstitial atoms (extra atoms in interstitial positions), substitution impurity atoms (impurity atoms, substituting atoms in the crystal lattice), and Frenkel defects (additional self-interstitial atoms, which are responsible for nearby voids)
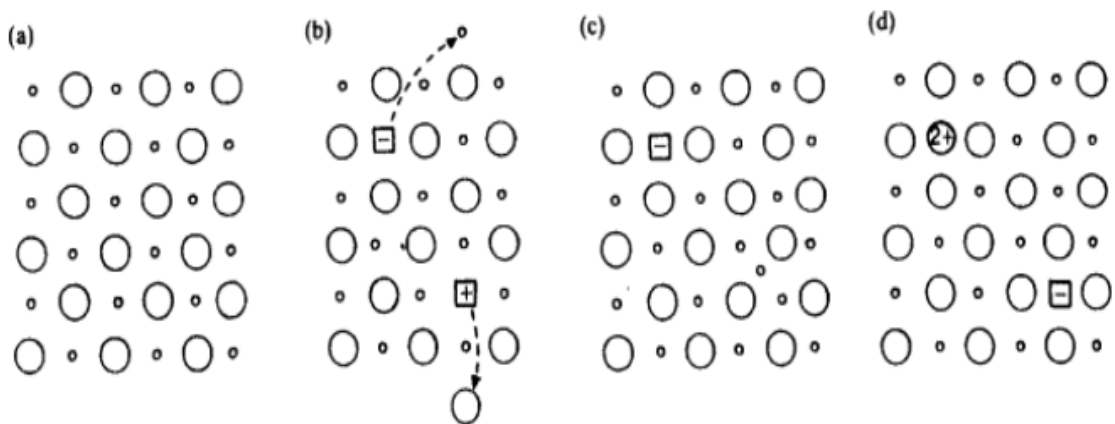


Figure 50. Representation of point defects in two-dimensional ion structure:
(a) monovalent ions and ideal structure; (b) Schottky defects; (c) Frenkel defect, and (d) cation vacancy and divalent cation impurity replacement [103].

## 4.2.1.2 Line Defects or Dislocation

In a crystal structure, dislocations are regions where atoms are out of position. When increasing amounts of stress are applied, dislocations are formed and mobilised. A slip, or plastic deformation, is caused by the movement of the dislocations. Edge dislocations and screw dislocations are the two most common kinds of dislocations. The two pure types of possible dislocation mechanisms that may occur are edge and screw dislocations. Typically, dislocations in crystals tend to be hybrid forms of both edge and screw dislocation types (see Figures 51-52).
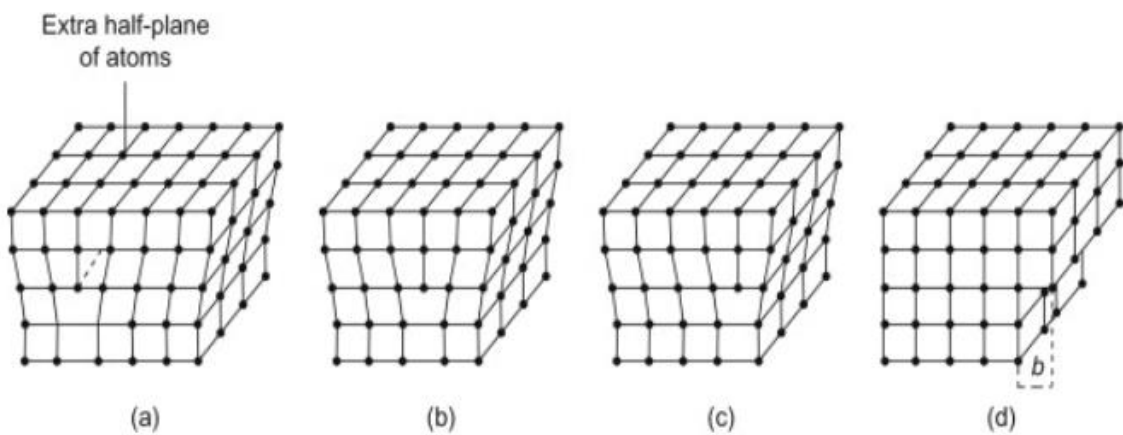
Figure 51. Demonstrated how the Dislocation movement propagates the slip in response to the motion of that force. For example, when a crystal is sheared, an additional half-plane shifts to the right, and a negative dislocation moves from the right to the left [43].
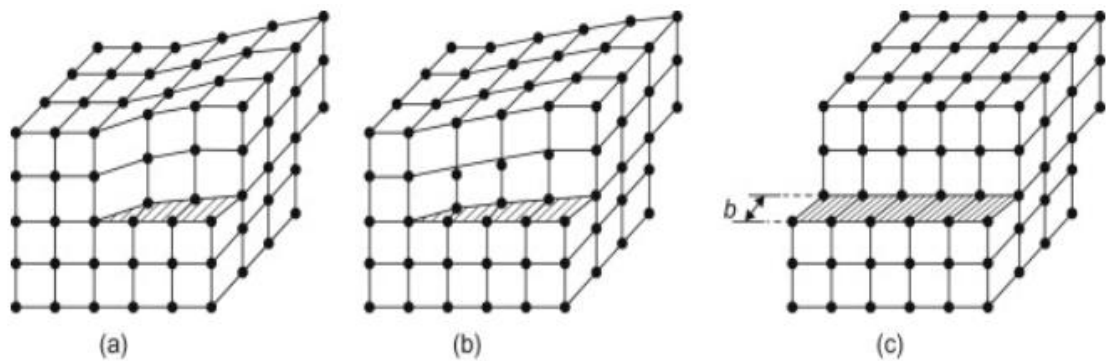
Figure 52. A screw dislocation, the slip process [43].

### 4.2.1.3 Surface defects or planar defects

Surface defects or planar defects are interfaces between two different homogeneous regions in a material. Planar defects are due to grain structure formation, including grain boundaries, stacking faults, and external surfaces. A plane defect is the discontinuity of the perfect crystal structure around the plane. Interfacial defects have two dimensions, and, as a rule, they are separate regions in a material with different crystal structures and crystalline orientations. These defects occur at free surfaces, domain boundaries, grain boundaries, and interphase boundaries. Interfacial defects occur at an angle between the two faces of the crystal or crystal type.
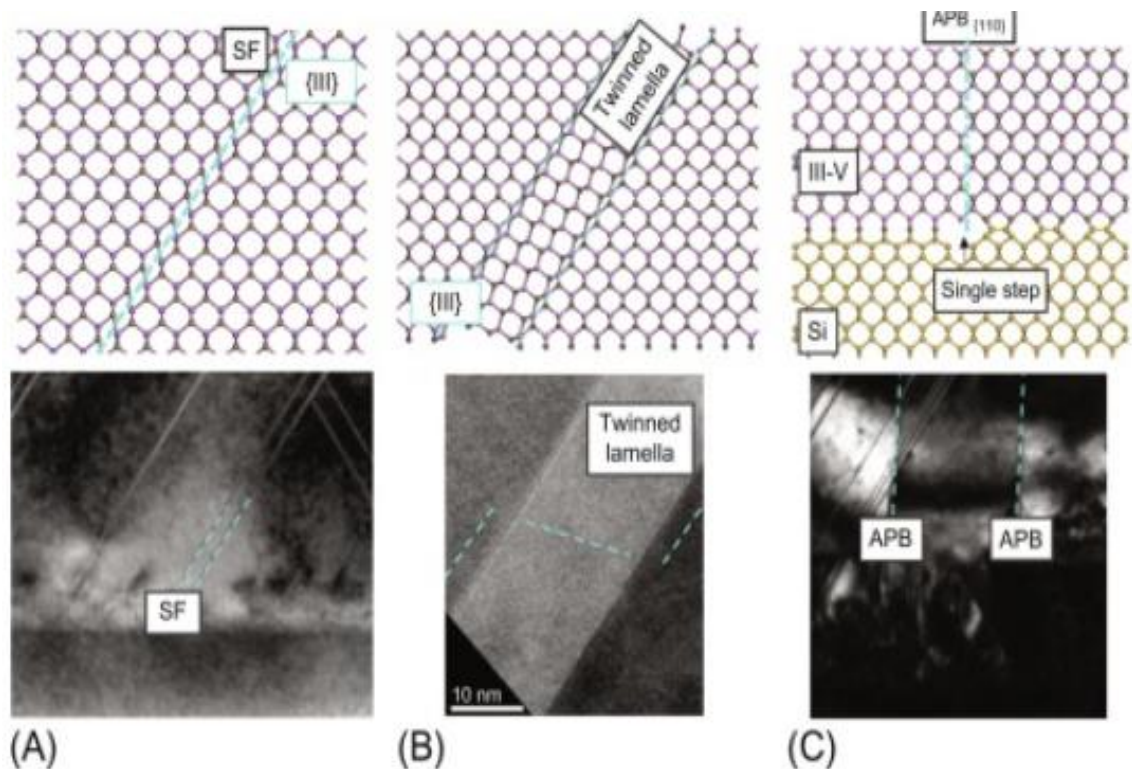


Figure 53. Representation of typical planar defects: (A) stacking fault (pilling up faults during recrystallisation due to collapsing), (B) twins boundaries (formed during plastic deformation and recrystallisation), and (C) antiphase boundary [104].

### 4.2.1.4 Volume defects or Bulk defects

Three-dimensional macroscopic defects are called volume defects or bulk defects. Overall, they are much larger than microscopic defects. When a material is refined from its raw condition or fabricated, these macroscopic defects are introduced into the material, with foreign inclusions, cracks, pores, and other phases. In addition, metalworking can result in dislocation defects that induce local compressive stresses that strengthen the material. A bulk defect may be defined as any welding or joining defect. Pores, fractures, and inclusions are examples of macroscopic or bulk defects, which are three-dimensional. Voids are atom-free regions in a relatively small material. Thus, they may be thought of as clusters of vacancies. Impurities may produce small regions of a distinct phase when they cluster together. There are two types of inclusions: inclusions and precipitates.

### 4.1.2 Micro Mechanisms of Fracture in Metals

When considering material behaviour and structural integrity, fracturing is the most important phenomenon. Brittle fracture processes in metals are the most common (trans- or intergranular cleavage).



(a) Ductile fracture        (b) Cleavage        (c) Intergranular fracture
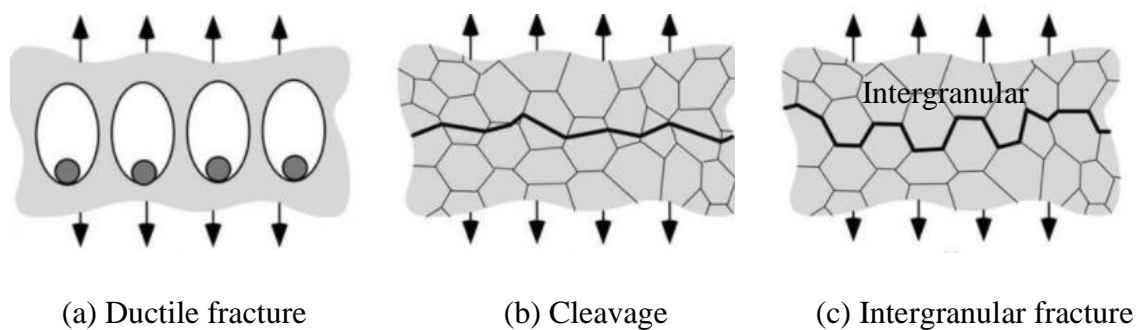
Figure 54. Three micro-mechanisms of fracture in metals: (a) ductile fracture, (b) transgranular fracture at the microscopic level, and (c) intergranular fracture; cracks grow along grain boundaries in this case [105].

(a) The nucleation, propagation, and coalescence of small voids that tend to form from inclusions and second-phase particles are the most common causes of failure in ductile materials.

(b) Cleavage fracture occurs when crystallographic planes are separated. The fracture pattern is transgranular, which should be recognised. Despite the fact that cleavage fractures are often referred to as brittle fractures, they may be preceded by large-scale plasticity and ductile crack development.

(c) Intergranular fracture occurs when the observed fracture direction in the material is the grain boundary.
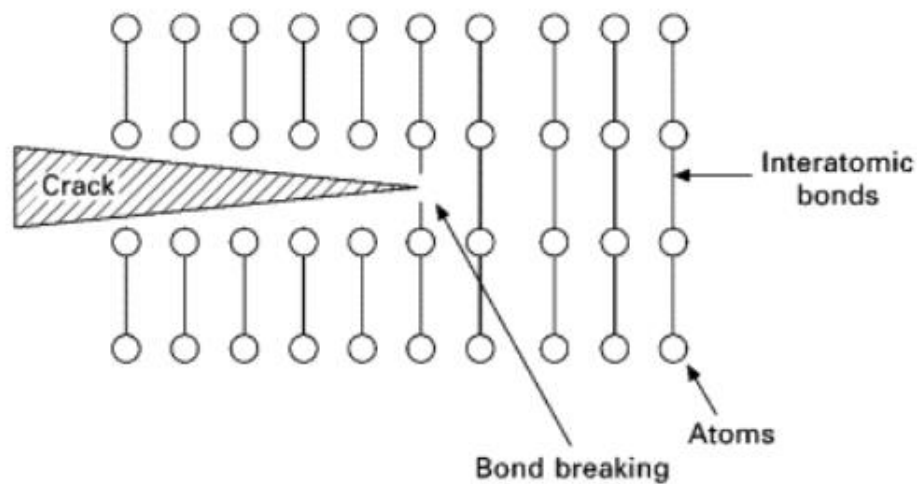


Figure 55. A schematic of the brittle fracture mechanism involves breaking interatomic bonds at the atomic level of a crack-tip region, where the circles represent metal atoms [106].

The ductile fracture is accompanied by extensive plastic deformation ahead of the crack tip, with the crack growing relatively slowly. This, apart from allowing enough time for inspection, also permits repair or replacement actions to be completed before final failure occurs unexpectedly, which would be the case in brittle fracture. A brittle fracture happens typically unnoticed, giving very little if any indication before the sudden final catastrophic failure occurs. The crack overgrows with slight plastic deformation being

produced. Far more strain energy is required to facilitate the ductile fracture in comparison with brittle fracture. To characterize the resistance of the material to brittle fracture, a critical expression relating stress with fracture toughness has been proposed, as shown in Equation 3-5 below.

$$K_c = Y\sigma_c\sqrt{\pi a}$$

… (3-5)

$K_C$ is defined as fracture toughness, Y is a parameter related to specimen size and geometry and loading configuration, $\sigma_c$ is the critical stress and $\alpha$, is the crack length. Based on equations 3-5, the likelihood of brittle fracture increases with the crack length for the same loading mode. The $K_C$ value decreases with the thickness of the specimen for the same material. The $K_C$ becomes constant when the thickness reaches a critical threshold. Conditions of plane strain begin to develop. Kc is often referred to as plane strain fracture toughness ($K_{IC}$), and it is preferred over Kc in damage tolerant design and fatigue life prediction [107].

## 4.2 MATERIALS CHARACTERISATION METHODS

This section contains a comprehensive explanation of the experimental methods and processes utilised to characterise the rail steel specimens. The materials considered in this study were pearlitic rail steel and austenitic cast manganese steel grades. Both materials are the standard steel grades used for plain rails and turnouts, respectively.

### 4.2.1 Scanning Electron Microscopy (SEM) Method

Scanning Electron Microscopy (SEM) was carried out using a JEOL6060 SEM in order to analyse the physical characteristics of the test specimens and evaluate the elemental composition of the areas of interest in the materials considered in this study. The compositional evaluation was carried out using Energy Dispersive X-Ray

Spectroscopy (EDX or EDS). SEM is based on the principle of accelerating thermionically generated electrons from a high voltage source (~5-30 kV). The electron beam is then focused on the sample surface of the conductive sample using electromagnetic lenses. Secondary electrons emitted from the surface of the sample are subsequently detected in order to display the image on the computer screen after the signals have been digitised. Alternatively, back-scattered electrons can be detected.

### 4.2.2   X-Ray Diffraction (XRD) Method

X-ray diffraction (XRD) is a non-destructive test method used to evaluate the crystal structure of crystalline materials of interest. Epp,2016 presents the theoretical and functional basis of XRD techniques and their use in testing various materials, lattice planes, and the Bragg-Wulf equation and equations for calculating interplanar distances [108]. XRD was performed in this study using a Bruker D8 Advance instrument, which employs a Cu K$\alpha$ ($\lambda = 1.5406$ Å) anode with Ni filters. The diffractometer operated at 40 kV voltage and 30 mA current and obtained data at a scan rate of 0.5$^{o}$ /min in a range from 10$^{o}$ to 90$^{o}$ controlled by DiffracPlus software. The intensity of the X-ray diffraction pattern was calculated from 18q-70q with a step of 0.02q per second as a function of the diffraction angle (2T). The D8 advance has a theta: theta ($\theta{:}\theta$) geometry, often called Bragg-Brentano, focusing geometry providing reliable and accurate diffraction data. In order to obtain the crystallographic parameters, the Rietveld method was used refined using the Fullprof software package.
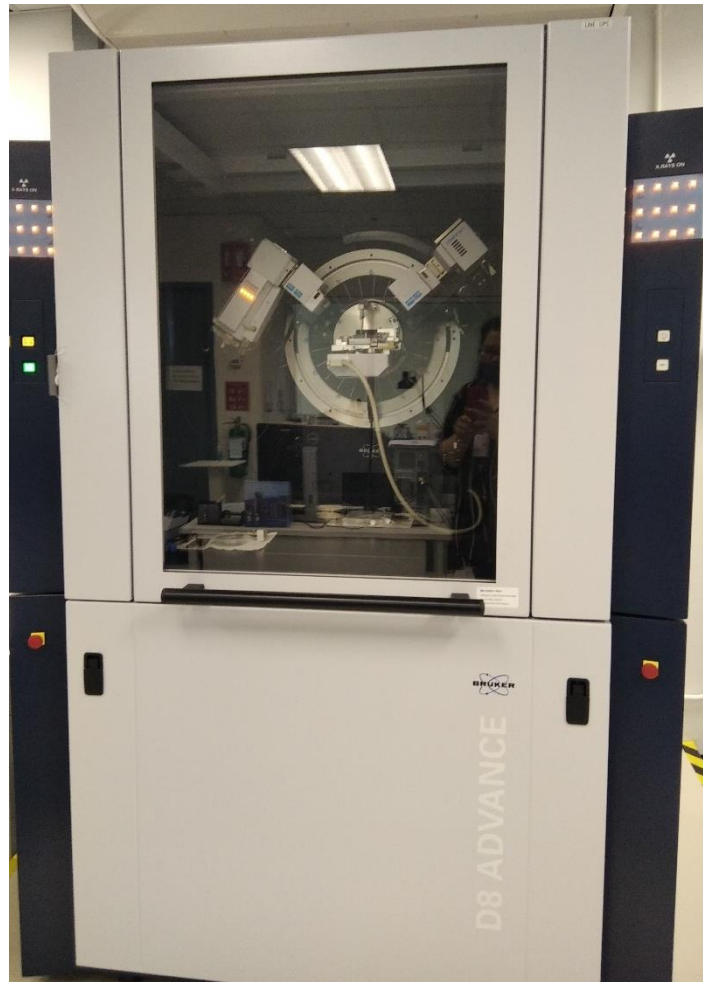
Figure 56. Photographs of the D8 Advance Bruker X-ray diffractometer show an outer view.
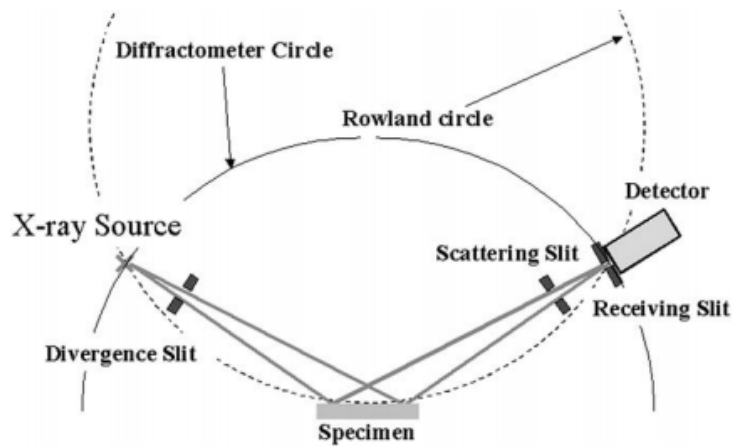


Figure 57. schematic representation of the Bragg-Brentano geometry [109].

**Bragg's law**

$$n\lambda = 2d.\sin\theta$$

Where $\lambda$ is the wavelength of X-rays, moving electrons, protons, and neutrons, n is an integer defined by the order given, $\theta$ is the reflection angle defined as the angle between the primary radiation beam and the crystalline plane, d is the spacing between the planes and the angle between the incident ray and the scattering planes in the atomic lattice.

The conversion of the diffraction peaks to d-spacings helps define elements since each element has a particular set of d-spacings. It is typically achieved by comparing d-spacing with standard reference patterns available by The International Centre for Diffraction Data (ICDD).

### 4.2.3 Micro Vicker Hardness Test Method

Vicker's microhardness testing was employed in order to evaluate the hardness of the tested material at the microstructural level. The microhardness test is based on the use of a diamond micro indenter. The depth of the indentation is subsequently calculated in order to evaluate the hardness of the material.

Cutting, mounting, grinding, and polishing samples resulted in a scratch-free mirror finish. The Vicker's scale was tested using a Mitutoyo MVK-H1 micro-hardness tester for measuring metal hardness. The hardness test is measured using a digital ocular, which provides accurate d1 and d2 values measurements. The HV measurement value and stage location are shown on display [110].

Figure 58. Micro Vicker hardness tester Mitutoyo MVK-H1 [111].
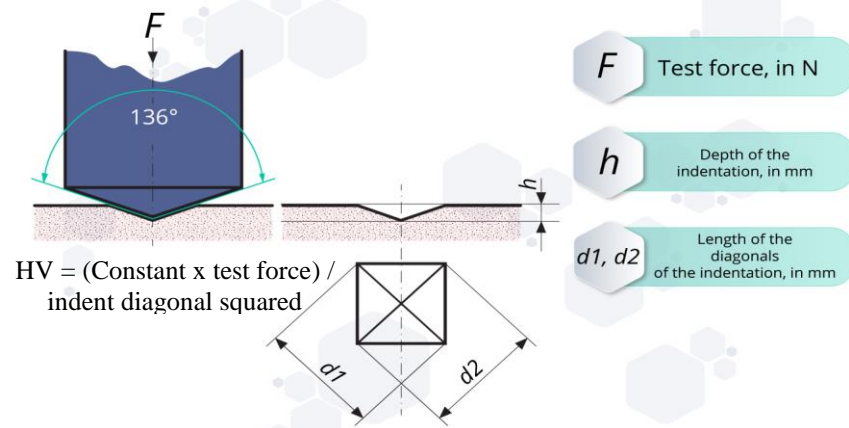


Figure 59. Vickers hardness indentation [165].

As illustrated in Figure 59, the angle between the pyramid's faces is 136°. The Vickers Hardness Number of a material is calculated by dividing the applied force F by the Vickers Hardness Number (in kgf).

$$VHN = \frac{1.8544P}{d^2}$$

Where $d$ is the average length of diagonals in millimetres.

Micro-hardness measurements were taken at different positions using a load of 300 gf to measure R260 rail steel and Hadfield manganese steel samples. The ASTM E384 standard defines the micro-indentation testing process of materials [112].

## 4.3 RESULT AND ANALYSIS

### 4.3.1 R260 Rail Steel

The experimental investigation used samples of pearlitic rail steel R260 grade. The material grade was confirmed using micro-Vicker hardness testing to confirm the rail grade. This steel grade has a fully pearlitic structure. Rail steel 260 with a pearlitic structure is the standard steel used for manufacturing modern rails [113]. The nominal mechanical properties and chemical composition of R260 steel grade are given in Tables 9-10.

| Carbon | Silicon | Manganese | Phosphorous | Chromium |
|--------|---------|-----------|-------------|----------|
| 0.62-0.80% | 0.15-0.58% | 0.70-1.20% | 0.025% | 0.15% |

Table 9. Typical chemical composition of R260 rail steel (in weight %).

| Hardness Brinell (approx.) | Tensile Strength N/mm$^2$ | Yield Strength N/mm$^2$ | Elongation % |
|----------------------------|---------------------------|-------------------------|--------------|
| 260/330 | ≥880 | 320 | ≥10 |

Table 10. Mechanical properties of rail steel 260 grade (EN).

SEM was used to analyse the microstructure of the pearlitic rail steel samples in order to validate the hardness test results. Mechanical polishing was performed on the cut samples using polishing solutions with particle sizes of 9 m, 6 m, and 1 m, respectively. Finally, the samples were chemically etched with 2% Nital acid solution. Figure 60 shows an SEM cross-section of one of the R260 rail steel samples tested. It clearly shows a two-phased lamellar structure composed of alternating layers of α-ferrite and cementite (Fe$_3$C). The alternating phase layers in pearlite are produced because the layered structure of eutectic structures is formed: atomic diffusion redistributes C atoms between ferrite and cementite ((0.022 wt% and 6.7 wt%, respectively). Alloying and refinement of grain

size have a direct effect on inter-lamellar spacing influences. Interlamellar spacing has subsequently a direct effect on the mechanical properties exhibited by the material. The smaller the interlamellar spacing, the higher the stiffness is whilst ductility decreases slightly [107].

Compared to bainitic rail steel, pearlitic rail steel has a better wear resistance but a lower toughness due to the lamellar structure. By decreasing the interlamellar spacing, wear rates were decreased as hardness increased, and lamellar spacing had a significant effect on hardness—reduced or finer spacing results in increased hardness [114].

- **Metallographic examination**
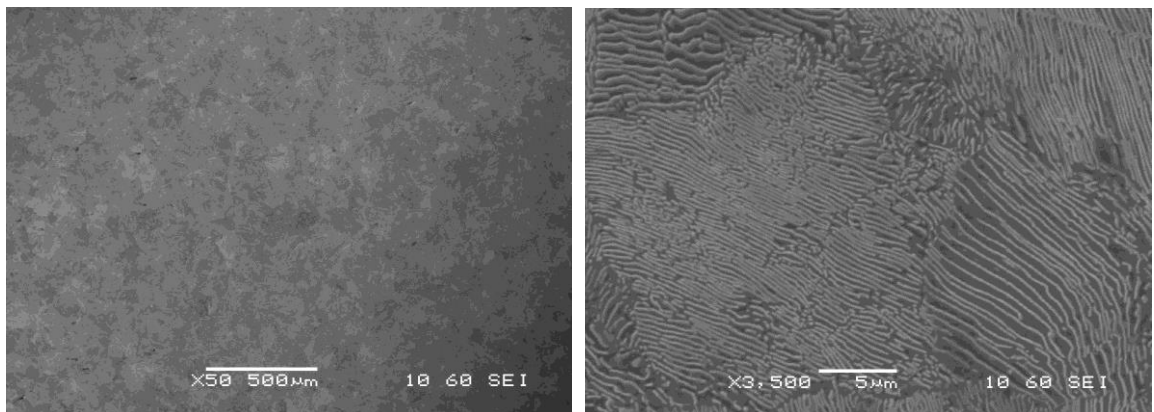


Figure 60. The Microstructure of the R260 rail steel shows pearlitic lamellae colonies (As a result of the SEM pictures, carbide is light and ferrite is dark.).
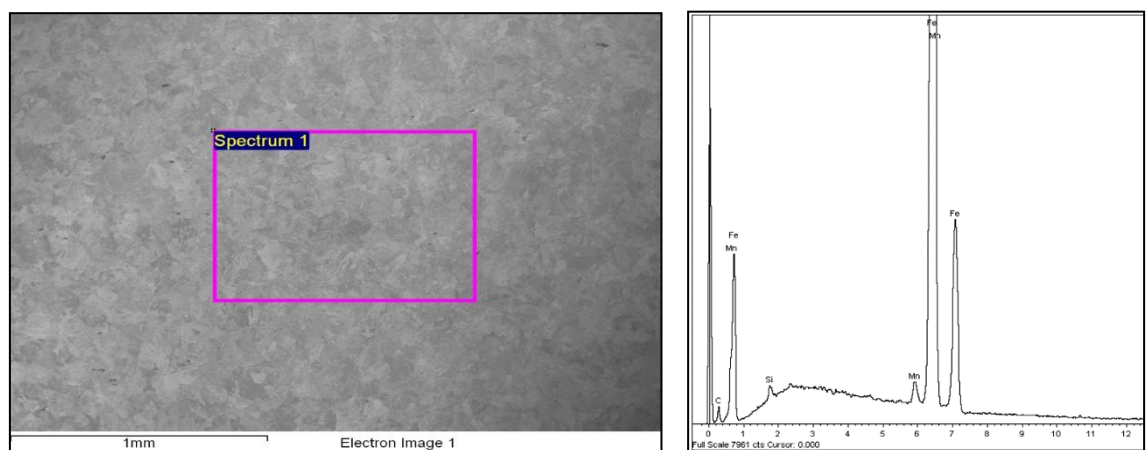


Figure 61. SEM image of the R260 rail steel analysed area and spectra from EDX analysis of the steel sample.
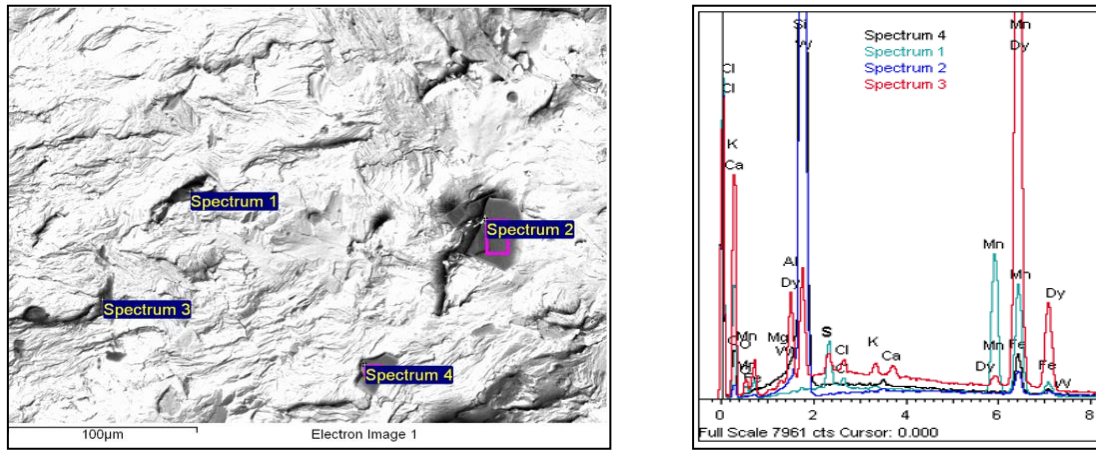
| Spectrum | C | O | Mg | Al | Si | S | Cl | K | Ca | Mn | Fe | W | Total |
|---|---|---|---|---|---|---|---|---|---|---|---|---|---|
| Spectrum 1 | 43.77 | 3.71 | | | 0.19 | 2.81 | 0.58 | | | 26.78 | 22.15 | | 100 |
| Spectrum 2 | 13.26 | | | | 76.94 | | | | | | 4.05 | 5.75 | 100 |
| Spectrum 3 | 36.74 | 1.67 | 0.17 | 2.18 | 2.40 | 0.42 | 0.30 | 0.29 | 0.30 | 0.66 | 52.14 | 0.60 | 100 |
| Spectrum 4 | 24.98 | | | | 65.99 | | | | | | 3.91 | 5.11 | 100 |

Figure 62. SEM image (BEC) and spectra from EDX show the inclusions in the rail sample, spectrums 1, 3, and 4 are Iron carbide, and spectrum 2 is Silicon carbide.
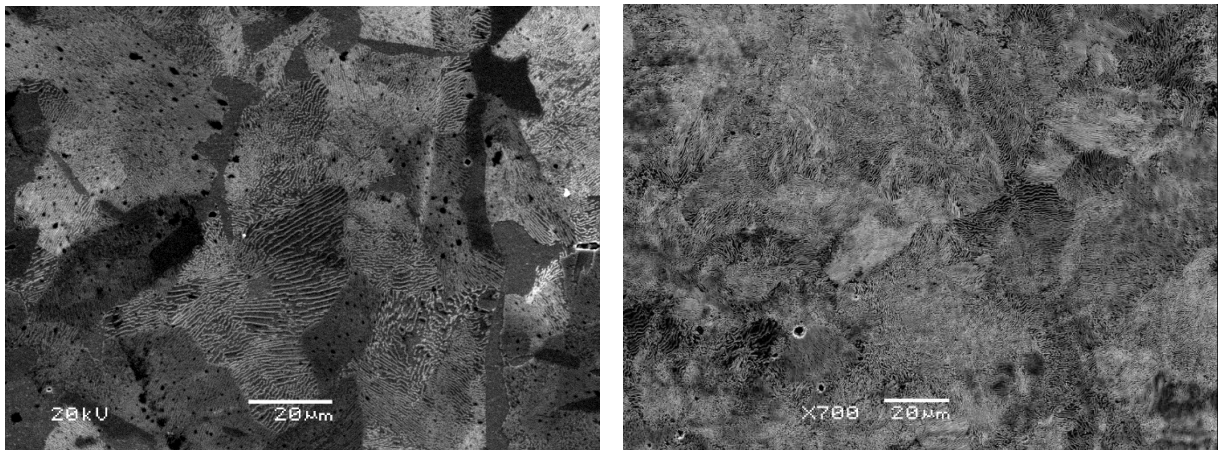


Figure 63. The microstructure of the R220 rail steel (left) and R260 rail steel (right) shows pearlitic lamellae colonies. R260 rail steel has a finer interlamellar spacing.
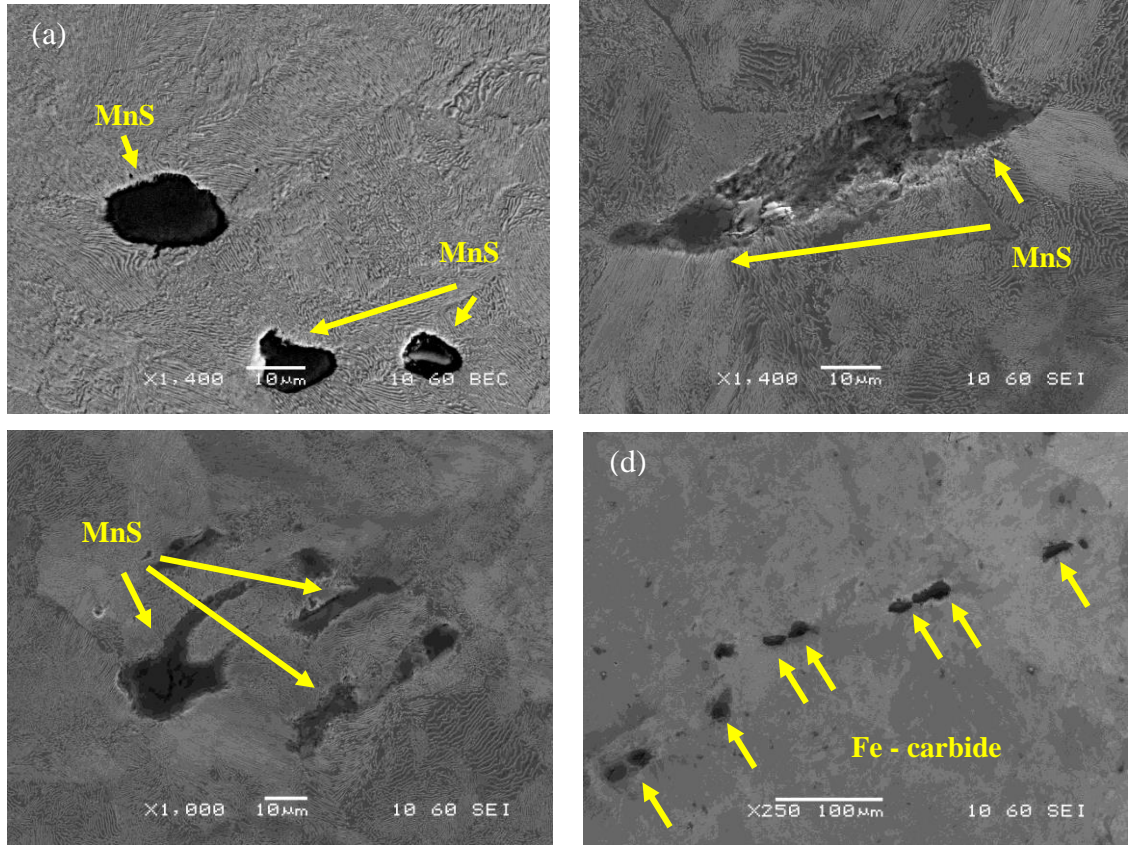
Figure 64. Non-metallic inclusions found in the study of R260 rail steels analysed point of interest using EDX (a), and (c) are the MnS inclusion defects (b) showing MnS inclusion debonded and pulled out from matrix (d) Iron carbide defects.

- **XRD analysis**
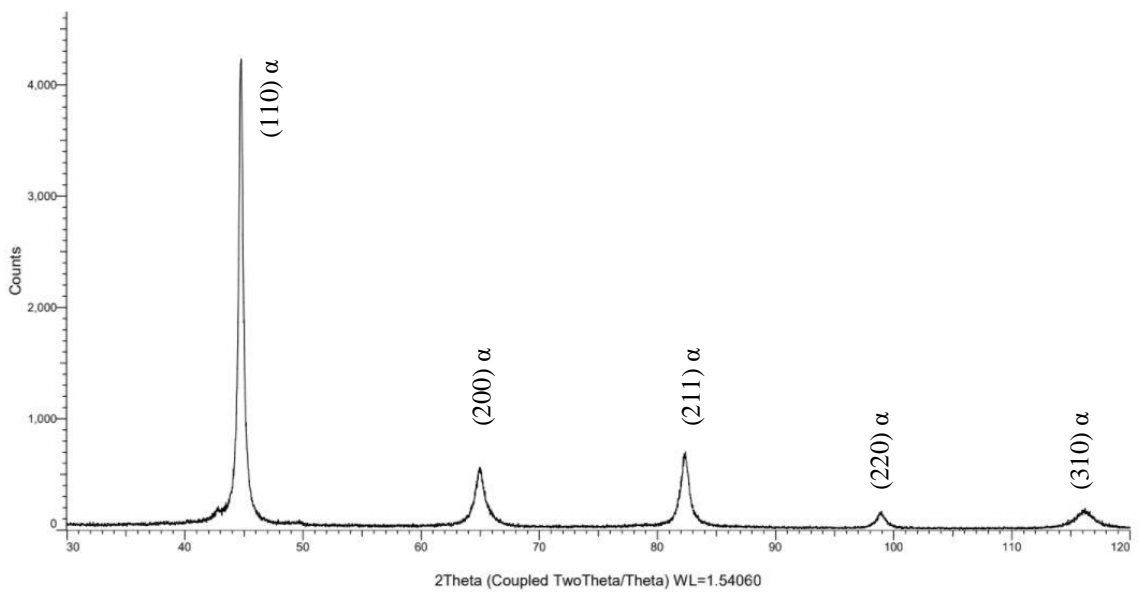


Figure 65. X-ray diffraction patterns were obtained from the R260 rail steel specimens.

Figure 65 shows the X-ray diffraction patterns corresponding to the presence of ferrite and cementite. The more intense peaks correspond to the matrix ferrite phase. R260 rail steel samples cut from the rail web. An evaluation of the diffraction patterns shows that the main microstructural feature of all tested rail steel specimens is ferrite (α), with the lattice plane 110 as the dominant texture direction. Kiraga et al. employed X-ray diffraction analysis to obtain data on rail steel phase composition to carry out a detailed analysis of the magnetic properties to optimise the induction heating process simulation of railway turnouts. In the acquired data from diffraction pictures of head specimens (γ), low-intensity peaks from residual austenite can be seen. A1 (head), A2 (web), and A3 (foot) are test specimens taken from three different sites for each rail [115].
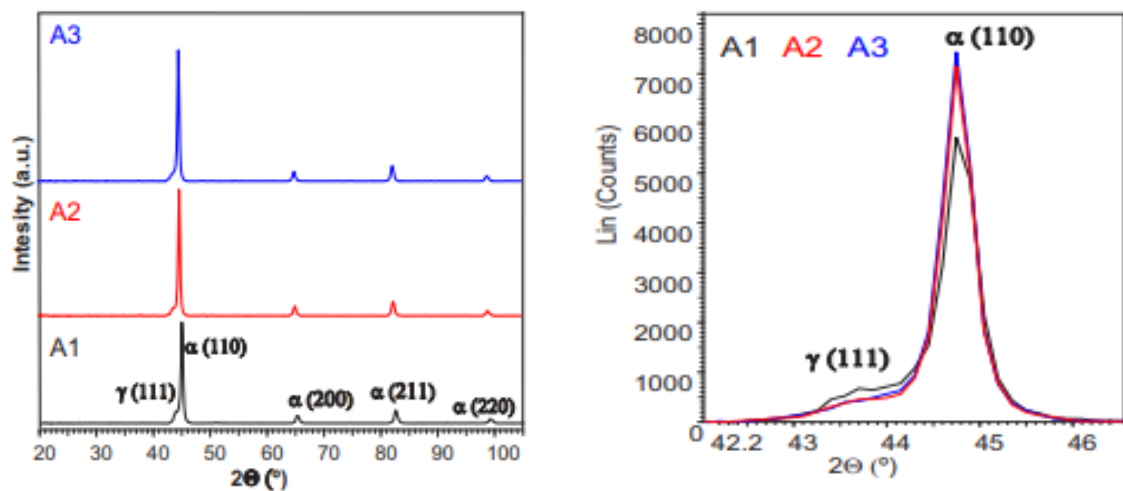


Figure 66. X-ray diffraction patterns of steel specimens were used to evaluate railways (Left) and rail phase composition within the range 41°- 47° of 2Θ (Right) [115].

- **Microhardness**

The rail steel was taken from the web of a used rail section withdrawn from the UK rail network does not specify exactly what grade it is. Therefore, the hardness value must be measured to confirm the steel grade being tested by comparing the hardness value with Table1. Note that this is an empirical approach-based test.

Twenty micro-hardness measurements were taken to allow for fluctuations in the hardness across the material due to changes in the microstructure on R260 rail steel samples to confirm the average hardness exhibited by the material. The average hardness value of the test was 284.08 Vicker Hardness (HV). The minimum is 275.0 HV, and the maximum is 300.8 HV. The tests' hardness values are compared with the tables showing rail steel grades with their hardness range, as shown in Table 2. Conversion of HV to HBW hardness. In HBW, the hardness is about 272.78 HBW. The steel used in this experiment is verified to be rail steel 260 grade.
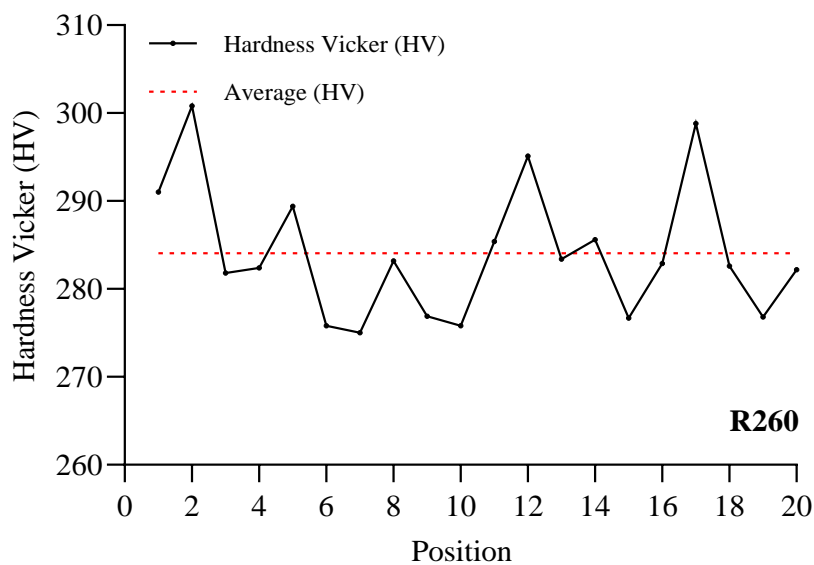


Figure 67. The hardness values were taken at twenty points across the area of the R260 rail steel.

### 4.3.2 Hadfield Manganese Steel

Hadfield steel samples similar to the grade used for manufacturing crossings were tested. Hadfield steel contains a high level of manganese (Mn), about 11–14 %, exhibiting high work-hardening rates. The rapid work-hardening exhibited by this alloy is responsible for its excellent wear resistance, which is beneficial in addressing the impact loads sustained by crossings in-service. Mn is an austenite stabilizer, allowing the faced-centred cubic (f.c.c) austenitic structure to remain stable even at room temperature. Thus, Hadfield steel exhibits an austenitic metastable microstructure due to the presence of high amounts of Mn. Figure 68 shows the schematic representation of the system's evolution from a metastable equilibrium state to a state of stable equilibrium and different ways of martensitic formation in metastable austenitic steels. Its hardness is higher than the original structure and thus, exhibits excellent wear resistance. The impact does not affect the microstructure in the deeper layers, so it does not exhibit substantial work-hardening. The mechanical properties of Hadfield manganese steel can be improved using various ways, such as solid solution strengthening, heat treatment, etc. However, if this steel is heated for the wrong time and temperature range, it will form carbides along the grain boundary and make the steel harder but brittle, making it unsuitable for use. Hadfield manganese steel has high toughness, high hardening capacity, high ductility in the pre-work-hardened condition, and it is very resistant to abrasion. This steel has been used successfully for the "frog" of railway track, replaceable switch point tips, and crossings.

The chemical composition of Hadfield manganese steel is shown in Table 11, and the mechanical properties are shown in Table 12.

Table 11. Typical chemical composition Austenitic cast manganese steel (in weight %).

| Carbon | Silicon | Manganese | Phosphorous | Sulphur |
|---|---|---|---|---|
| 1.20% | 0.15% | 11.00-14.00% | 0.020% | 0.020% |

Table 12. Mechanical properties in the supply condition of Hadfield manganese steel.

| Hardness Brinell (approx.) | Tensile Strength N/mm$^2$ | Yield Strength N/mm$^2$ | Elongation % |
|---|---|---|---|
| 200 | 880 | 320 | 40 |
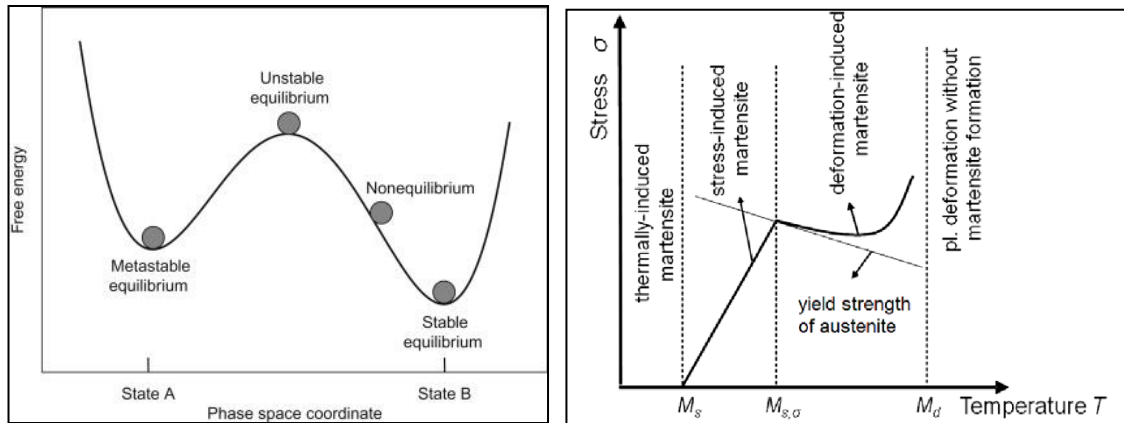


Figure 68. Schematic representation of the evolution of the system from a metastable equilibrium state through a state of stable equilibrium (Left) and different ways of martensite formation in metastable austenitic steels (Right) [116].

- **Metallographic examination**

A Struers Accutom was used to cut metallographic samples, then mounted on bakelite using a MetPrep HA 30 mounting press. The samples were subsequently ground and polished before being etched using a Marble etching agent to reveal the austenitic microstructure. The microstructure of the cut samples is shown in Figure 69. The microstructure was evaluated using a JEOL 6060 scanning electron microscope (SEM) equipped with an Oxford instruments Inca 300 EDS system.
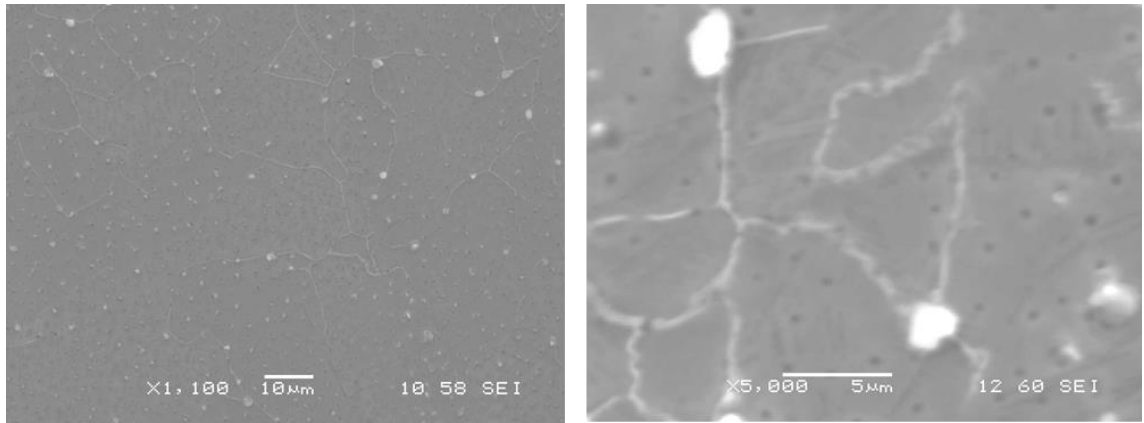
Figure 69. SEM micrographs of the metallographic samples show a predominantly austenitic structure.

The microstructure of Hadfield manganese steel consists of an austenite phase with carbide precipitate being also present. The carbide precipitates form along the grain boundary, resulting in reduced ductility and higher hardness. It is thus easier for cracks to propagate along the grain boundary (intergranular cracking). Figure 70 shows a schematic diagram of the austenitic s microstructure.
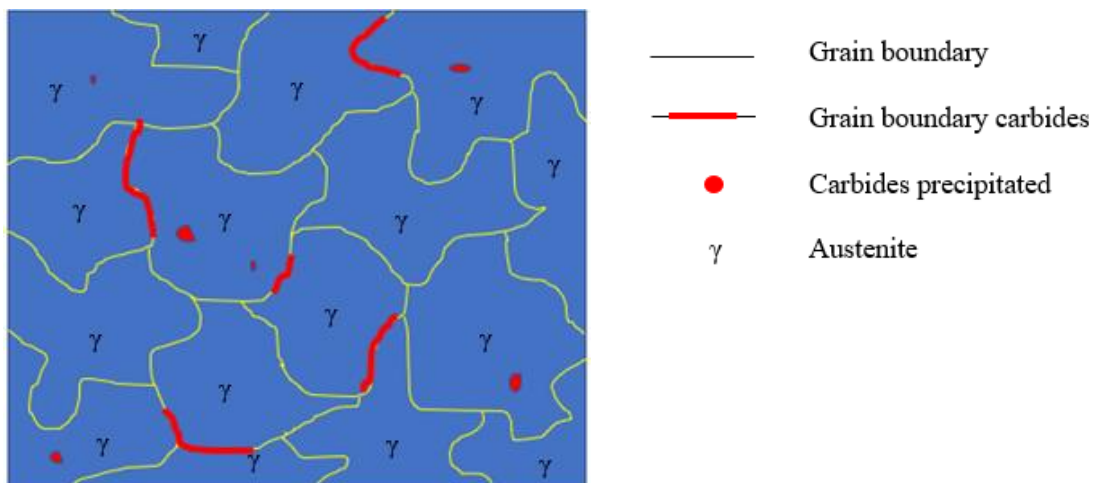


Figure 70. Schematic of austenitic microstructure showing austenite phase, grain boundary, and carbide precipitation in grain.
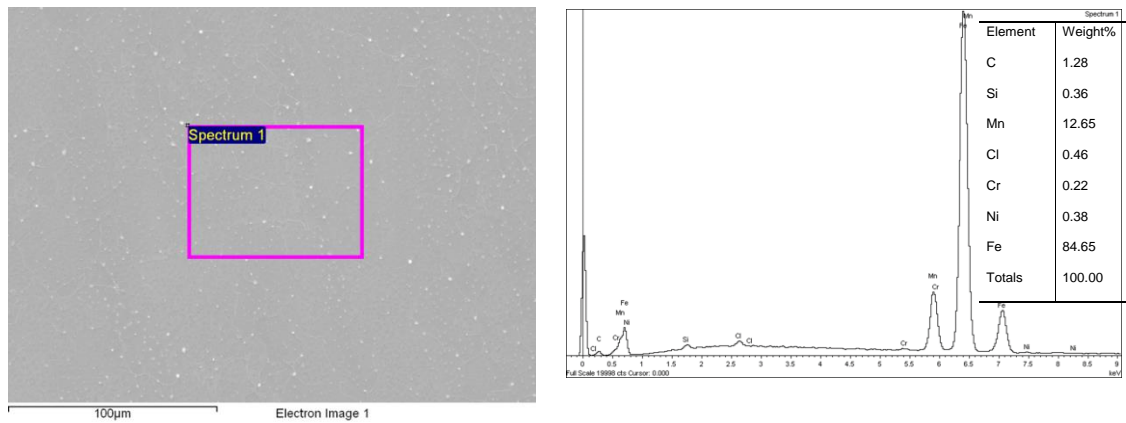
Figure 71. SEM image of the Hadfield manganese steel analysed area and the results of
EDX analysed of the sample.

- **XRD analysis**
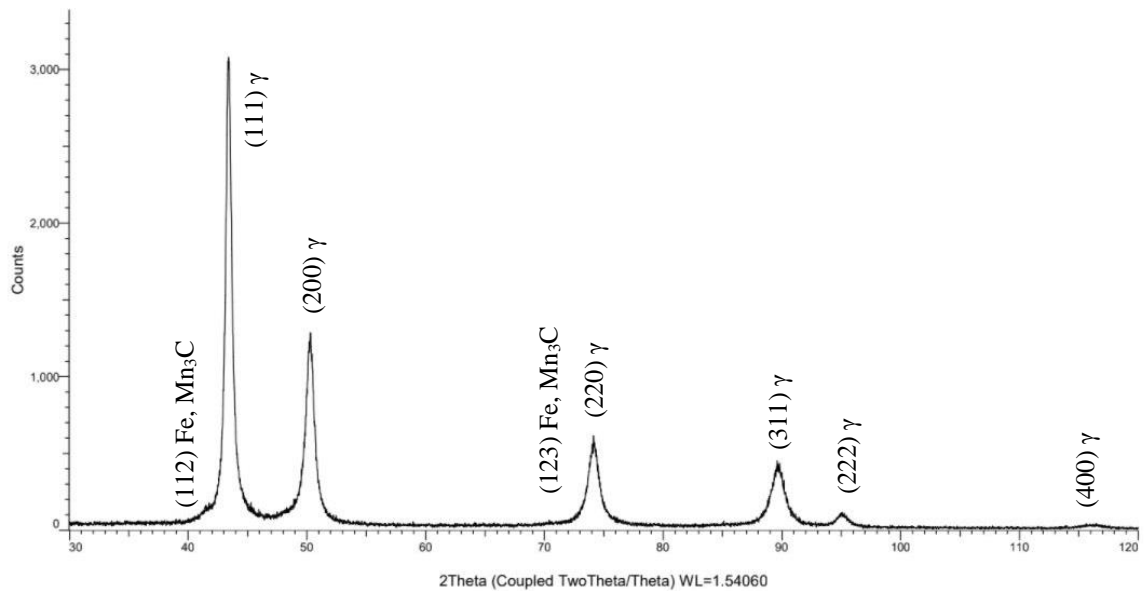


Figure 72. X-ray diffraction patterns of tested of Hadfield manganese steel.
(Note that this is an empirical approach-based test)

Each dot in the diffraction pattern above is formed by the constructive interference
of X-rays travelling through a crystal, according to Bragg's Law [164]. The XRD phase
analysis results obtained for a sample of the Hadfield manganese steel are shown in Figure
72. As it can be seen, austenite is the dominant phase present in the sample. It can also be
seen in the peak that Fe, $Mn_3C$ is the primary carbide form present in the sample.

Zambrano et al. [117] did not observe any secondary phases other than FCC austenite. On 20 mm x 10 mm x 2mm samples, Measurements of X-ray diffraction were obtained. Because the scanned area is so large, it is possible that small fractional phases will not be detected. The relative intensity of the peak location rises as the samples become more plastically deformed, with Section I being the least plastically deformed and Section III being the most plastically deformed.
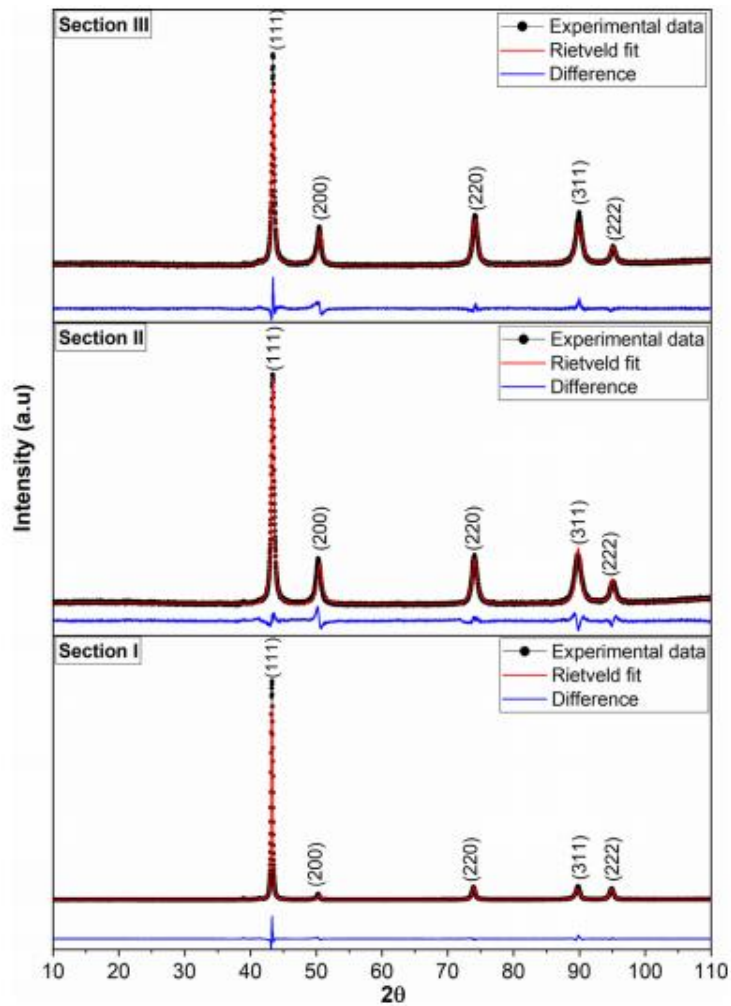


Figure 73. XRD results for each analysed section [117].

- **Microhardness**

Twenty hardness measurements were carried out on Hadfield steel samples. The average hardness value of the as-received samples was 230.13 HV with a 220-240 HV measurement range. From HV to HBW, the hardness is converted. In HBW, the hardness is about 223 HBW. The steel utilised in this experiment was verified to be Hadfield manganese steel. In the as-received condition, Hadfield manganese steel has an initial hardness range of 200-255 HV. In-service, the material rapidly work-hardens to approximately 530 HV. Note that this is an empirical approach-based test.
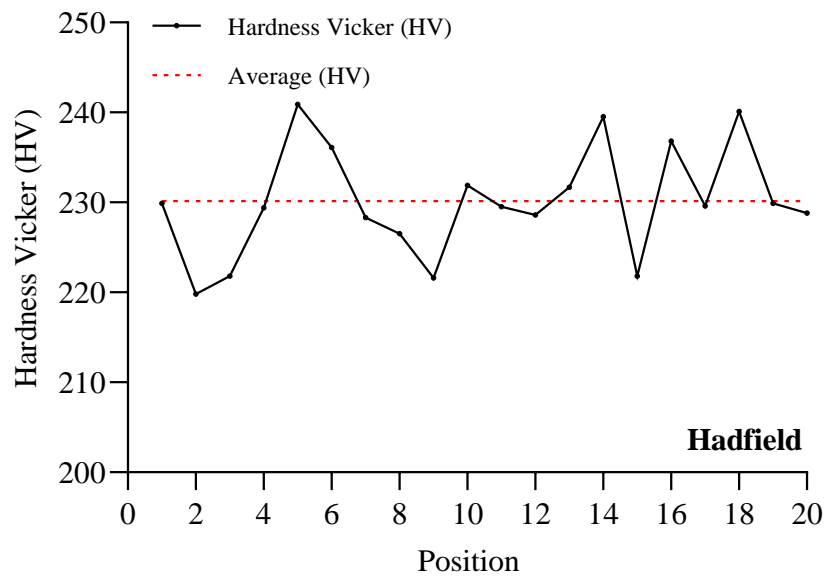


Figure 74. The hardness values were taken at twenty points across the area of Hadfield manganese steel.

Table 13. Maximum hardness values for Hadfield steels and steels with comparable chemical compositions were published in the literature for comparison (Adapted from [117].

| Reference | Maximum Hardness (HV) | Hardened condition |
|---|---|---|
| (Harzallah *et al.*, 2010) [19] | 1000 | RCF (Laboratory) |
| (Zambrano, Tressia and Souza, 2020)[117] | 894 | Wheel-crossing (In-service) |
| (Jost and Schmidt, 1986) [118] | 830 | Sliding (Laboratory) |
| (Kim and Bourdillon, 1992) [119] | 810 | Sliding (Laboratory) |
| (Chen *et al.*, 2018) [120] | 800 | High-speed pounding (Laboratory) |
| (Feng *et al.*, 2013) [121] | 750 | High-speed pounding (Laboratory) |
| (Yan *et al.*, 2007) [122] | 774 | Shot peening (Laboratory) |
| (Petrov *et al.*, 2006) [123] | 741 | Tension test (Laboratory) |
| (Machado *et al.*, 2017) [124] | 700 | Abrasive and impact (Laboratory) |
| (Shariff *et al.*, 2011) [125] | 700 | Sliding (Laboratory) |
| (Guo *et al.*, 2013) [20] | 610 | Wheel-crossing (In-service) |
| (Wen *et al.*, 2014) [126] | 575 | Impact (Laboratory) |
| (Kovács, Völgyi and Sikari, 2014) [127] | 500 | Hardening explosion |
| (Zhang *et al.*, 2019) [128] | 480 | Hardening explosion |

# CHAPTER 5

# EXPERIMENTAL METHODOLOGY

# CHAPTER 5: EXPERIMENTAL METHODOLOGY

This chapter describes the fatigue crack growth method starting from samples preparation, initiating the fatigue crack and the main fatigue test, as well as methods for examining the cracked surface of samples after the end of the test. All experiments were conducted under laboratory conditions. The results of the experiment will be shown and discussed in chapters 6 and 7.

## 5.1    SAMPLE PREPARATION

The R260 rail steel samples were taken from the web of a used rail section withdrawn from the UK rail network. In addition, a plate of Hadfield manganese steel was procured from West Yorkshire Steel. Sections from the Hadfield steel plate was plasma cut to produce ten samples of dimensions 120 mm x 20 mm x 10 mm (length x height x width) suitable for fatigue testing (Figure 75). A central notch was spark eroded in each sample with a depth of 2 mm and a 30° angle to concentrate stress during fatigue testing (Figure 76). The samples were pre-cracked using a vibrophore electro-mechanical high-frequency fatigue machine to an initial crack length of 3-4 mm. approximately.
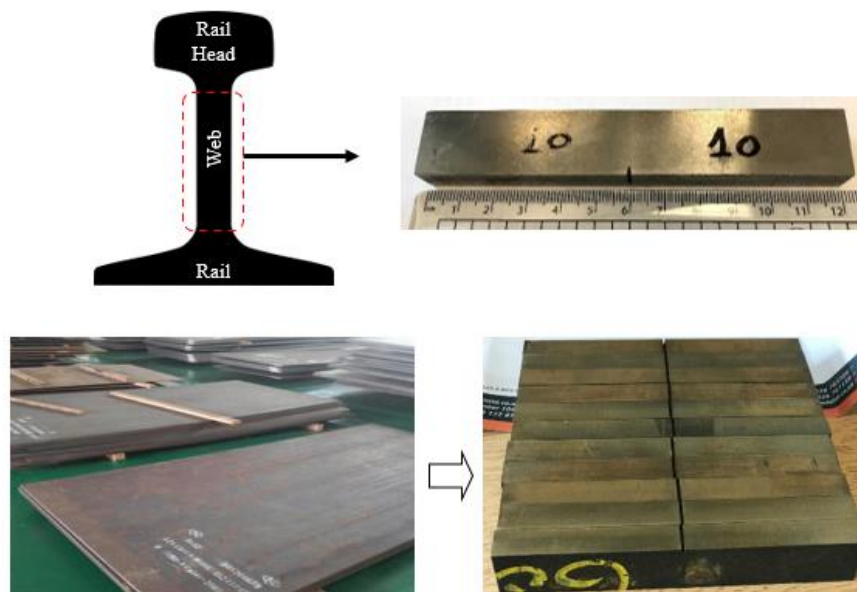


Figure 75. Photograph of the prepared samples.
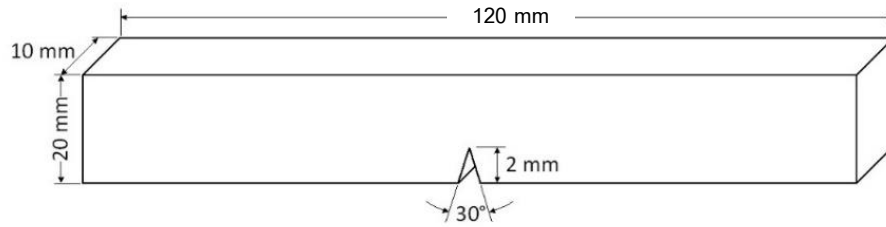
Figure 76. Single edge-notch specimen extraction in a three-point bending fatigue test.

The surfaces of metallographic samples were prepared using grinding, polishing, and etching (Figure 77). Metallographic specimens were mounted on bakelite using a MetPrep HA 30 mounting press (Figure 79). After mounting, the specimens were wet ground to reveal the surface of the metal. The samples were successively ground with finer silicon carbide abrasive paper (SiC) grades. After grinding the specimens, polishing was performed with diamond suspension (starting at a particle size of 9 micrometres, subsequently with 6 micrometres and finishing off at 1 micrometre) to achieve scratch-free mirror finis. After polishing, the specimen microstructure constituents were revealed by using a suitable etchant. Nital with a concentration of 2% Nitric acid in Methanol was employed to etch the R260 samples and Marble's reagent for etching Hadfield manganese steel samples to reveal the microstructure. The most often used metallographic etchant is a 2% Nital solution for etching mild steel, carbon steels, and low alloy steels. It has a high etching rate, can attack ferrite, and indicates ferrite boundaries while being safe to keep. Marble's etching is a metallographic etchant for etching austenitic stainless steels in the 300 series, nickel-based superalloys, and cobalt-based superalloys. The etchant darkens austenitic grains, attacks sigma phases, and causes grain flow to appear. The etched samples were examined using a Karl Zeiss optical microscope with digital imaging capability.

By Optical microscope (OM) and Scanning Electron Microscope (SEM)

Observing

Using 2% Nital for R260 and Marble's etch for Hadfield steel

Etching

Using cloth specialize and diamond suspension 9µm, 3µm, and 1µm respectively

Polishing

Using abrasive grinding disc 80, 200, 400, 800, 1200 and 2000 respectively

Grinding

Hot mounted using Bakelite powder

Mounting

Cutting

Figure 77. Samples Preparation for metallographic and microhardness testing.

Due to the work hardening ability of the Hadfield manganese steel, it is impossible to use a usual vertical cutting method because the hardness of the sample is gradually increased until one point is the same as the cutting blade. It results in the blade being broken and unable to cut. In this case, it is necessary to rotate the cutting axis to cut this type of steel. The parameter used for cutting the Hadfield manganese steel is shown in Figure 78.

Figure 78. The parameter used for cutting the Hadfield manganese steel.
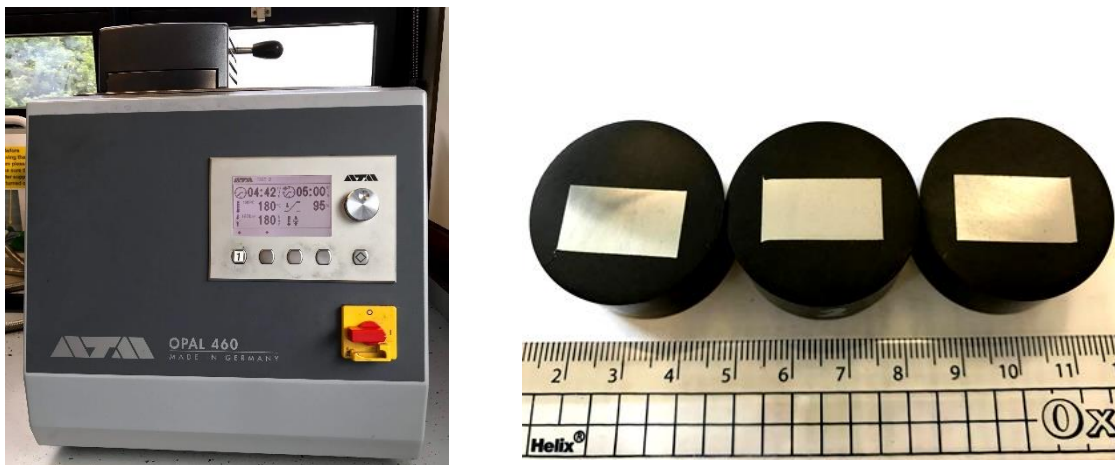


Figure 79. The Opal 460 - Automatic hot mounting press for mould sizes of up to 50mm.
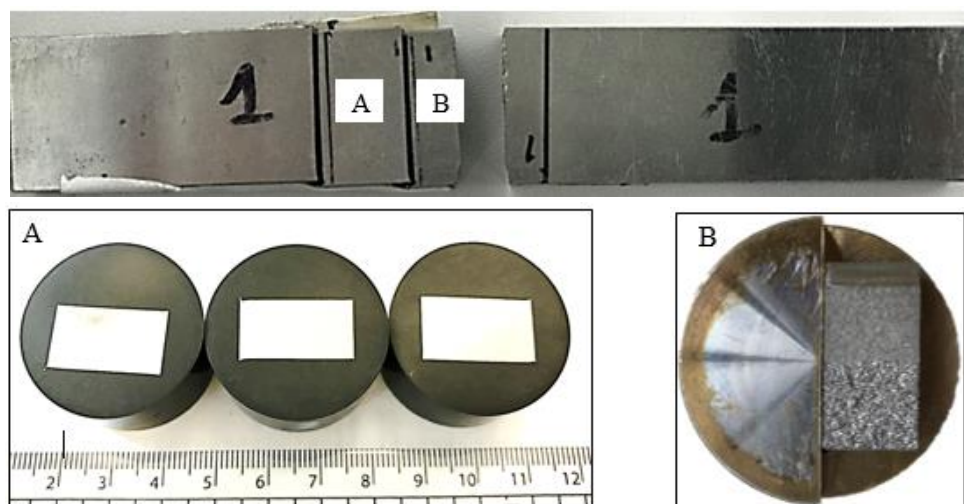


Figure 80. Samples for metallographic analysis (A) and sample for fractographic analysis (B).

## 5.2   PRE-CRACKING METHOD AND MEASUREMENT

Fatigue pre-cracking is used to initiate the fatigue crack prior to the main fatigue test sequence. This step is important because the notch can be affected by any curvature arising during its cutting resulting in variations during testing. Once the fatigue crack has initiated from the notch, the fatigue test can be started since any further growth will occur through the propagation of the tip of the formed crack and not from the notch, which may have some variability from sample to sample.
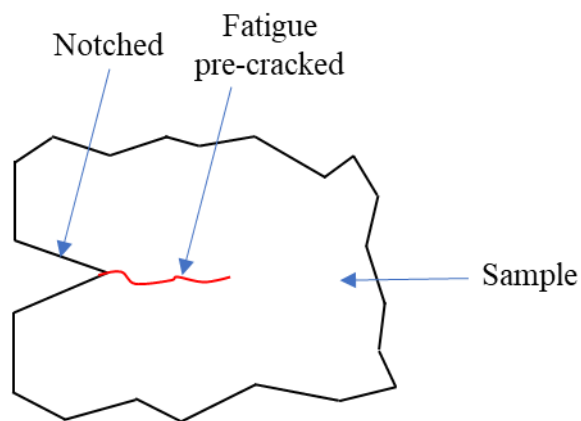
Figure 81. Schematic of fatigue pre-cracking.

The samples tested were placed in a three-point fatigue bending configuration under laboratory conditions at room temperature (Figure 82). If the stress at the notch tip is higher than the yield strength, a plastic zone will develop ahead of the notch, and any compressive residual stress in the plastic zone will remain after unloading. After pre-cracking, the presence of the crack and its length was confirmed by taking an acetone replica of the notch surface and observing it under an optical microscope.
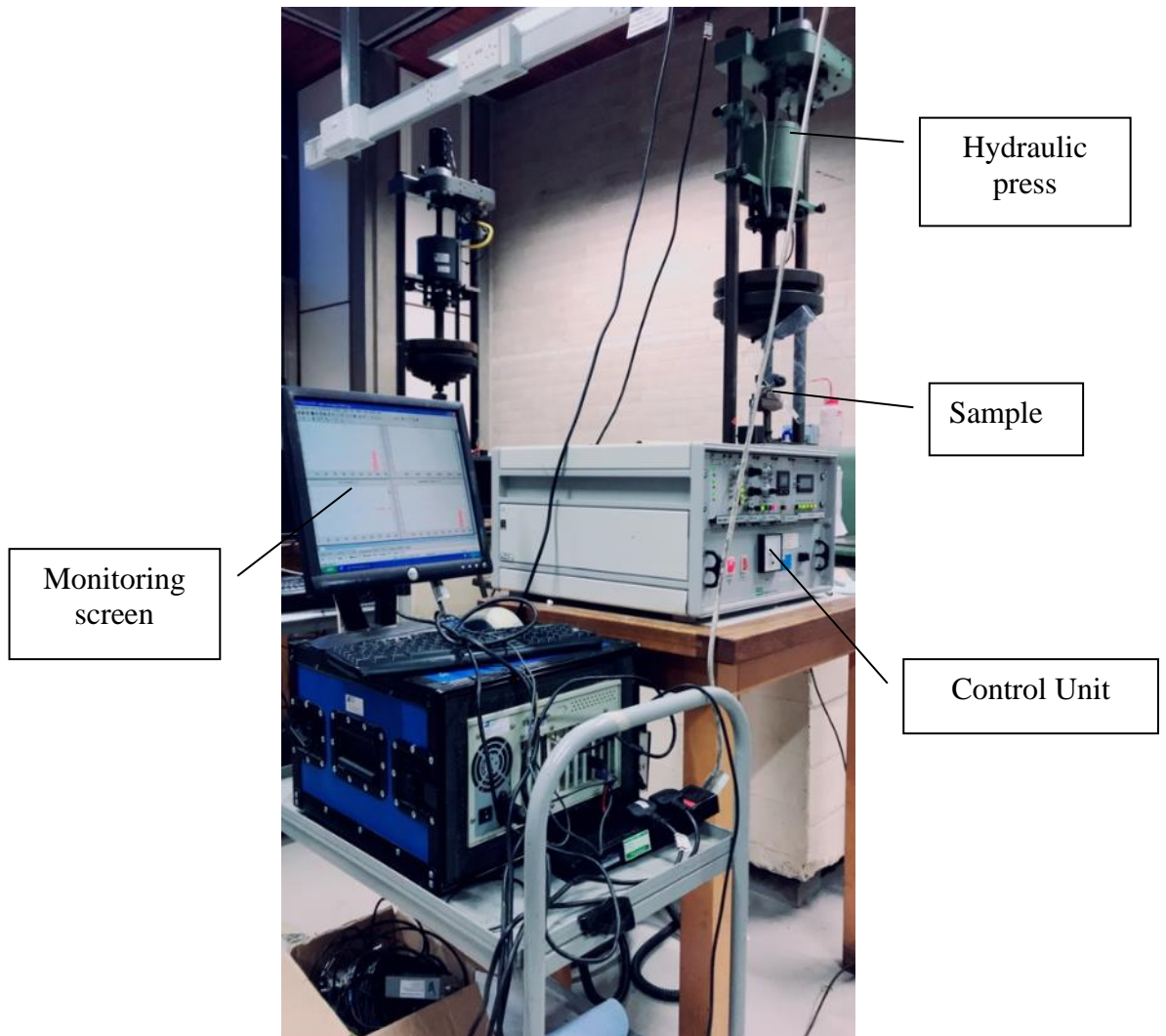
Figure 82. The set-up of equipment used for pre-cracking, shown with a sample in a three-point bending test.
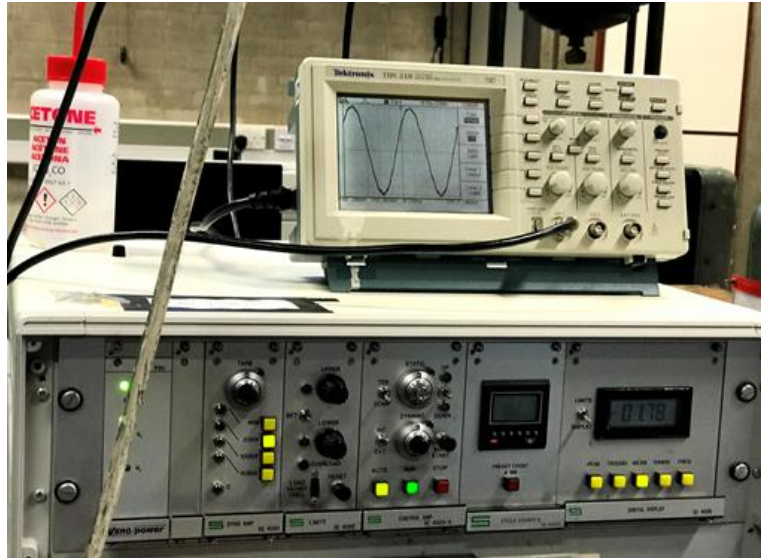
Figure 83. Control unit.

At a magnification of 100x, optical images on both sides of each pre-cracked sample were taken using a Karl Zeiss optical microscope (Figure 84). The length of the fracture was determined using the Image J software [129]. The crack size was measured from the surface to the ends of the cracks, including the eroded notch caused by the spark wire.
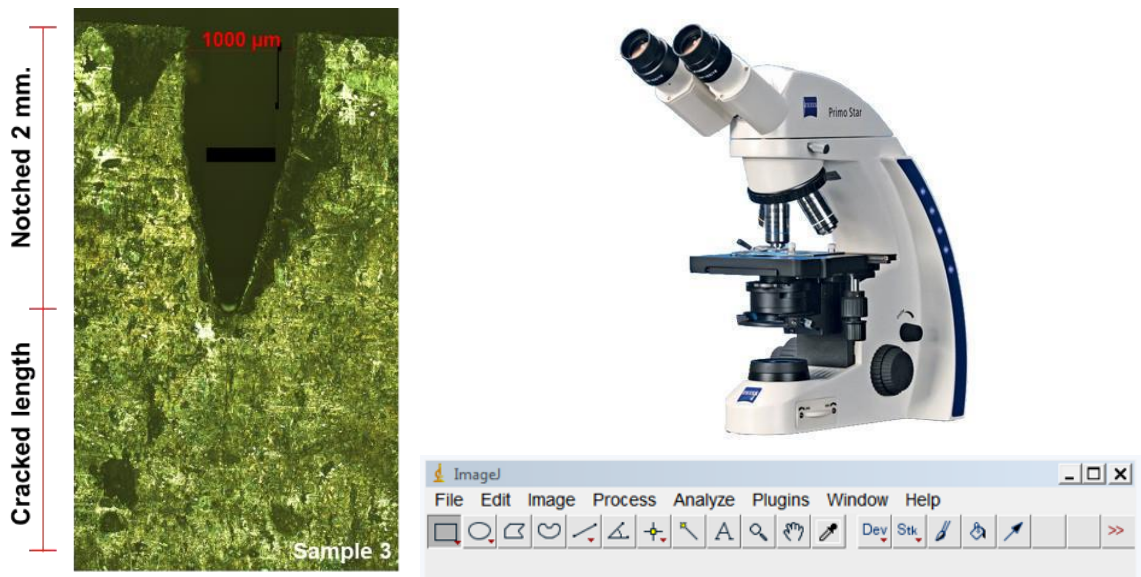


Figure 84. Karl Zeiss OM and ImageJ software measured the crack length.

The AE signals were detected for pre-cracking and fatigue testing using a four-channel AE system (Figure 85) obtained from PAC (Physical Acoustics Corporation, now Mistras). Two 150-700 kHz PAC R50a resonant piezoelectric sensors were used as AE sensors, coupled to a 2/4/6 pre-amplifier with a gain of 40 dB. The sensors were glued to the sample using Araldite epoxy glue, and the signals were acquired using the AEWin data acquisition software.

.
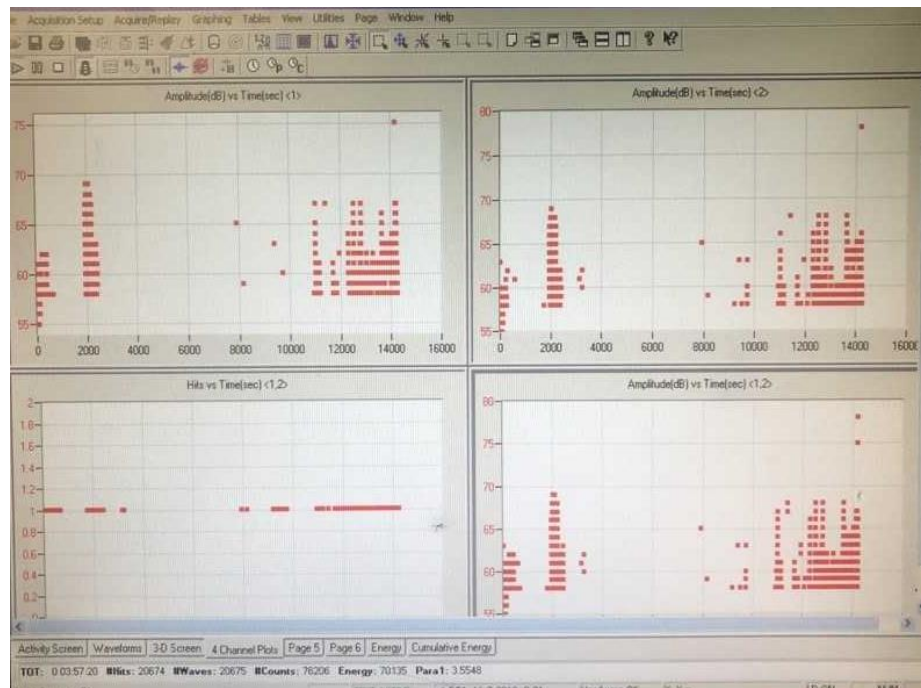


Figure 85. 4-channel AE system bought from PAC.

**AE sensor** - R50a resonant AE sensors (Figure 86) were employed for the AE laboratory experiment. The R50α sensor has a diameter of 19 mm and a height of 22.4 mm. The R50a sensor is a narrow resonant sensor with high sensitivity, with an operating frequency range between 150 kHz and 700 kHz. The case material is made of stainless steel, and the face material is made of alumina ceramic [87].

Figure 86. R50a AE sensor [130].

**Preamplifier** – AThe 2/4/6 preamplifiers (Figure 87) procured from Physical Acoustics Corporation (PAC) were used. The output voltage of this preamplifier is switch-selectable with 20, 40, and 60 dB levels. In this instrument, the plug-in filters are combined to maximize the sensor's selectivity and noise rejection. Low-pass, high-pass, and band-pass configurations can be supplied via filters. The preamplifier boosts the input signal's strength while reducing electromagnetic noise produced by the cables during signal transmission between the sensor and the instrument. It can also transform a high-impedance signal to a low-impedance signal for long-length cable transmission.



Figure 87. Preamplifier

**Adhesive -** The AE sensors, typically, must be held in place for an extended period, and coupling stability is needed; adhesive couplings such as Araldite® (Figure 88) and superglue are preferred. Silicon rubber compound and rigid bond are the two most popular adhesive couplants used in AE. The rubber compound can have outstanding stability in

the case of surface vibration or movement. If properly mounted, a rigid bond can have the strongest longitudinal and shear displacement transmission.



Figure 88. Araldite® - Industrial Rapid Epoxy

**Pre-cracking method**

Pearlitic rail steel R260 and Hadfield manganese steel samples were pre-cracked using an Amsler 20KN Vibrophore electro-mechanic high-frequency fatigue machine to an initial crack length of 3-4 mm approximately. A force of 0.85 - 8.5 kN and fixed stress ratio (R=0.1) were applied at a frequency of roughly 100 Hz. The AE threshold was set at 70 dB for the pearlitic rail steel R260 samples. A force of 0.65 - 6.5 kN and fixed stress ratio (R=0.1) were applied at about 85 Hz, and the AE threshold was set at 70 dB for the Hadfield manganese steel samples. The load was applied until the onset of crack growth was observed either in the form of AE signals or a significant drop in the vibrophore loading frequency. The presence of a crack was then confirmed by optical microscopy using an acetone replica of the notched surface area.

## 5.3    FATIGUE TEST (CYCLIC THREE-POINT BENDING)

The three-point fatigue bending tests were carried out under laboratory conditions. The machine used for this set of tests was a DARTEC 50 kN servo-hydraulic universal test machine. All tests were carried out at room temperature. The fatigue crack length was monitored throughout testing using a Direct Current Potential Drop (DCPD) instrument. AE signals generated during the fatigue tests were recorded and analysed using two R50a acoustic emission sensors produced by Physical Acoustic Corporation (PAC). These sensors can also be used in the field. One sensor was connected to a customized AE system developed in-house to capture the complete waveform produced during loading and unloading for some of the tests, whilst the other was connected to the PAC commercial system to monitor the overall AE activity. The commercial AE system deletes the complete waveform and keeps only the data related to the definition of an AE hit as set by the user. The R50a sensors were mounted away from the centre of the sample, one on either side of the cracked region, using Araldite®. A Phoenix Alpha Digital Control System was used to monitor the applied load level and the number of cycles, as shown in Figure 91. Raw AE data acquired using AE Win software were subsequently analysed using NOESIS software supplied by Envirocoustics, a PAC Group member.
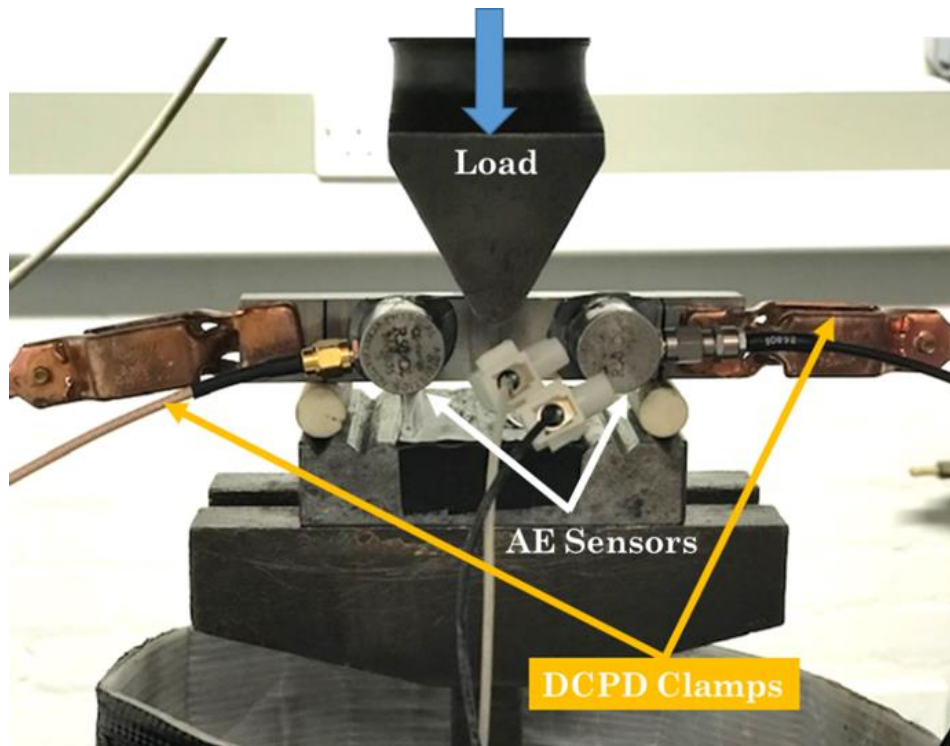
Figure 89. Cyclic Three-point-bending test (fatigue testing).

In the fatigue test, the imposed stress cycle is typically a sine wave. The schematic representation of the cyclic stress versus time relationship is shown in Figure 90, and the following terms are defined.
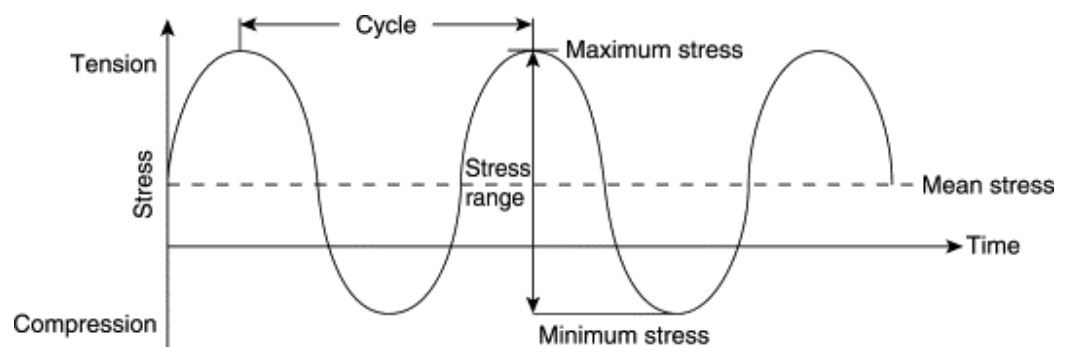


Figure 90. Definitions of stress in cyclic loading* [131].
* Compressive stresses are negative, the convention that tensile stresses are positive,

**Maximum stress ($\sigma_{max}$):**   the largest stress in the cycle.

**Minimum stress ($\sigma_{min}$):**   the smallest stress in the cycle.

**Stress range ($\Delta\sigma$):**   the algebraic difference between the maximum and the minimum stress; $\Delta\sigma = \sigma_{max} - \sigma_{min}$

**Stress amplitude (S):**   $S = \Delta\sigma/2$

**Mean stress ($\sigma_m$):**   the average of the minimum and maximum stresses.

$$\sigma_m = (\sigma_{max} + \sigma_{min})/2$$

**Stress ratio (R):**   $R = \sigma_{max}/\sigma_{min}$

**Cycle:**   the interval between one peak of stress and the next one

**Frequency:**   the number of cycles per second.
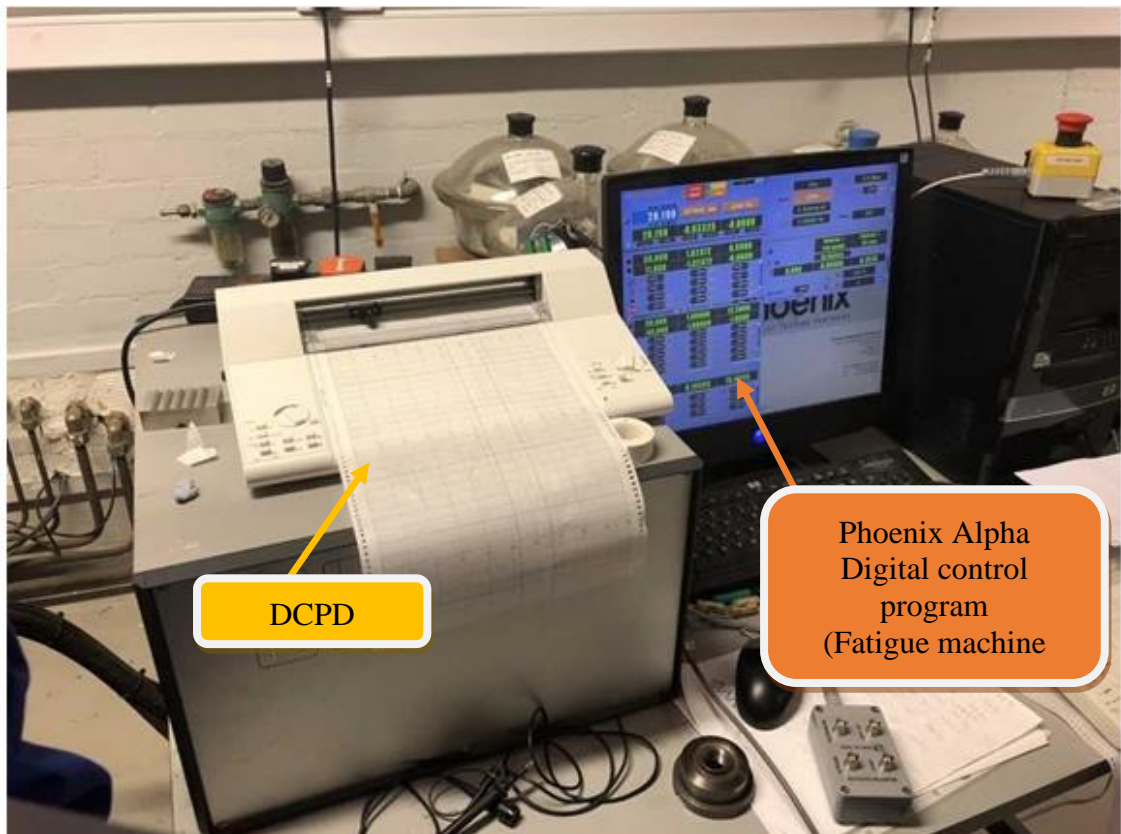


Figure 91. Monitoring and recording equipment, the plotter for DCPD and Phoenix Alpha Digital control program.

Paris and Erdogan investigated how long fatigue cracks are distributed in the linear elastic fracture mechanics system. They demonstrated that the propagation velocity is not constant with time but varies according to the Stress Intensity Factor (SIF) range ΔK. The crack growth rate da/dN is the power function of the SIF range during stable crack propagation, commonly referred to as the Paris regime. This results in the well-known Paris equation. The fatigue crack growth (FCG) curve is a function of the crack growth rate (da/dN) and the range of applied stress intensity factors. The Paris-Erdogan law can be used to describe the relationship between ΔK and da/dN between the rates of crack growth from low to high [132].

$$\frac{da}{dN} = C\Delta K^m, or : \log\left(\frac{da}{dN}\right) = \log C + m\log\Delta K \qquad \text{... (1)}$$

The crack length *da/dN* is the crack growth rate, *C* and *m* are material constants.

$$\Delta K = K_{max} - K_{min} \qquad \text{... (2)}$$

For a specific geometry, $K_I$ coefficients are defined. The stress intensity factor ($K_I$) at the crack tip of a three-point bending sample is [133];

$$K_I = \frac{4P}{B}\sqrt{\frac{\pi}{W}}\left[1.6\left(\frac{a}{W}\right)^{\frac{1}{2}} - 2.6\left(\frac{a}{W}\right)^{\frac{3}{2}} + 12.3\left(\frac{a}{W}\right)^{\frac{5}{2}} - 21.2\left(\frac{a}{W}\right)^{\frac{7}{2}} + 21.8\left(\frac{a}{W}\right)^{\frac{9}{2}}\right] \text{... (3)}$$

The applied load is the thickness of the specimen, *a* the crack length, and *W* is the width of the specimen.
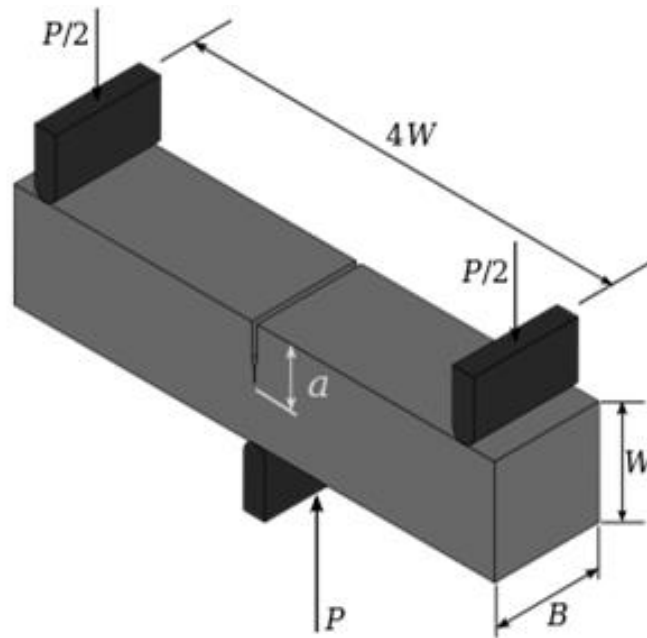
Figure 92. Three-point bending sample [133].

The three regions of a fatigue crack growth resistance curve are shown in the figure below.
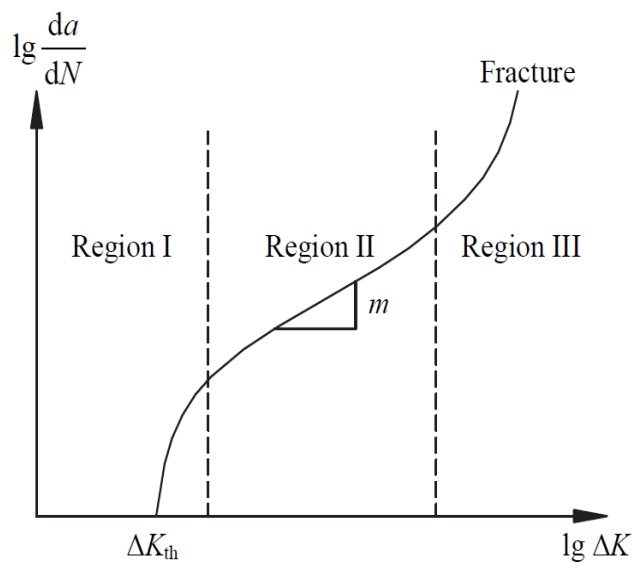


Stage I (threshold effect) includes crack initiation and in the form of micro-sized cracks, which the microstructures can arrest before they coalesce in order to form a macrocrack. The threshold is too low in most cases to use in design, but the threshold value can be significant for certain designs where no fatigue cracking is allowed.

Stage II (Paris' Law) is a critical stage in predicting crack growth before leading to final failure. During stage II crack growth follows a linear rate when plotted in the logarithmic scale stage II is used for design and is also helpful for failure diagnosis

<u>Stage III</u> (unstable crack growth). During stage III, the fatigue crack has grown to a critical size, and propagation becomes unstable, leading to final failure after only a few cycles. In addition, cracks in critical structures cannot reach stage III in the design, leading to brittle failure.

The fractured surface is described as a dimple due to surface roughness at high crack growth rates and smoothness at low crack growth rates. A stretched band develops during the transition from low to high crack growth rates.

Principles for applying fracture mechanics in fracture analysis can be summarized as follows:

1. Based on the actual problem, the material to be analysed under the conditions of the load exerted on that material was used in the ASTM E-647 [134].

2. Select the appropriate specimen type for testing under the laboratory.

3. Perform the test to obtain necessary data; crack length (a) and number of cycles (N)

4. Calculate the obtained values and plot the relationship between da/dN and $\Delta K$. By fitting the best fit line, the C and m values are obtained.

5. From (4), it is possible to calculate the service life of materials under a specified load when a crack is detected at a certain length.

The most commonly used technique for detecting AE signals is based on detecting signals exceeding the threshold. Processing and hit measurement are initiated when signals surpass a pre-set fixed or floating amplitude threshold level. However, other approaches based on the statistical or spectrum characteristics are available in addition to threshold-based hit detection strategies.

### 5.3.1 Direct current potential drop

The DCPD method has been employed to measure the length of cracks during fatigue crack growth under laboratory tests. The principle is to apply a continuous DC voltage across the specimen and measure variations as the crack grows, causing changes in resistance. When the crack is extended, the electrical resistance increases, and the measured potential increases. This method is useful since it has good stability and repeatability, whilst no optical access is needed [135]. The DCPD traces are directly associated with the crack length increase. The crack length can be calculated using **Johnson's formula** [136].

$$\frac{V(a)}{V(a_0)} = \frac{\mathrm{arccos}\,h\left[\dfrac{\cosh(\pi y/2W)}{\cos(\pi a/2W)}\right]}{\mathrm{arccos}\,h\left[\dfrac{\cosh(\pi y/2W)}{\cos(\pi y/2W)}\right]} \qquad \ldots(4)$$

Johnson's formula $a$ can be obtained by solving

$$a = \frac{2W}{\pi}\cos^{-1}\frac{\cosh\left(\dfrac{\pi y}{2W}\right)}{\cosh\left\{\left(\dfrac{V_a}{V_{a_0}}\right)\cosh^{-1}\left[\cosh\left(\dfrac{\pi y}{2W}\right)/\cos\left(\dfrac{\pi a_0}{2W}\right)\right]\right\}} \qquad \ldots(5)$$

Where $a_o$ is the initial crack length, $V(a_o)$ is the corresponding potential, $W$ represents the specimen width, and $y$ represents the distance of electrodes from the potential probe to the crack mouth.
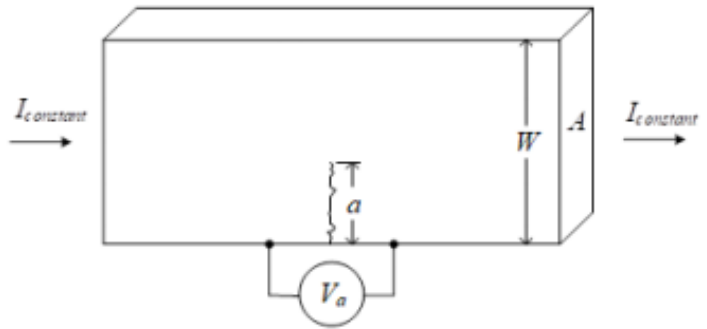
Figure 93. DCPD instrument (Left) and a cracked material in the DCPD testing (Right).

### 5.3.2 Experimental Procedures

### R260 Rail Steel

The fatigue tests were conducted at room temperature under a sinusoidal loading pattern with a frequency of 5 Hz and a fixed stress ratio (R=0.1). The maximum and minimum loads are 5.5 kN and 0.5 kN, respectively, which are less than the R260 steel yield points. The commercial PAC system and the customized AE system consisted of two 150-700 kHz R50 piezoelectric sensors connected to a 2/4/6 pre-amplifier to record the AE activity. Sampling rates were set at 5 MS/s, with Peak Definition Time at 600 µs, Hit Definition Time at 1000 µs, and Hit Lockout Time at 3000 µs. The AE amplifier is set at 40 dB, while the minimum measurement threshold is set at 60 dB for samples 1 and 2. The reduced to 58dB for the rest of the samples. The fatigue crack propagation is monitored by the DCPD method.

**Hadfield Manganese Steel**

A force 0.45 kN – 4.5 kN, which is lower than the determined yield point of Hadfield manganese steel was applied under applied constant amplitude sinusoidal wave loading at a frequency of 5 Hz and a fixed stress ratio (R=0.1). The commercial PAC system and the customized AE system consisting of two 150-700 kHz R50α piezoelectric sensors connected to a 2/4/6 pre-amplifier are used to record the AE activity. The sampling rate was set at 5 MS/s, with Peak Definition Time at 600 µs, Hit Definition Time at 1000 µs, and Hit Lockout Time at 2000 µs. The AE amplifier is set at 40 dB while the minimum measurement threshold is set at 50 dB, reduced from 70 dB for pre-cracking for greater sensitivity. The fatigue crack propagation was monitored by the DCPD method.
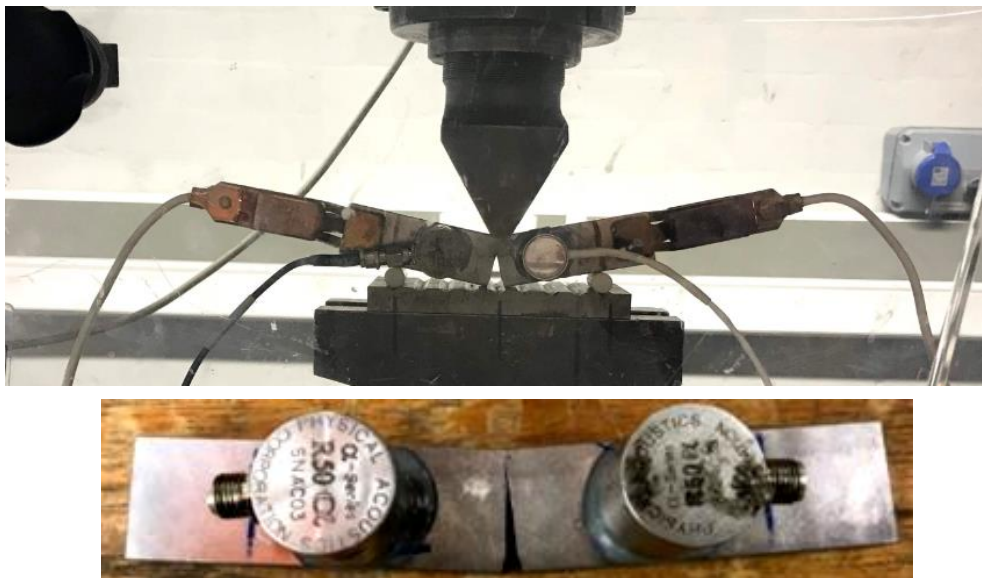


Figure 94. AE sensors were mounted on the broken specimen.

After fatigue testing, all crack surface samples were opened with a Charpy test hammer and cut to roughly 5mm x 10mm x 20 mm for microscopy.

## 5.4   FRACTURE SURFACE ANALYSIS

### 5.4.1 2D Analysis using Scanning Electron Microscope

The intensity of the image shown on the screen is controlled by the variable signal intensity. Figure 95 shows an overview of the SEM and EDS units.



Figure 95. SEM JEOL 6060 with EDS Unit Overview.

Both backscattered electrons (BECs) and secondary electrons (SEs) are generated when a primary beam interacts with a sample (Figure 96). SEs would be released from inelastic collisions with electrons in the k-orbital of the specimen's atoms in the SEM photoemission mode, allowing topological features to be seen. BCEs are elastically scattered electrons whose scattering effect is proportional to the atom's atomic number, Z. Backscattered electrons are more elastically dispersed and caught by detectors with higher atomic numbers than those of lower ones. BSE mode allows users to see different phases and precipitates in the microstructure without using an etched sample.
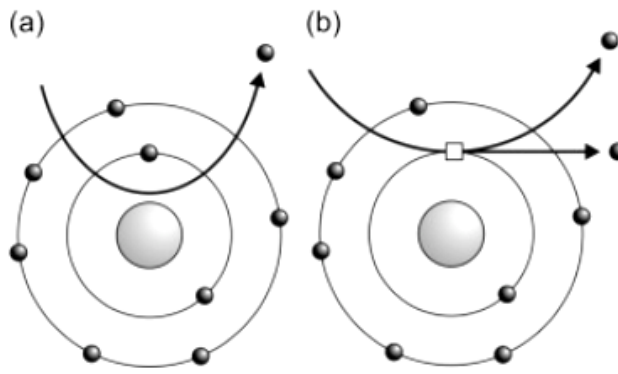
Figure 96. Electron–matter interactions at the origin of electron microscopy. (a) Backscattered electron (BSE) and (b) secondary electron (SE) [137].
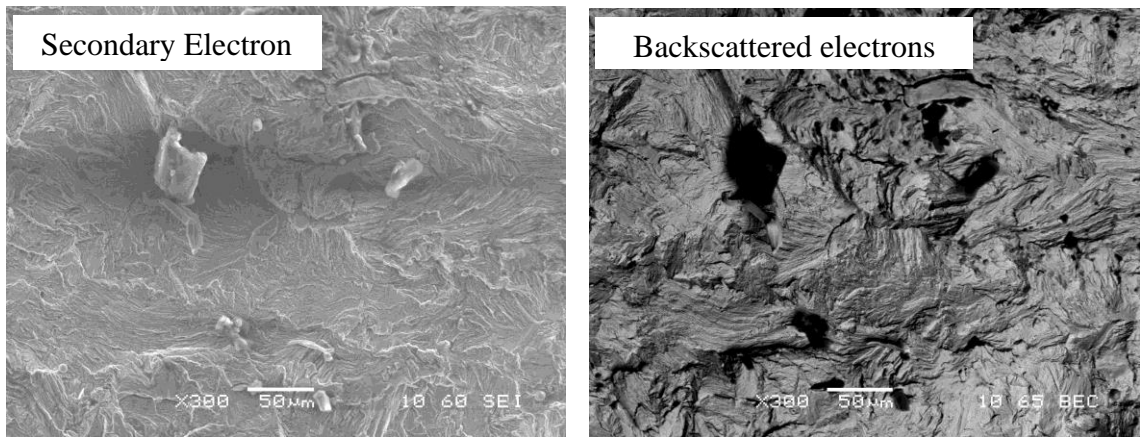


Figure 97. Carbide inclusion in pearlitic fracture surface. In SE image has no contrast difference. However, carbide inclusion was visible in the BSE image. In Backscatter imagery, the signal depends on the atomic number.

The elemental analysis or chemical characterisation is performed using Energy Dispersive X-Ray Spectroscopy (EDX or EDS). All elements have distinct, element-specific or characteristic energy levels, resulting in the generation of X-rays. Consequently, EDS does not provide chemical bonding data (Figure 98).
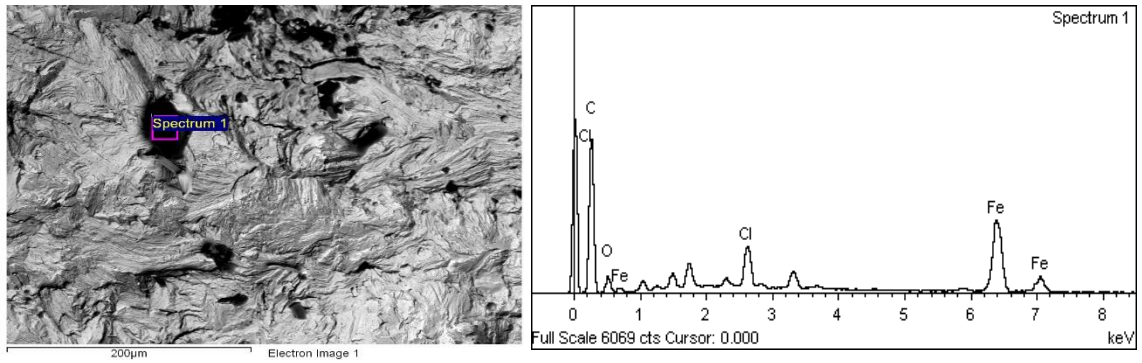
Figure 98. Elements are identified and labelled. The higher the peak, the higher the concentration of that element.

### 5.4.2 Non-metallic Inclusion Size Analysis in Steel

The composition of inclusions was measured using EDS after examining them in a JEOL 6060 SEM. The size of the inclusion was measured manually using ImageJ software. A binary black-and-white image is needed for automated particle analysis (Figure 99). To separate the objects of interest from the background, a threshold range is set. Evaluate the particle size by going to Analyze and choosing Analyze Particles.
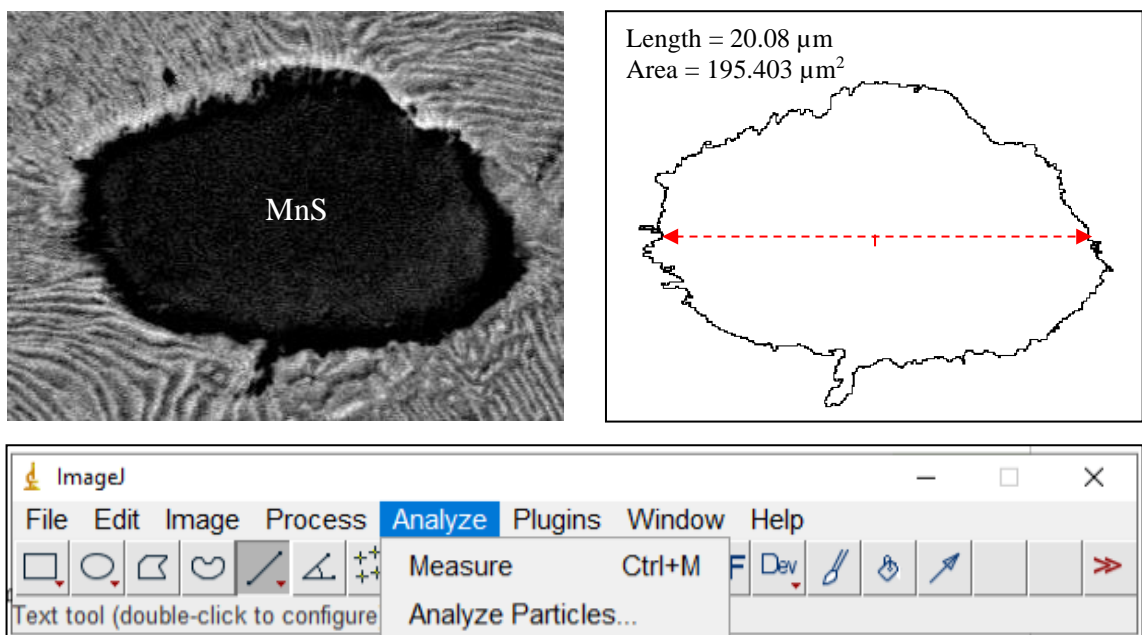


Figure 99. Particle Analysis Using ImageJ.

### 5.4.3 3D Analysis using Laser Confocal Scanning Microscopy (LCSM)

In 1961, Marvin Minsky developed the first confocal microscope, pioneered laser scanning confocal microscopy (LCSM). LCSM is widely applied in numerous biological science disciplines, optics and crystallography. Compared to a conventional optical microscope, the device's primary advantage was its confocal optical technology, which removed undesired out-of-focus light scattered and improved the resolution of an object's in-focus area [138]. A pin-hole aperture was added between the objective lens and the light detector to create this effect. From stage one, an intensely focused optical image of an object's in-focus area could be produced by point-by-point lighting of the sample and the moving object. Since its inception, thanks to the synergistic combination of precision mechanisms and modern computational capabilities, LCSM has grown and developed significantly during the last several years [139]. As a light source, the short-wavelength laser improved the confocal image speed's brightness and lateral resolution. However, the most significant advancement occurred with the development and integration of the Z-axis objective drive with computer processes, allowing the collection of a sequence of optical slices that produced three-dimensional surface topological information.

Fractography, along with metallography and mechanical inspection, is a significant technique for analysing failures and evaluating mechanical characteristics. However, even though observations are made on different scales, The huge percentage of fractographic investigations are qualitative and only focus on visualising fracture surface characteristics. As a result, the objectivity and reliability of fracture surface analysis are highly dependent on the specialist knowledge and knowledge of the observer. Furthermore, the lack of detailed topographic features may significantly impede quantitative fractographic evaluation using standard scanning electron microscopy or

transmission electron microscopy. In contrast to the microstructure, which can be completely described using two-dimensional metallographic images, the fracture surface is a three-dimensional entity that requires three coordinates at each location to measure the surface topology properly.

The area surface roughness and specific surface area of the fracture surfaces are measured quantitatively. The ductility of the cracked surface is determined by the typical fracture surface area rather than the area roughness. According to the results obtained during this study, LCSM may be beneficial for determining qualitative and quantitative characteristics of various fractured surfaces [140-141]. [142] investigated three-dimensional images. The point cloud was acquired using a confocal laser scanning microscope Zeiss LCSM 700 with an objective lens of 5x. The goal was to classify failure modes into three categories: sudden ductile fracture, sudden brittle fracture, and progressive fracture due to fatigue in order to help the fractographic study in failure analysis. The findings presented here are a good starting point for future texture analysis studies using three-dimensional data. In this study, the sample's fracture surfaces were examined using both the SEM and LCSM techniques. XYZ ultra-fast scan plus the colour was used as a scanning mode; the MPLFLN10X was used to scan multiple $1279 \times 1279$ µm fracture surface areas.
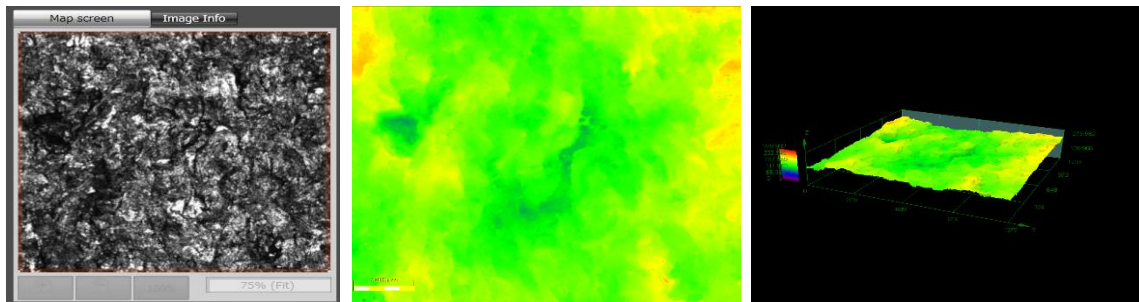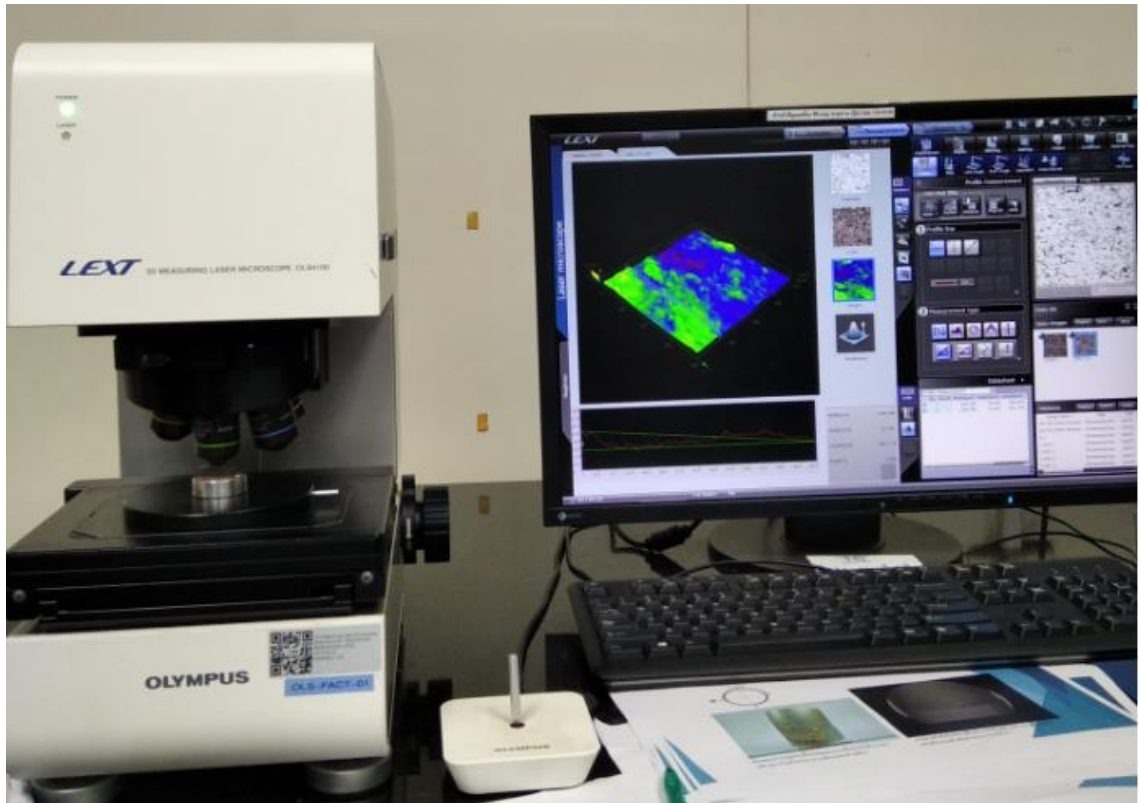
Figure 100. The OLYMPUS LEXT OLS4100 3D measuring laser microscope and the imaging process outline in a confocal microscope.

# CHAPTER 6

# FATIGUE TESTING

**CHAPTER 6: FATIGUE TESTING**

This chapter describes the experimental results to study the ability of PAC commercial AE system and customized AE system developed in house to compare signal detection and analysis of three types of samples. R260 rail steel and Hadfield manganese steel samples were performed by the author self-test, and the R220 rail steel sample was merely an observer to study the experimental method. This chapter also includes a quantitative analysis of reliability for a select number of AE parameters.

**6.1    PRE-CRACKING MEASUREMENT**

Reference to standard ISO 12108 [182], conduct fatigue pre-cracking with the single edge notch three-point bend, minimum pre-crack length shall exceed the greater the notch height 1mm. The specimen used in this study has a notch height of 2 mm, so the initial crack length should not be less than 3mm ($a_0 \geq 3$). The importance of the pre-cracking method described in **Section 5.2**.

Table 14 shows some images of the pre-cracked size taken with a Karl Zeiss optical microscope at a magnification of 10x. Due to equipment failures during testing, the data for sample 10 of R260 rail steel and sample 5 of Hadfield manganese steel are not shown in Table 14. The initial crack length of each sample of the R260 rail steel and Hadfield manganese steel is taken from the tip of the notch to the end of the crack using ImageJ software for measurement.

Note that R260 rail steel samples 2 and 4 have an acceptable initial crack length since the values were obtained by averaging the three measurements, but sample 3 is considered inappropriate.

| Pre-cracked image | Sample no. | Initial crack length (mm.) | | | |
|---|---|---|---|---|---|
| | | R260 (mm.) | % the original area | Hadfield (mm.) | % the original area |
|  R260 | 1 | 3.52 | 17.60 | 4.56 | 22.80 |
| | 2 | 2.95 | 14.75 | 3.25 | 16.25 |
| | 3 | 2.04 | 10.20 | 4.20 | 21.00 |
| | 4 | 2.83 | 14.15 | 3.77 | 18.85 |
| | 5 | 3.44 | 17.20 | - | - |
|  Hadfield | 6 | 4.29 | 21.15 | 4.57 | 22.85 |
| | 7 | 3.56 | 17.80 | 3.34 | 16.70 |
| | 8 | 3.95 | 19.75 | 3.37 | 16.85 |
| | 9 | 3.43 | 17.15 | 4.50 | 22.50 |
| | 10 | - | - | 3.49 | 17.45 |

Table 14. Pre-cracked images and the initial crack length of each R260 rail steel and Hadfield manganese steel sample are taken from the tip of the notch to the end.

Before the test, a pencil lead break, also known as the Hsu-Nielson source, must be used as an artificial acoustic source to verify the reliability of the acoustic coupling between the sensors and the surface of the test piece by pressing the pencil lead firmly against the structure surface until the lead breaks, as illustrated in Figure 101.
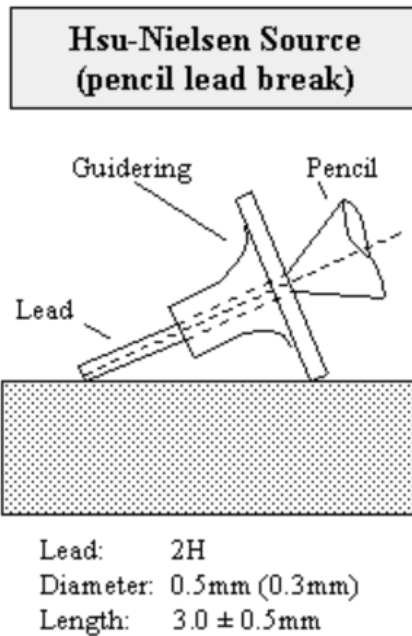
Figure 101. AE standard source by a pencil-lead break [143].

The Hsu-Nielsen source calibration tests involve breaking pencil lead tips with a hardness of 2H on the surface of the structure connected to an acoustic emission sensor. Since 2H allows for the emission of a signal across a wide frequency range ranging from a few kHz to several MHz, the proper pencil lead hardness must be utilised. This is an important aspect of the test for ensuring that high-frequency acoustic emission sensors are correctly connected and calibrated. Signals generated only over a low-frequency range of no more than 50 kHz may emerge from the use of pencil leads with a hardness other than 2H. A considerable percentage of undesirable mechanical noise typically has a frequency range of up to 50 kHz [173].

## 6.2 FATIGUE TESTING

### 6.2.1 Previous Study on Pearlitic Rail Steel Grade R220

As mentioned in the objectives, this study has tested the reliability of the AE technique for monitoring railway tracks in Thailand, where R260 rail steel and Hadfield manganese steel are used to manufacture plain rails and crossings. Steels typically used for wheels and rails have a pearlitic microstructure, which combines strong cementite lamellae for excellent wear resistance and toughness. The rails used in previous studies have considered R220 steel grade. This steel grade is similar in structure to R260 grade in that it has a pearlitic structure; nevertheless, because it contains less carbon, more pro-eutectoid remains (Figure 102).
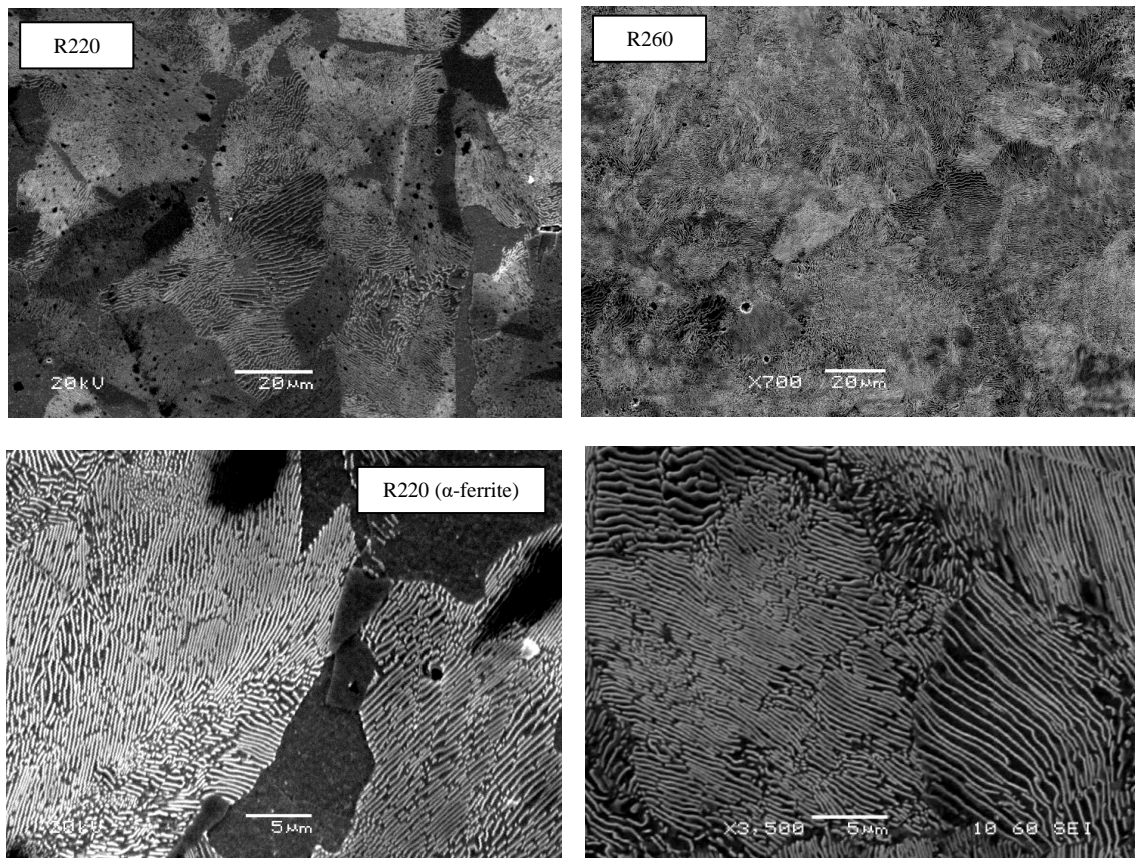


Figure 102. The microstructure of the R220 rail steel and R260 rail steel (SEM images, therefore, carbide light and ferrite dark). The mechanical characteristics of pearlite are intermediate between ductile ferrite and brittle-hard cementite.

R220 rail steel samples were cut from the web of used rails provided by Network Rail. A force of 0.85 – 8.5 kN was applied at approximately 100 Hz and used to pre-crack all the samples. The machine for fatigue testing of the samples was set to apply a sinusoidal loading sequence at 1 Hz, with an applied force range of 0.55 – 5.5 kN at a frequency of 5 Hz. The AE amplifiers were set to 40 dB, and the data acquisition threshold was set to 50 dB. A PAC wideband and an R50a AE sensor were used to monitor the AE activity for comparative purposes.
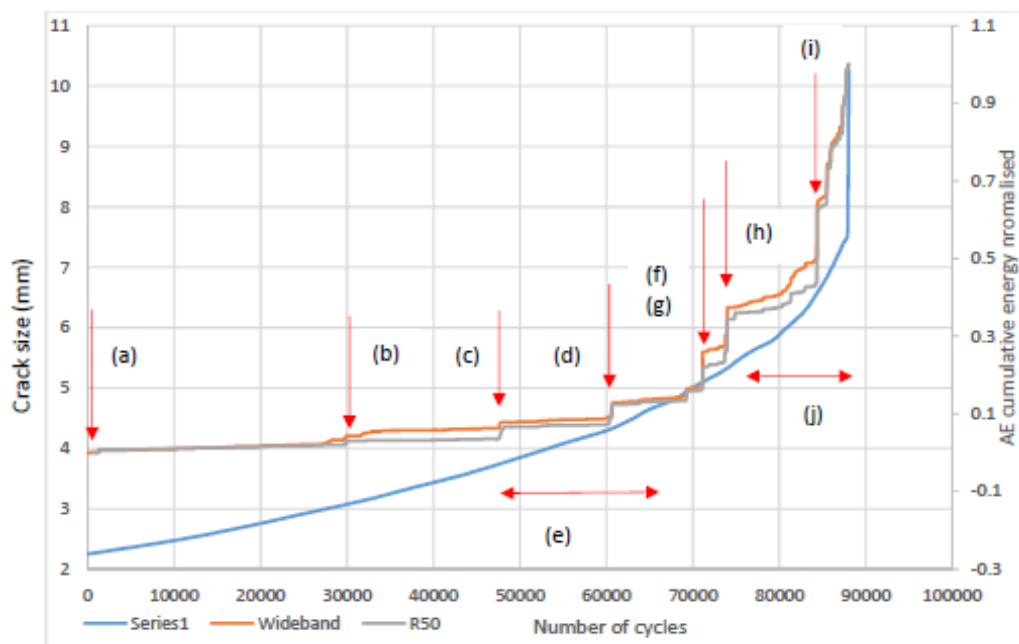


Figure 103. The cumulative AE energy plot obtained from both the Wideband and R50a sensors is compared to the crack size determined in the previous experiment using the DCPD instrument on R220 rail steel sample 7 [144].

For all tested samples, it can seem that as the crack propagates, the cumulative AE energy increases accordingly. However, the crack propagation determined by DCPD is a classic exponential curve pattern. The rapid increase in the AE activity is caused by high energy AE signals originating from more significant events as the crack propagates. The AE response of the wideband and R50a sensors is the same for most of the samples. Both sensors often detect the same signals simultaneously; they vary only in the amount of

energy detected. This is due to the fact that each sensor detects different acoustic frequency ranges at different levels.

Optical and scanning electron microscopy were used to identify and analyse the location of the rapidly growing cracks. The associated AE events correlate to characteristics on the fractured surfaces that seem to have produced an immediate rise in the crack growth rate when a dramatic increase in cumulative AE energy is detected.
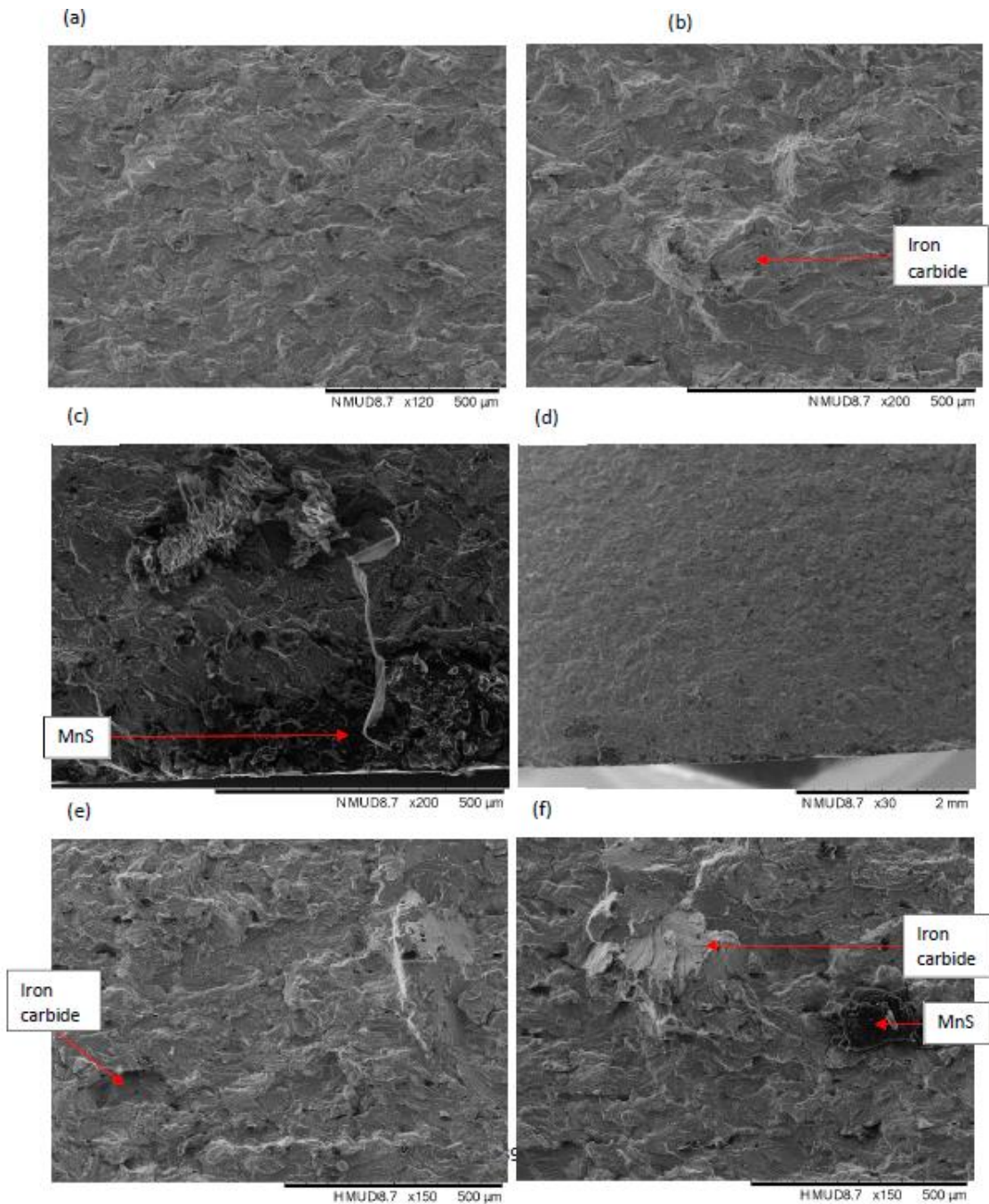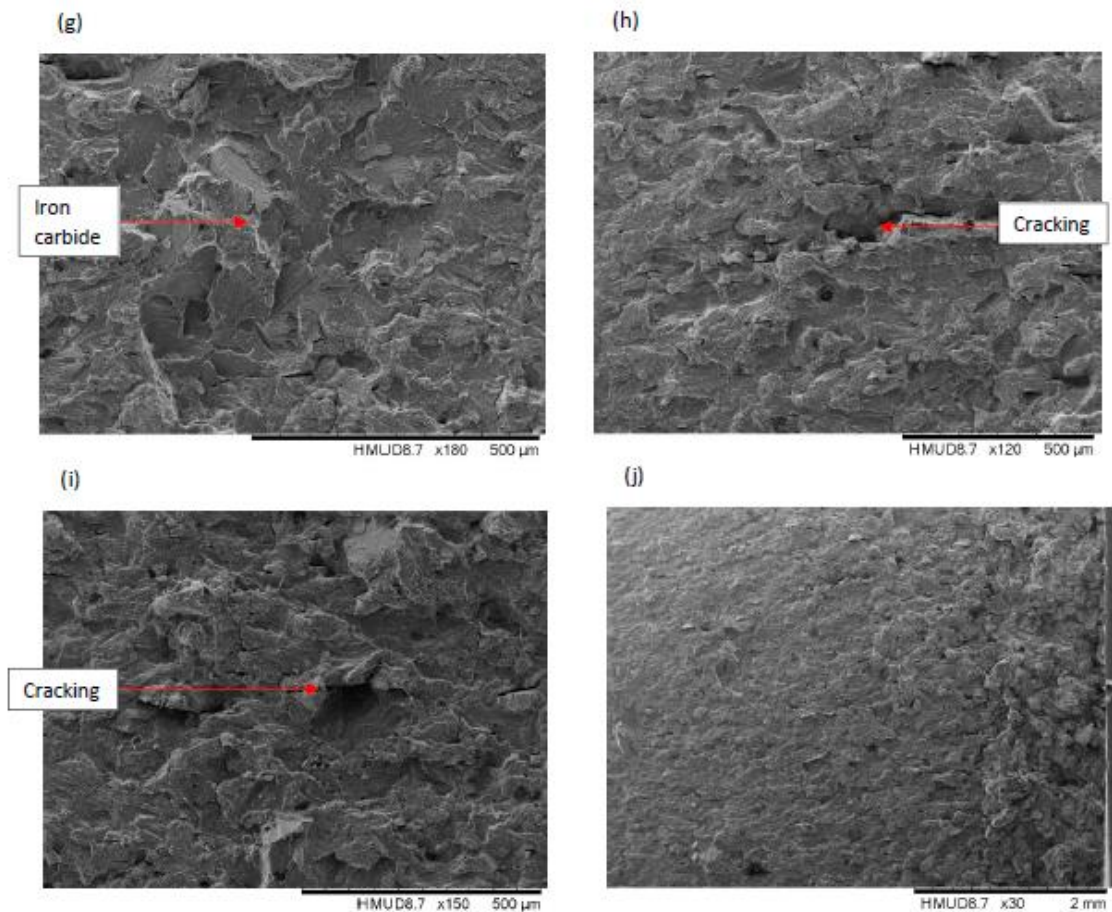
Figure 104. SEM Micrographs show the fracture surface and the direction of fatigue crack growth (a) It is possible to observe pre-crack to fatigue crack surface interface cracking, (b) Mns defects at a 3 mm distance, (c) – (e) Iron carbide and cracking defects at a distance 4 mm cracking is evident in (c), (f) – (g) at a distance of 4.5 mm, iron carbide and cracking defects, (h) Cracking at a 5 mm distance, (i) ultimate brittle fatigue of sample with apparent cracking [144].

Usually, fatigue crack surfaces follow the standard morphology of the fatigue crack shape expected during the three-point fatigue bending process. Thus, there is initially a fine fatigue surface, ending in a larger structure, whereas when the fatigue fracture reaches a critical point, the brittle fracturing occurs. However, in none of the samples were striations which are typically associated with fatigue crack growth was observed. This lack of striations in the fractured surfaces of the fatigue tested R220 samples is believed to be due to the interaction of two fracturing surfaces.

The events resulting in the sudden increase of the AE activity were associated with defects with dimensions in the 300-500 μm range. These defects generated powerful AE signals which were not visible in the DCPD traces.

### 6.2.2 R260 Rail Steel

The R260 rail steel has a similar pearlitic structure as R220 rail steel but less ferrite due to the slightly lower carbon content. The R260 grade, on the other hand, lacks the pro-eutectoid ferrite that forms at grain boundaries in the R220 rail steel grade since the increased manganese (Mn) and carbon (C) content promotes a completely pearlitic structure.

Cyclic three-point fatigue bending test results of rail steel R260 grade are shown in Table 15. It is noted that the test of sample 10 failed due to unexpected overloading at the start of the experiment. The fatigue crack growth events were detected and monitored using the AE method during testing. The time for testing each specimen was approximately 5-8 hours. In all samples, brittle fracture behaviour was observed using SEM. Fatigue crack growth curves are respectively specified as in Figure 105.

Table 15. A cyclic three-point-bending test result of ten samples of R260 rail steel.

| Sample | Number of Cycle | Time (s) | Initial crack (mm) | Maximum load (kN) | Minimum load (kN) | R-ratio |
|---|---|---|---|---|---|---|
| 1 | 112,517 | 22,503 | 3.52 | 5.5 | 0.55 | 0.1 |
| 2 | 104,929 | 20,986 | 2.95 | 5.5 | 0.55 | 0.1 |
| 3 | 151,205 | 30,241 | 2.04 | 5.5 | 0.55 | 0.1 |
| 4 | 116,830 | 23,366 | 2.83 | 5.5 | 0.55 | 0.1 |
| 5 | 147,760 | 29,552 | 3.44 | 5.5 | 0.55 | 0.1 |
| 6 | 111,143 | 22,229 | 4.29 | 5.5 | 0.55 | 0.1 |
| 7 | 136,169 | 27,234 | 3.56 | 5.5 | 0.55 | 0.1 |
| 8 | 120,357 | 24,071 | 3.95 | 5.5 | 0.55 | 0.1 |
| 9 | 90,574 | 18,115 | 3.43 | 5.5 | 0.55 | 0.1 |
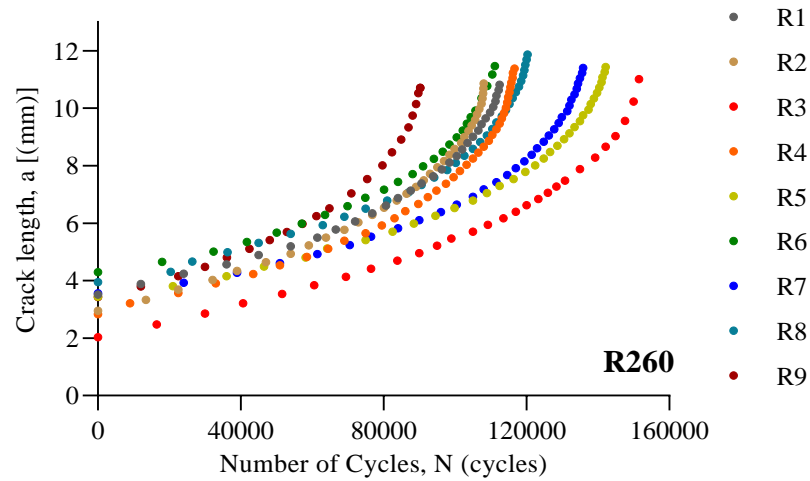
Figure 105. Crack length against Fatigue life for different nine samples of R260 rail steel.

### 6.2.3 Hadfield Manganese Steel

Cyclic three-point fatigue bending fatigue test results of Hadfield manganese steel are shown in Table 16. The fatigue crack growth was detected and monitored using DCPD and AE testing. It is noted that the test of sample 5 failed due to sudden overloading at the beginning of the experiment, and hence, it has not been included in the results. The time for testing each specimen was approximately 3-5 hours in this case. Samples exhibit ductile behaviour as it can be observed from the fractured surface using SEM. Fatigue crack growth curves are respectively specified as in Figure 106.

Table 16. A cyclic three-point-bending test result of ten samples of Hadfield manganese steel.

| Sample | Number of Cycle | Time (s) | Initial crack (mm) | Maximum load (kN) | Minimum load (kN) | R-ratio |
|--------|----------------|----------|--------------------|-------------------|-------------------|---------|
| 1 | 44,632 | 8,927 | 4.562 | 4.5 | 0.45 | 0.1 |
| 2 | 98,647 | 19,729 | 3.255 | 4.5 | 0.45 | 0.1 |
| 3 | 57,670 | 11,534 | 4.197 | 4.5 | 0.45 | 0.1 |
| 4 | 70,114 | 14,023 | 3.770 | 4.5 | 0.45 | 0.1 |
| 6 | 36,164 | 7,233 | 4.569 | 4.5 | 0.45 | 0.1 |
| 7 | 99,901 | 19,980 | 3.337 | 4.5 | 0.45 | 0.1 |
| 8 | 67,420 | 13,484 | 3.366 | 4.5 | 0.45 | 0.1 |
| 9 | 77,752 | 15,550 | 3.493 | 4.5 | 0.45 | 0.1 |
| 10 | 56,418 | 11,284 | 3.484 | 4.5 | 0.45 | 0.1 |
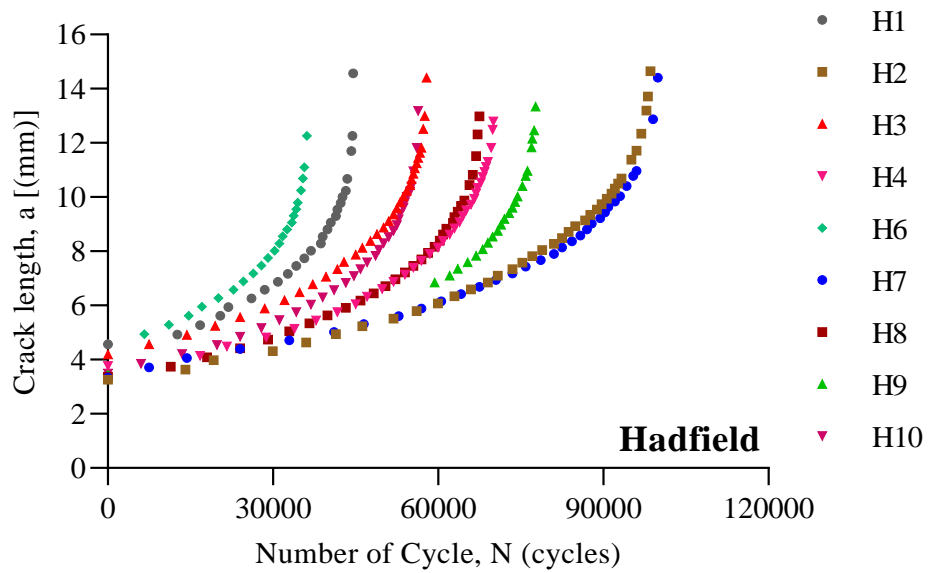
Figure 106. Crack length against Fatigue life for different nine samples of Hadfield manganese steel.

The crack length, *a*, versus the number of cycles, *N*, for the R260 pearlitic rail steel and Hadfield manganese steel is shown in Figures 105-106. It can be seen from Figure 105 that the total fatigue lifetime of the R260 is much higher than that of the Hadfield manganese steel. The total average fatigue lifetime for the R260 rail steel was approximately 120,000 cycles, while the fatigue lifetime in Hadfield manganese steel was lower than conventional rail materials since all the samples broke before completing 100,000 cycles for the stress range used.

## 6.3    QUANTITATIVE EVALUATION

### 6.3.1    AE signal analysis

In Hadfield manganese steel, both sensors generally follow the same pattern. However, on some occasions, one sensor failed to pick up lower amplitude signals or detected the AE signals at lower amplitudes. This was likely due to insufficient sensor coupling to the sample.  In Hadfield manganese steel samples 1 and 3, the energy of the AE signal increases slowly in early crack propagation but rapidly closer to failure. This is consistent with cracks from initiation to propagation during the fatigue test. This pattern is the same as found in previous results of R220, as shown in Figure 108 and R260, as shown in Figure 109.
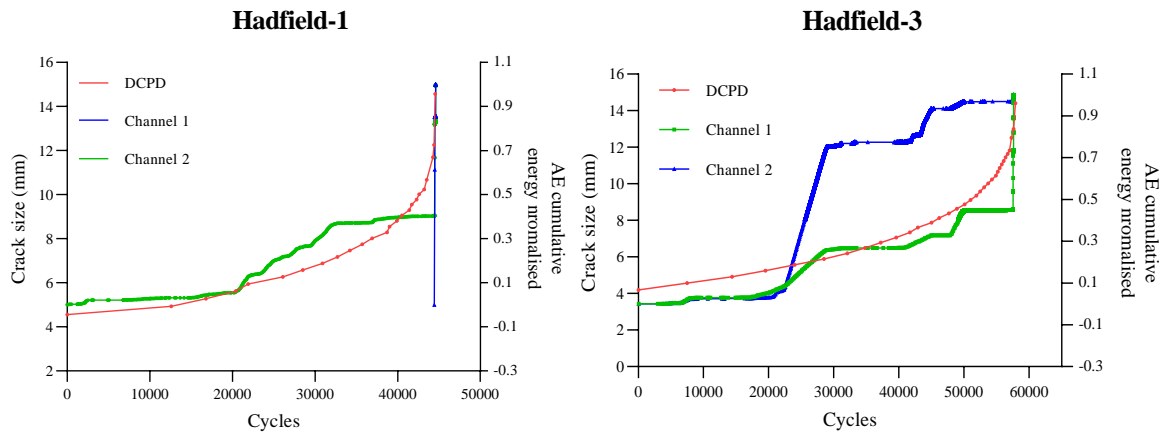


Figure 107. A cumulative AE energy plot from R50α Sensors compares to the crack size measured using the DCPD instrument of Hadfield manganese steel samples 1 and 3.
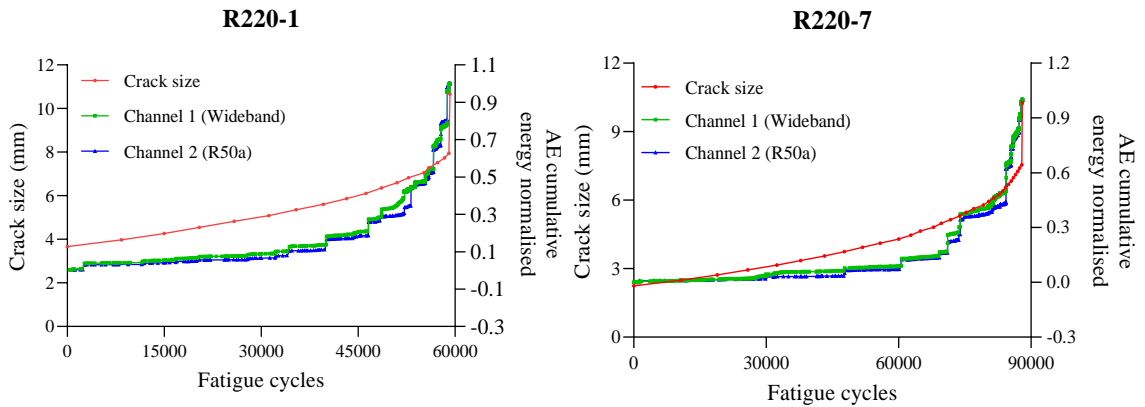
Figure 108. A plot of cumulative AE energy from both the Wideband (Channel 1) and R50α Sensors (Channel 2) compares to the crack size measured using the DCPD instrument of R220 rail steel samples 1 and 7.
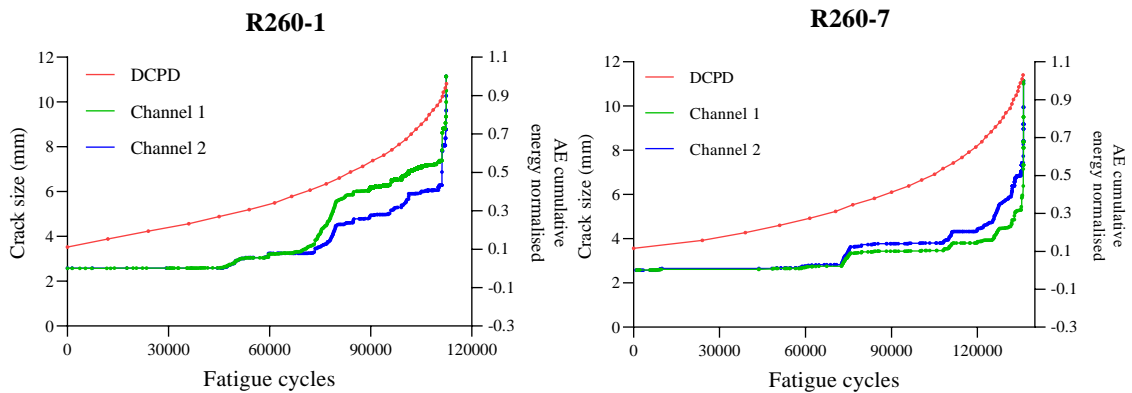


Figure 109. A cumulative AE energy plot from R50α Sensors compares to the crack size measured using the DCPD instrument of R260 rail steel samples 1 and 7.

Other samples of Hadfield manganese steel, such as samples 4 and 6, show that the energy of the AE signal increases steadily initially, indicating that the AE signals recorded at this stage are solely caused by the development of the plastic zone ahead of the crack tip [167]. Whilst plotting the amplitude against fatigue cycles in Figure 112 helps show this difference in activity more clearly, with only short peaks of AE activity in early crack propagation ending with a high peak at failure, compared with more continuous AE activity in Figure 113.

The correlation of the AE signal amplitude with crack length during fatigue testing of both R260 rail steel and Hadfield manganese steel samples is shown in Figures 110-112. The threshold was set at 60 dB for samples 1 and 2, then reduced to 58 dB for the rest of the R260 rail steel samples and 50 dB for Hadfield Manganese steel samples.
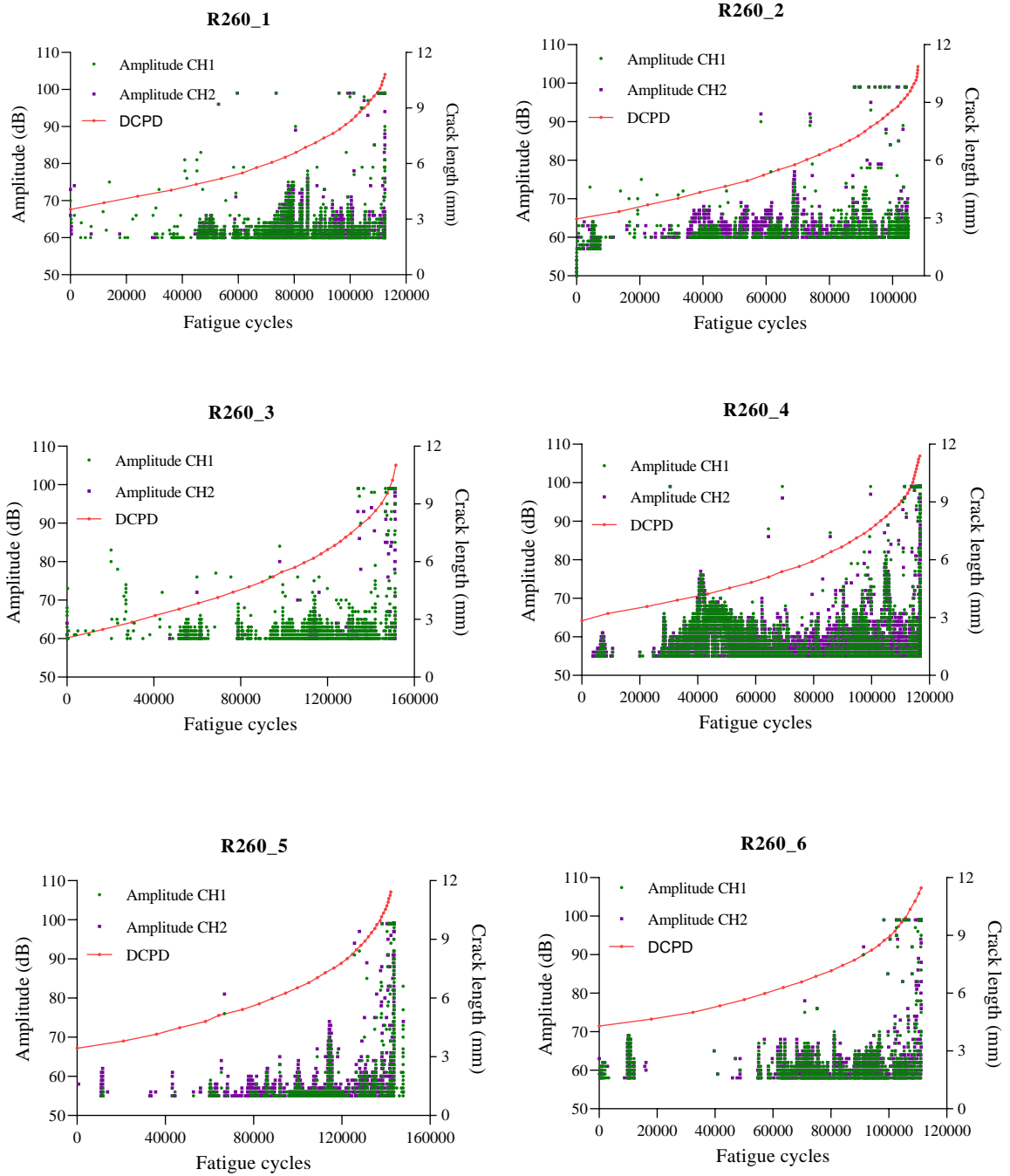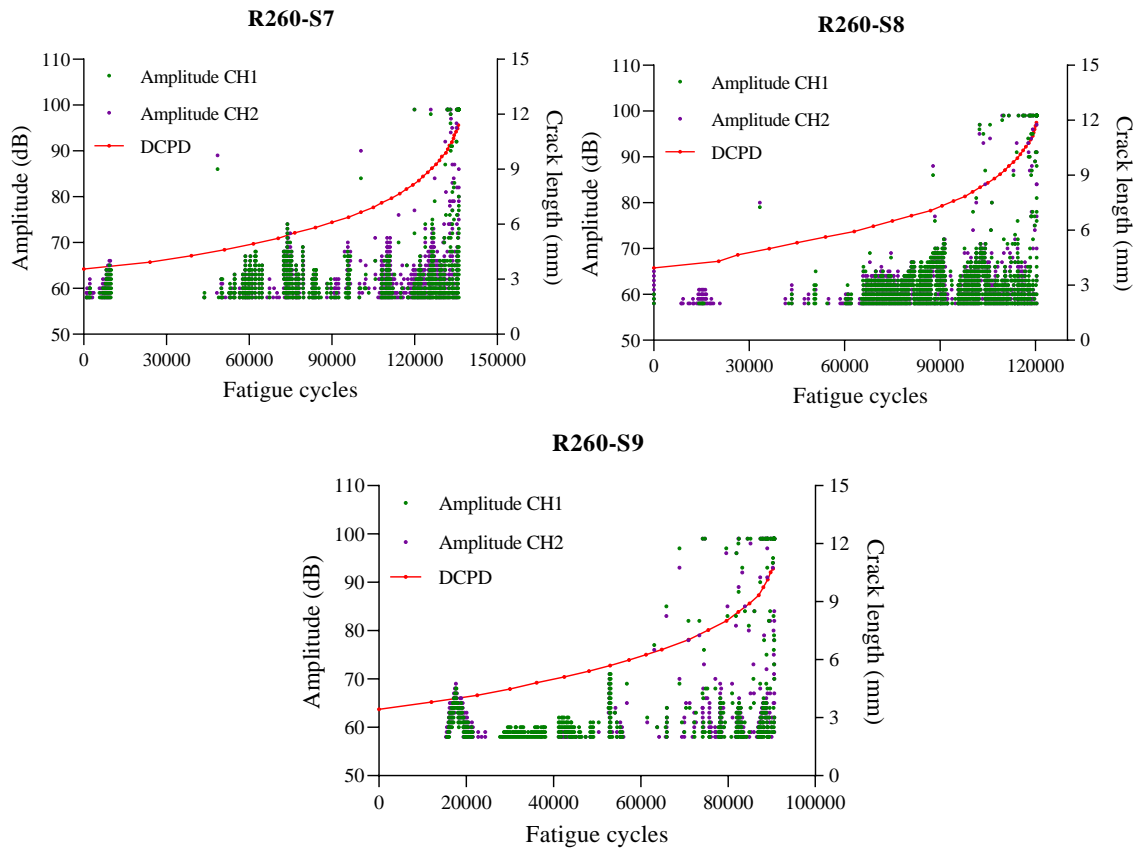
Figure 110. AE signal Amplitude (dB) against fatigue cycles with crack growth (mm) for R260 rail steel samples 1 - 9.

The maximum amplitude AE signals captured during experiments on R260 rail steel and Hadfield manganese steel samples have different distributions. During stable crack propagation, captured AE signals with amplitudes above 60 dB exist in the R260 steel samples tested. The distribution of high amplitude AE events in the experiments is more scattered. During crack evolution, this is due to a continuous brittle cleavage fracturing process. Each of the R260 rail steel samples showed a sudden increase in crack growth at a specific point before final failure. This is due to greater regions of cleavage in the fractured sample surface, which results in higher AE energy released in these instances. The explanation for larger areas of cleavage fracture is possibly related to the presence of a brittle inclusion in the growing crack direction, causing a greater region to

fracture until the crack slows down again. Another explanation is that tensile residual stresses result in higher local stress levels and a larger fracture region.
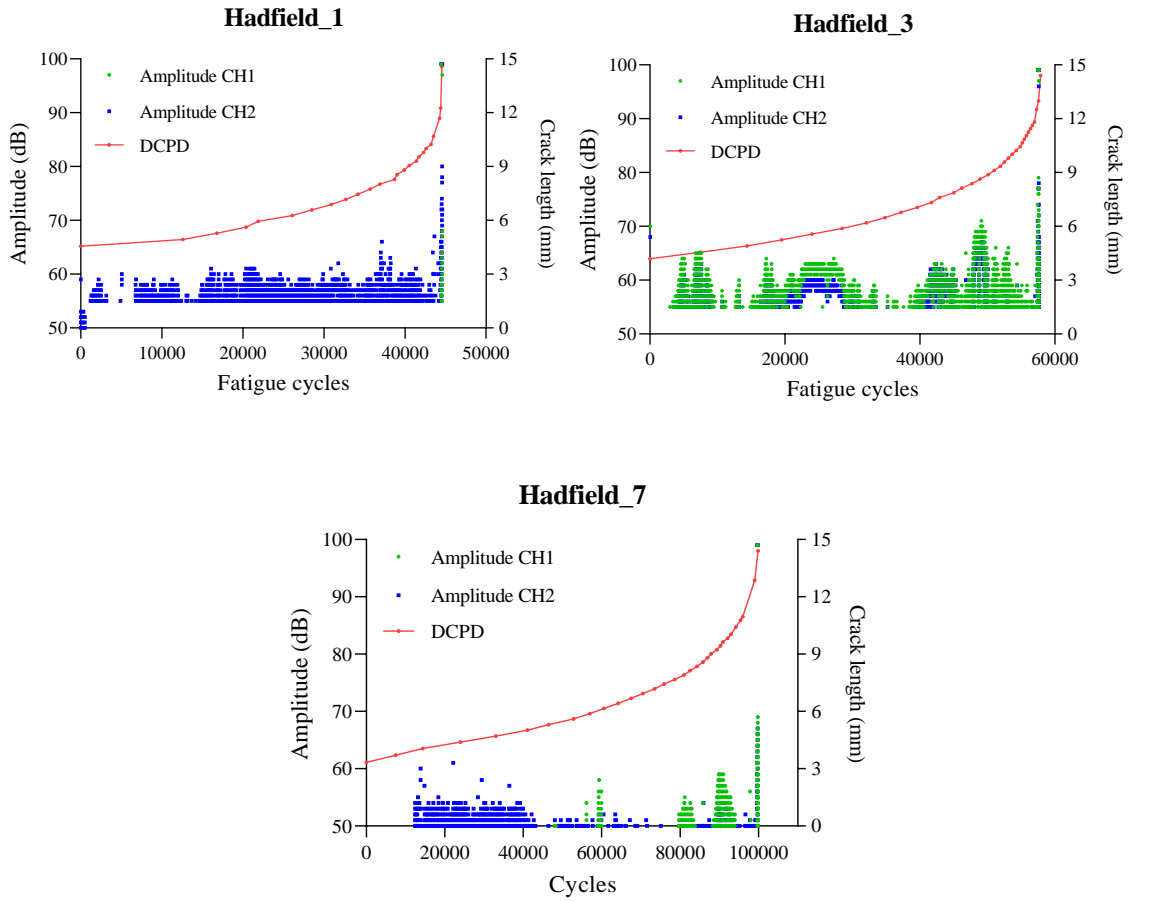


Figure 111. Amplitude against fatigue cycles for Hadfield steel samples 1,3 and 7 (continuous crack activity).
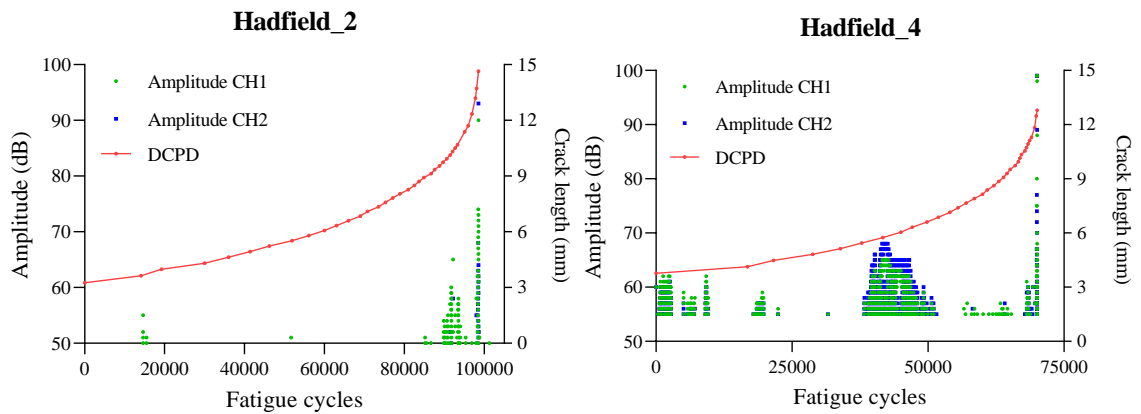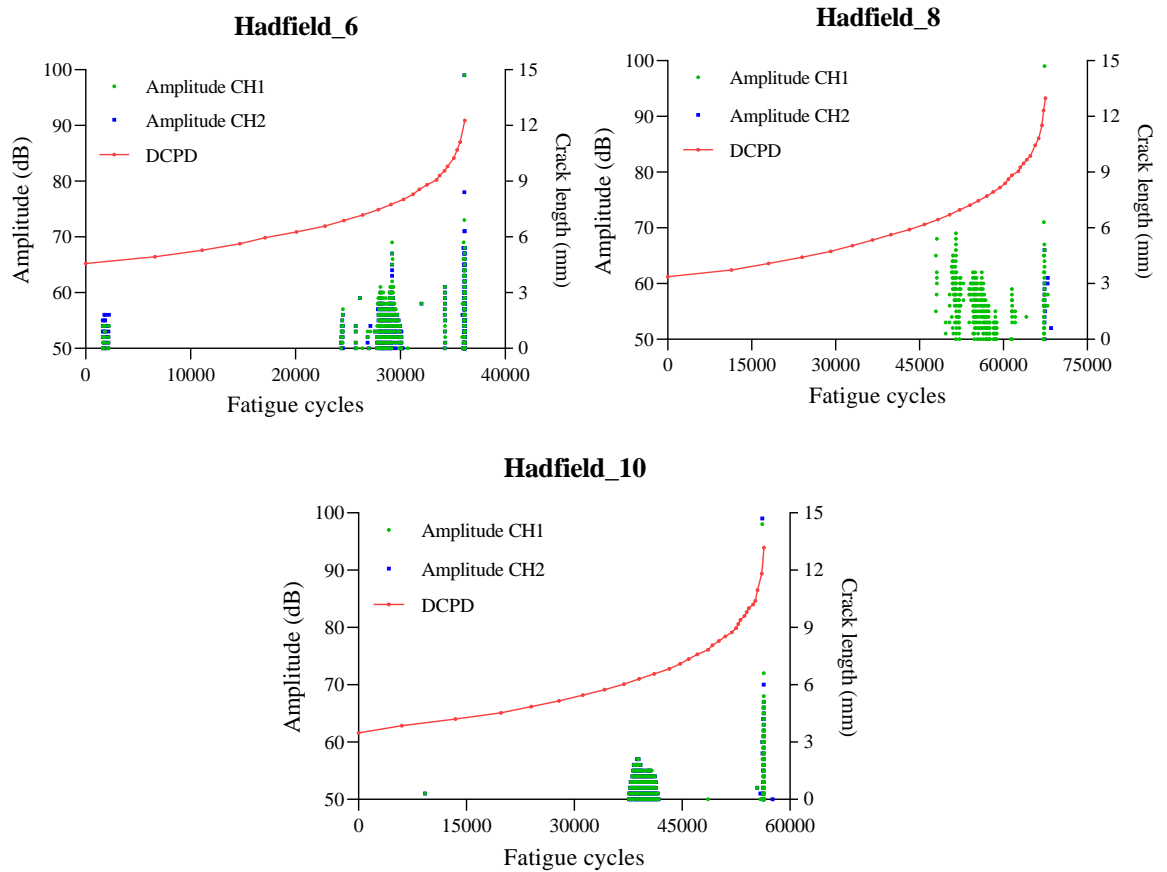
Figure 112. Amplitude against fatigue cycles for Hadfield steel samples 2, 4, 6, 8, and 10 (short peaks in early – ending with a high peak at failure).
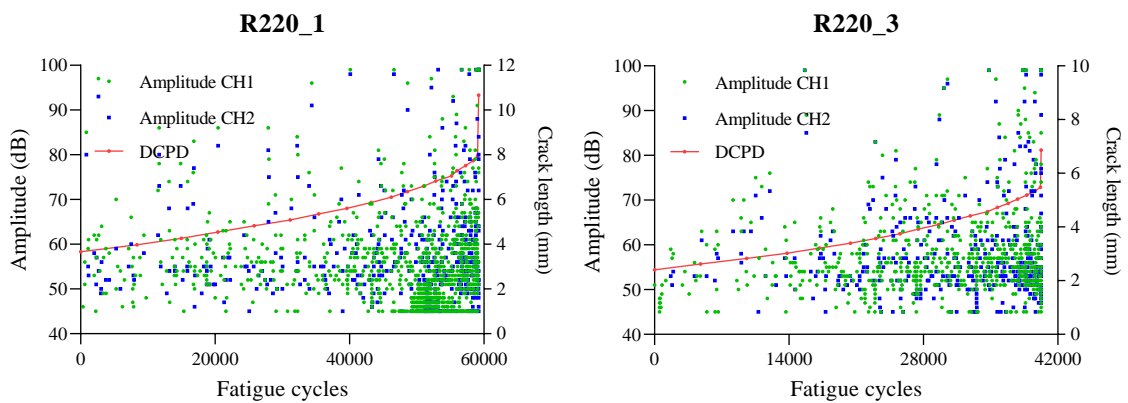


Figure 113. Amplitude against fatigue cycles for R220 rail steel samples 1 and 3.

The majority of AE signals with amplitudes greater than 60 dB occur during the final stage of damage evolution in the Hadfield manganese steel samples. Because of the plasticity at the crack tip, the highest amplitude during the tests for all Hadfield samples is lower than for R260 rail steel, resulting in lower AE energy levels being emitted. Hadfield steel has an austenitic microstructure, as previously mentioned. Hadfield steel has an FCC crystal structure as a result. Many slip systems exist in FCC crystal lattices, allowing dislocations to slip. Plastic deformation of Hadfield steel is primarily caused by twining and dislocation slipping [145][149]. This steel has a Low Stacking Fault Energy (SFE) due to its FCC lattice and random distribution of manganese atoms and carbon atoms [146]. Shear stress increases in the presence of a low SFE and a high concentration of interstitial solute atoms (5–8 wt.% C), which causes dislocation gliding to occur more often and the twining to serve as a more active mechanism of slipping [147-148].

The correlation of count and duration with crack length during fatigue test on both R260 rail steel and Hadfield manganese steel sample is shown in Figure 114-121.
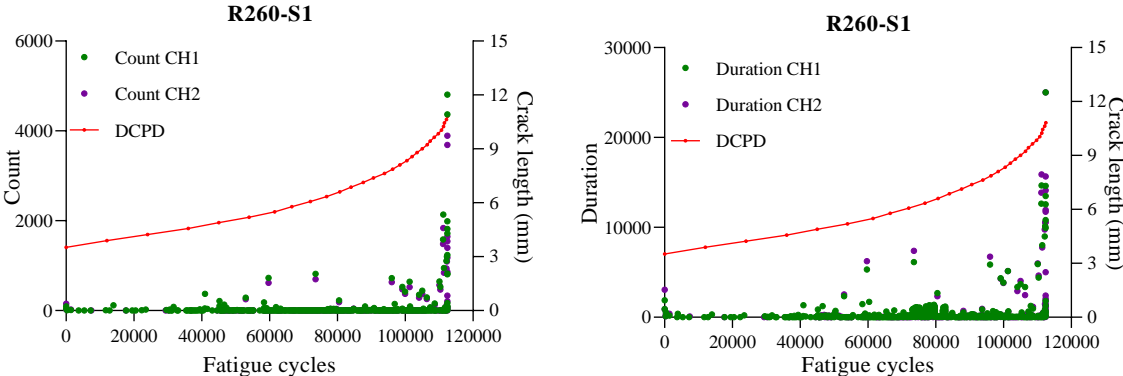


Figure 114. AE signal Count and duration against fatigue cycles with crack growth (mm) for R260 rail steel samples 1.
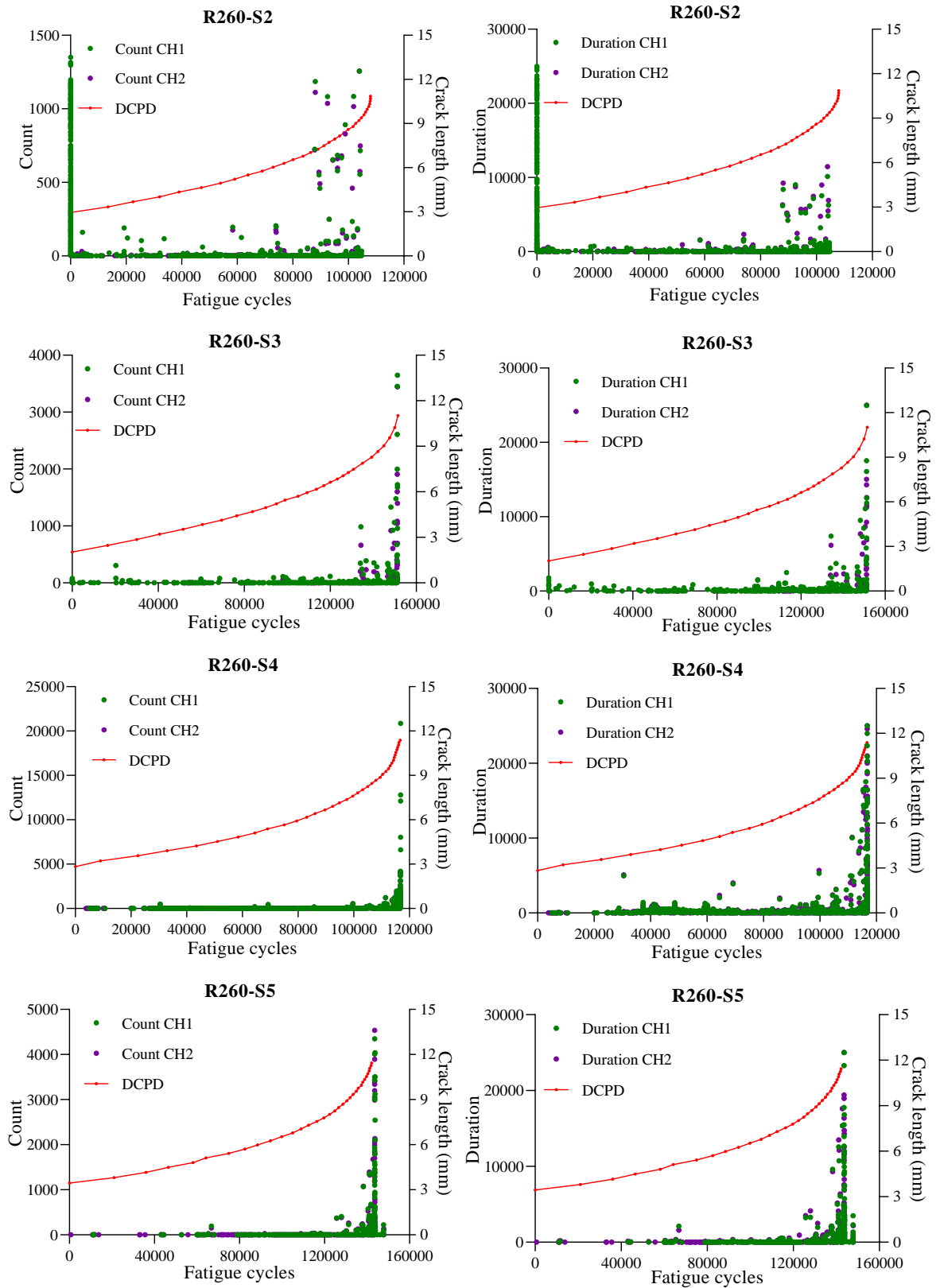
Figure 115. AE signal Count and duration against fatigue cycles with crack growth (mm) for R260 rail steel samples 2 - 5.
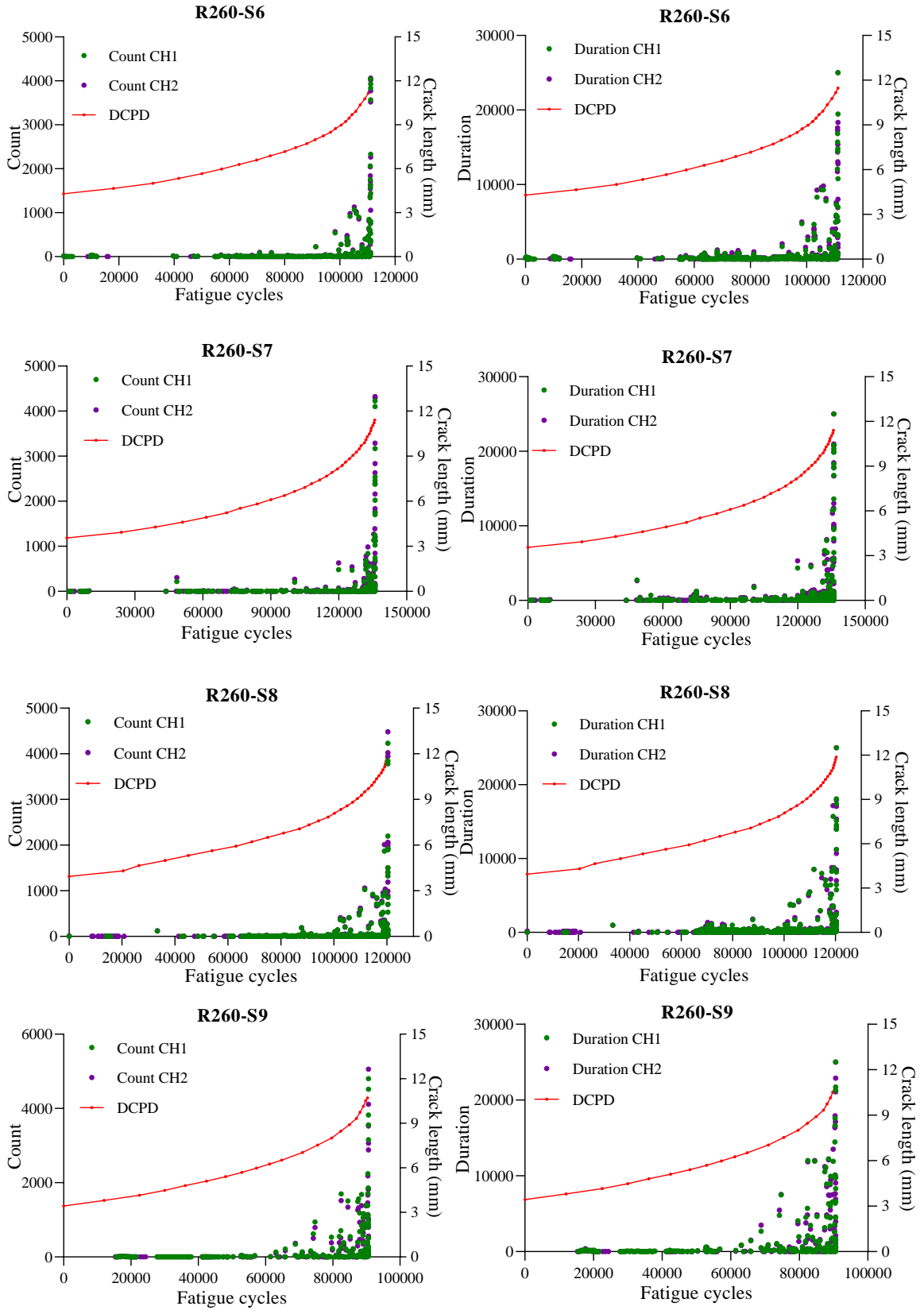
Figure 116. AE signal Count and duration against fatigue cycles with crack growth (mm) for R260 rail steel samples 6-9.
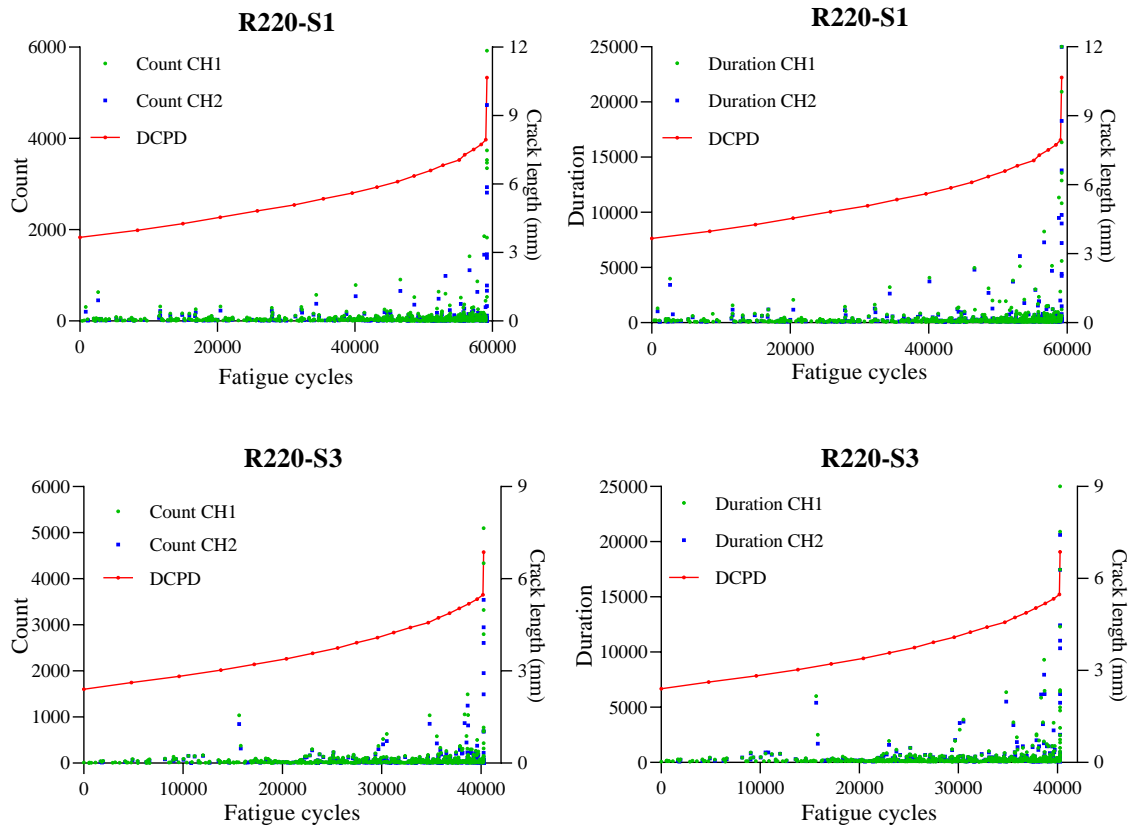
Figure 117. AE signal Count against fatigue cycles with crack growth (mm) R220 rail steel samples 1 and 3
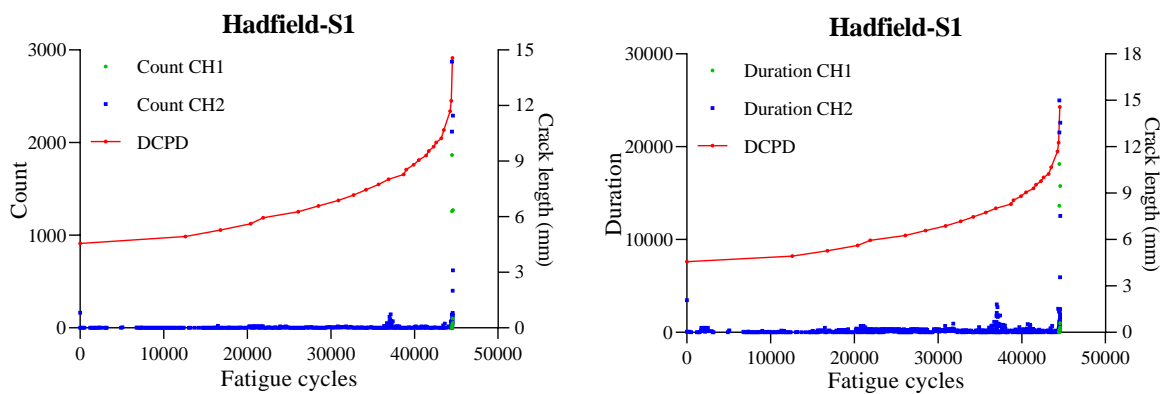


Figure 118. AE signal Count against fatigue cycles for Hadfield steel sample 1 (continuous crack activity)
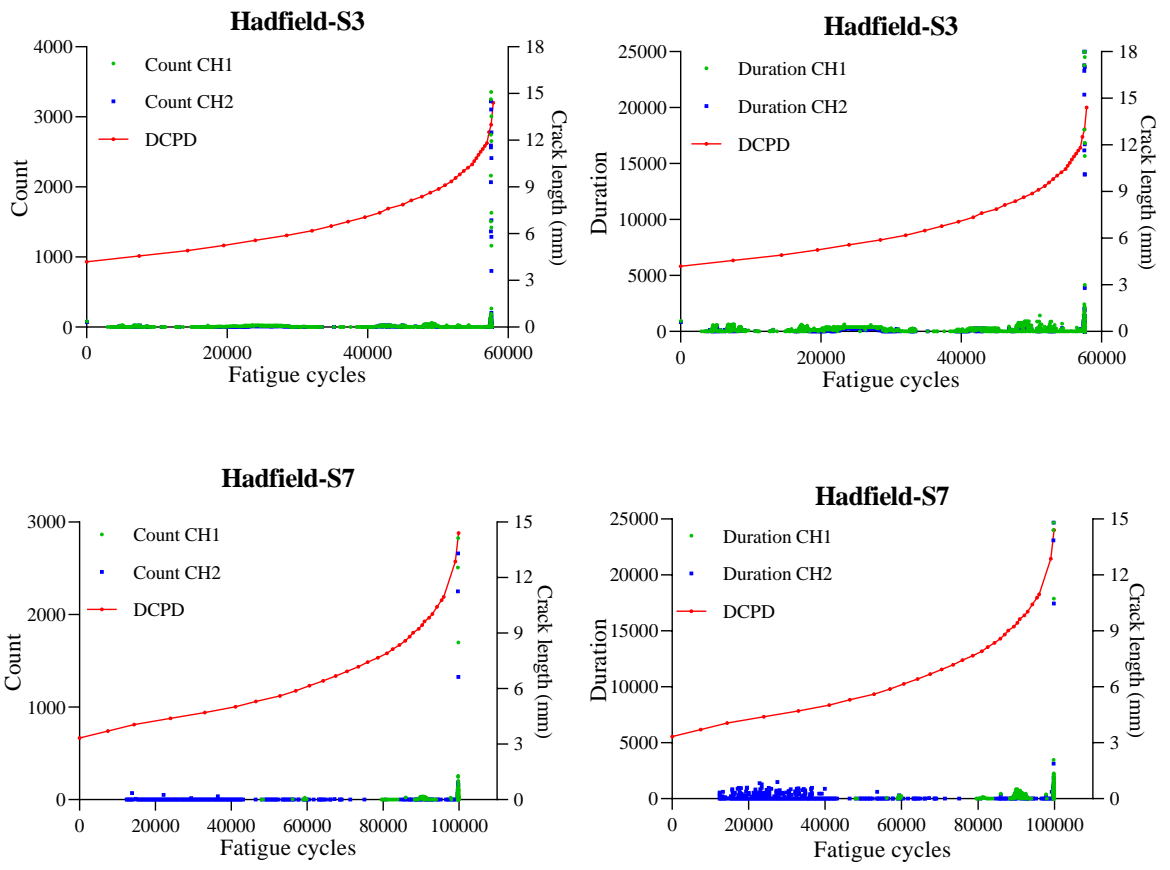
Figure 119. AE signal Count against fatigue cycles for Hadfield steel samples 3 and 7 (continuous crack activity).
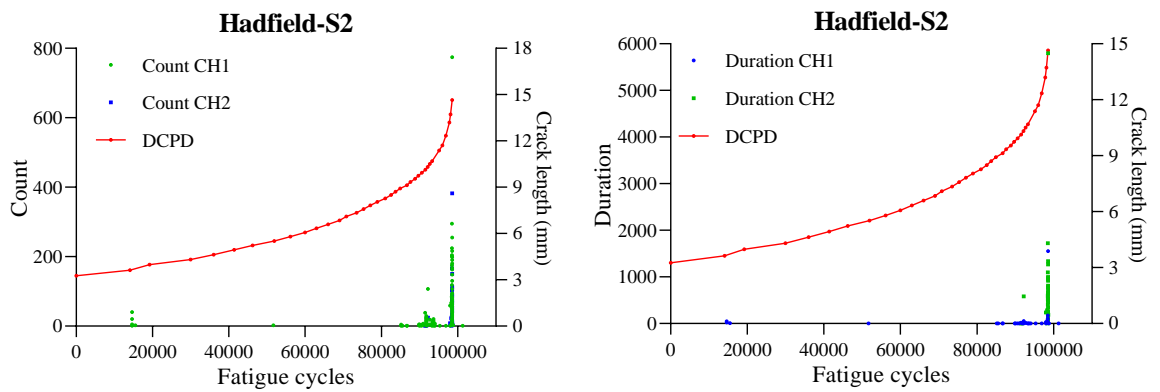


Figure 120. AE signal Count against fatigue cycles for Hadfield steel sample 2 (short peaks in early – ending with a high peak at failure).
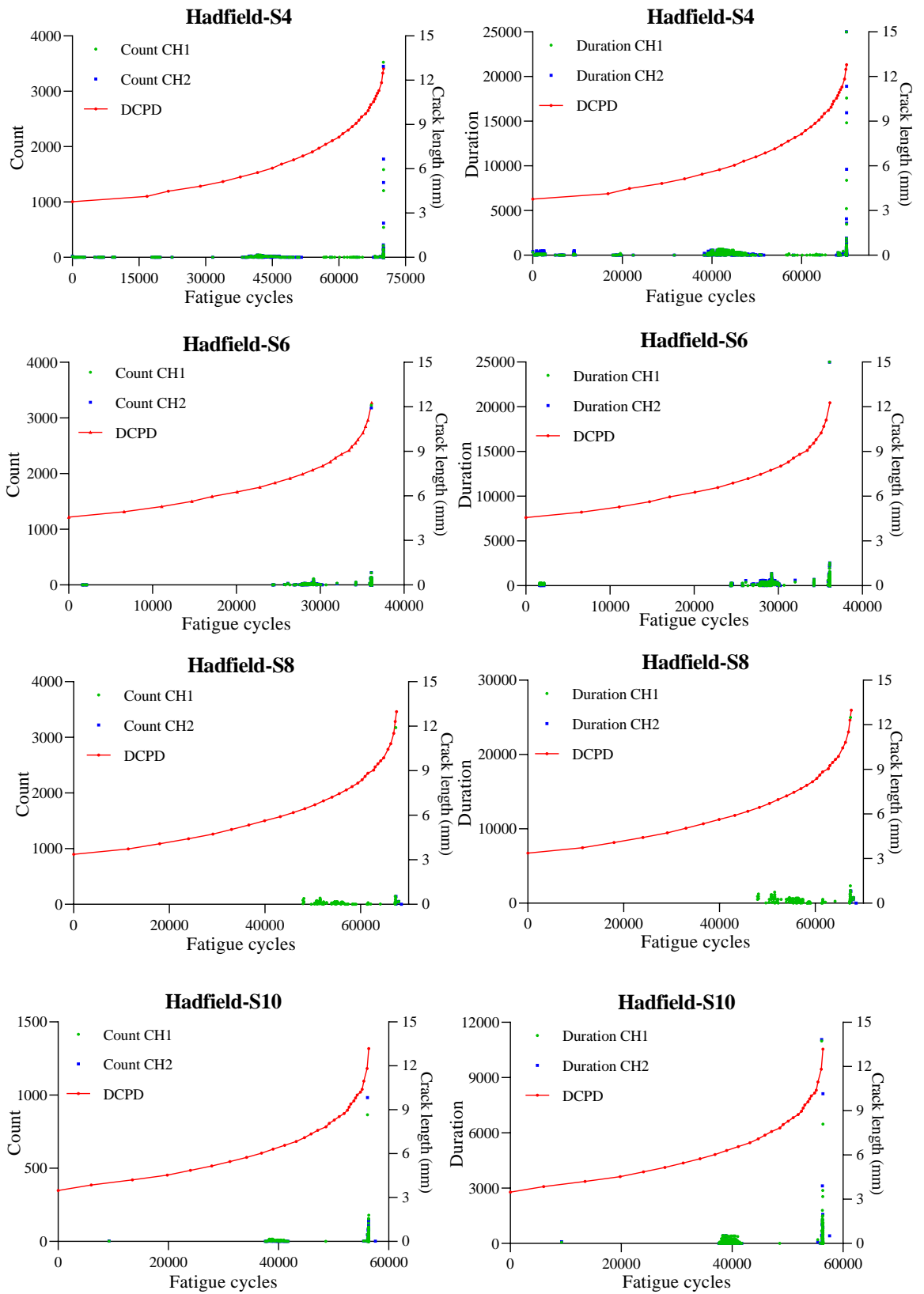
Figure 121. AE signal Count against fatigue cycles for Hadfield steel samples 4, 6, 8, and 10 (short peaks in early – ending with a high peak at failure).

The correlation between count and crack length for both R260 rail steel and Hadfield manganese steel samples are shown in Figures 114-121. Count and duration are closely linked and follow the same pattern. The sudden increase in crack growth rate in the R260 steel samples is consistent with the amplitude and counts observed in the AE signals captured. Due to the higher AE activity observed during the final stages of stable crack growth for both materials, indicators of nearing failure may be seen. Compared to the initial stages of damage evolution in the samples tested, both hit number and hit counts increase. These AE events can be considered a predictor of oncoming final failure and hence as a warning. The amplitude-crack length plots alone cannot indicate some of these AE events. Other events with comparable high amplitude levels can occur at different stages of damage evolution—the count grows in a similar pattern as the duration grows.

### 6.3.2 Fatigue crack growth rate

Cracked materials subjected to cyclic loading were assessed using Paris's Law to predict fatigue crack growth rates (*da/dN*) shown in Figure 122-123. According to the test standard ASTM E647, 1990 [174], the experiment uses cyclic load under constant amplitude loading. The primary data obtained from the experiment is the relationship between crack size (*a*) and cycle (*N*). Then use the data obtained to calculate and plot the relationship between fatigue crack growth rates (*da/dN*) and crack-tip stress-intensity factor range (*ΔK*).

**R260 rail steel crack growth rate**
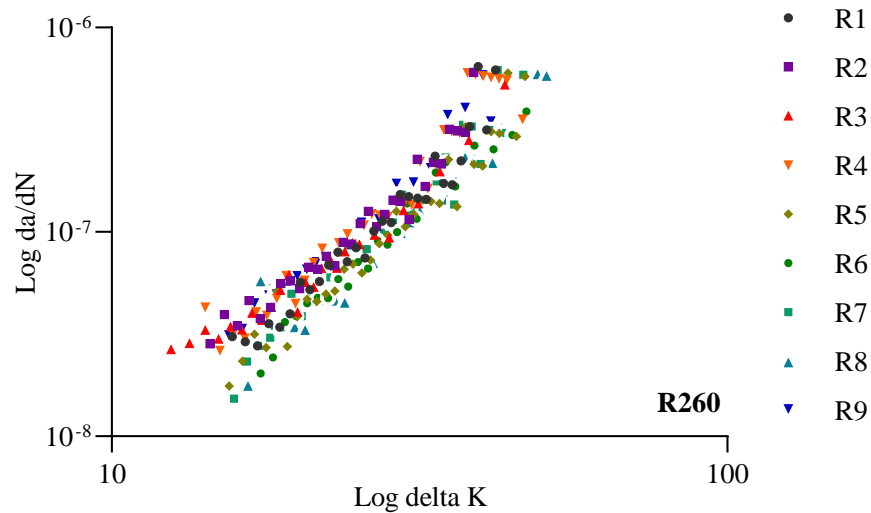


Figure 122. The Paris law for fatigue crack growth rates of pearlitic rail steel R260 (Stage II in Micro-mechanism of Fatigue).

After plotting log *da/dN* as a function of log *ΔK*, the slope of the plot would give the *m*, and the Y-intercept will provide the value of *C*. The *C* and *m* values from the experiment in R260rail steels have an average of *C = 1.60 x10$^{-11}$* and *m = 2.82*.
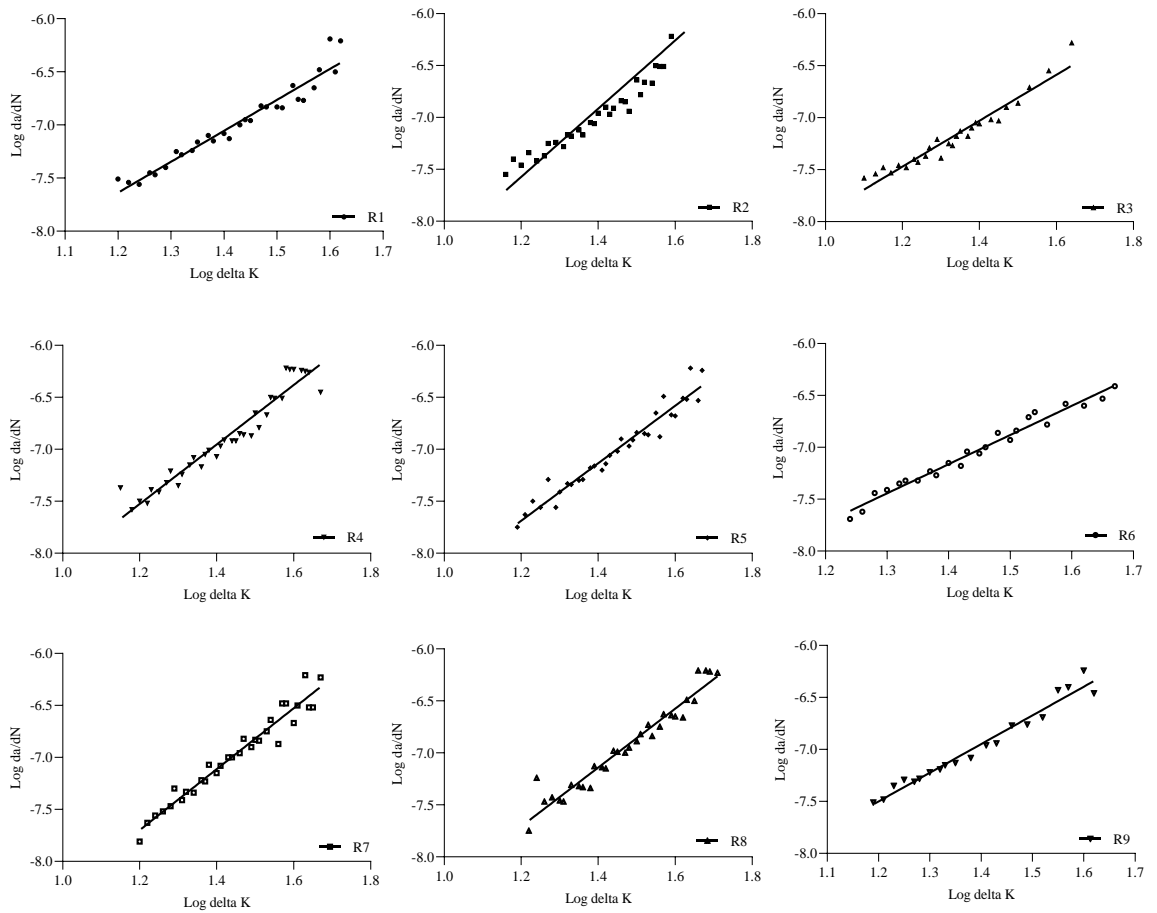
Table 17. Plots log da/dN and log ΔK to obtain the C and m value of R260 rail steel.

| Sample | R260_1 | R260_2 | R260_3 | R260_4 | R260_5 | R260_6 | R260_7 | R260_8 | R260_9 |
|---|---|---|---|---|---|---|---|---|---|
| **Best-fit values** | | | | | | | | | |
| Slope | 2.913 | 3.284 | 2.209 | 2.861 | 2.767 | 2.812 | 2.929 | 2.832 | 2.758 |
| Y-intercept | -11.130 | -11.510 | -10.120 | -10.960 | -11.010 | -11.100 | -11.210 | -11.110 | -10.810 |
| X-intercept | 3.822 | 3.506 | 4.582 | 3.831 | 3.979 | 3.947 | 3.829 | 3.922 | 3.919 |
| 1/slope | 0.343 | 0.306 | 0.453 | 0.349 | 0.361 | 0.356 | 0.342 | 0.353 | 0.363 |
| **Std. Error** | | | | | | | | | |
| Slope | 0.140 | 0.262 | 0.111 | 0.135 | 0.120 | 0.096 | 0.121 | 0.126 | 0.120 |
| Y-intercept | 0.200 | 0.370 | 0.149 | 0.194 | 0.175 | 0.139 | 0.175 | 0.187 | 0.167 |
| **Goodness of Fit** | | | | | | | | | |
| r | 0.970 | 0.914 | 0.970 | 0.963 | 0.972 | 0.987 | 0.975 | 0.972 | 0.984 |
| R squared | 0.941 | 0.836 | 0.941 | 0.928 | 0.945 | 0.975 | 0.952 | 0.944 | 0.967 |
| **Number of XY Pairs** | 29 | 33 | 27 | 37 | 33 | 24 | 32 | 32 | 20 |

**Hadfield manganese steel crack growth rate**
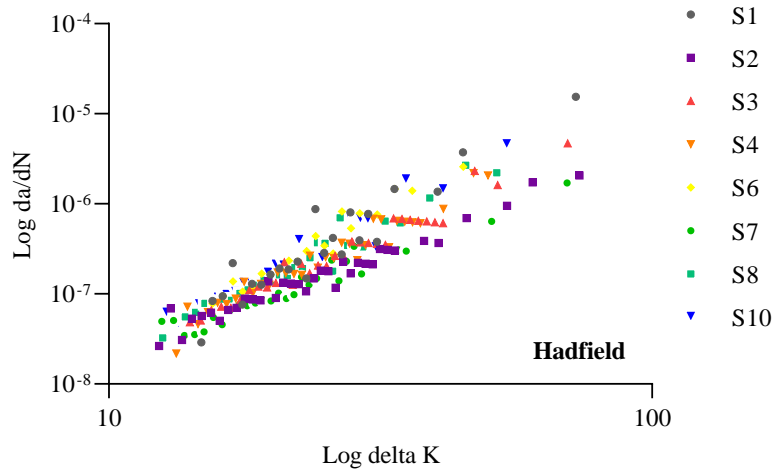


Figure 123. The Paris law for fatigue crack growth rates of Hadfield manganese steel (Stage II in Micro-mechanism of Fatigue).

After plotting log *da/dN* as a function of log *ΔK*, the plot's slope would give the m, and the Y-intercept will provide the value of *C*. The *C* and m values from the experiment in Hadfield manganese steels have an average of *C = 4.08 x10$^{-11}$* and *m = 2.604*.
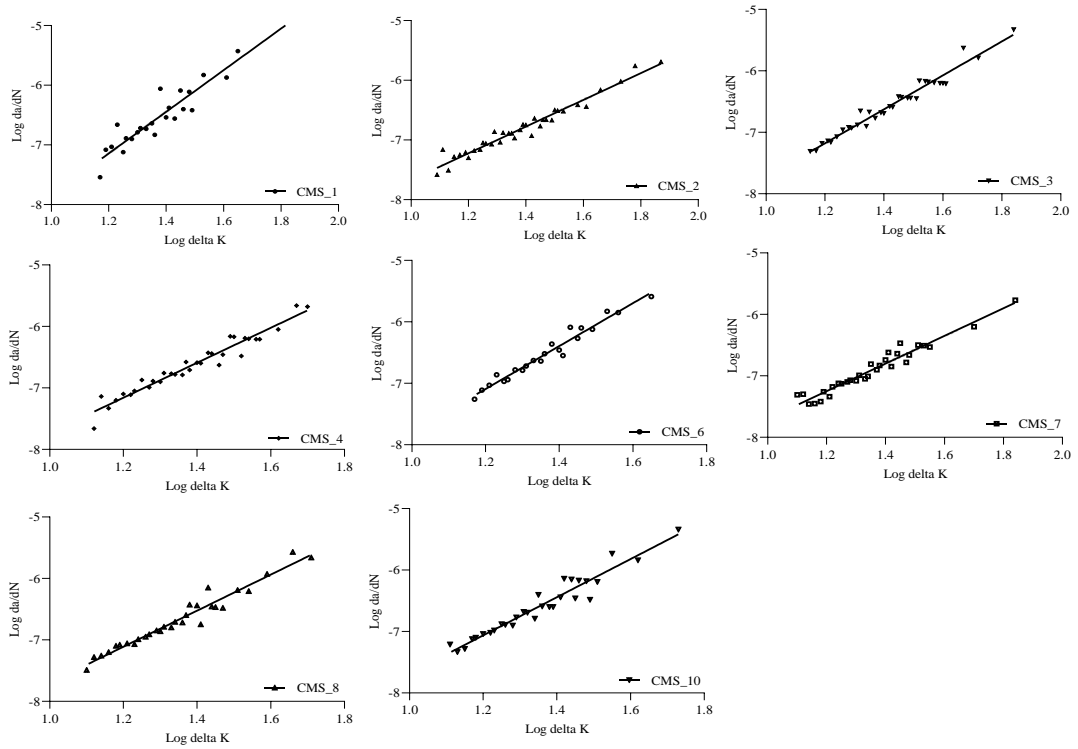


Table 18. Plot log da/dN and log ΔK to obtain the C and m value of Hadfield manganese steel.

| Sample | H1 | H2 | H3 | H4 | H6 | H7 | H8 | H10 |
|---|---|---|---|---|---|---|---|---|
| **Best-fit values** | | | | | | | | |
| Slope | 3.486 | 2.236 | 2.761 | 2.842 | 3.490 | 2.247 | 2.933 | 3.102 |
| Y-intercept | -11.330 | -9.906 | -10.490 | -10.570 | -11.280 | -9.946 | -10.630 | -10.790 |
| X-intercept | 3.249 | 4.430 | 3.800 | 3.719 | 3.232 | 4.427 | 3.625 | 3.477 |
| 1/slope | 0.287 | 0.447 | 0.362 | 0.352 | 0.287 | 0.445 | 0.341 | 0.322 |
| **Std. Error** | | | | | | | | |
| Slope | 0.249 | 0.082 | 0.095 | 0.127 | 0.152 | 0.100 | 0.123 | 0.154 |
| Y-intercept | 0.348 | 0.114 | 0.136 | 0.177 | 0.208 | 0.137 | 0.167 | 0.209 |
| **Goodness of Fit** | | | | | | | | |
| Correlation (r) | 0.948 | 0.978 | 0.982 | 0.971 | 0.982 | 0.972 | 0.976 | 0.967 |
| R squared | 0.899 | 0.957 | 0.965 | 0.942 | 0.963 | 0.946 | 0.953 | 0.935 |
| **Number of XY Pairs** | 24 | 36 | 33 | 33 | 22 | 31 | 30 | 30 |
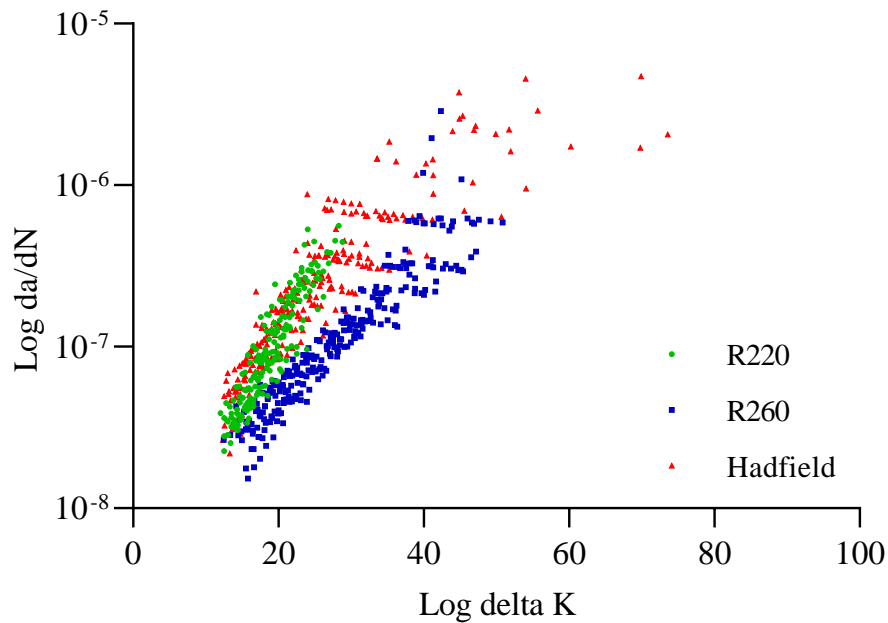


Figure 124. Logarithmic Plot of the Paris Law for the R220 rail steel, R260 rail steel, and Hadfield manganese steel.

### 6.3.2.1 Propose a model for crack growth parameter

The average C value, m values, and conventional approach to interpreting a correlation coefficient from the experiment are shown in Table 19.

Table 19. The average value of Paris law constants for the R220 rail steel, R260 rail steel, and Hadfield manganese steel.

| Material | C | m | R | $R^2$ | Interpretation |
|----------|---|---|---|-------|----------------|
| R220 rail steel | $1.88E^{-12}$ | 3.779 | 0.904 | 0.817 | Very strong correlation |
| R260 rail steel | $1.60E^{-11}$ | 2.821 | 0.967 | 0.936 | Very strong correlation |
| Hadfield steel | $4.08E^{-11}$ | 2.604 | 0.972 | 0.945 | Very strong correlation |

The Pearson correlation coefficient is used to interpret the strength and direction of a linear relationship between two variables in correlation analysis. On the other hand, simple linear regression analysis predicts parameters that estimate one value of a variable based on the other in a linear equation [80]. The crack growth rate shows a clear correlation, confirming the Paris law relationship between da/dN and ΔK for R220 rail steel, R260 rail steel, and Hadfield Manganese steel has a very strong correlation. Thus, material behaviour is considered an important period in predicting crack growth before leading to material damage. Besides, this model can be viewed as a total fatigue life model under a specified load when used in conjunction with the existing initial crack size. Compared with those presented in the literature, the findings obtained in the low Paris regime were compared. Any values of $\Delta K_{th}$ found in the cited literature are also seen in Table 20 [150]. In this contrast, an excellent consensus was observed, and the very small changes observed may result from variations in the chemical composition or manufacturing of the wheel-rail.

Table 20. Results of the average value of Paris law constants from the literature [150].

| Author | R-ratio | Material | Paris law constants C | m | $\Delta K_{th}$ (MPa m$^{1/2}$) |
|---|---|---|---|---|---|
| El-Shabasy and Lewandowski (2004) | 0.1 | Rail | – | 3.50 | 9.1 |
| El-Shabasy and Lewandowski (2004) | 0.7 | Rail | – | 6.20 | 6.0 |
| Zain et al. (2010) | 0.1 | Rail | $2.63 \times 10^{-12}$ | 3.29 | |
| Kim and Kim (2002) | 0.1 | Rail | $4.47 \times 10^{-09}$ | 3.13 | |
| Heshmat (2011) | 0.1 | Rail (pearlitic) | $1.13 \times 10^{-11}$ | 2.17 | |
| Sivaprasad et al. (2005) | 0.1 | Cast wheel (rim-radial) | $1.08 \times 10^{-09}$ | 3.35 | 12.97 |
| Sivaprasad et al. (2005) | 0.1 | Cast wheel (rim-circumferential) | $1.08 \times 10^{-10}$ | 4.07 | 12.65 |
| Sivaprasad et al. (2005) | 0.1 | Forged wheel (rim-radial) | $8.21 \times 10^{-10}$ | 3.53 | 12.07 |
| Sivaprasad et al. (2005) | 0.1 | Forged wheel (rim-circumferential) | $7.39 \times 10^{-11}$ | 4.30 | 12.18 |
| Hamam et al. (2007) | 0.2 | Wheel | $1.95 \times 10^{-09}$ | 3.40 | |
| Hamam et al. (2007) | 0.4 | Wheel | $2.47 \times 10^{-09}$ | 3.38 | |

The material behaviour is considered to be necessary for predicting cracks growth before leading to material damage. Besides, this model can be regarded as a total fatigue life model under a specified load when used in conjunction with the existing initial crack size.

### 6.3.3 Fatigue parameters rate

On a logarithmic scale, the crack growth rate was shown versus ΔK, along with rates of PAC-energy, amplitude, duration and counts per cycle derived from AE data, in an attempt to find a quantitative relationship between AE and crack growth parameters, it was hoped that a correlation or simple linear regression could be used to evaluate whether two numeric variables had a relevant linear relationship. The strength and direction of the linear relationship between two variables can be determined using correlation analysis. On the other hand, simple linear regression analysis predicts parameters that approximate one value of a variable based on the other in a linear equation [80]. The crack growth rate and the energy rate were calculated in the same way. As a result, the energy rate and ΔK relationship can be defined as follows (and similarly for *dA/dN*, *dC/dN*, and *dC/dN*).

$$\frac{dE}{dN} = C\Delta K^m, or : \log\left(\frac{dE}{dN}\right) = \log C + m \log \Delta K$$

Notice that the PAC-energy is calculated in 10 µvolt-sec/count, the duration in µs (microseconds), and the amplitude in dB (decibel) [169].

Figures 125-136 show the crack growth rate with parameters rate and ΔK in the logarithmic scale for the R220 rail steel, R260 rail steel, and Hadfield manganese steel samples.

**6.3.3.1 Energy rate**

## Hadfield Energy Rate
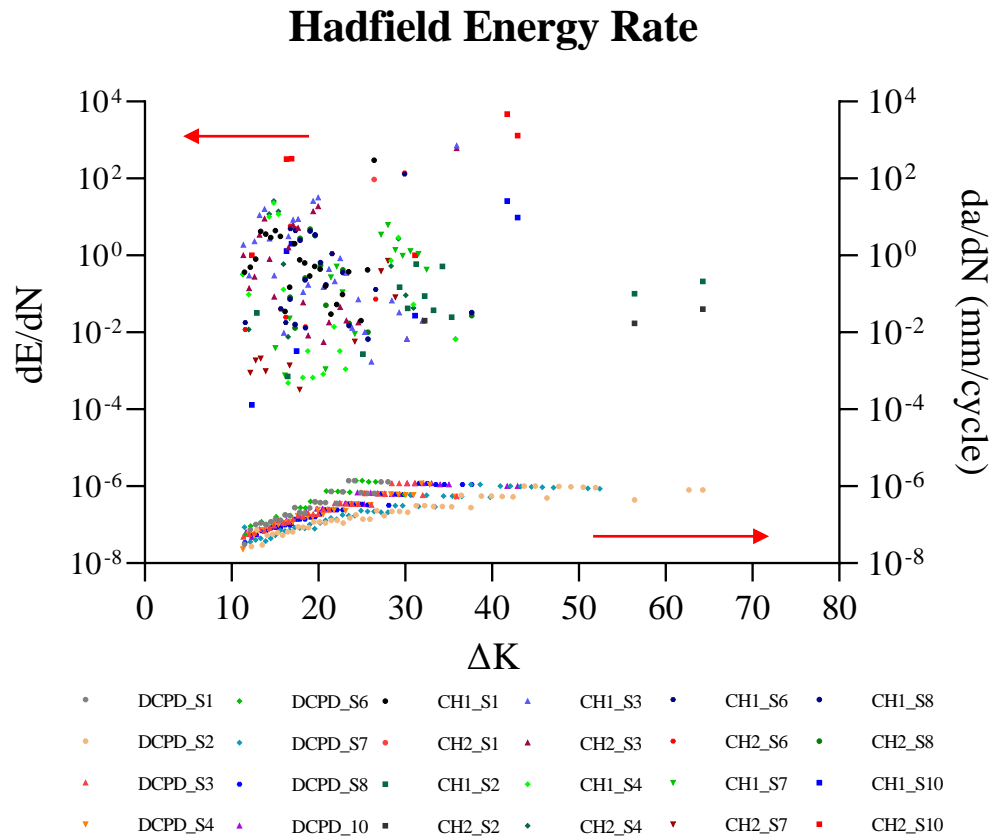


Figure 125. The Energy rate and crack growth rate with ΔK for all Hadfield manganese steel samples on a logarithmic scale.

Table 21. Plots log dE/dN and da/dn against ΔK for all Hadfield manganese steel.

| Sample | H1 | H2 | H3 | H4 | H6 | H7 | H8 | H10 |
|---|---|---|---|---|---|---|---|---|
| **Best-fit values** | | | | | | | | |
| Slope | -0.927 | 2.568 | -5.843 | -2.743 | 6.703 | 8.639 | -7.390 | 6.325 |
| Y-intercept | 0.944 | -5.105 | 7.165 | 2.448 | -8.685 | -12.750 | 12.370 | -9.165 |
| X-intercept | 1.018 | 1.987 | 1.226 | 0.893 | 1.296 | 1.476 | 1.674 | 1.449 |
| 1/slope | -1.079 | 0.389 | -0.171 | -0.365 | 0.149 | 0.116 | -0.135 | 0.158 |
| **Std. Error** | | | | | | | | |
| Slope | 1.570 | 1.188 | 1.520 | 2.706 | 3.464 | 1.268 | 2.888 | 2.939 |
| Y-intercept | 1.998 | 1.780 | 1.966 | 3.536 | 4.422 | 1.681 | 3.837 | 4.036 |
| **Goodness of Fit** | | | | | | | | |
| Correlation (r) | -0.120 | 0.565 | -0.602 | -0.239 | 0.590 | 0.849 | -0.629 | 0.694 |
| R squared | 0.014 | 0.319 | 0.363 | 0.057 | 0.349 | 0.721 | 0.396 | 0.481 |
| **Number of XY Pairs** | 26 | 12 | 29 | 19 | 9 | 20 | 12 | 7 |

# R260 Energy Rate
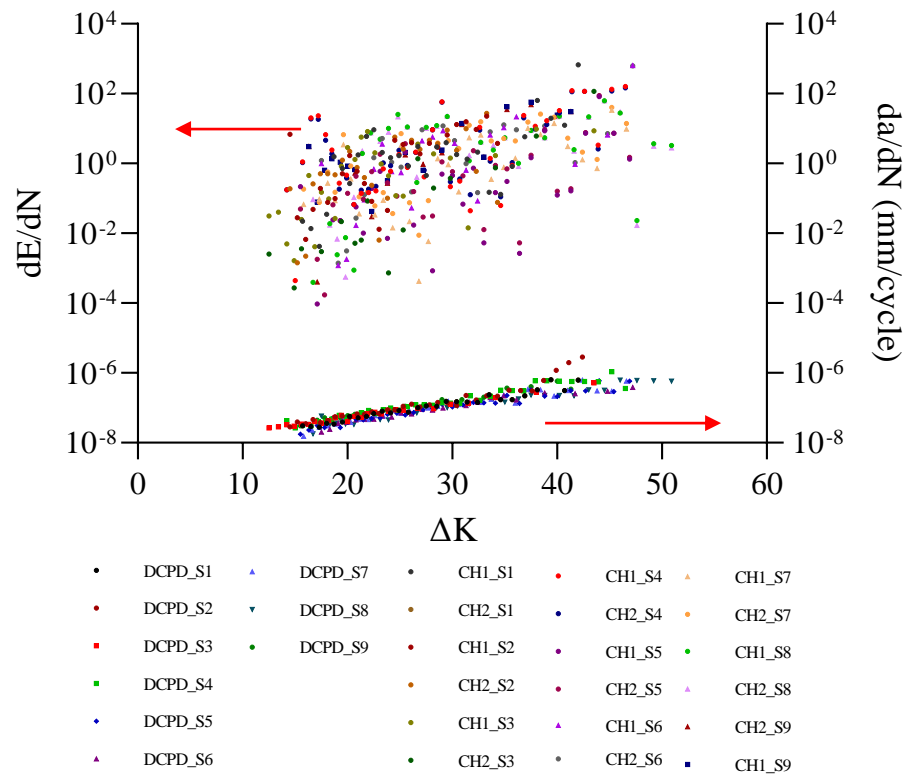


Figure 126. The Energy rate and crack growth rate with ΔK for all R260 rail steel samples on a logarithmic scale.

Table 22. Plots log dE/dN and da/dn against ΔK for all R260 rail steel.

| Sample | R1 | R2 | R3 | R4 | R5 | R6 | R7 | R8 | R9 |
|---|---|---|---|---|---|---|---|---|---|
| **Best-fit values** | | | | | | | | | |
| Slope | 6.250 | 6.218 | 5.966 | 4.352 | 5.188 | 7.351 | 4.911 | 4.022 | 5.462 |
| Y-intercept | -8.565 | -8.211 | -8.411 | -5.664 | -7.949 | -10.310 | -6.885 | -5.370 | -7.148 |
| X-intercept | 1.370 | 1.321 | 1.410 | 1.302 | 1.532 | 1.402 | 1.402 | 1.335 | 1.309 |
| 1/slope | 0.160 | 0.161 | 0.168 | 0.230 | 0.193 | 0.136 | 0.204 | 0.249 | 0.183 |
| **Std. Error** | | | | | | | | | |
| Slope | 1.288 | 1.421 | 1.250 | 1.148 | 1.320 | 1.694 | 1.086 | 1.333 | 1.128 |
| Y-intercept | 1.839 | 1.933 | 1.676 | 1.649 | 1.923 | 2.466 | 1.584 | 1.982 | 1.589 |
| **Goodness of Fit** | | | | | | | | | |
| Correlation | 0.682 | 0.674 | 0.691 | 0.540 | 0.583 | 0.688 | 0.643 | 0.489 | 0.771 |
| R squared | 0.466 | 0.454 | 0.477 | 0.291 | 0.340 | 0.473 | 0.414 | 0.239 | 0.594 |
| **Number of XY Pairs** | 29 | 25 | 27 | 37 | 32 | 23 | 31 | 31 | 18 |
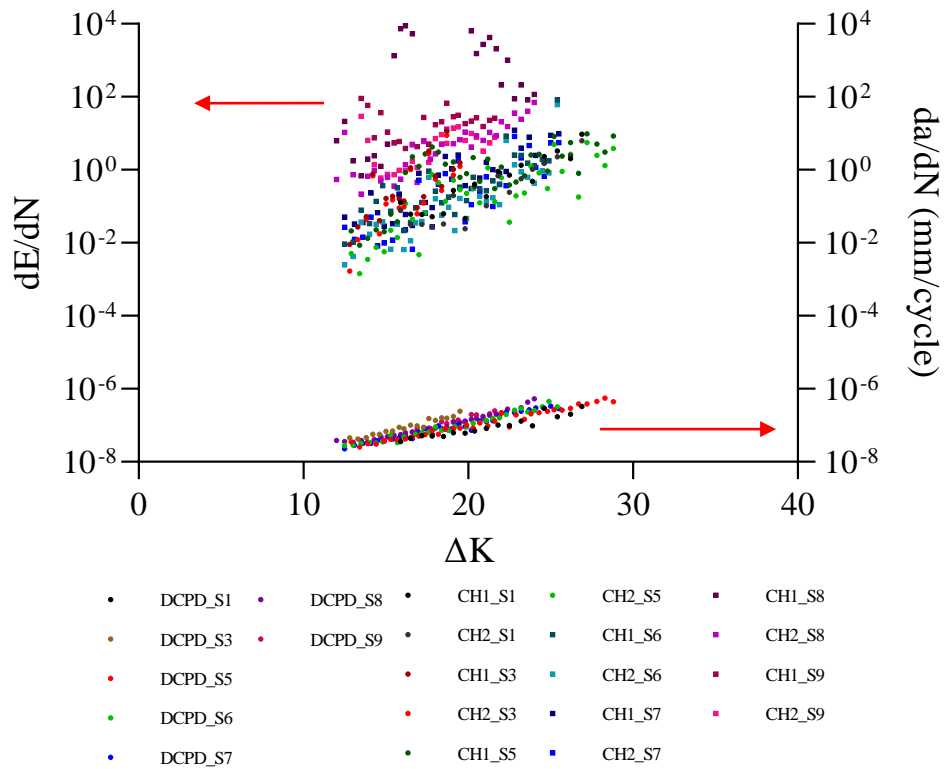
Figure 127. The Energy rate and crack growth rate with ΔK for all R220 rail steel samples on a logarithmic scale.

Table 23. Plots log dE/dN and da/dn against ΔK for all R220 rail steel.

| Sample | R1 | R3 | R5 | R6 | R7 | R8 | R9 |
|---|---|---|---|---|---|---|---|
| Best-fit values | | | | | | | |
| Slope | 9.825 | 7.761 | 7.083 | 7.931 | 6.817 | 8.636 | 1.459 |
| Y-intercept | -13.170 | -9.782 | -9.246 | -10.460 | -8.862 | -7.998 | -0.484 |
| X-intercept | 1.340 | 1.260 | 1.305 | 1.318 | 1.300 | 0.926 | 0.332 |
| 1/slope | 0.102 | 0.129 | 0.141 | 0.126 | 0.147 | 0.116 | 0.685 |
| Std. Error | | | | | | | |
| Slope | 0.814 | 2.238 | 0.816 | 1.053 | 0.863 | 2.742 | 1.073 |
| Y-intercept | 1.092 | 2.728 | 1.075 | 1.340 | 1.109 | 3.438 | 1.347 |
| Goodness of Fit | | | | | | | |
| Correlation (r) | 0.949 | 0.644 | 0.826 | 0.809 | 0.822 | 0.499 | 0.378 |
| R squared | 0.901 | 0.414 | 0.683 | 0.654 | 0.675 | 0.249 | 0.077 |
| **Number of XY Pairs** | 18 | 19 | 37 | 32 | 32 | 32 | 24 |

### 6.3.3.2 Count rate

The count rate is defined as the ratio of the sum of counts of all AE hits to the time interval

during which these AE hits are captured.

## Hadfield Count Rate
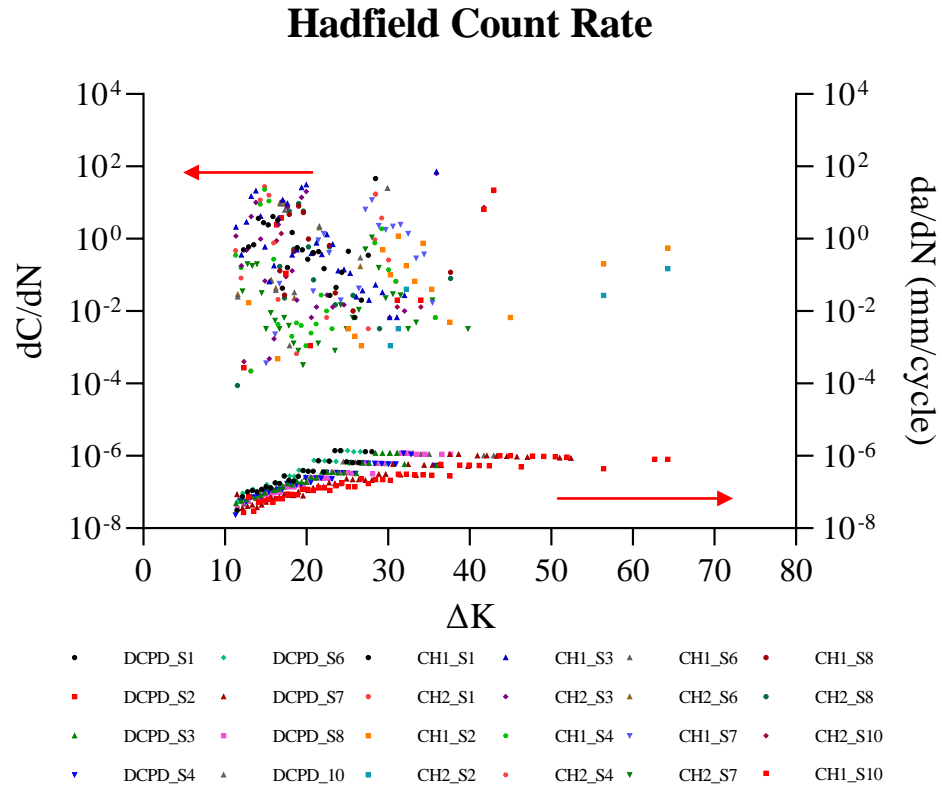


Figure 128. The Count rate and crack growth rate with ΔK for all Hadfield manganese steel samples in logarithmic scale.

Table 24. Plots log dC/dN and da/dn against ΔK for all Hadfield manganese steel.

| Sample | H1 | H2 | H3 | H4 | H6 | H7 | H8 | H10 |
|---|---|---|---|---|---|---|---|---|
| **Best-fit values** | | | | | | | | |
| Slope | -1.892 | 3.142 | -5.896 | -1.868 | 5.605 | 3.894 | 1.555 | 4.089 |
| Y-intercept | 2.051 | -6.138 | 7.402 | 1.256 | -7.407 | -6.343 | -2.657 | -6.256 |
| X-intercept | 1.084 | 1.953 | 1.256 | 0.672 | 1.322 | 1.629 | 1.709 | 1.530 |
| 1/slope | -0.529 | 0.318 | -0.169 | -0.535 | 0.178 | 0.257 | 0.643 | 0.245 |
| **Std. Error** | | | | | | | | |
| Slope | 1.429 | 1.495 | 1.139 | 2.377 | 3.916 | 1.471 | 3.416 | 2.971 |
| Y-intercept | 1.824 | 2.248 | 1.488 | 3.104 | 4.989 | 1.971 | 4.512 | 4.115 |
| **Goodness of Fit** | | | | | | | | |
| Correlation (r) | -0.256 | 0.490 | -0.687 | -0.169 | 0.452 | 0.430 | 0.130 | 0.462 |
| R squared | 0.065 | 0.240 | 0.4716 | 0.029 | 0.204 | 0.184 | 0.017 | 0.213 |
| **Number of XY Pairs** | 27 | 16 | 33 | 23 | 10 | 33 | 14 | 9 |

# R260 Count Rate



Figure 129. The Count rate and crack growth rate with ΔK for all R260 rail steel samples on a logarithmic scale.

Table 25.  Plots log dC/dN and da/dn against ΔK for all R260 rail steel.

| Sample | R1 | R2 | R3 | R4 | R5 | R6 | R7 | R8 | R9 |
|---|---|---|---|---|---|---|---|---|---|
| **Best-fit values** | | | | | | | | | |
| Slope | 4.159 | 5.067 | 4.952 | 1.932 | 4.278 | 4.782 | 3.598 | 3.735 | 2.798 |
| Y-intercept | -5.834 | -6.706 | -7.089 | -2.221 | -6.488 | -6.811 | -5.116 | -5.235 | -3.675 |
| X-intercept | 1.403 | 1.324 | 1.431 | 1.150 | 1.516 | 1.424 | 1.422 | 1.402 | 1.313 |
| 1/slope | 0.240 | 0.197 | 0.202 | 0.518 | 0.234 | 0.209 | 0.278 | 0.268 | 0.357 |
| **Std. Error** | | | | | | | | | |
| Slope | 1.121 | 1.357 | 0.976 | 0.863 | 1.050 | 1.599 | 0.920 | 1.417 | 1.086 |
| Y-intercept | 1.600 | 1.845 | 1.309 | 1.240 | 1.523 | 2.328 | 1.342 | 2.096 | 1.530 |
| **Goodness of Fit** | | | | | | | | | |
| Correlation | 0.581 | 0.614 | 0.712 | 0.354 | 0.591 | 0.547 | 0.588 | 0.434 | 0.541 |
| R squared | 0.338 | 0.378 | 0.507 | 0.125 | 0.349 | 0.299 | 0.345 | 0.188 | 0.293 |
| **Number of XY Pairs** | 29 | 25 | 27 | 37 | 33 | 23 | 31 | 32 | 18 |

# R220 Count Rate
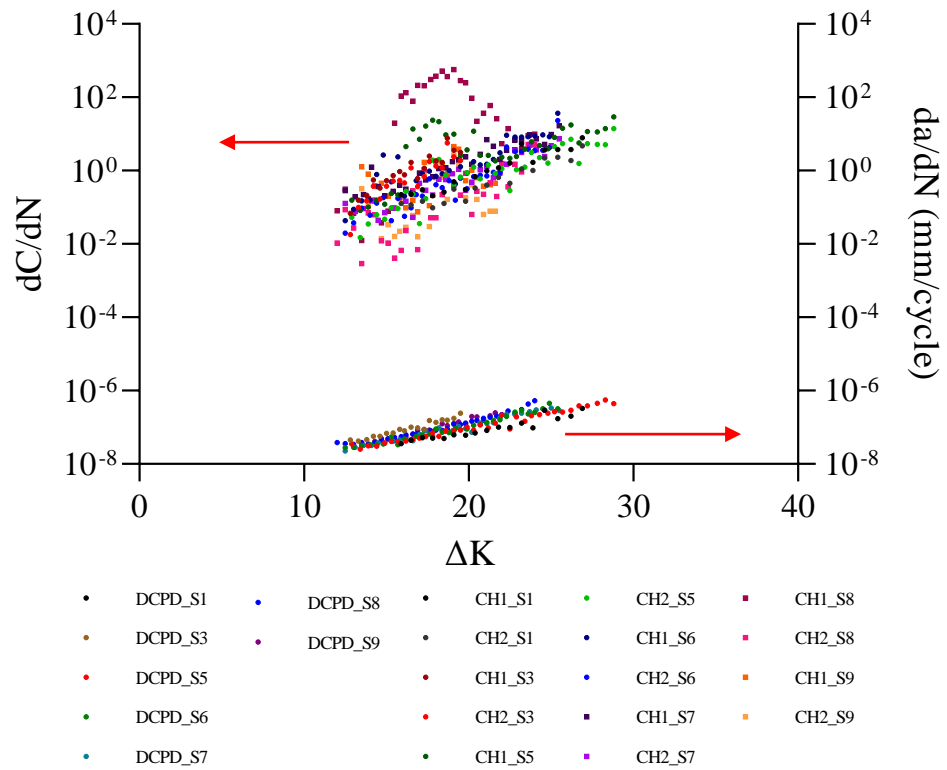


Figure 130. The Count rate and crack growth rate with ΔK for all R220 rail steel samples on a logarithmic scale.

Table 26. Plots log dC/dN and da/dn against ΔK for all R220 rail steel.

| Sample | R1 | R3 | R5 | R6 | R7 | R8 | R9 |
|---|---|---|---|---|---|---|---|
| **Best-fit values** | | | | | | | |
| Slope | 7.367 | 6.729 | 5.271 | 6.877 | 5.440 | 8.906 | 3.031 |
| Y-intercept | -9.575 | -8.021 | -6.258 | -8.477 | -6.634 | -10.020 | -3.952 |
| X-intercept | 1.300 | 1.192 | 1.187 | 1.233 | 1.220 | 1.125 | 1.304 |
| 1/slope | 0.136 | 0.149 | 0.190 | 0.145 | 0.184 | 0.112 | 0.330 |
| **Std. Error** | | | | | | | |
| Slope | 0.426 | 1.057 | 0.756 | 0.677 | 0.446 | 2.405 | 1.396 |
| Y-intercept | 0.571 | 1.289 | 0.995 | 0.862 | 0.574 | 3.016 | 1.752 |
| **Goodness of Fit** | | | | | | | |
| Correlation (r) | 0.974 | 0.839 | 0.763 | 0.880 | 0.912 | 0.560 | 0.520 |
| R squared | 0.949 | 0.704 | 0.582 | 0.775 | 0.832 | 0.314 | 0.177 |
| **Number of XY Pairs** | 18 | 19 | 37 | 32 | 32 | 32 | 24 |

### 6.3.3.3 Duration rate

Figure 131 plots the correlation between the duration and growth rates of cracks with ΔK on a logarithmic scale. The duration rate for all samples follows a similar pattern to the crack growth rate.

## Hadfield Duration Rate
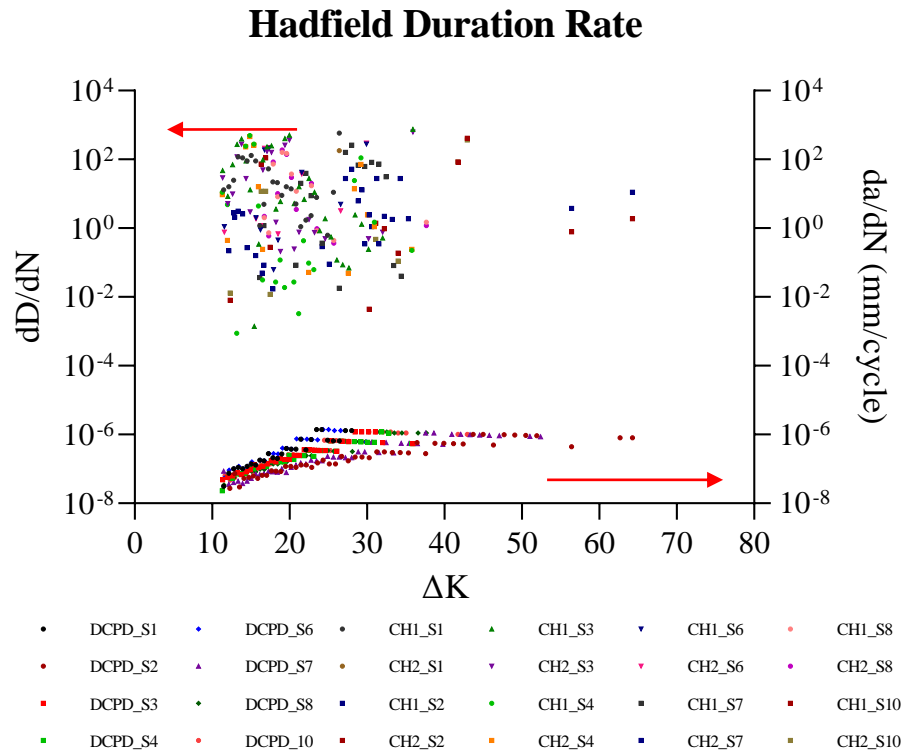


Figure 131. The Duration rate and crack growth rate with ΔK for all Hadfield manganese steel samples in logarithmic scale.

Table 27. Plots log dD/dN and da/dn against ΔK for all Hadfield manganese steel.

| Sample | H1 | H2 | H3 | H4 | H6 | H7 | H8 | H10 |
|---|---|---|---|---|---|---|---|---|
| **Best-fit values** | | | | | | | | |
| Slope | -3.211 | 2.352 | -5.273 | -1.645 | 4.501 | 3.290 | -3.542 | 3.632 |
| Y-intercept | 5.158 | -3.064 | 7.714 | 2.156 | -4.626 | -4.041 | 5.892 | -4.176 |
| X-intercept | 1.606 | 1.303 | 1.463 | 1.311 | 1.028 | 1.228 | 1.664 | 1.150 |
| 1/slope | -0.311 | 0.425 | -0.189 | -0.608 | 0.222 | 0.304 | -0.282 | 0.275 |
| **Std. Error** | | | | | | | | |
| Slope | 1.280 | 1.231 | 1.771 | 2.727 | 3.648 | 1.863 | 2.793 | 2.855 |
| Y-intercept | 1.629 | 1.844 | 2.303 | 3.563 | 4.648 | 2.500 | 3.710 | 3.979 |
| **Goodness of Fit** | | | | | | | | |
| Correlation (r) | -0.456 | 0.517 | -0.484 | -0.134 | 0.400 | 0.352 | -0.372 | 0.461 |
| R squared | 0.208 | 0.268 | 0.234 | 0.018 | 0.160 | 0.124 | 0.139 | 0.213 |
| **Number of XY Pairs** | 26 | 12 | 32 | 22 | 10 | 24 | 12 | 8 |

# R260 Duration Rate
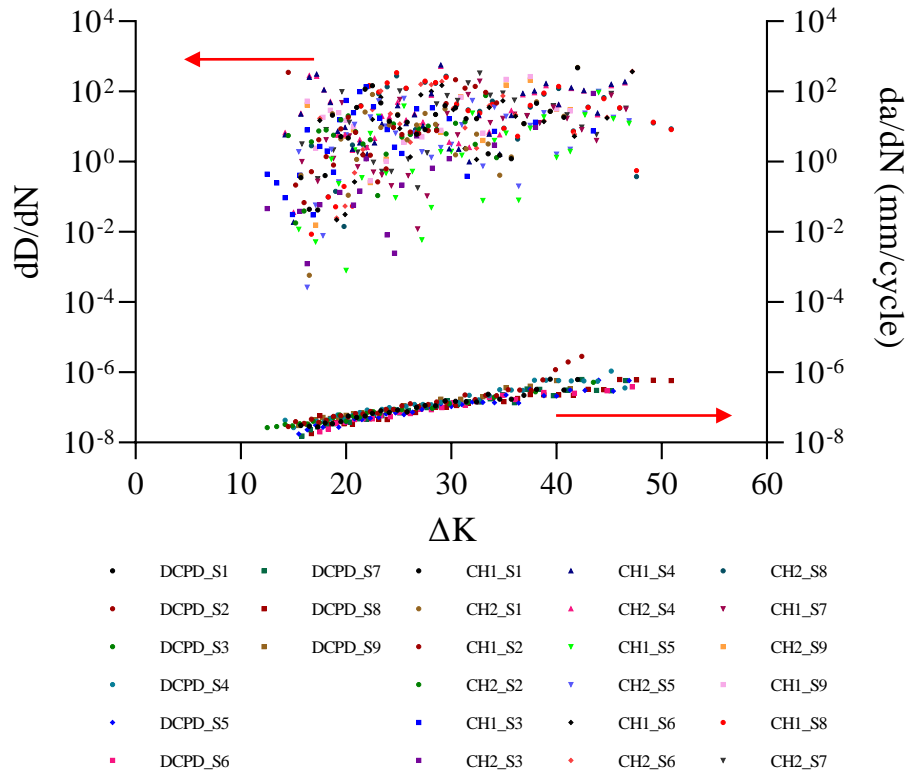


Figure 132. The Duration rate and crack growth rate with ΔK for all R260 rail steel samples on a logarithmic scale.

Table 28. Plots log dD/dN and da/dn against ΔK for all R260 rail steel.

| Sample | R1 | R2 | R3 | R4 | R5 | R6 | R7 | R8 | R9 |
|---|---|---|---|---|---|---|---|---|---|
| **Best-fit values** | | | | | | | | | |
| Slope | 4.049 | 4.096 | 4.569 | 1.918 | 4.680 | 4.334 | 3.444 | 1.915 | 2.473 |
| Y-intercept | -4.601 | -4.449 | -5.456 | -1.145 | -6.084 | -4.971 | -3.785 | -1.290 | -2.117 |
| X-intercept | 1.136 | 1.086 | 1.194 | 0.597 | 1.300 | 1.147 | 1.099 | 0.674 | 0.856 |
| 1/slope | 0.247 | 0.244 | 0.219 | 0.521 | 0.214 | 0.231 | 0.290 | 0.522 | 0.404 |
| **Std. Error** | | | | | | | | | |
| Slope | 1.298 | 1.471 | 1.247 | 0.903 | 1.280 | 1.675 | 1.081 | 1.298 | 1.262 |
| Y-intercept | 1.852 | 2.001 | 1.672 | 1.298 | 1.857 | 2.439 | 1.577 | 1.930 | 1.777 |
| **Goodness of Fit** | | | | | | | | | |
| Correlation | 0.515 | 0.502 | 0.591 | 0.338 | 0.549 | 0.492 | 0.509 | 0.264 | 0.440 |
| R squared | 0.265 | 0.252 | 0.350 | 0.114 | 0.301 | 0.242 | 0.259 | 0.070 | 0.194 |
| **Number of XY Pairs** | 29 | 25 | 27 | 37 | 33 | 23 | 31 | 31 | 18 |

# R220 Duration Rate
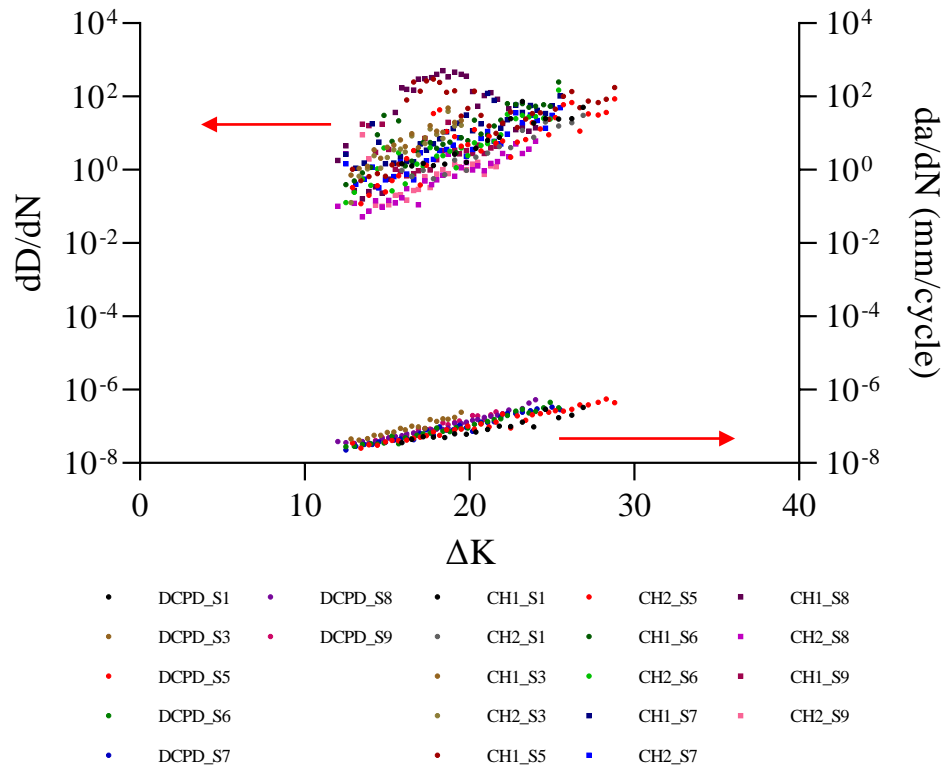


Figure 133. The Duration rate and crack growth rate with ΔK for all R220 rail steel samples in logarithmic scale.

Table 29. Plots log dD/dN and da/dn against ΔK for all R220 rail steel.

| Sample | R1 | R3 | R5 | R6 | R7 | R8 | R9 |
|---|---|---|---|---|---|---|---|
| **Best-fit values** | | | | | | | |
| Slope | 7.631 | 6.320 | 4.836 | 6.650 | 5.169 | 6.853 | 0.193 |
| Y-intercept | -9.084 | -6.701 | -4.768 | -7.331 | -5.408 | -7.078 | 0.377 |
| X-intercept | 1.190 | 1.060 | 0.986 | 1.102 | 1.046 | 1.033 | -1.958 |
| 1/slope | 0.131 | 0.158 | 0.207 | 0.150 | 0.194 | 0.146 | 5.196 |
| **Std. Error** | | | | | | | |
| Slope | 0.571 | 1.051 | 0.975 | 0.778 | 0.579 | 1.956 | 1.179 |
| Y-intercept | 0.766 | 1.282 | 1.284 | 0.990 | 0.744 | 2.453 | 1.479 |
| **Goodness of Fit** | | | | | | | |
| Correlation (r) | 0.958 | 0.825 | 0.643 | 0.842 | 0.852 | 0.539 | 0.035 |
| R squared | 0.918 | 0.680 | 0.413 | 0.709 | 0.727 | 0.290 | 0.001 |
| **Number of XY Pairs** | 18 | 19 | 37 | 32 | 32 | 32 | 24 |

**6.3.3.4 Amplitude rate**

## Hadfield Amplitude Rate
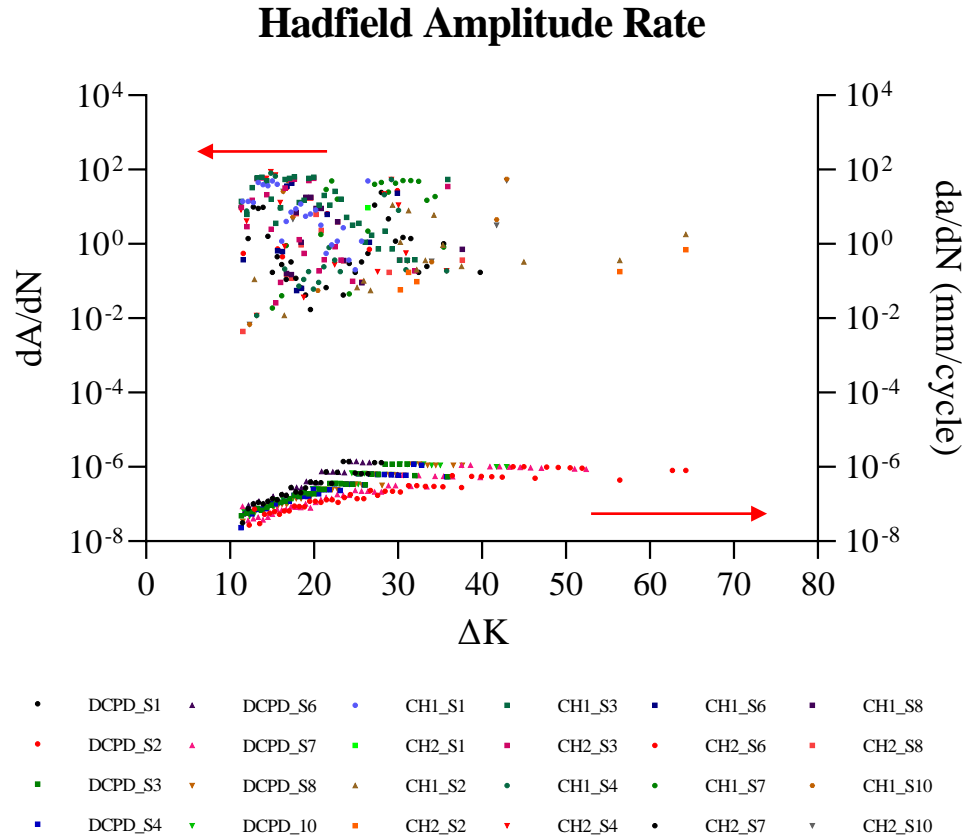


Figure 134. The Amplitude rate and crack growth rate with ΔK for all Hadfield manganese steel samples in logarithmic scale.

Table 30. Plots log dA/dN and da/dn against ΔK for all Hadfield manganese steel.

| Sample | H1 | H2 | H3 | H4 | H6 | H7 | H8 | H10 |
|---|---|---|---|---|---|---|---|---|
| **Best-fit values** | | | | | | | | |
| Slope | -4.103 | 2.453 | -4.499 | -1.477 | 2.812 | 2.414 | 1.905 | 1.947 |
| Y-intercept | 5.920 | -4.010 | 6.871 | 2.162 | -3.084 | -2.862 | -2.322 | -2.209 |
| X-intercept | 1.443 | 1.635 | 1.527 | 1.464 | 1.097 | 1.185 | 1.219 | 1.135 |
| 1/slope | -0.244 | 0.408 | -0.222 | -0.677 | 0.356 | 0.414 | 0.525 | 0.514 |
| **Std. Error** | | | | | | | | |
| Slope | 0.947 | 1.121 | 0.749 | 1.951 | 3.226 | 1.281 | 2.590 | 2.598 |
| Y-intercept | 1.208 | 1.686 | 0.978 | 2.548 | 4.110 | 1.710 | 3.421 | 3.598 |
| **Goodness of Fit** | | | | | | | | |
| Correlation (r) | -0.655 | 0.505 | -0.739 | -0.163 | 0.295 | 0.316 | 0.208 | 0.273 |
| R squared | 0.429 | 0.255 | 0.546 | 0.027 | 0.087 | 0.100 | 0.043 | 0.074 |
| **Number of XY Pairs** | 27 | 16 | 33 | 23 | 10 | 34 | 14 | 9 |
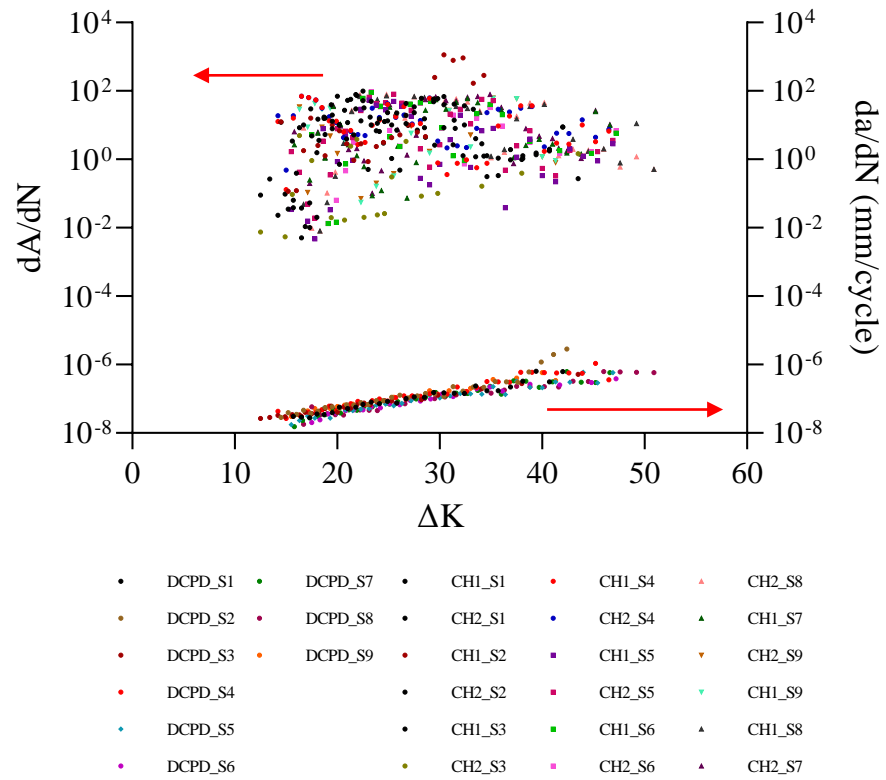
Figure 135. The Amplitude rate and crack growth rate with ΔK for all R260 rail steel samples in logarithmic scale.

Table 31. Plots log dA/dN and da/dn against ΔK for all R260 rail steel.

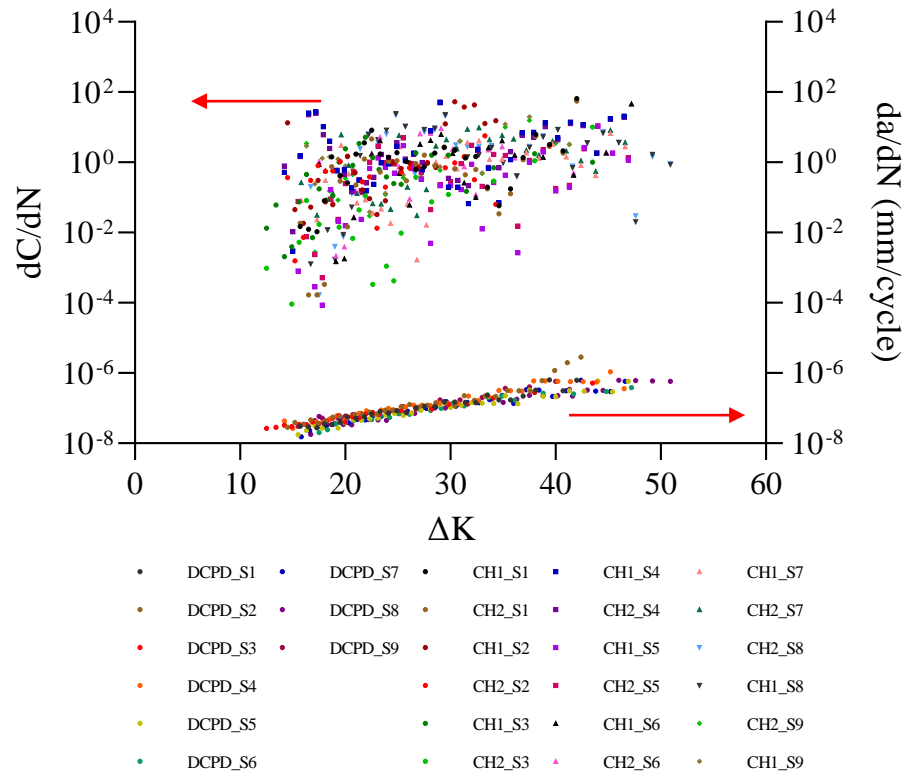| Sample | R1 | R2 | R3 | R4 | R5 | R6 | R7 | R8 | R9 |
|---|---|---|---|---|---|---|---|---|---|
| **Best-fit values** | | | | | | | | | |
| Slope | 1.599 | 5.254 | 3.410 | -0.751 | 0.975 | 1.785 | 1.682 | 1.283 | -0.599 |
| Y-intercept | -1.275 | -5.867 | -3.846 | 2.371 | -0.639 | -1.561 | -1.404 | -0.821 | 1.788 |
| X-intercept | 0.797 | 1.117 | 1.128 | 3.158 | 0.656 | 0.874 | 0.835 | 0.640 | 2.986 |
| 1/slope | 0.625 | 0.190 | 0.293 | -1.332 | 1.026 | 0.560 | 0.595 | 0.779 | -1.670 |
| **Std. Error** | | | | | | | | | |
| Slope | 1.453 | 1.419 | 1.412 | 0.610 | 1.207 | 1.705 | 1.077 | 1.401 | 1.615 |
| Y-intercept | 2.075 | 1.930 | 1.893 | 0.876 | 1.751 | 2.483 | 1.571 | 2.074 | 2.274 |
| **Goodness of Fit** | | | | | | | | | |
| Correlation | 0.207 | 0.611 | 0.435 | -0.204 | 0.144 | 0.223 | 0.279 | 0.165 | -0.092 |
| R squared | 0.043 | 0.373 | 0.189 | 0.042 | 0.021 | 0.050 | 0.078 | 0.027 | 0.009 |
| **Number of XY Pairs** | 29 | 25 | 27 | 37 | 33 | 23 | 31 | 32 | 18 |

# R220 Amplitude Rate
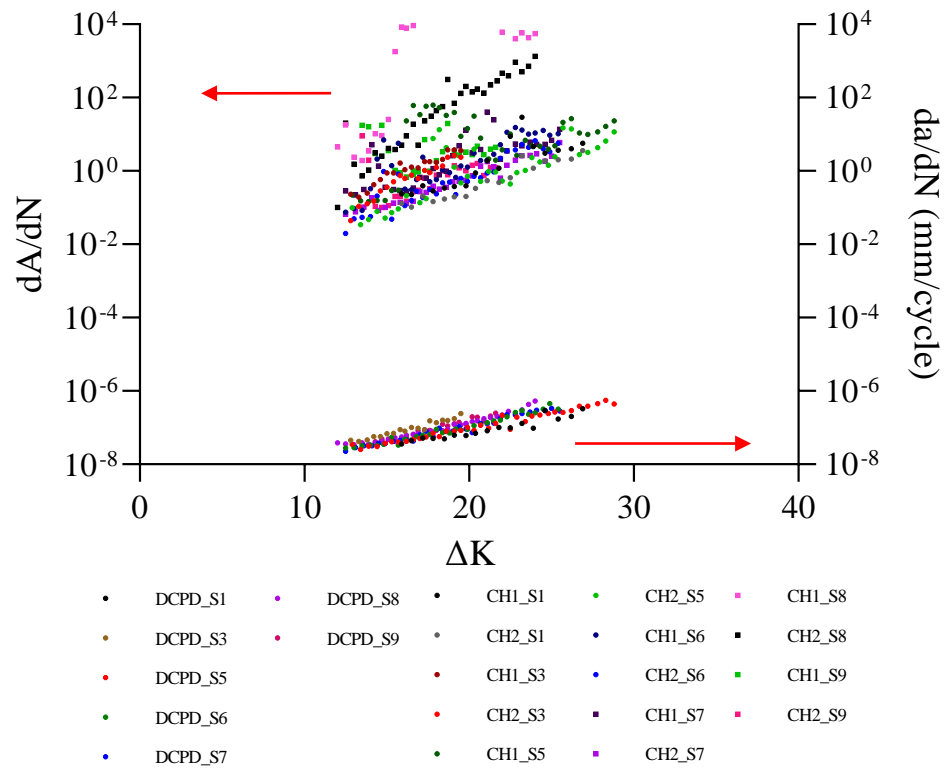


Figure 136. The Amplitude rate and crack growth rate with ΔK for all R260 rail steel samples in logarithmic scale

Table 32. Plots log dA/dN and da/dn against ΔK for all R220 rail steel.

| Sample | R1 | R3 | R5 | R6 | R7 | R8 | R9 |
|---|---|---|---|---|---|---|---|
| **Best-fit values** | | | | | | | |
| Slope | 5.618 | 5.652 | 4.009 | 6.192 | 4.790 | 13.470 | 0.767 |
| Y-intercept | -7.172 | -6.651 | -4.390 | -7.491 | -5.703 | -13.390 | -4.913 |
| X-intercept | 1.277 | 1.177 | 1.095 | 1.210 | 1.191 | 0.994 | 6.407 |
| 1/slope | 0.178 | 0.177 | 0.249 | 0.162 | 0.209 | 0.074 | 1.304 |
| **Std. Error** | | | | | | | |
| Slope | 0.884 | 0.744 | 1.037 | 0.809 | 0.679 | 2.142 | 1.238 |
| Y-intercept | 1.186 | 0.906 | 1.366 | 1.030 | 0.873 | 2.687 | 1.554 |
| **Goodness of Fit** | | | | | | | |
| Correlation (r) | 0.846 | 0.879 | 0.547 | 0.813 | 0.790 | 0.754 | 0.285 |
| R squared | 0.716 | 0.773 | 0.299 | 0.661 | 0.624 | 0.569 | 0.017 |
| **Number of XY Pairs** | 18 | 19 | 37 | 32 | 32 | 32 | 24 |

Table 33-35 shows the correlation of the calculated AE parameter rate, crack growth rate, and $\Delta K$ for the R220 rail steel, R260 rail steel, and Hadfield manganese steel samples on a logarithmic scale. It should be mentioned that all AE parameter rates considered in the analysis were calculated using the same method as the crack growth rate, meaning that the Paris-Erdogan law is directly relevant.

Since R220 rail steel generates more consistent elastic waves, a better fit between their AE signal parameters and cracks growth parameters is feasible. R220 rail steel demonstrates an apparent fit between the energy rate, count rate, and amplitude rate of AE signals and $\Delta K$. The average C value, m values, and conventional approach to interpreting a correlation coefficient from the experiment are shown in Table 33.

Table 33. Average fit parameters against $\Delta K$ of R220 rail steel.

| R220 Rail Steel | | | | | |
|---|---|---|---|---|---|
| AE Parameters | C | m | R | $R^2$ | Interpretation |
| Energy rate | $2.68 \times 10^{-8}$ | 7.073 | 0.704 | 0.495 | Strong correlation |
| Duration rate | $1.94 \times 10^{-6}$ | 5.379 | 0.670 | 0.450 | Moderate correlation |
| Count rate | $2.74 \times 10^{-8}$ | 6.232 | 0.778 | 0.606 | Strong correlation |
| Amplitude rate | $7.92 \times 10^{-8}$ | 5.785 | 0.702 | 0.493 | Strong correlation |

Samples 8 and 9 resulted in extremely erratic plots. After eliminating both samples, the crack growth rate parameters with $\Delta K$ for all R220 rail steel samples except samples 8 and 9 are shown in Figure 137, and the interpretation is all strong correlation (Table 34).
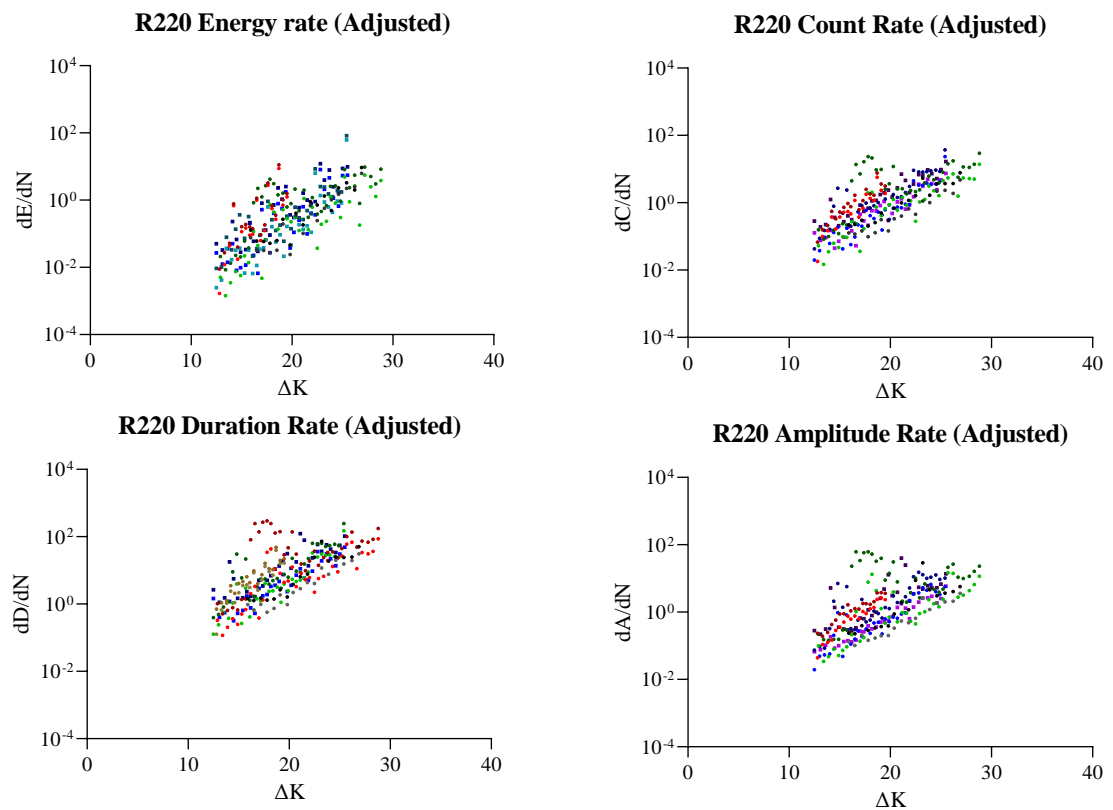
Figure 137. The crack growth rate parameters with ΔK for all R220 rail steel samples but samples 8 and 9.

Table 34. Interpretation of R220 rail steel after neglected samples 8 and 9

| R220 Rail Steel (adjusted) | | | |
|---|---|---|---|
| **AE Parameters** | **R** | **$R^2$** | **Interpretation** |
| Energy rate | 0.810 | 0.656 | Strong correlation |
| Duration rate | 0.874 | 0.763 | Strong correlation |
| Count rate | 0.824 | 0.679 | Strong correlation |
| Amplitude rate | 0.775 | 0.601 | Strong correlation |

The count rate for R260 steel samples follows the same pattern as the crack growth rate for each sample, though the variation between samples is greater than the crack growth rate. Thus, R260 rail steel qualification is also feasible, but with a larger margin of error due to data point scattering. All parameters except only the Amplitude rate have a moderate correlation.

Table 35. Average fit parameters against ΔK of R260 rail steel.

| R260 Rail Steel | | | | | |
|---|---|---|---|---|---|
| AE Parameters | C | m | R | $R^2$ | Interpretation |
| Energy rate | $2.44 \times 10^{-8}$ | 5.524 | 0.624 | 0.410 | Moderate correlation |
| Duration rate | $1.71 \times 10^{-4}$ | 3.498 | 0.467 | 0.218 | Moderate correlation |
| Count rate | $3.44 \times 10^{-6}$ | 3.922 | 0.551 | 0.304 | Moderate correlation |
| Amplitude rate | $5.62 \times 10^{-2}$ | 1.626 | 0.196 | 0.039 | Weak correlation |

The AE data did not fit the Paris law trend so well. For all parameters, Hadfield manganese steel provides a significantly worse fit. Since the samples had not been work-hardened and the plate is in the as-received condition, this is due to plasticity. This is expected to be less of an issue in actual Hadfield manganese crossings, which have been work-hardened and will not exhibit much plasticity, a hypothesis confirmed by literature data and SEM fractography.

Table 36. Average fit parameters against ΔK of Hadfield manganese rail steel.

| Hadfield Manganese Steel | | | | | |
|---|---|---|---|---|---|
| AE Parameters | C | m | R | $R^2$ | Interpretation |
| Energy rate | $2.53 \times 10^{-2}$ | 0.917 | 0.139 | 0.019 | Weak correlation |
| Duration rate | $4.24 \times 10$ | 0.013 | 0.036 | 0.001 | Negligible correlation |
| Count rate | $5.47 \times 10^{-3}$ | 1.079 | 0.107 | 0.011 | Weak correlation |
| Amplitude rate | $1.14 \times 10$ | 0.182 | 0.005 | 0.000 | Negligible correlation |

Hadfield manganese steel and other high Mn manganese steels have been confirmed to exhibit ductile crack growth. However, ductility will be noticeably reduced as work hardening progresses, resulting in more cleavage. The Hadfield steel samples show a quasi-cleavage fracture during high cycle fatigue, the most common fracture mode. This form of fracture corresponds to the very low energy rate observed in pearlitic

rail steel samples. The lower growth rate of the crack is consistent with the presence of plasticity ahead of the crack tip and work hardening [152-153]. The twin nucleation is an outstanding source of AE since it is caused by the cumulative motion of several hundred dislocations [63]. There is no detectable AE generated by the twin growth, as shown in [151]. While an elliptical twin grows at a rate of $10^{-3}$ ms$^{-1}$, the surface displacement induced by twin growth is approximately $\Delta U = 5 \times 10^{-22}$ m, according to Papirov et al. [168]. This surface displacement is unquestionably less than the AE setup's resolution [154].

# CHAPTER 7

# FRACTOGRAPHY

## CHAPTER 7: FRACTOGRAPHY

In this chapter, study the fracture surface of the samples to answer the aim question of the link between microstructural features and AE signals generated from crack growth. An in-depth analysis of the non-metallic inclusion helps explain the areas responsible for detecting the increased signals. A summary of the possibilities of using the LCSM method is presented at the end of the chapter.

## 7.1    FRACTURED SURFACE ANALYSIS

The samples were fractured under a single load after the fatigue tests. The crack propagation zone (CP) is where fatigue cracks grow, and the final fracture zone (FF) is the rest of the surface. A fracture surface morphology evaluation was carried on typical fatigue-failed specimens of each material to define the fatigue damage types. In the characteristic fracture analysis, the fractures are classified into ductile fractures and brittle fractures. Both types are categorised by the quantity of plastic deformation and energy absorbed before fracture. Fracture surface observations were performed along the pathways found in the fatigue study of crack extensions on the surface. Figure 138 shows the fracture surface of the R260 rail steel and Hadfield manganese steel.
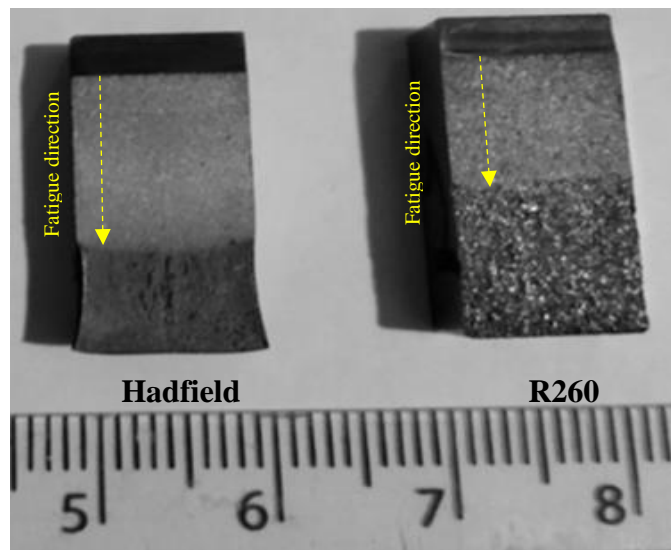


Figure 138. Macroscopic of R260 rail steel and Hadfield manganese steel.

From the Figure 138, it can be seen that the fatigue area of Hadfield steel is longer than the R260 rail steel. The fatigue crack length of the R260 is approximately 80 mm, while the Hadfield manganese steel, it has a longer length of about 110 mm.

### 7.1.1 R260 Rail Steel

R260 rail steel fatigue samples fracture surfaces were studied and analysed after being subjected to cyclic three-point fatigue bending test. The fractured surfaces were investigated using a JEOL 6060 SEM. A macroscopic view of the fracture areas is seen in Figure 139.
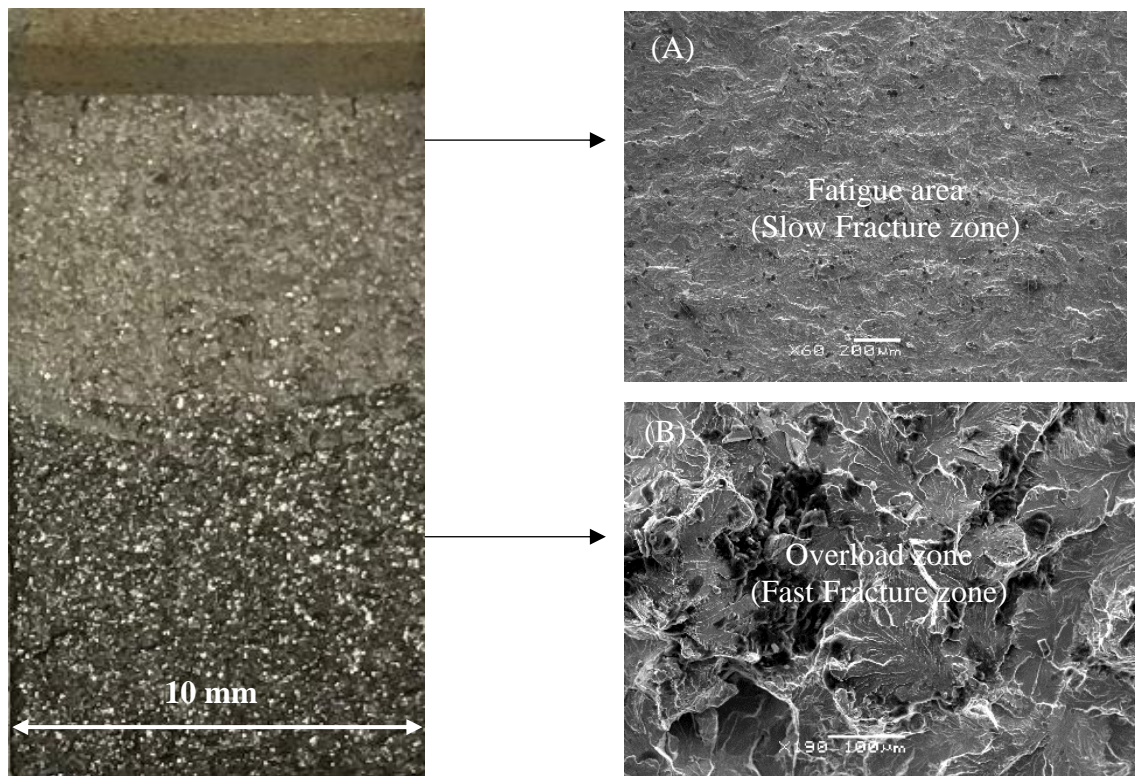


Figure 139. Macroscopic view of a fractured surface showing the morphologies of the fatigue crack growth area (A) and the brittle fracture area (B) to show that the fatigue zone is smoother than the overload zone, a lighter shade of grey may be used.

The difference between the fatigue area and the final ductile fracture area during plastic deformation of R260 rail steel is shown in Figure 139. The macroscopic appearance of the fracture surfaces demonstrates reveals a clear connection between

fatigue surfaces and fracture surfaces. The cracks begin in the pre-cracked area and gradually progress across the fatigue zone or area affected by cyclic stresses. In general, the fatigue area will develop cracks at an average rate of $10^{-8}$ to $10^{-6}$ millimetres each stress cycle [88]. The material will become less forceful as the cracks grow, resulting in an overload zone. The "fractures zone" was defined in these areas by a brittle fracture. Cleavage facets, intergranular facets, and striations (a micro-extension of the fatigue fracture) are three types of cracks that suggest brittle fracture mechanisms [155], as shown in Figure 140-141.
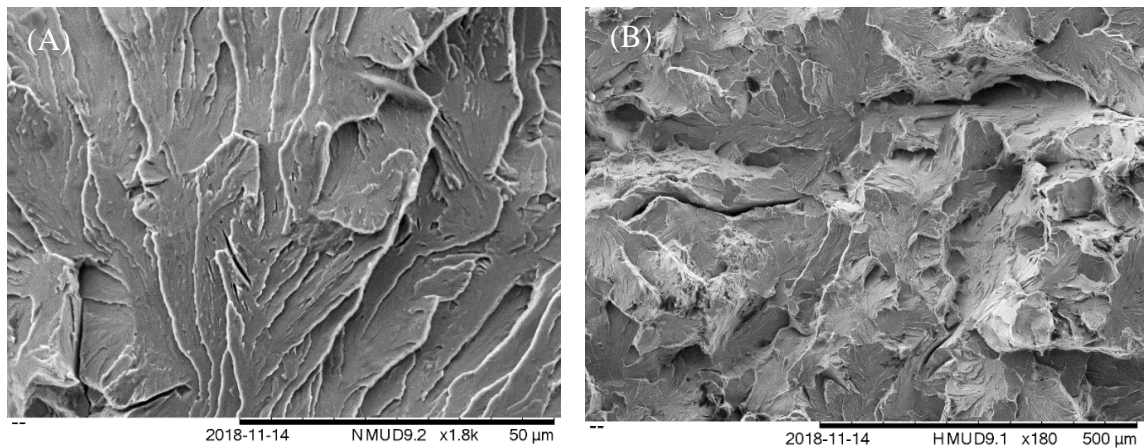


Figure 140. A cleavage process causes a river pattern of radiating lines, typical of a brittle fracture mechanism (A). In addition, there were transgranular and intergranular fractures in this area, suggesting that the environment had contributed to its failure (B).
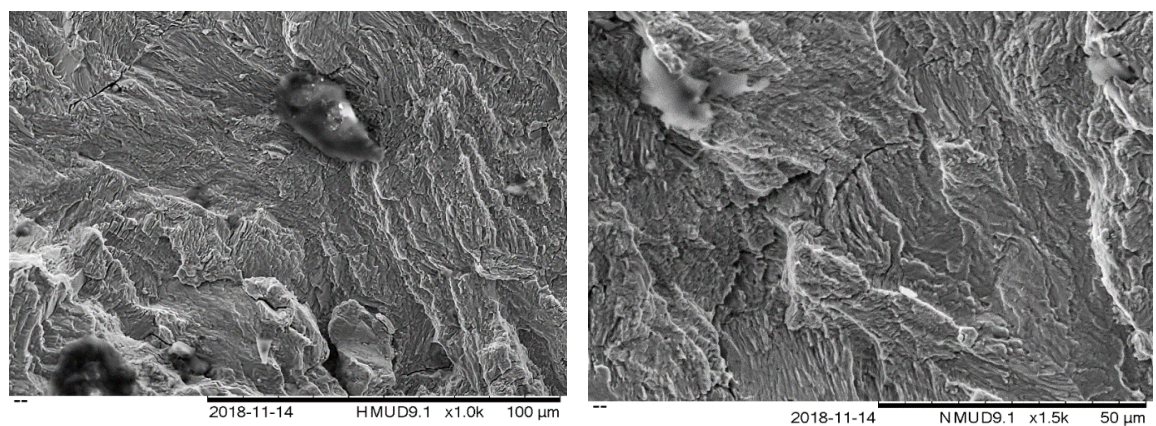


Figure 141. Fatigue striations are marks that occur on material due to fatigue failure and represent individual crack-growth steps. A material that failed due to fatigue may have hundreds of fatigue striations on its surface. Therefore, many fatigue striations may only be seen under a magnification greater than 100x.

The fracture surfaces on all the samples were shimmering and smooth. There were no dimples or other signs of ductile fracture in the early stages of fatigue near the threshold, indicating that the sample fracture appears brittle. The lamellar structure of the pearlitic microstructure explains the surface staircase-like appearance. In addition, the R260 steel fracture was discovered to have a large number of inclusions. Both steels have facets on their surfaces at the final fracture zone (FF). Cleavage fracture occurs more frequently in dense atomic planes (Table 37). For the cleavage fracture of BCC metals, this fragmentation process is much more important. Because the number of cleavage planes is fewer than the number of potential slip planes, the geometry needed to cross-grain boundaries through cleavage fractures is severely limited. Ferrite steels tested in the low toughness regime or the transition zone between ductile and brittle stages show considerable fracture toughness resistance as a result of transgranular and intergranular fracture interactions [179].

Table 37. Cleavage plans in various materials [179].

| Structure | Cleavage plane | Some materials |
|---|---|---|
| BCC | {100} | Ferritic steels, Mo; Nb, W |
| FCC | {111} | Very rarely observed |
| HCP | {0002} | Be, Mg, Zn |
| Diamond | {111} | Diamond, Si, Ge |
| NaCl | {100} | NaCl, LiF, MgO, AgCl |
| ZnS | {110} | ZnS, BeO |
| CaF$_2$ | {111} | CaF$_2$, UO$_2$, ThO$_2$ |

The overload resulted in much more brittle behaviour and increased cleavage. The fracturing occurs within these fully pearlitic steels within the pearlite colonies through the different cementite and lamellas of ferrite. The crystallographic orientation of the ferrite in the pearlite is used to identify each exposed fracture surface facet. The size of the facets may be compared to the grain size of the prior austenite due to the ferrite crystallographic connection.

The traces obtained from and from the DCPD instrument were used to measure the actual crack duration and fatigue crack growth rate. Subsequently, crack lengths were compared with the cumulative AE energy produced by the two different sensors. However, the actual number of failure cycles depends on the initial crack duration ($a_0$) at the start of each fatigue test. Therefore, the values obtained from both the AE and DCPD instruments were calculated to measure the crack length and fatigue crack growth rate following the equation in **5.3**. The graph of the experiment will be plotted to describe the crack growth in the same direction.

**R260 Sample 1**



Figure 142. A cumulative AE energy plot from R50α sensors compares to the crack size measured using the DCPD instrument of R260 sample 1. The labelled spikes are identified in Figure 143.

An optical microscope and a scanning electron microscope were used to examine the cracks. As shown in Figure 142, the area has an effect on the growth of each point.
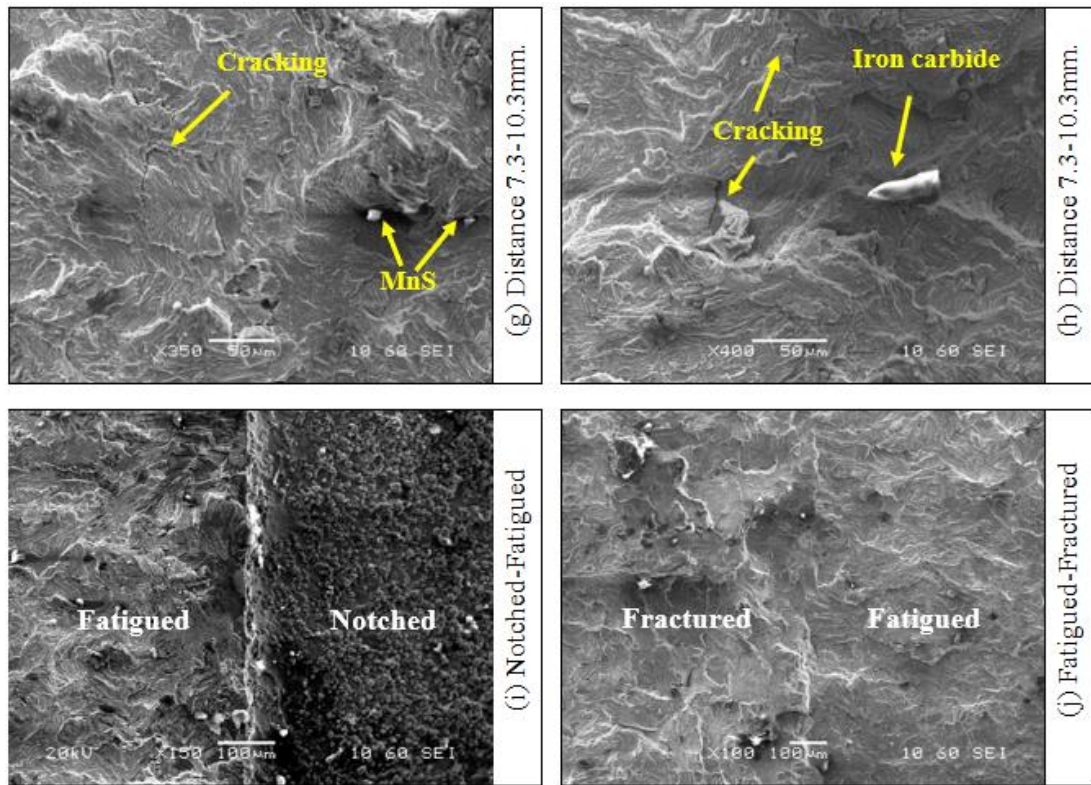
Figure 143. SEM Micrographs showing the fracture surface (a) Iron carbide and SiO₂ defect at a distance of 5 mm, (b)(c) Iron carbide and cracking at a distance of 5.5 mm - 6.2 mm, (d) Cracking at a distance of 6.4 mm, (e) Iron carbide and porosity at a distance of 6.6 mm, (f)(g)(h) Cracking, MnS, and Iron carbide at a distance of 7.3 mm - 10.3 mm, (i) Interface between notched area and fatigued area, (j) Interface between fatigued area and fractured area.

**R260 Sample 2**
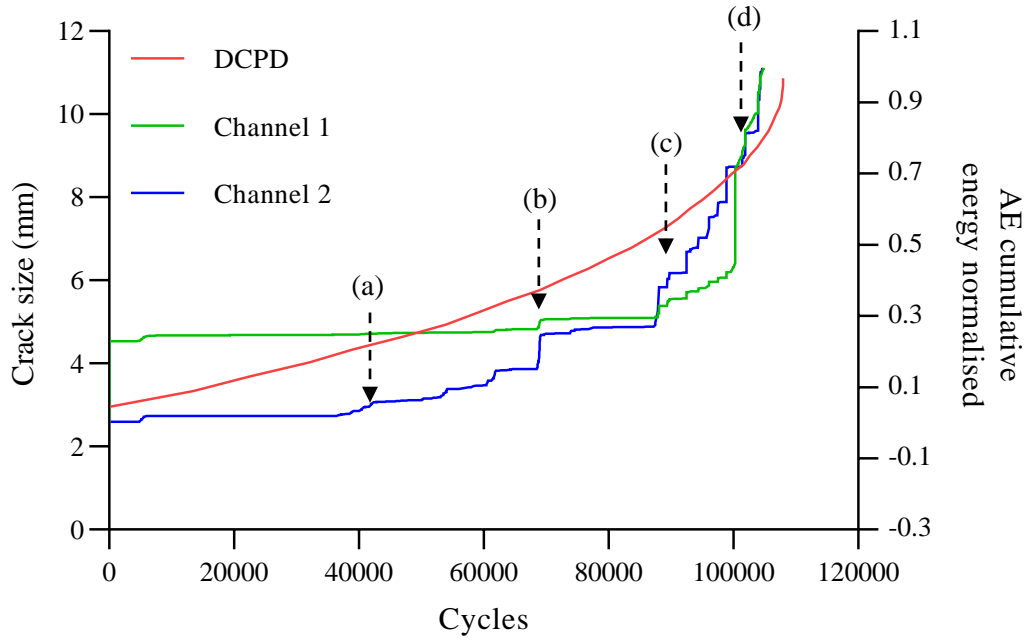


Figure 144. A cumulative AE energy plot from R50α sensors compares to the crack size measured using the DCPD instrument of R260 sample 2. The labelled spikes are identified in Figure 145.
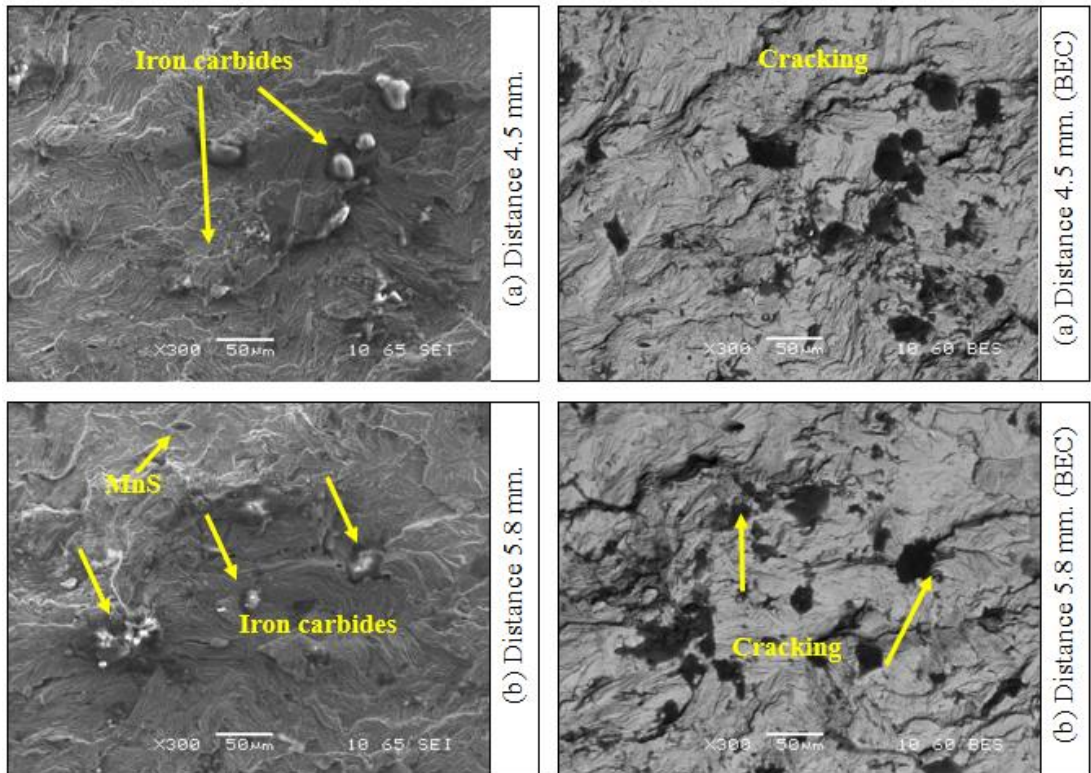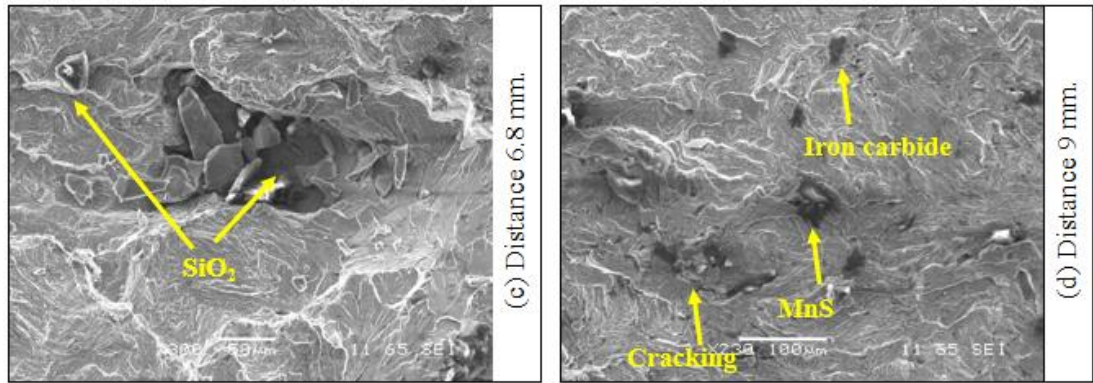
Figure 145. SEM Micrographs showing the fracture surface distance (a) Iron carbide 4.5 mm, (b) Cracking and Iron carbide at a distance of 5.8 mm, (c) Iron carbide and $SiO_2$ at a distance of 6.8 mm, (d) Cracking, MnS, and Iron carbide at a distance of 9 mm.

**R260 Sample 3**
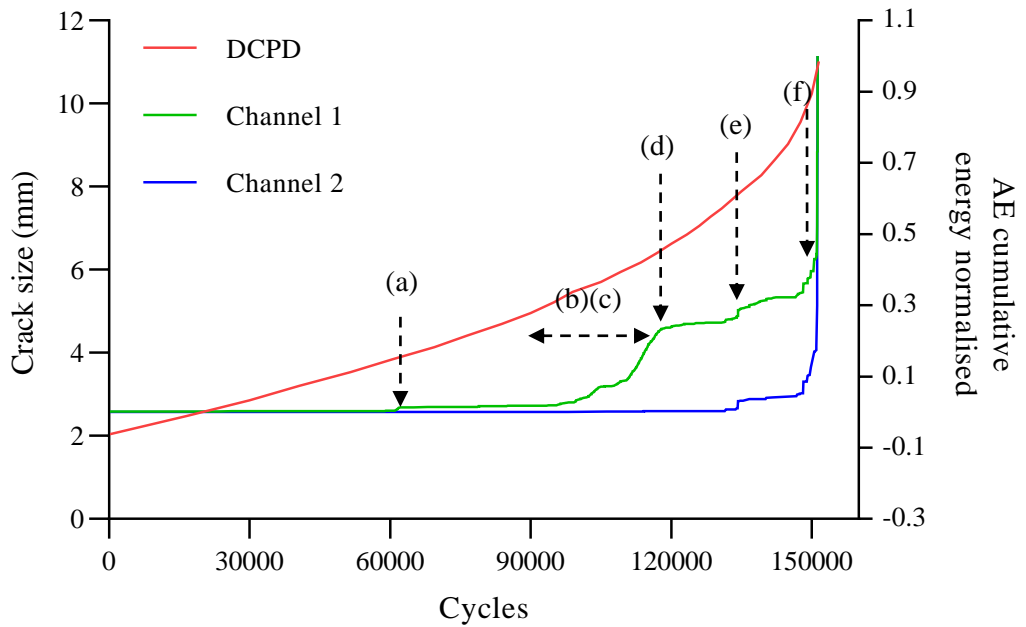


Figure 146. A cumulative AE energy plot from R50α sensors compares to the crack size measured using the DCPD instrument of R260 sample 3. The labelled spikes are identified in Figure 147.
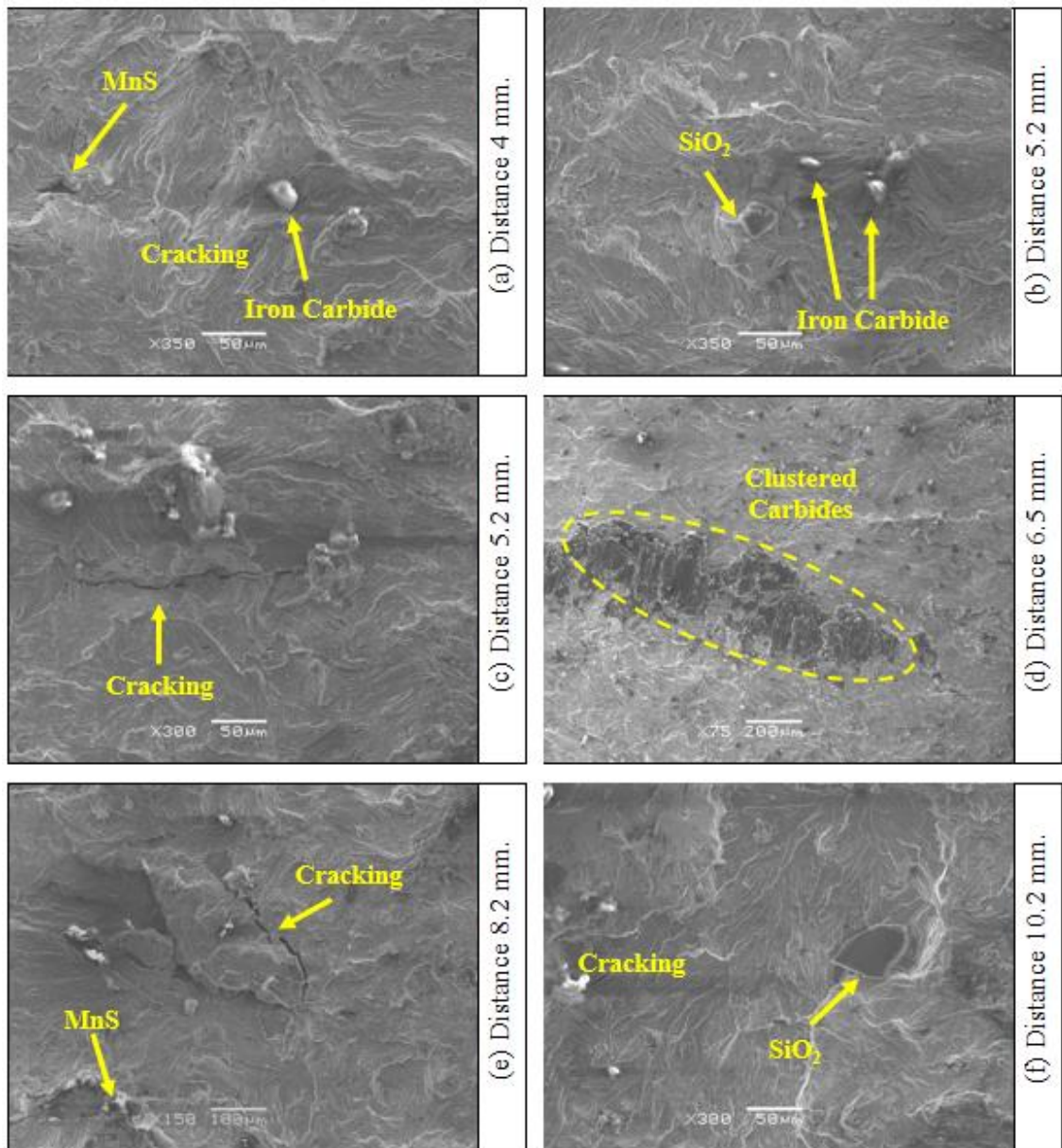
Figure 147. SEM Micrographs showing the fracture surface (a) MnS, SiO$_2$, and cracking defect at a distance 4 mm, (b)(c) Iron carbide and large cracking defect at a distance of 5.2 mm - 6.1 mm, (d) Clustered carbides defect at a distance of 6.5 mm, (e) Cracking and MnS at a distance of 8.2 mm, (f) SiO$_2$, and cracking defect at a distance of 10.2 mm.

**R260 Sample 4**



Figure 148. A cumulative AE energy plot from R50α sensors compares to the crack size measured using the DCPD instrument of R260 sample 4. The labelled spikes are identified in Figure 149.
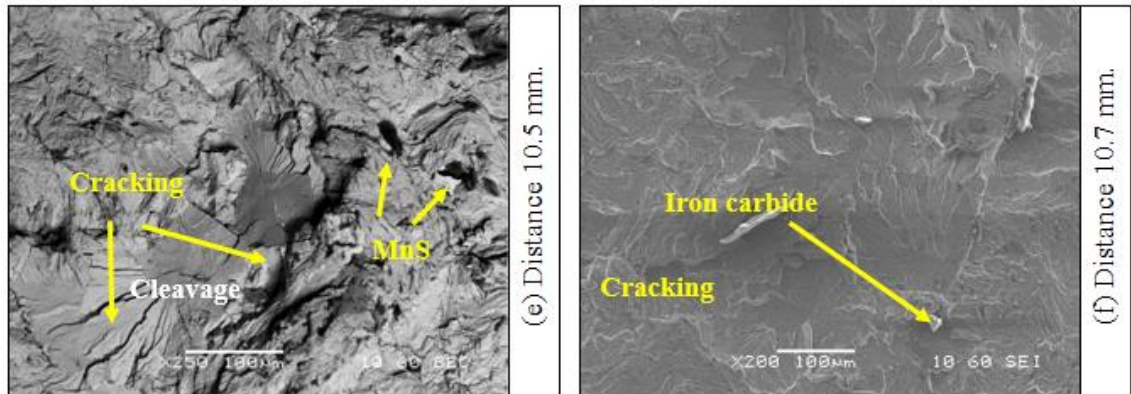
Figure 149. SEM Micrographs showing the fracture surface (a) (b) (c) Cracking, $Al_2O_3$, and Iron carbide at a distance of 3.8 mm - 5.2 mm, (d) Cracking and Iron carbide at a distance of 9.5 mm, (e) Cracking and MnS at 10.5 mm, (f) Iron carbide and cracking at a distance of 10.7 mm.

**R260 Sample 5**



Figure 150. A cumulative AE energy plot from R50α sensors compares to the crack size measured using the DCPD instrument of R260 sample 5. The labelled spikes are identified in Figure 151.
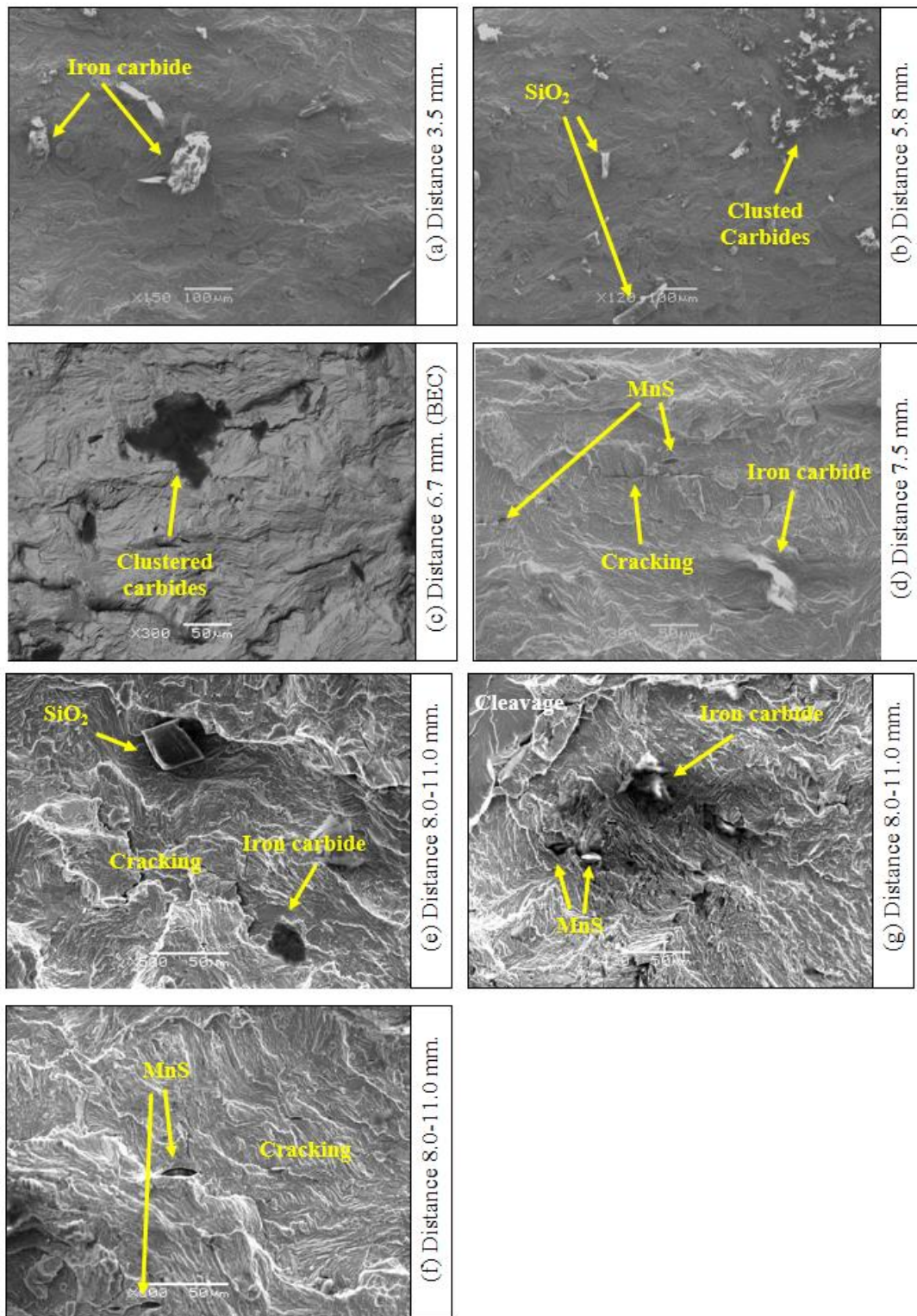
Figure 151. SEM Micrographs show the fracture surface (a) Iron carbides defects at a distance of 3.5 mm, (b) $SiO_2$ and Clustered carbide defects at a distance of 5.8 mm, (c) Clustered carbide defect at a distance of 6.7 mm, (d) Cracking and Iron carbide defects at a distance of 7.5 mm, (e) (f) (g) Cracking, MnS, $SiO_2$, and Iron carbide defects at a distance of 8 mm -11 mm.

**R260 Sample 6**



Figure 152. A cumulative AE energy plot from R50α sensors compares to the crack size measured using the DCPD instrument of R260 sample 6. The labelled spikes are identified in Figure 153.
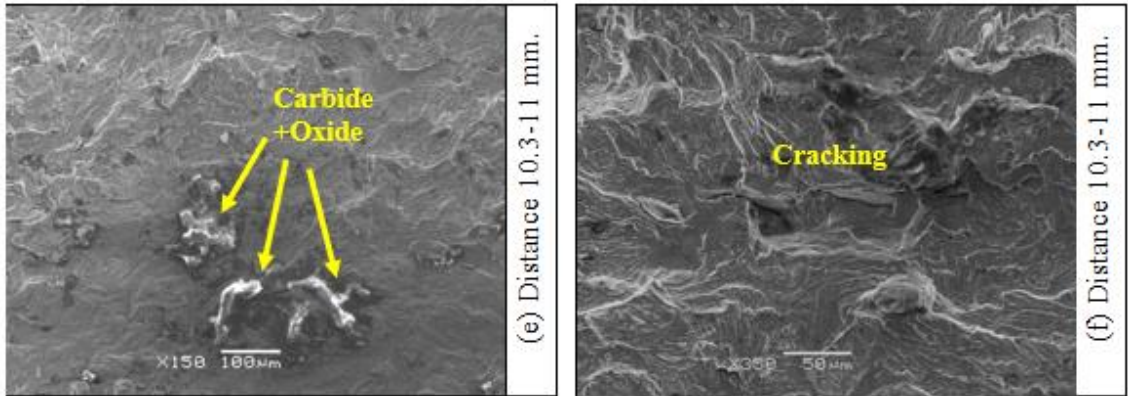
Figure 153. SEM Micrographs show the fracture surface (a) Iron carbide and cracking defects at a distance of 4.5 mm, (b)(c)(d) Cracking, Clustered carbides, $SiO_2$, and MnS defects at a distance of 6.5 mm - 9.0 mm, (e) (f) Cracking, carbide, and oxide defects at a distance of 10.3 mm -11 mm.

**R260 Sample 7**



Figure 154. A cumulative AE energy plot from R50α sensors compares to the crack size measured using the DCPD instrument of R260 sample 7. The labelled spikes are identified in Figure 155.
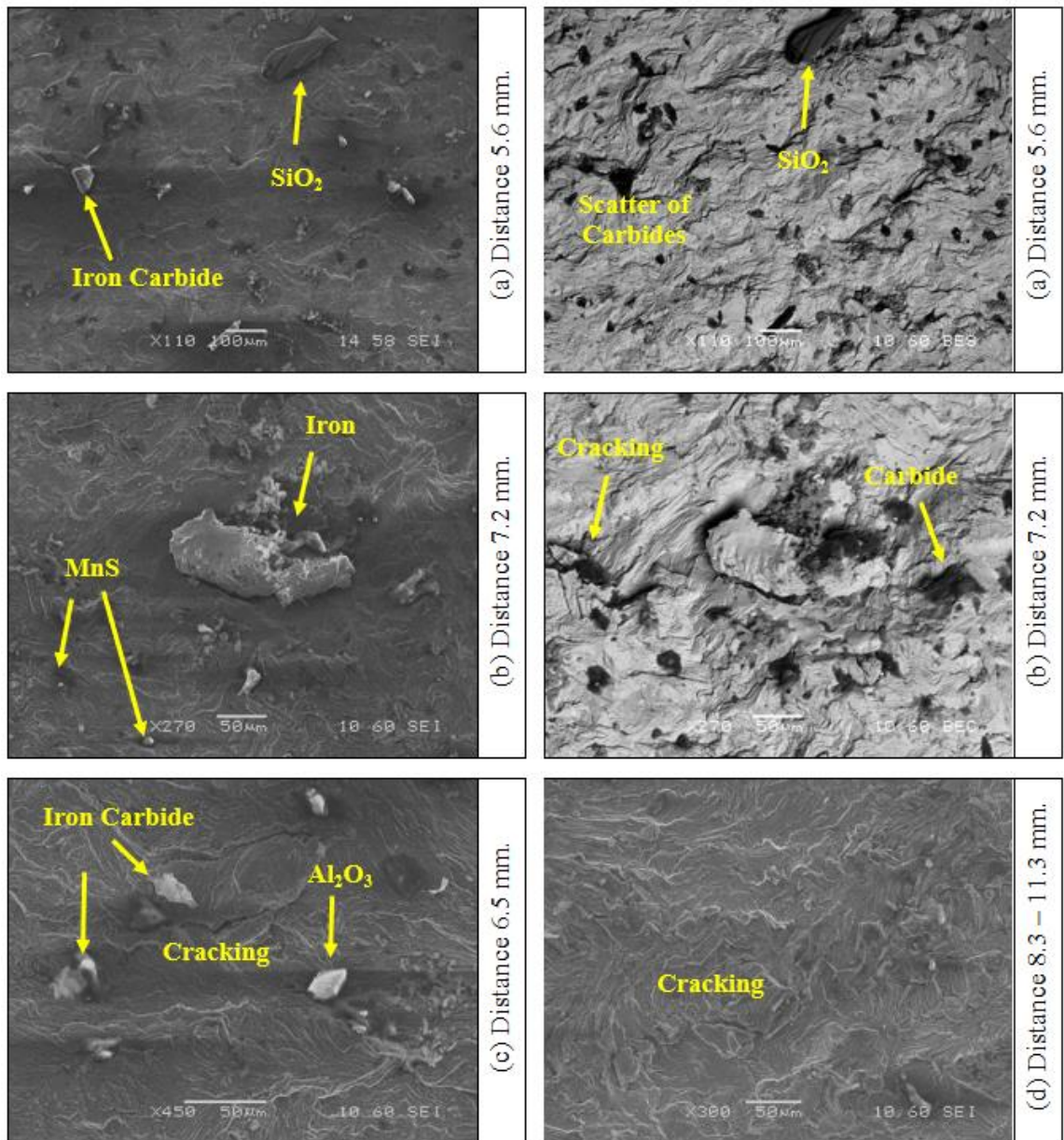
Figure 155. SEM Micrographs are showing the fracture surface (a) Iron carbide, Scatter of carbides and $SiO_2$ defect at a distance of 5.6 mm, (b) Cracking, MnS, and Iron carbide at a distance of 7.2 mm, (c) Cracking, $Al_2O_3$, and Iron carbide at a distance of 6.5 mm, (d) Cracking at a distance of 8.3 mm – 11.3 mm.

Figure 156. A cumulative AE energy plot from R50α sensors compares to the crack size measured using the DCPD instrument of R260 sample 8. The labelled spikes are identified in Figure 157.
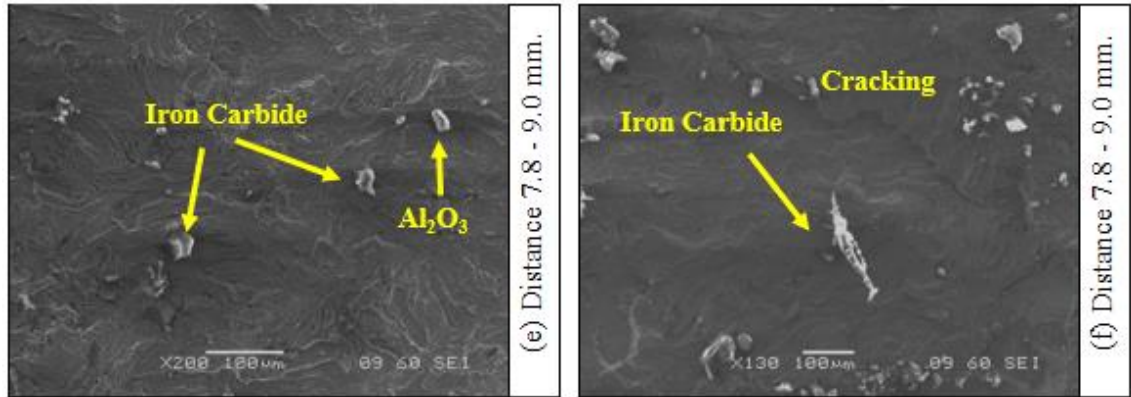
Figure 157. SEM Micrographs show the fracture surface (a) (b) (c) Cracking, $Al_2O_3$, MnS, and carbide at a distance of 6.0 mm- 7.2 mm (d) Cracking, $Al_2O_3$, and Iron carbide at a distance of 7.5 mm, (e) (f) $Al_2O_3$, Cracking and Iron carbide at a distance of 7.8 mm- 9.0 mm.



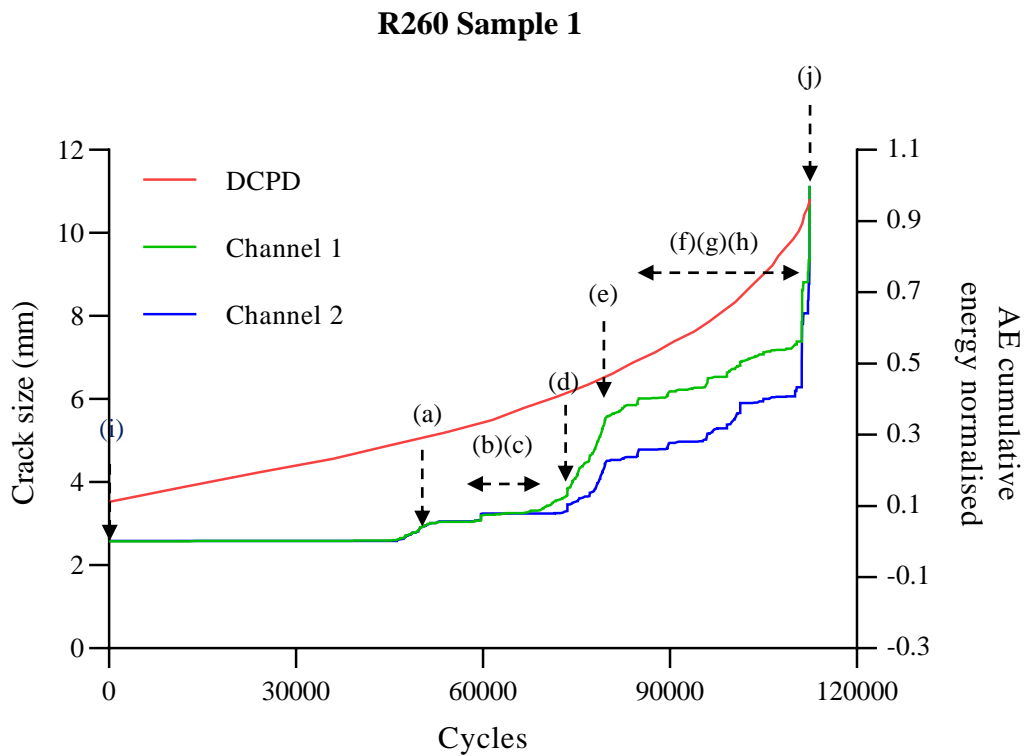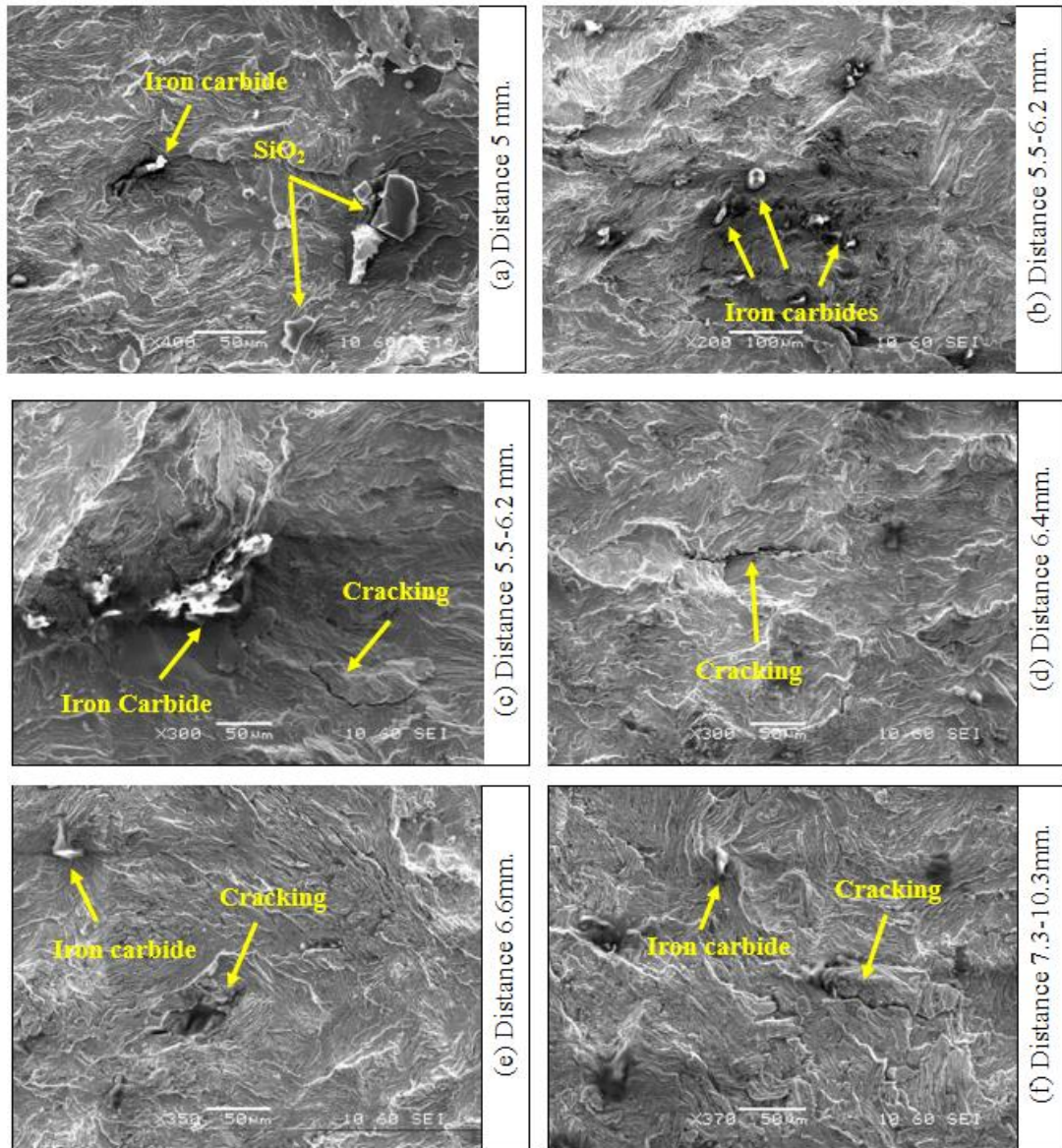Figure 158. A cumulative AE energy plot from R50α sensors compares to the crack size measured using the DCPD instrument of R260 sample 9. The labelled spikes are identified in Figure 159.
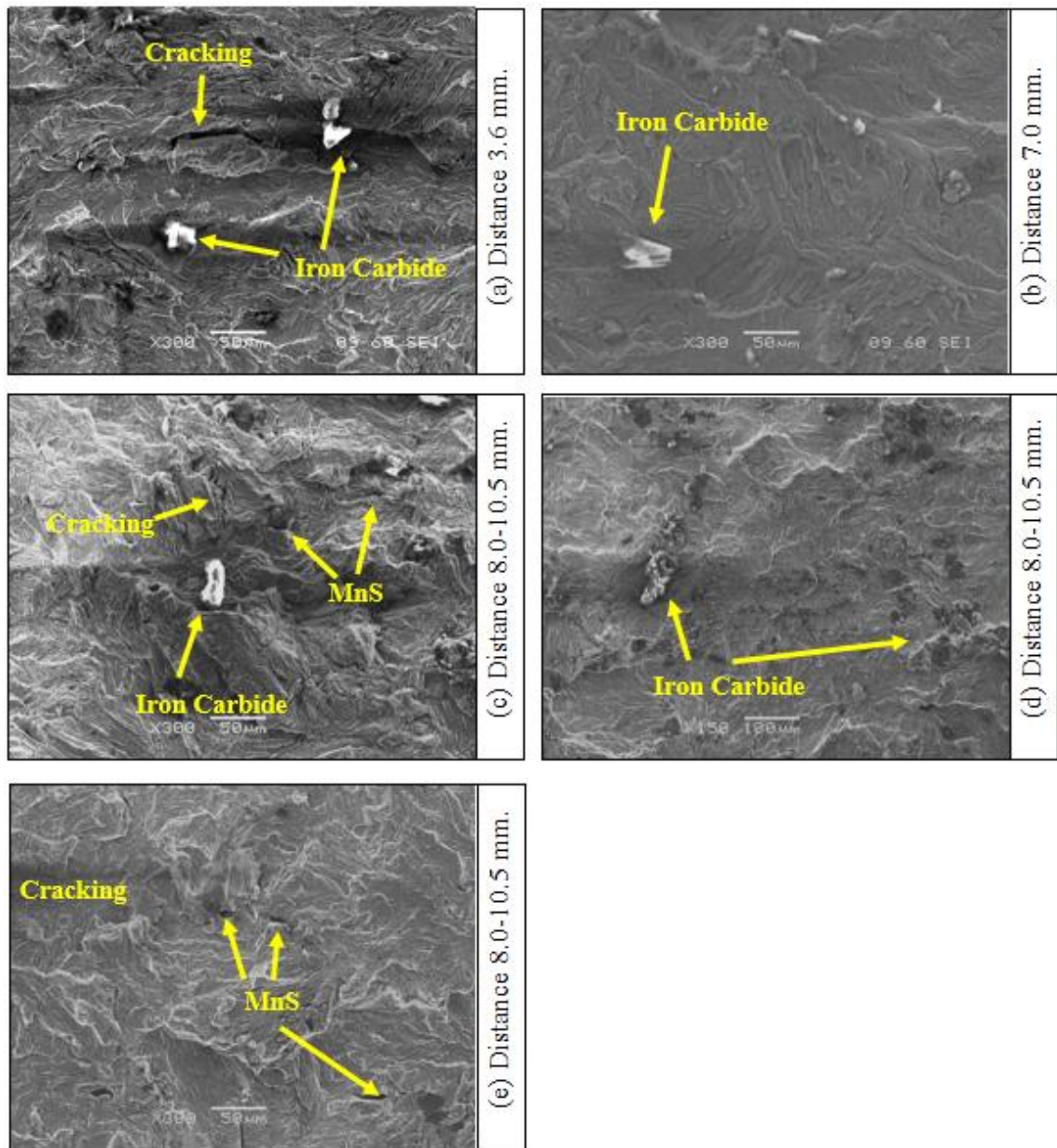
Figure 159. SEM Micrographs show the fracture surface (a) Cracking, Iron carbide at a distance of 3.6 mm (b) Iron carbide at a distance of 7.0 mm, (c) (d) (e) Iron carbide, MnS, and Cracking at a distance of 8.0 mm -10.5 mm.

The data for sample ten are not shown due to sudden overloading at the beginning of the experiment. The accumulated AE energy increases as the crack propagates, as observed to be the case for all samples tested. The crack propagation calculated by DCPD follows a classic exponential curve pattern, and the AE emission increases gradually but

with some abrupt increases. When damage propagates, high-energy AE signals resulting from more significant events trigger these sudden increases. The AE response of both R50a sensors detects the same signals with spikes at the same points in most of the samples. The source of these high-energy burst signals has been characterized using SEM and the AE results obtained. This work has shown that some type of defect, such as inclusion, exists in the sample at that location with any dramatic spike in AE energy captured.

There were three significant types of defects found in R260 (as well as R220): MnS inclusions, iron carbides, and cracks. In R220, many of the MnS inclusions were found to be typically seen as a grouping of minor steps on AE results, while alumina ($Al_2O_3$) inclusions were found on some fracture surfaces [144]. In R260 rail steel, several SEM micrographs reveal regions containing iron carbide within the crack surfaces. These iron carbides were more brittle than the surrounding regions, affected crack growth behaviour, and resulted in the generation of increased AE energy. The MnS inclusions were commonly seen as a category relative to the AE results. It can be seen either as a pattern of small steps or as a slope. SEM micrographs detected cracks at sites where a range of high-energy AE peaks was observed. The growth of these cracks and the fatigue crack that passes through this area would lead to a considerable rise in AE energy. Some studies have indicated that these cracks arise from the inclusions in the sample. Although it was predicted to find inclusions in fatigue surfaces, voids and string-like iron deposits were fascinating. String like iron deposits has been seen mainly on SEM micrographs, attributed to a slight ductility in the fracture surface. This mild ductility was also seen in secondary cracking and the final fracture surface. This has been shown in other studies linked to fatigue crack growth in steel. As the volume fraction of pro-eutectic (PE) ferrite

decreases, it will cease to play a role in crack initiation, and the steel becomes completely pearlitic. MnS inclusions in steel will then act as significant crack initiators. Therefore, R260 rail steel has been used instead of R220 rail steel.

### 7.1.2 Hadfield Manganese Steel

The fracture surfaces of Hadfield manganese steel samples tested were analyzed microscopically after completing the cyclic three-point-bending test using a JEOL 6060 SEM. Figure 160 shows the micrographs of the different regions of the fractured surface of the sample. Fatigue cracks will grow slowly through the fatigue zone. However, as the crack grows, it eventually becomes unstable once it has reached a critical size, eventually causing brittle failure.
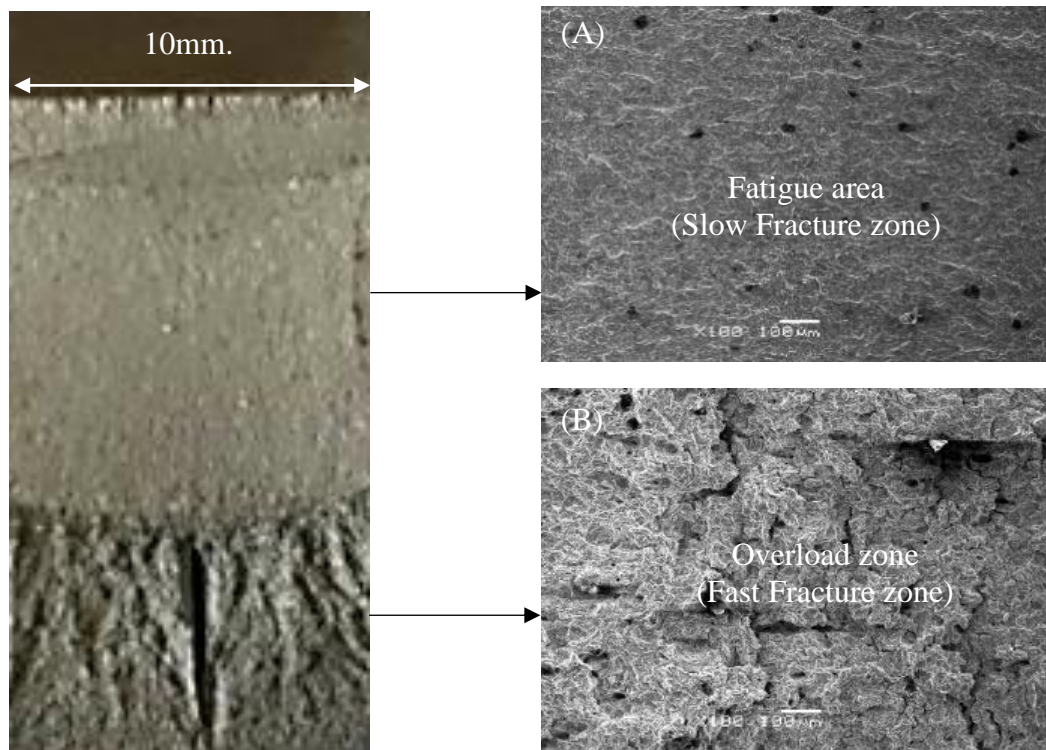


Figure 160. The morphologies of the fatigue crack growth area (A) and the brittle fracture area (B) are shown in a macro view of the fractured surface.

**Hadfield sample 1**
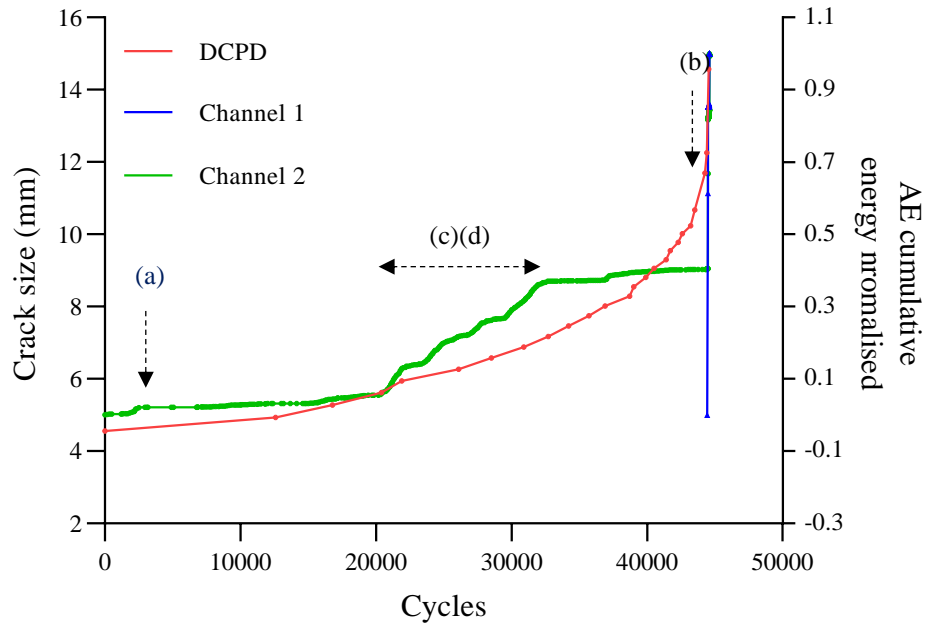
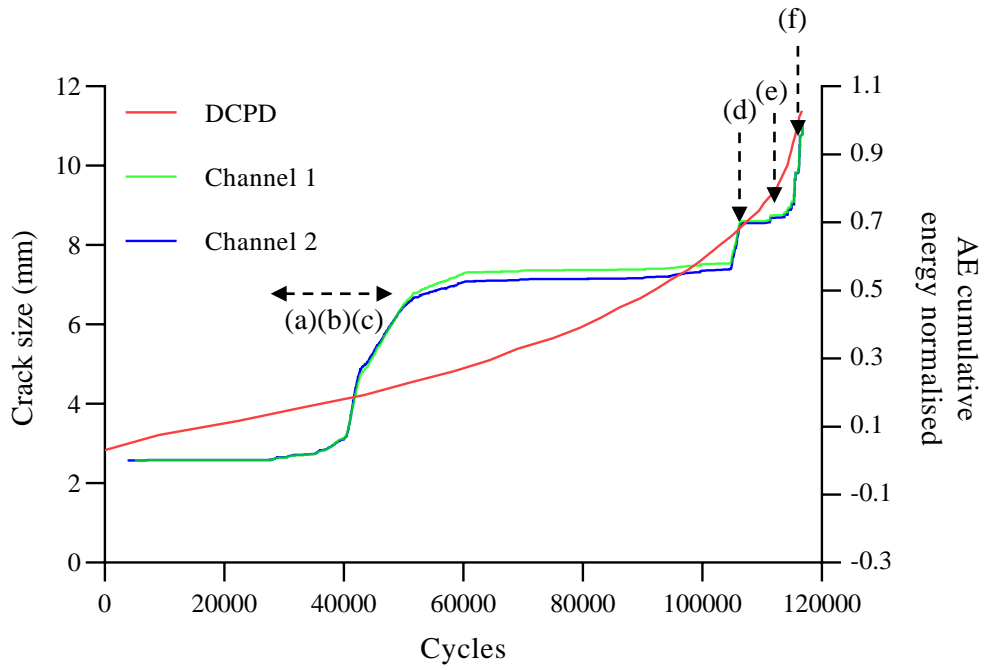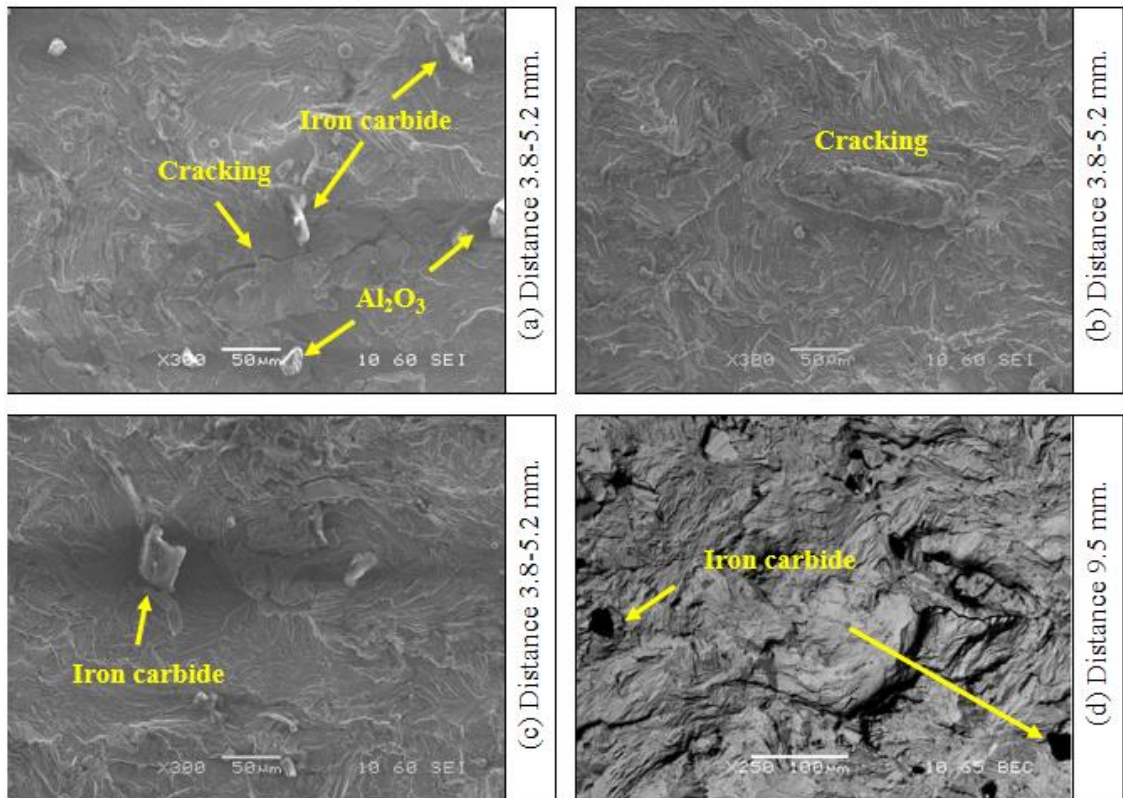

Figure 161. A cumulative AE energy plot from R50α sensors compares to the crack size measured using the DCPD instrument of Hadfield manganese steel sample 1. The labelled spikes are identified in Figure 162.
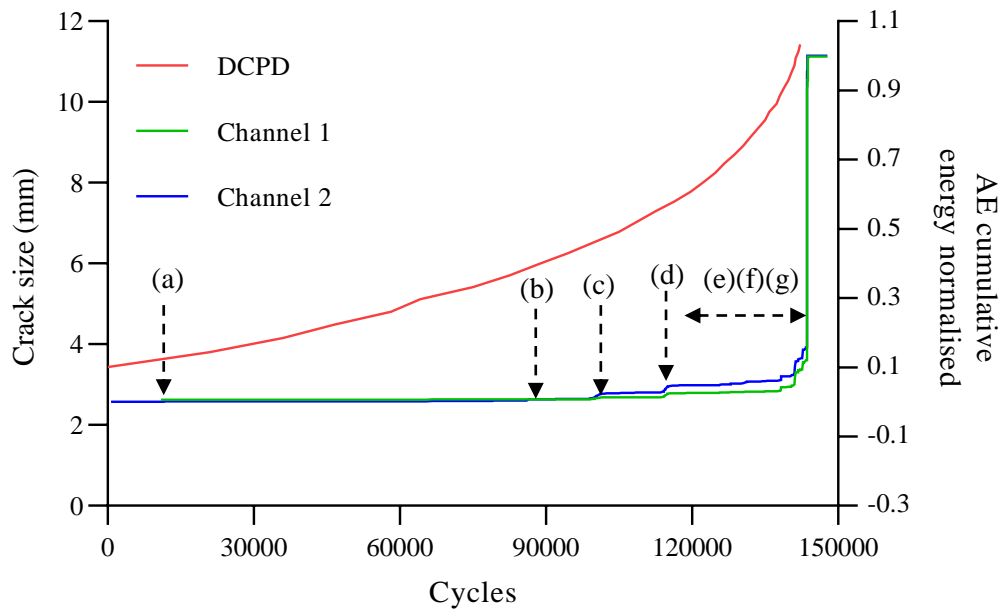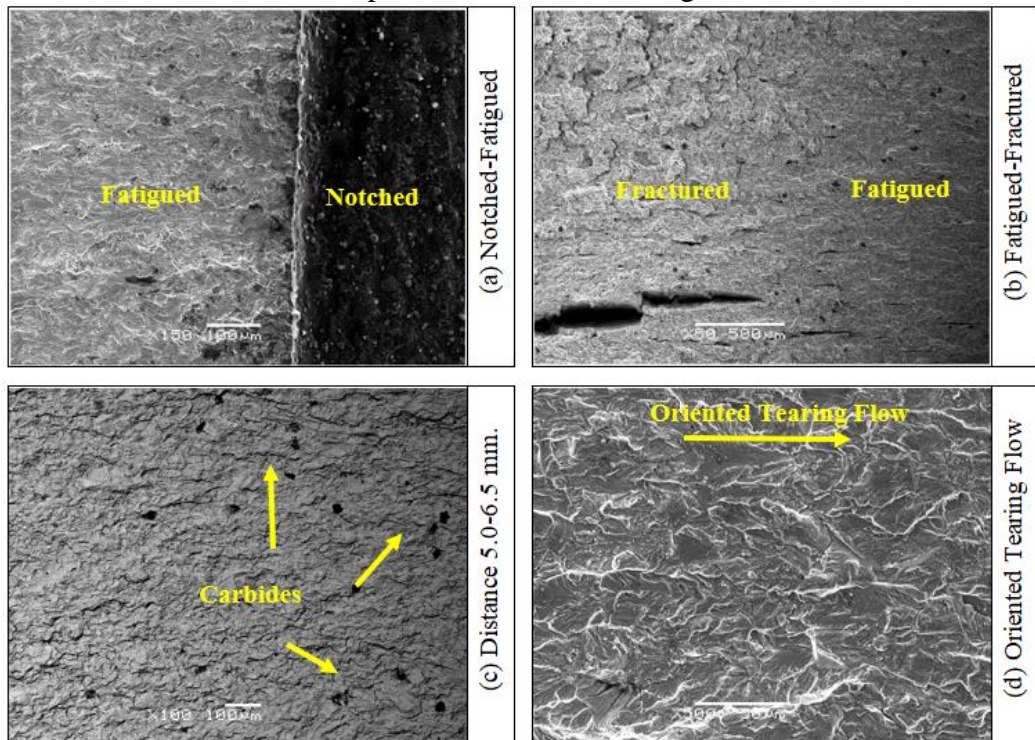


Figure 162. SEM Micrographs show the fracture surface (a) Interface between notched area and fatigued area, (b) Interface between fatigued and fractured areas, (c) Scatter of carbides at a distance of 5.0-6.5 mm. (d) Oriented tearing flow at the middle of fatigue crack propagation.

**Hadfield sample 2**
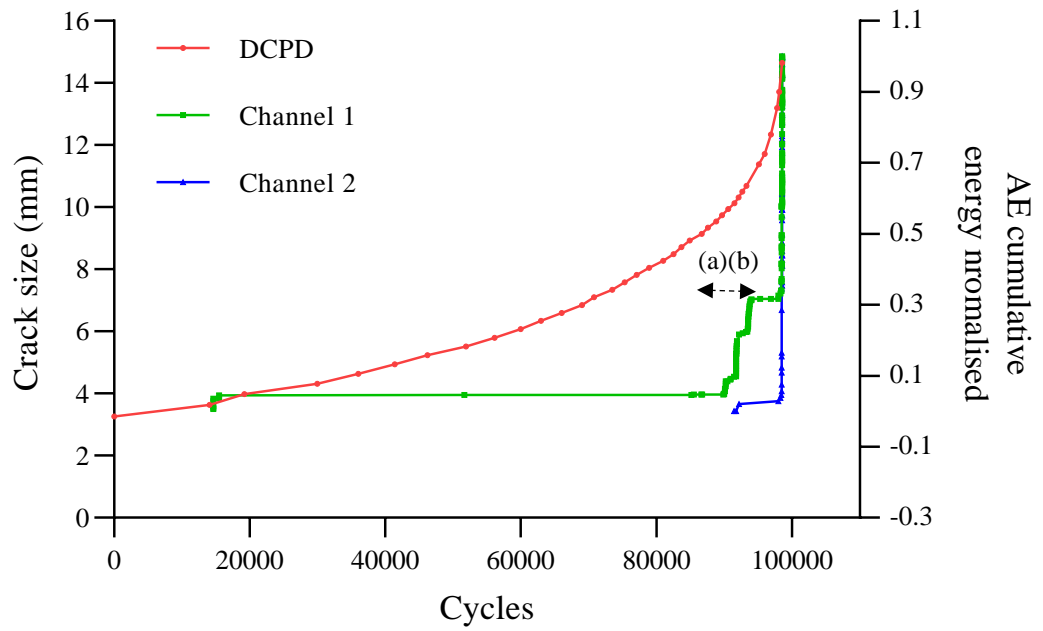


Figure 163. A cumulative AE energy plot from R50α sensors compares to the crack size measured using the DCPD instrument of Hadfield manganese steel sample 2. The labelled spikes are identified in Figure 164.
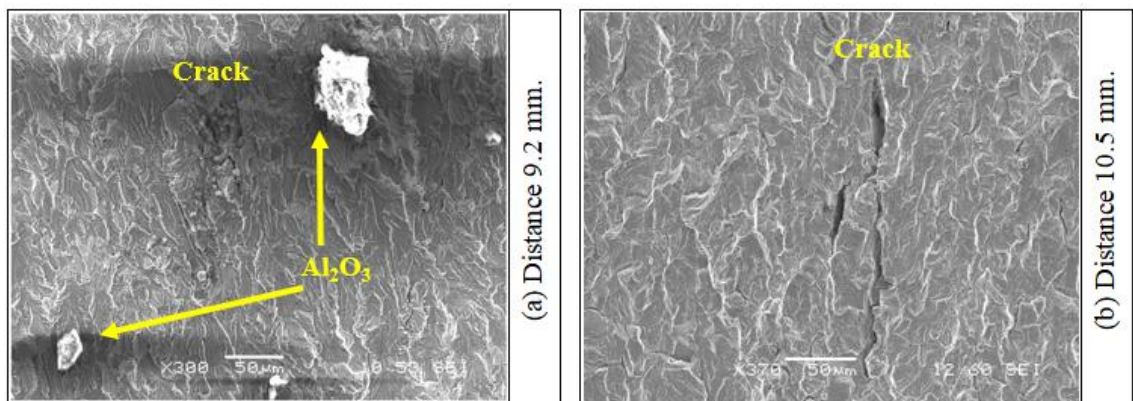


Figure 164. SEM Micrographs show the fracture surface (a) $Al_2O_3$ and crack at a distance of 9.2 mm. (b) Crack at approximately 10.5 mm crack length.

**Hadfield sample 3**
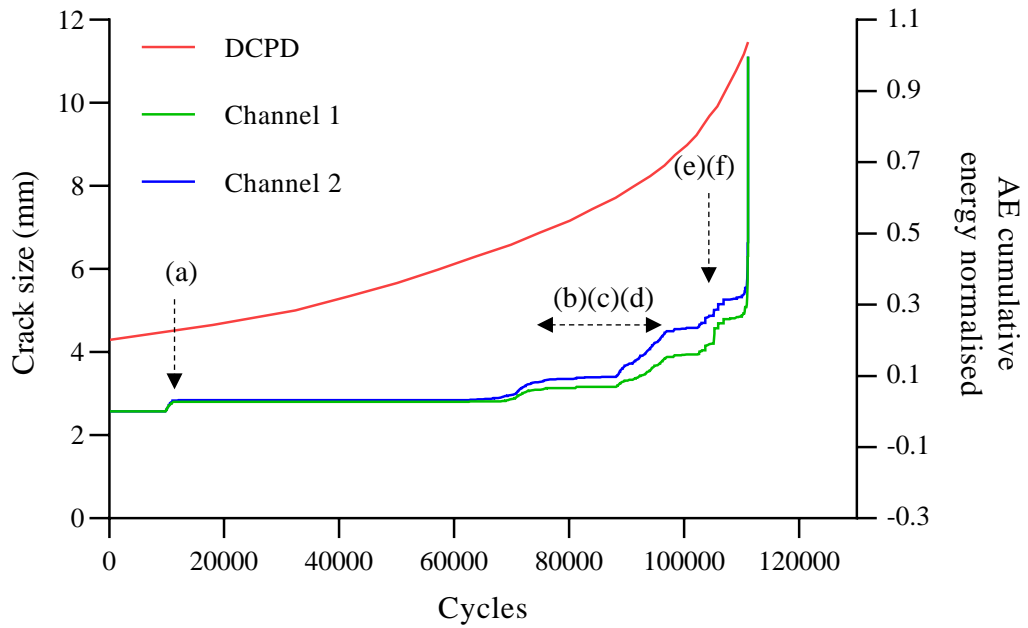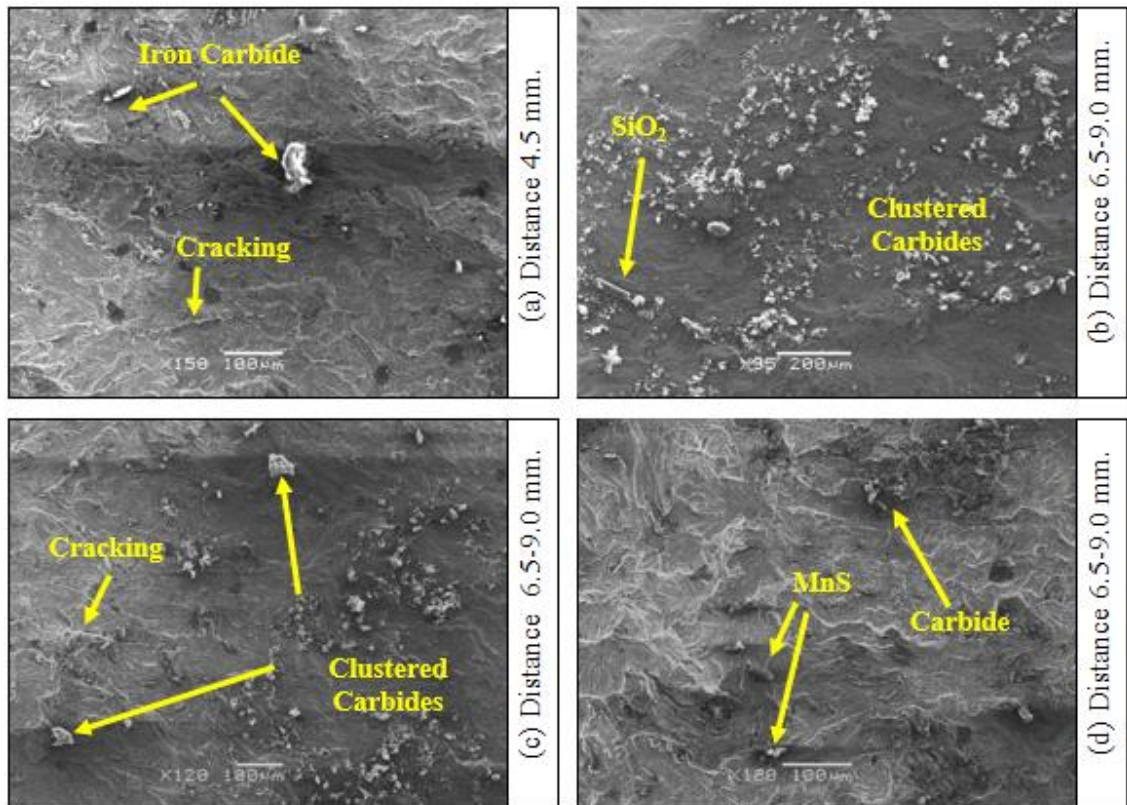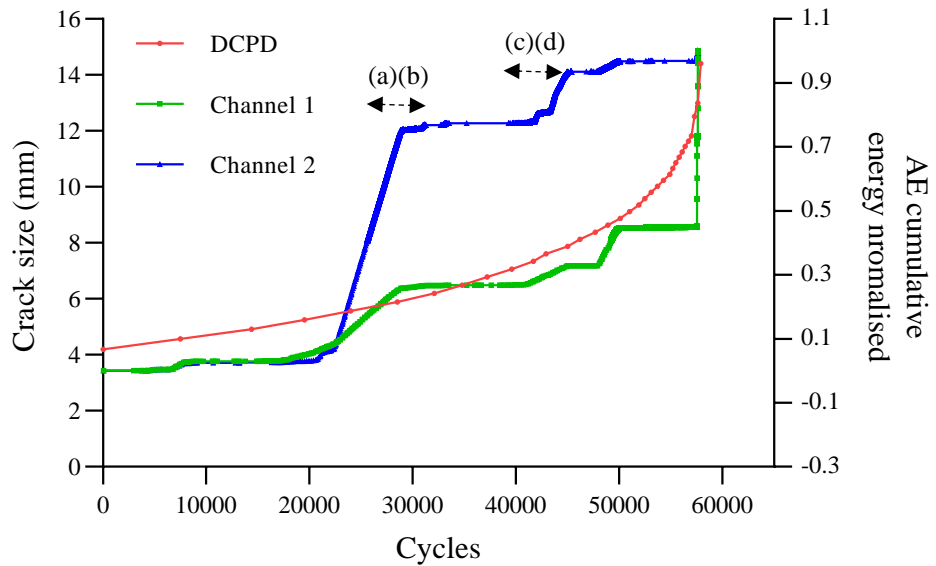


Figure 165. A cumulative AE energy plot from R50α sensors compares to the crack size measured using the DCPD instrument of Hadfield manganese steel sample 3. The labelled spikes are identified in Figure 166.
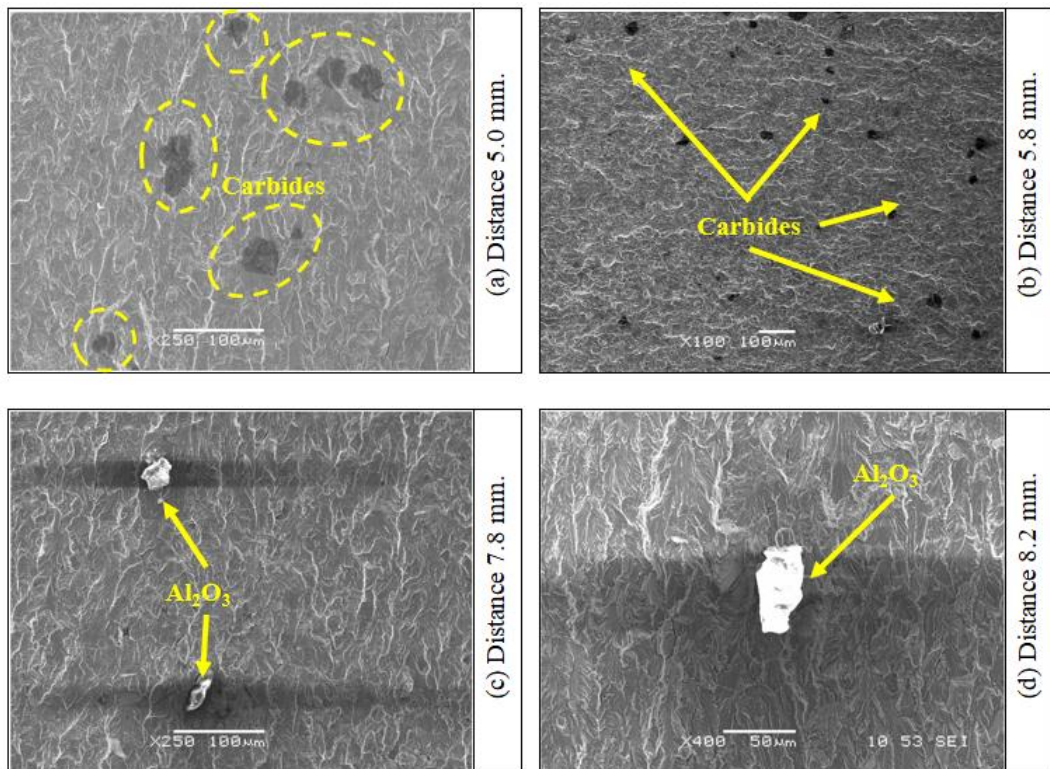


Figure 166. SEM Micrographs show the fracture surface (a) Scatter of carbides at a distance of 5.0 mm. (b) Scatter of carbides at a distance of 5.8 mm, (c)(d) $Al_2O_3$ at a distance of 7.8-8.2 mm.

**Hadfield sample 4**
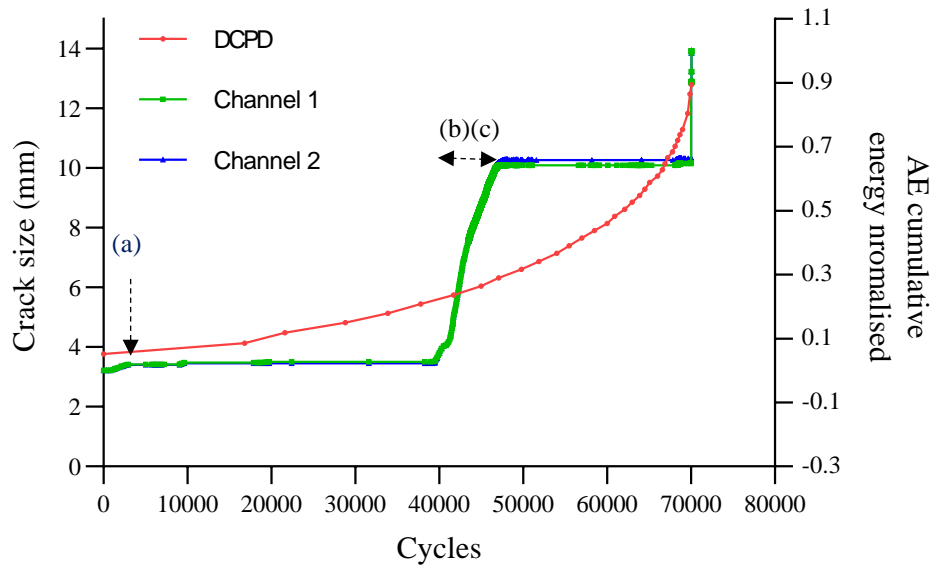


Figure 167. A cumulative AE energy plot from R50α sensors compares to the crack size measured using the DCPD instrument of Hadfield manganese steel sample 4. The labelled spikes are identified in Figure 168.
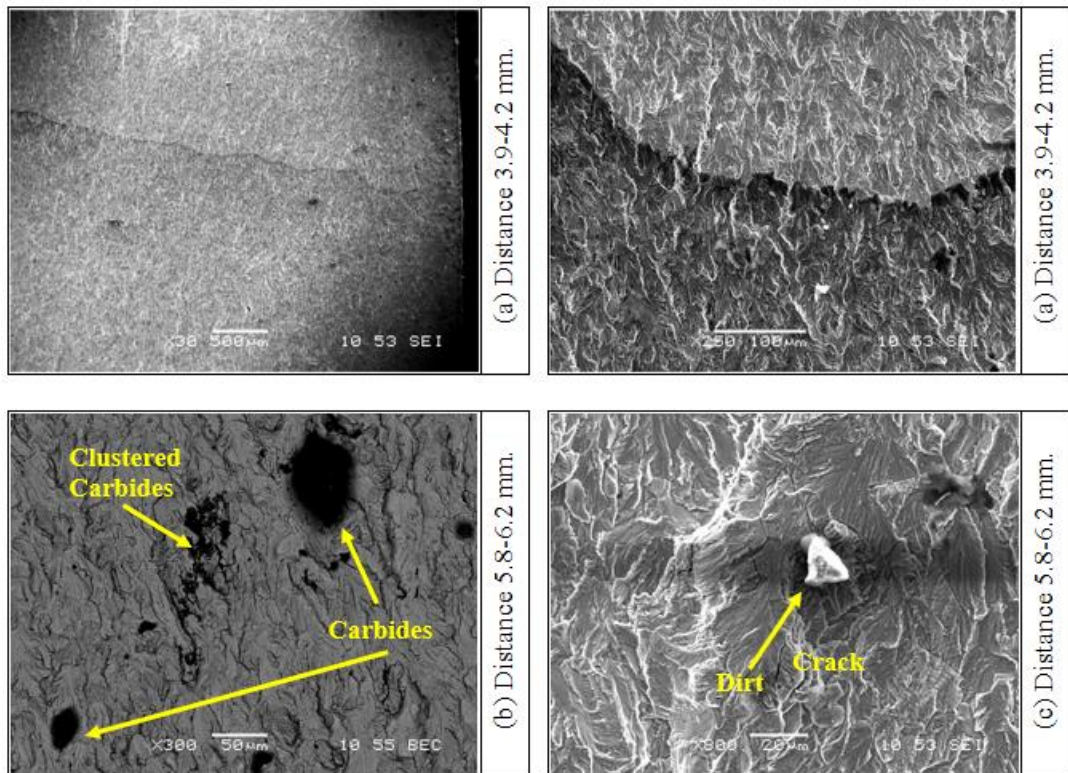


Figure 168. SEM Micrographs show the fracture surface (a)(b) the beginning of the fatigue crack at approximately 3.9-4.2 mm. (c) clustered carbides and carbides at a distance of 5.8-6.2 mm. (d) Crack and dirt at a distance of 5.8-6.2 mm.

**Hadfield sample 6**
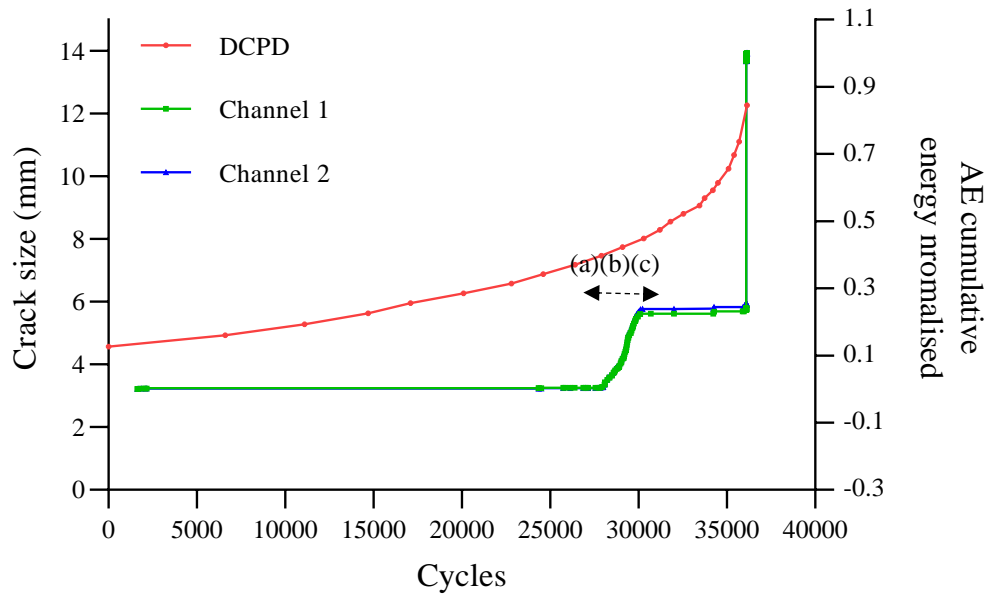


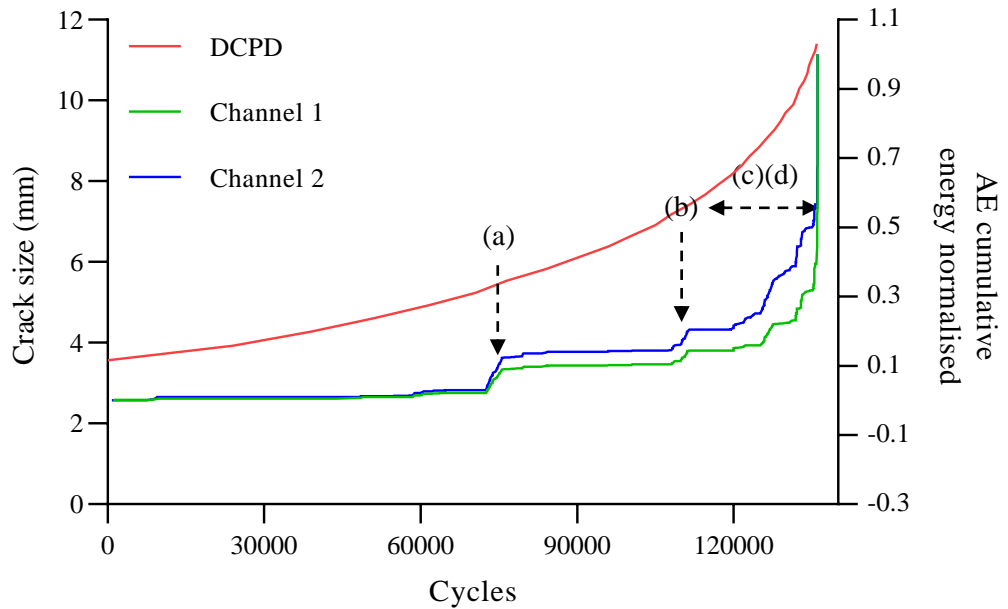Figure 169. A cumulative AE energy plot from R50α sensors compares to the crack size measured using the DCPD instrument of Hadfield manganese steel sample 6. The labelled spikes are identified in Figure 170.
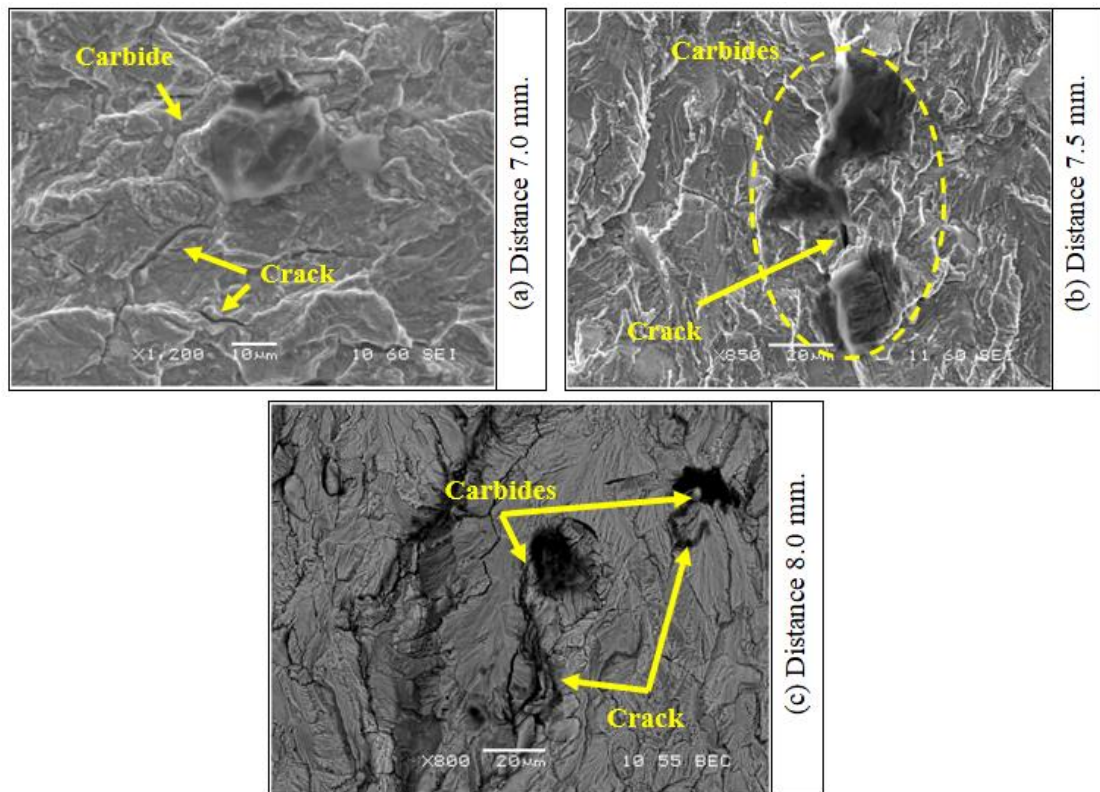


Figure 170. SEM Micrographs show the fracture surface (a) carbide and crack at a distance of 7.0 mm. (b) Carbide, and cracks at a distance of 7.5 mm (c) Carbide, and cracks at a distance of 8.0 mm.

**Hadfield sample 7**
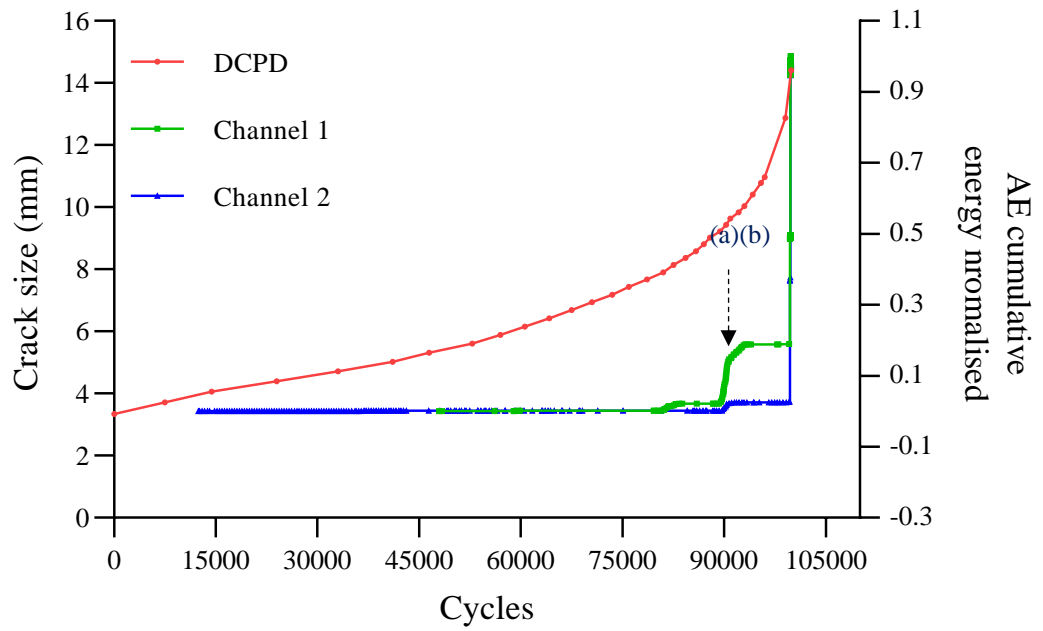


Figure 171. A cumulative AE energy plot from R50α sensors compares to the crack size measured using the DCPD instrument of Hadfield manganese steel sample 7. The labelled spikes are identified in Figure 172.
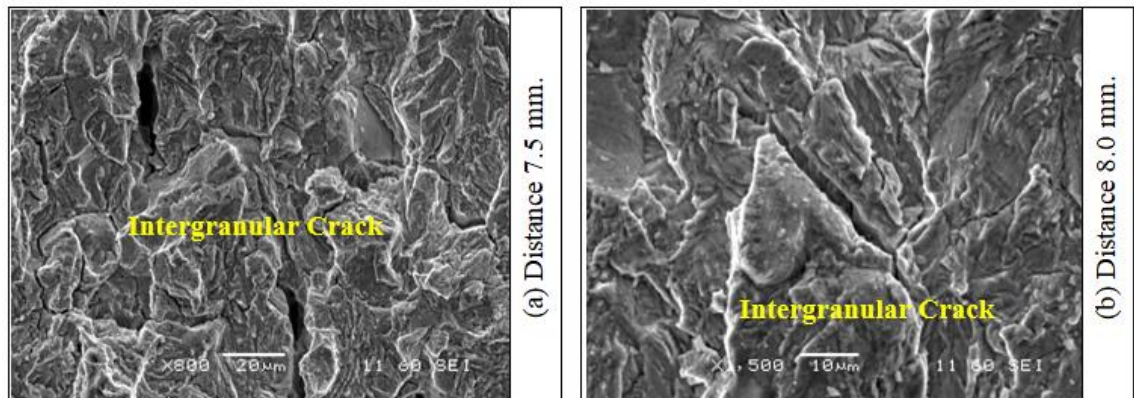


Figure 172. SEM Micrographs show the fracture surface (a)(b) Intergranular crack at approximately 7.5-8.0 mm crack length.

**Hadfield sample 8**
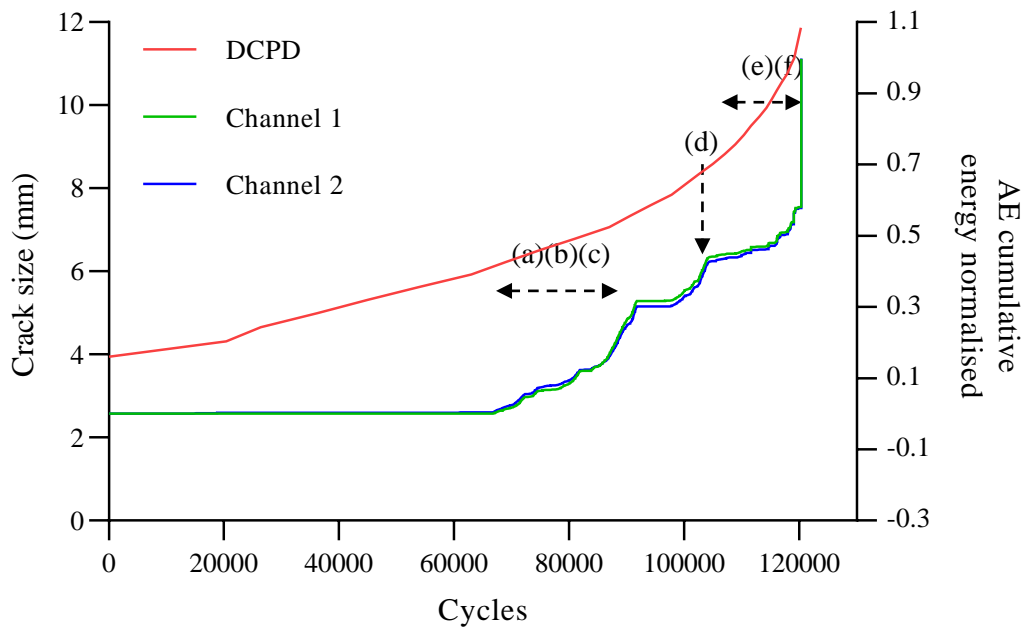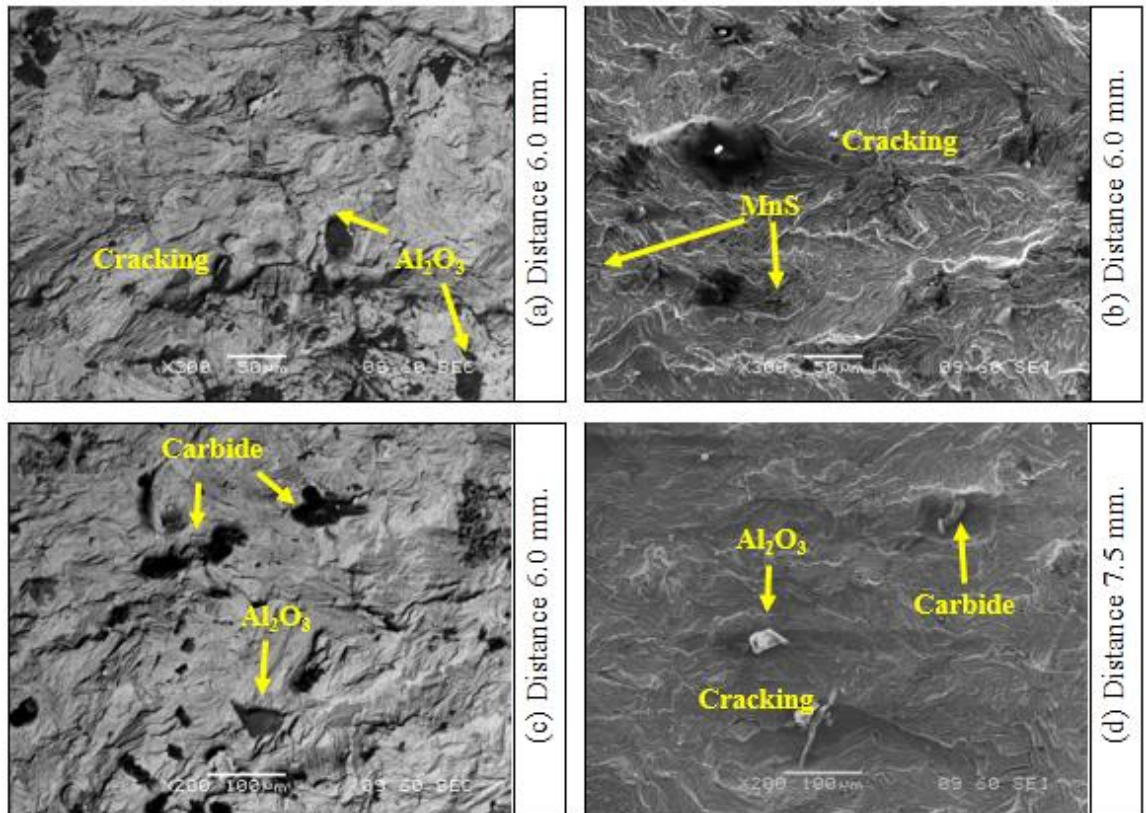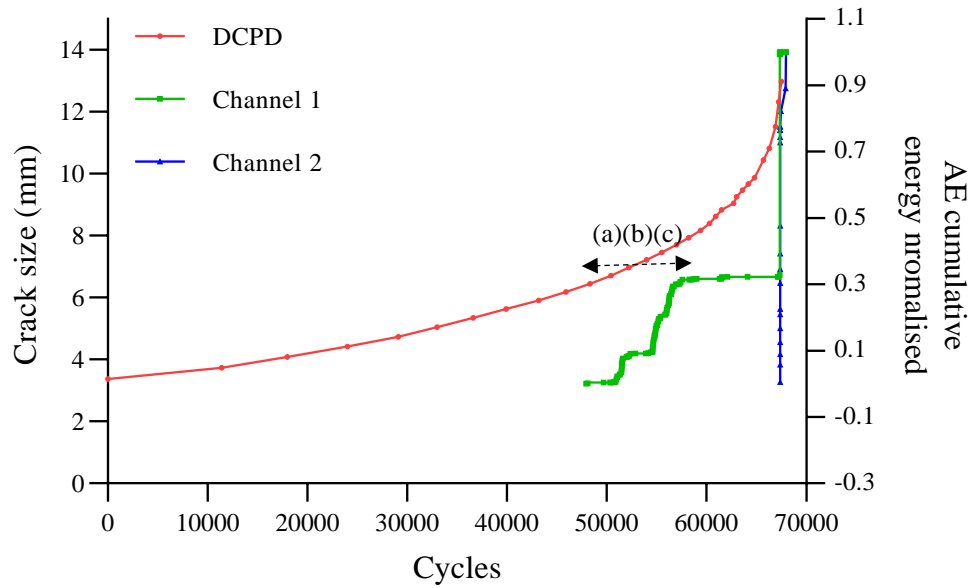


Figure 173. A cumulative AE energy plot from R50α sensors compares to the crack size measured using the DCPD instrument of Hadfield manganese steel sample 8. The labelled spikes are identified in Figure 174.
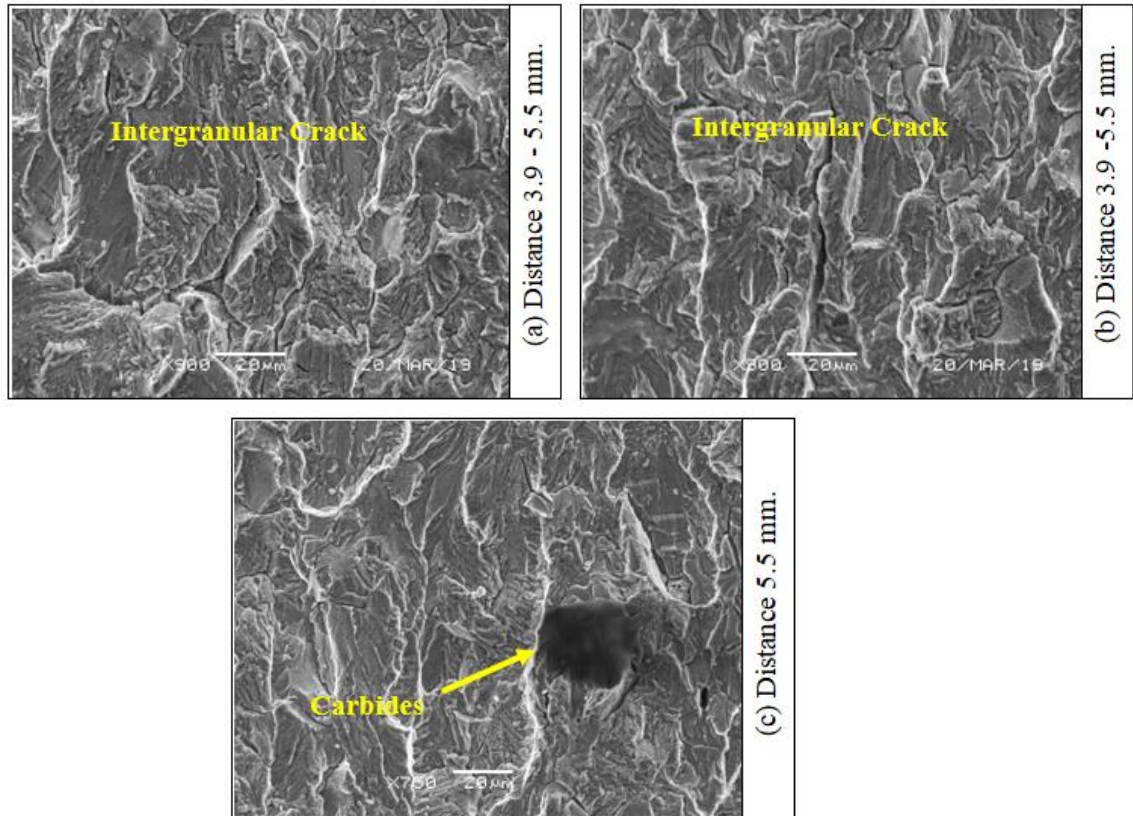


Figure 174. SEM Micrographs showing the fracture surface (a)(b) Intergranular crack at approximately 3.9-5.5 mm crack length, and (c) Iron carbide at a distance of 5.5 mm.

**Hadfield sample 9**
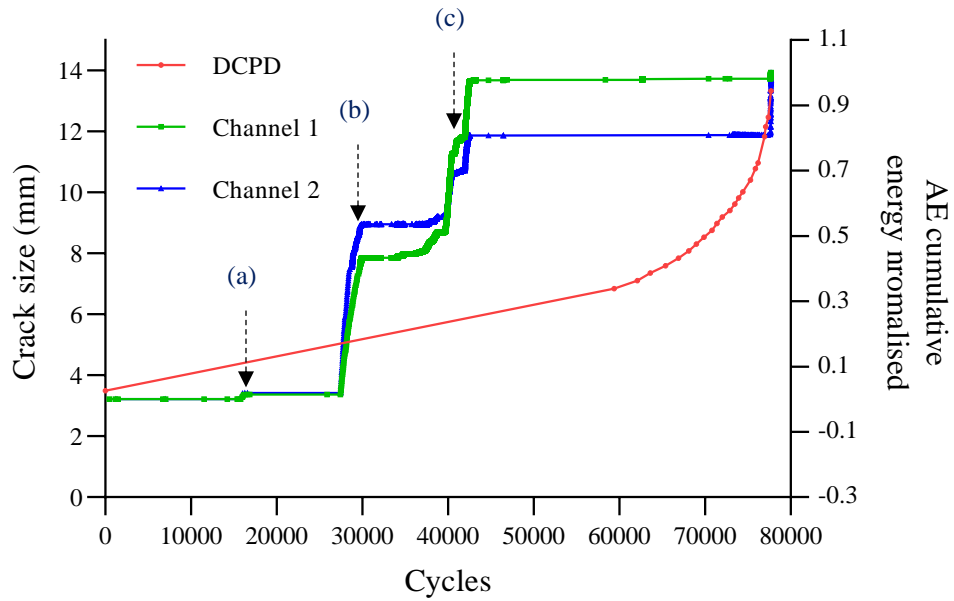
Figure 175. A cumulative AE energy plot from R50α sensors compares to the crack size measured using the DCPD instrument of Hadfield manganese steel sample 9. The labelled spikes are identified in Figure 176.
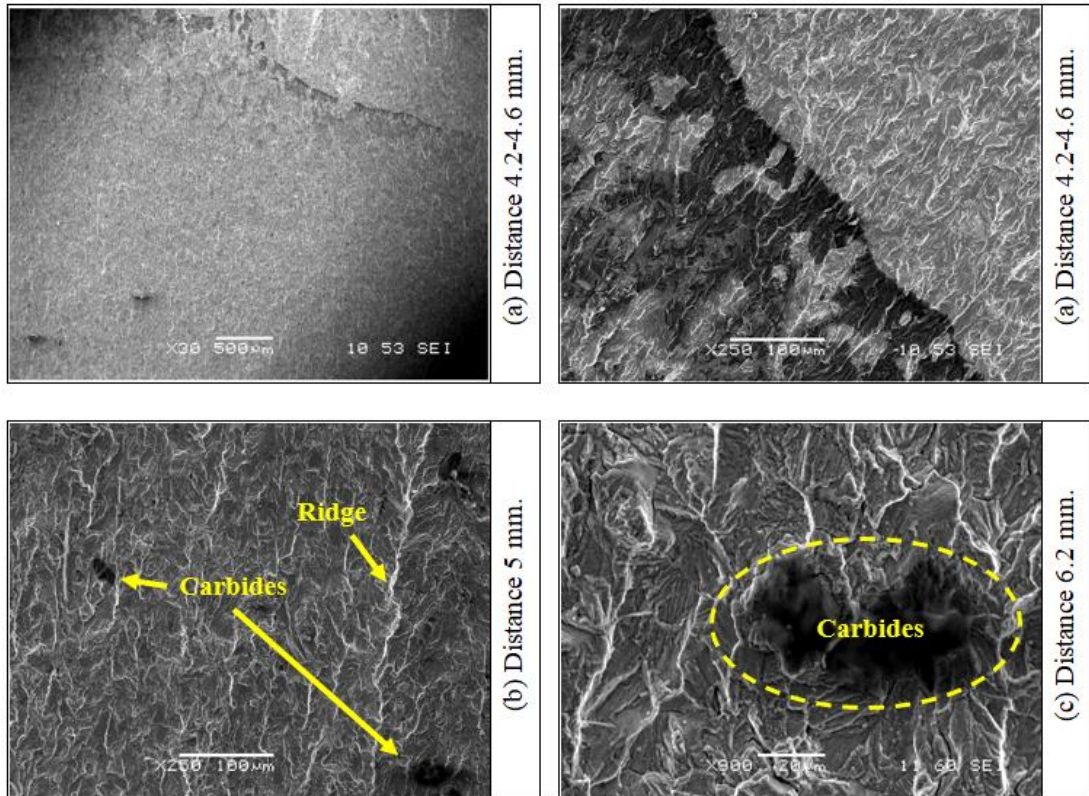


Figure 176. SEM Micrographs showing the fracture surface (a)(b) The beginning of the fatigue crack at a distance of 4.2-4.6 mm. (c)(d) Carbide at a distance of 5 mm. and 6.2 mm.

**Hadfield sample 10**
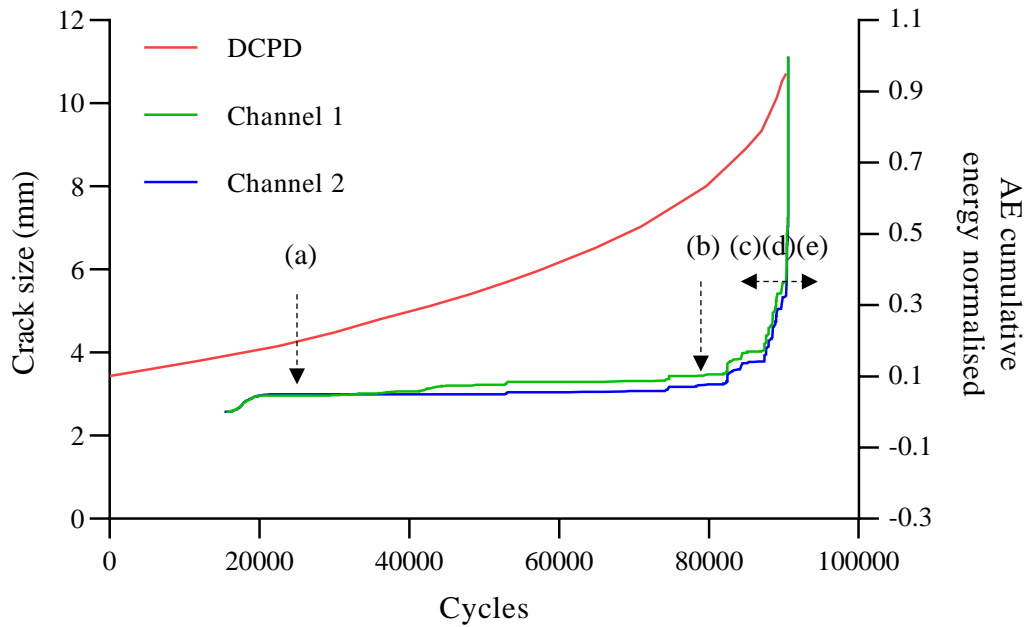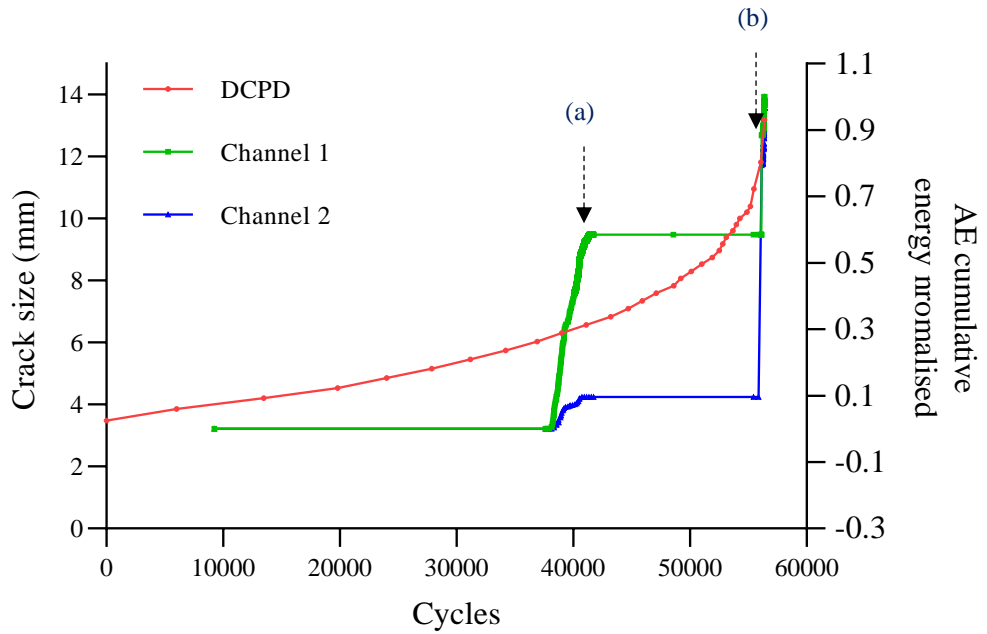


Figure 177. A cumulative AE energy plot from R50α sensors compares to the crack size measured using the DCPD instrument of Hadfield manganese steel sample 10. The labelled spikes are identified in Figure 178.
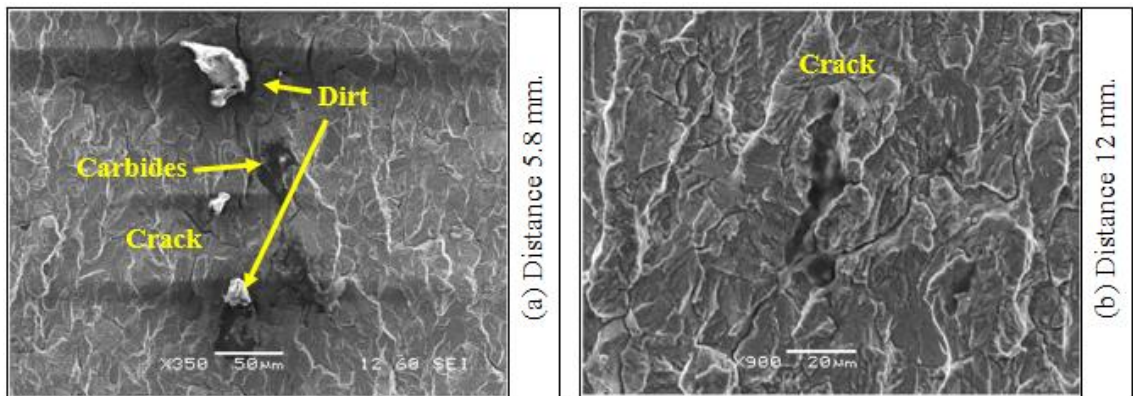


Figure 178. SEM Micrographs show the fracture surface (a) Carbide, dirt, and crack at approximately 5.8 mm (b) Crack at a distance of 12 mm.

Sample 5 failed due to sudden overloading at the beginning of the experiment; hence, it was not included in the results, and for sample 8, a sensor problem arose, so this particular test result was not very accurate. SEM analysis of Hadfield manganese steel fracture surfaces supports the plasticity hypothesis, as mentioned in Chapter 6. The microstructure of the fatigue zone of crack growth in the samples shows a ridge and ductile tearing. This is also characteristic of austenitic manganese steel, which explains why elastic waves do not produce energy. Microstructural evaluation of samples that showed relatively little AE activity before failure, with just a few energy jumps, revealed significant groups of inclusions in the microstructure, which are notably apparent along the crack length correlating to a dramatic rise in accumulated energy. More elastic processes are associated with the relative lack of carbides across the microstructure in samples 1 and 3, indicating that the absence of carbides in the microstructure is associated with more elastic processes. These data lead to the conclusion that carbide distribution is equally as important as carbide presence. High-concentration regions may result in more elastic behaviour as the crack is forced to pass through inclusions, resulting in a brittle fracture. Scattered inclusions may allow more plastic deformation in crack growth, whereas high-concentration regions may result in more elastic behaviour as the crack is forced to pass through inclusions, resulting in a brittle fracture.

Plastic deformation occurs in all cases, resulting in the formation of cracks. When a crack develops, it is more often seen near the surface, where loads are highest. Considering the weakest connection in the microstructures, most cracks are limited to the plastic deformation layer after initiation, a weaker non-twinned grains steel. Various processes can produce AE during plastic deformation, but in twin growth observed in Hadfield manganese steel, the signal strength is negligible. This hypothesis of higher

plasticity is also supported by SEM analysis of Hadfield manganese steel fracture surfaces. The presence of a ridge and ductile tearing can be seen in the microstructure of the fatigue area of crack growth in the samples. This also relates to Hadfield manganese steel, which helps understand why elastic waves emit no energy. Microstructural analysis of samples 4, 6, 9, and 10, which show very little activity only with a few jumps in energy before failure, reveals large groupings of inclusions in the microstructure, which are especially visible at regions along with the crack length corresponding to a rapid increase in accumulated energy. In samples 1 and 3, the relative lack of carbides is associated with more elastic processes, implying that the relative absence of carbides across the microstructure is associated with more elastic processes. One conclusion drawn from these findings is that the carbide distribution is just as significant as its presence. Scattered inclusions may allow more plastic deformation in crack growth, while high-concentration regions may result in more elastic behaviour as the crack is forced to pass through inclusions, resulting in a brittle fracture.

## 7.3 NON-METALLIC INCLUSION ANALYSIS

The accumulated AE energy increases as the crack propagate, as observed for all samples tested in sections 7.1 and 7.2. Cracks caused it either along the grain boundary or through the grain. This is often related to the type and nature of inclusions in the matrix. This section describes the expansion of knowledge in an in-depth study into each non-metallic inclusion and its effect on crack propagation in samples.

### 7.3.1   R260 Rail Steel Inclusion Analysis

Fatigue cracks that occur in the rail tracks often originate from inclusions. Therefore, it can be confirmed that inclusions play a key part in the mechanism of fatigue. As a result, it is critical to explain the various inclusions found in railway steels, classified

by composition and shape. MnS, $Al_2O_3$, and $SiO_2$ are the most common inclusions in nature of R260 rail steels. MnS inclusions were elongated, while aluminium inclusions remained small and spherical. MnS inclusions, particularly ductile compared to $SiO_2$ and $Al_2O_3$, are most associated with large inclusion deformation [175-176].



| Element | Spectrum 1 (Weight %) | Spectrum 2 (Weight %) |
|---|---|---|
| C | 34.30 | 30.86 |
| S | 22.13 | 26.16 |
| O | 4.55 | 4.32 |
| Mn | 37.47 | 34.87 |
| Fe | 1.55 | 3.79 |
| Totals | 100.00 | 100.00 |
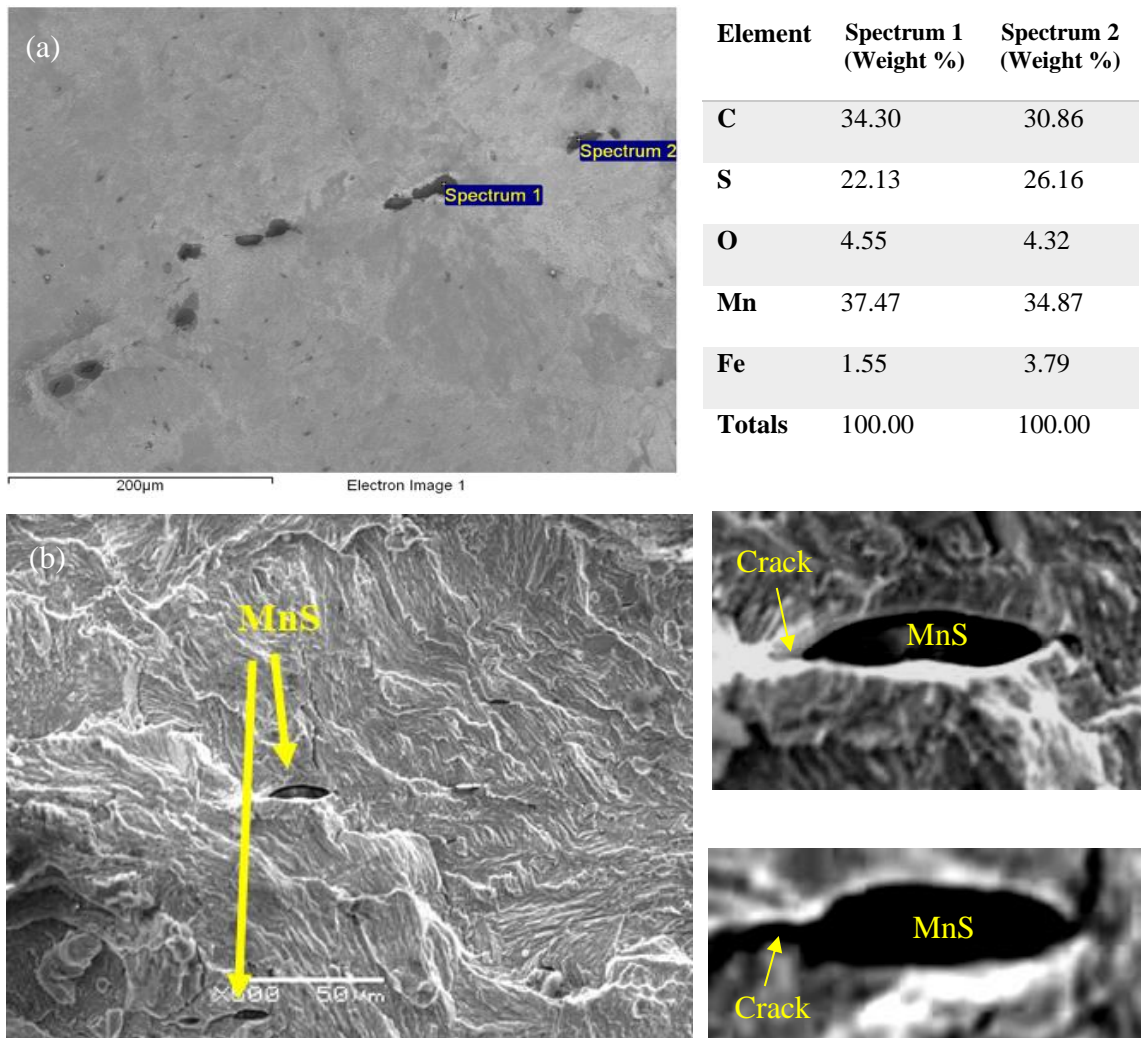
Figure 179. SEM micrographs of R260 samples showing (a) MnS inclusions observed from the polished surface and (b) MnS inclusion observed from the fractured surface.

Debonding is visible at the matrix-elongated inclusion interface (Figure 64). As the interface separates, along with the inclusion, a crack develops, increasing the stress concentration ahead of the inclusion. If the crack is subjected to further fatigue loading, it can propagate into the matrix. One of the inclusions is a stringer form composed mainly

of a white component of Aluminum oxide ($Al_2O_3$), and also another type of angular inclusion was detected to have only silicon (Si) peak. It seems to be possible that this inclusion is pure Silicon oxide ($SiO_2$). Within several fracture surfaces, $Al_2O_3$ and $SiO_2$ inclusions were detected. This was not present in a group like MnS inclusions and was more significant in size.
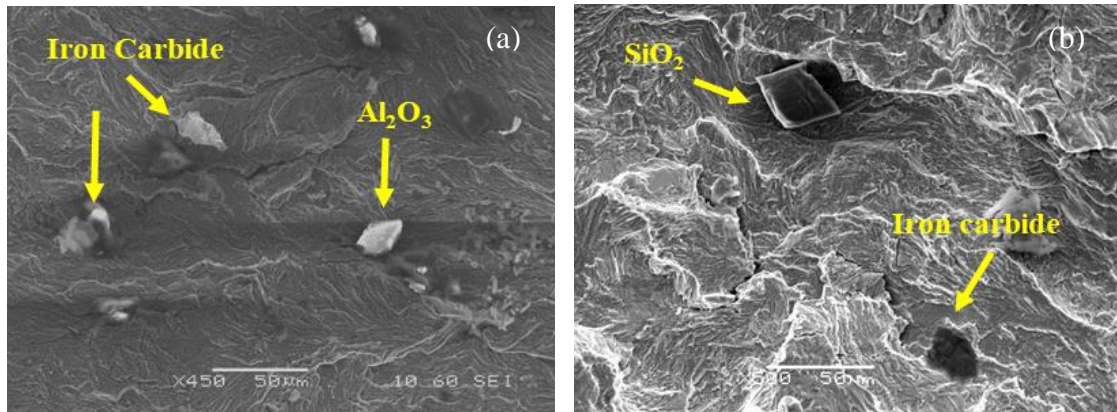


Figure 180. SEM micrographs of R260 samples showing (a) $Al_2O_3$ (small and circular shape), (b) $SiO_2$ (hard angular).

Iron carbide regions can be seen within the crack surfaces in several SEM micrographs (Figure 181). These iron carbides became more brittle than the surrounding area, altering crack growth behaviour and increasing the amount of AE energy captured.
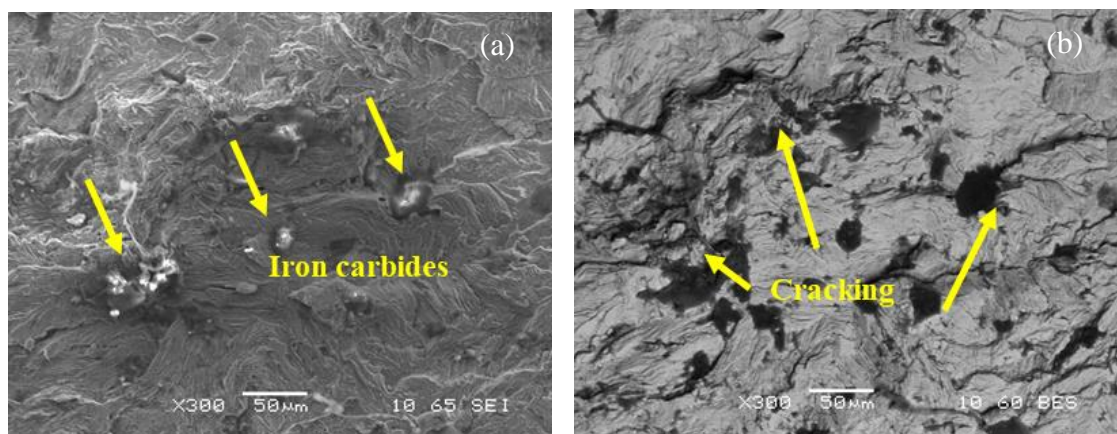


Figure 181. SEM micrographs of R260 samples show (a) Iron Carbide inclusions that are cracked under inclusion when using BEC mode (b).

The rapid growth spikes observed by AE monitoring around these flaws are significant, ranging from 300 to 600 µm, providing a significant signal when none can be

seen on the DCPD. Other usually applied detection techniques are unable to identify fracture propagation at this level. If a flaw could have been identified at this level, the National Rail tragedy may have been eliminated.

### 7.3.2 Hadfield Manganese Steel Inclusion Analysis

Both iron and manganese carbides are recognised as common defects in mechanical properties. However, Ductile MnS inclusions, which have been shown to impair AE characteristics in plain rail steel R220 rail steel and R260 rail steel, were not found in the sign of the tested sample of significant sulphur content in EDS.

The flat facets at the angles of each grain crystal are seen at high magnification in brittle fractures when the intergranular fracture is the crack propagation mechanism (Figure 183). As a result, the grain forms and sizes along the fracture path are easily visible.
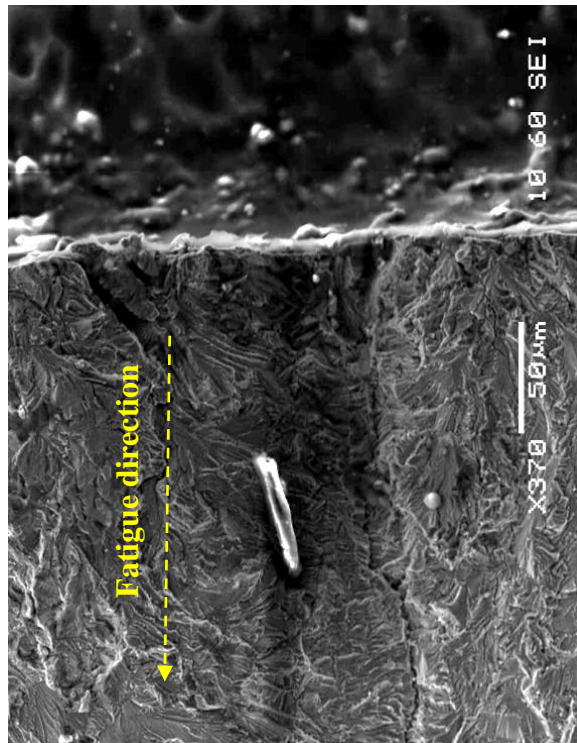


Figure 182. The fatigue cracks grow along grain boundaries.

Microcrack initiation driven by the accumulation of plastic deformation inside the grain, the coalescence of cracks within the grain, and the rapid propagation of cracks across grain boundaries and fractures is the crack initiation and propagation process steps. Intergranular propagation at the second phase interface, crack propagation mechanisms include transgranular propagation at dislocation pile-up sites and propagation at re-nucleated crack tips. The initial fracture originates at the dense twin's site and propagates mostly parallel to the tensile axis, deflecting often related to grain and twin boundaries [156].
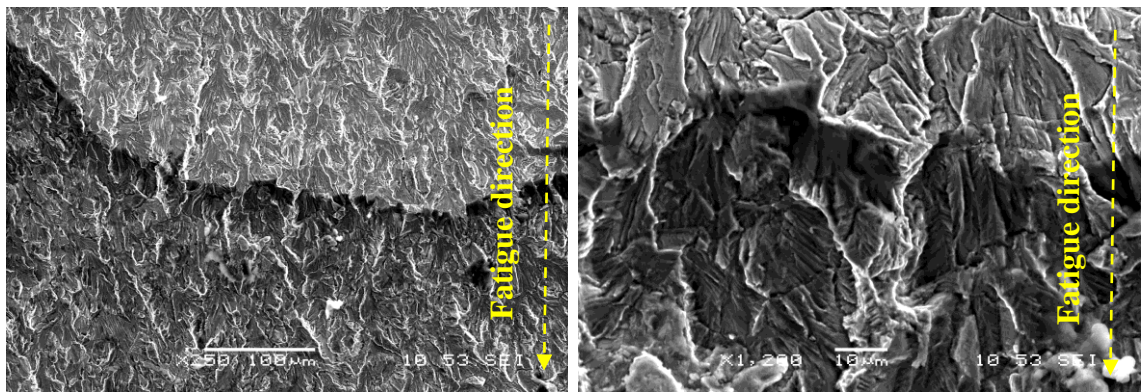


Figure 183. Fractography of tearing topography surface, the fatigue crack advances from up to down.

Due to their low stacking fault energy (SFE) or the local softening effect related to the particle cutting process in precipitation strengthened materials, fatigue cracks preferentially propagate along 111 planes, the stage I regime of fatigue loading, in certain FCC metals exhibit planar slip. The region associated with the beginning of cracking directly following a rapid reduction in load exhibits a distinct fractography that resembles microdamage, micro-tearing, ductile events and is oriented in crack propagation. This fractographic appearance is indicative of a non-traditional micromechanical fracture mechanism known as tearing the topographic surface. The ductile micro-tearing events may be seen at a magnificent scale of micrometres in this fractographic mode, and they

are likely indications of plasticity driven fatigue crack growth, such as plastic crack progress under cyclic loading [177].
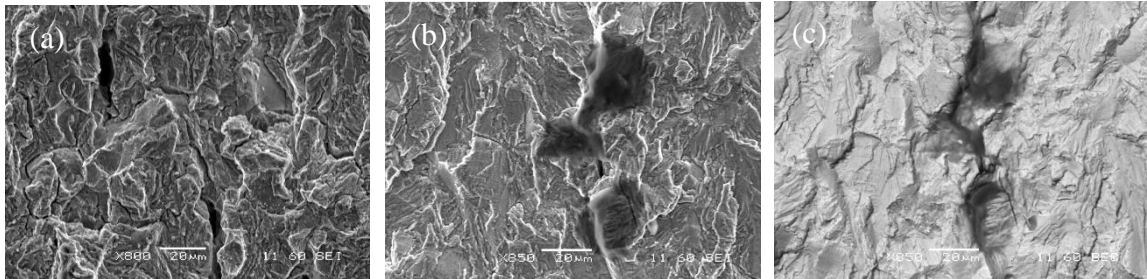


Figure 184. The fatigue cracks grow along grain boundaries (a); Carbide inclusion was observed at the grain boundary (b), and intergranular crack can be found under the inclusion when using the backscatter imagery mode (c).
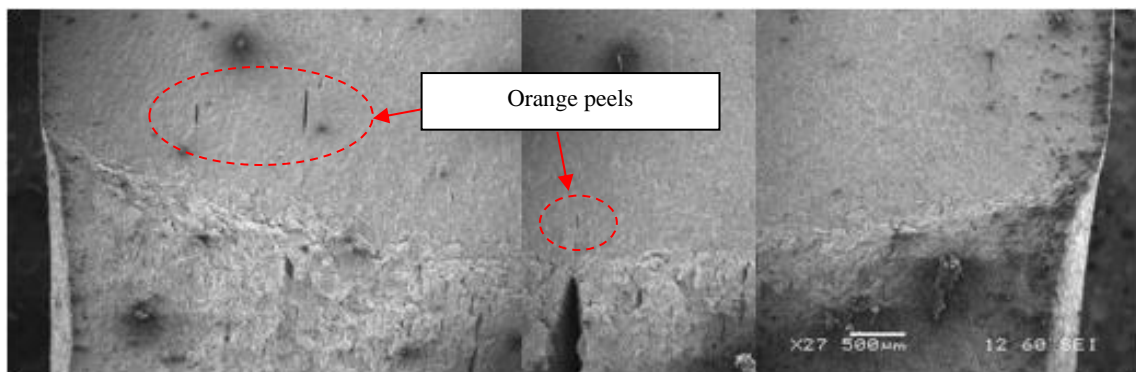


Figure 185. The orange peel phenomenon.

The orange peel effect, one of the most apparent features of plastic deformation in Hadfield manganese steel, is shown in Figure 185. The Orange peel is associated with the grain size of metal. The more considerable the deformation and the larger the grain size, the more apparent the effect. The orange peel effect is more common in grain size specimens with a high concentration of carbon atoms in the matrix, particularly grain boundaries [170].
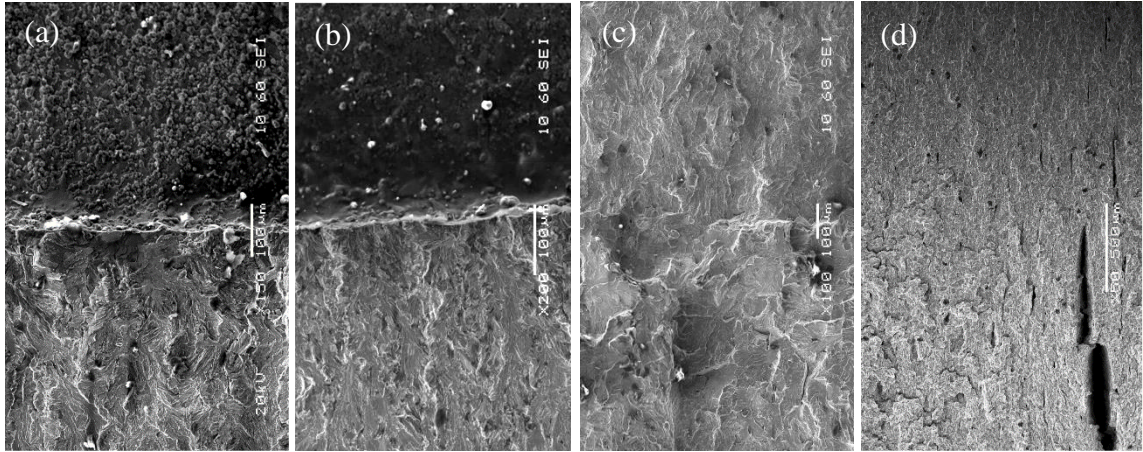
Figure 186. Interface between notch area and fatigue area of R260 rail steel (a), and Hadfield manganese steel (b); Interface between fatigue area and fractured area of R260 rail steel (c), and Hadfield manganese steel (d).

Pearlitic steels have a microstructure that aligns with the shear strain direction during significant plastic deformation. In pearlitic steel, the two-phase microstructure of ferrite and cementite plays a key role in deformation and, finally, crack initiation and propagation. Cracks develop at the pro eutectoid ferrite grain boundaries that are the softest microstructure region and experience the most strain hardening as the ferrite is strained in the direction of plastic deformation. Waviness in the crack direction is caused by cracks following the weakest connection in the microstructure. Along with inclusions, soft ferrite and other microstructure defects act as weak points, causing the crack to shift direction. Hadfield manganese steel deforms differently than pearlitic rail steel grade. Despite the inclusions, the Hadfield manganese steels have a more homogeneous microstructure since they are single-phase austenite. Dislocation and twinning processes cause deformation in Hadfield manganese steel, but only dislocations cause deformation in pearlitic grades. Besides dislocation movements, extra work hardening is commonly associated with Hadfield manganese steels with low SFE, favourable for twinning deformation. Carbon atoms are rearranged from octahedral to tetrahedral configurations may also contribute to Hadfield manganese steel's additional hardness. As a result,

218

correlations between various slip mechanisms, dislocations, and twining systems [177] can be due to the deformation mechanism of Hadfield manganese steel. The morphology of the crack propagation in this investigation in a Hadfield manganese steel crossing is identical to that observed in pearlitic rail steel used in standard rail tracks. In all cases, plastic deformation happens, resulting in the formation of cracks. The crack usually starts at the surface, where the loads are the maximum. The Hadfield manganese steel exhibited elastic-plastic behaviour and ductile fracture propagation that was stable. Elastic behaviour and cleavage fracture were seen in the pearlitic steel.

On the other hand, Hadfield manganese steel only has a few dimples, with evidence of oriented tearing flow lines and ridges visible on fracture surfaces at this high magnification. However, in pearlitic steel, cleavage and intergranular separation are connected with the rapid fracture area. In addition, Hadfield manganese has stronger ductile properties than pearlitic steel, indicating better fatigue separation properties.

While these plastic deformation mechanisms vary between the two types of materials, the crack mechanisms that grow in both seem to be similar. In pearlite and Hadfield manganese steel, most cracks are limited inside the plastically deformed layer by following the weakest connections in the microstructure, such as ferrite grain boundaries. As a result, the discovered crack network traverses several grains, and the majority of cracks propagate back to the surface at a shallow angle to the origin, comparable to pearlite behaviour.

## 7.4    LASER CONFOCAL SCANNING MICROSCOPY ANALYSIS (LCSM)

In this section are additional tests to explore the feasibility of inspecting fractured surfaces with a new technique that provides 3D image analysis. R260 sample 1 and Hadfield manganese steel sample 8 (from sections 7.1 and 7.2) were examined to characterize the fracture surface and determine the possibility of indicating a ductile or brittle fracture. The degree of grain alignment or any inclusion characteristics was not studied in this thesis.

Laser confocal scanning microscopy (LCSM) was used for fractographic analysis as described in the present section. It is noted that previous work on this research topic has never considered the use of LCSM to examine the fractured surface of rail materials. The LCSM examination may not produce accurate results due to the limited testing time, making it impossible to assess every sample and all areas of interest. There are also no reference articles to be considered in this case.

LCSM is different from most conventional fractographical methods in that it can determine depth profiles, offers fast analysis times, and involves simplified sample preparation, among other advantages of this technique. A limitation of LCSM optical microscopes is their limited depth of field; images of an object near the focus plane appear in confocal mode, while those further away are invisible. The applicability of confocal laser scanning microscopy as a fractographic approach has been proven by focusing on two examples of problems. LCSM resolution is comparable with other optical microscopes, making it appropriate for a wide range of fractographic investigations and allowing for excellent synergy with the SEM, which has higher resolution but no surface elevation capabilities [171-172]. According to Merson et al., LCSM is an effective instrument for the quantitative and qualitative characterisation of various fracture surfaces

and topography. By repositioning the focus plane vertically, a sequence of optical sections is generated from which the programme reconstructs a three-dimensional digital map, with short imaging durations and straightforward sample preparation methods [178].
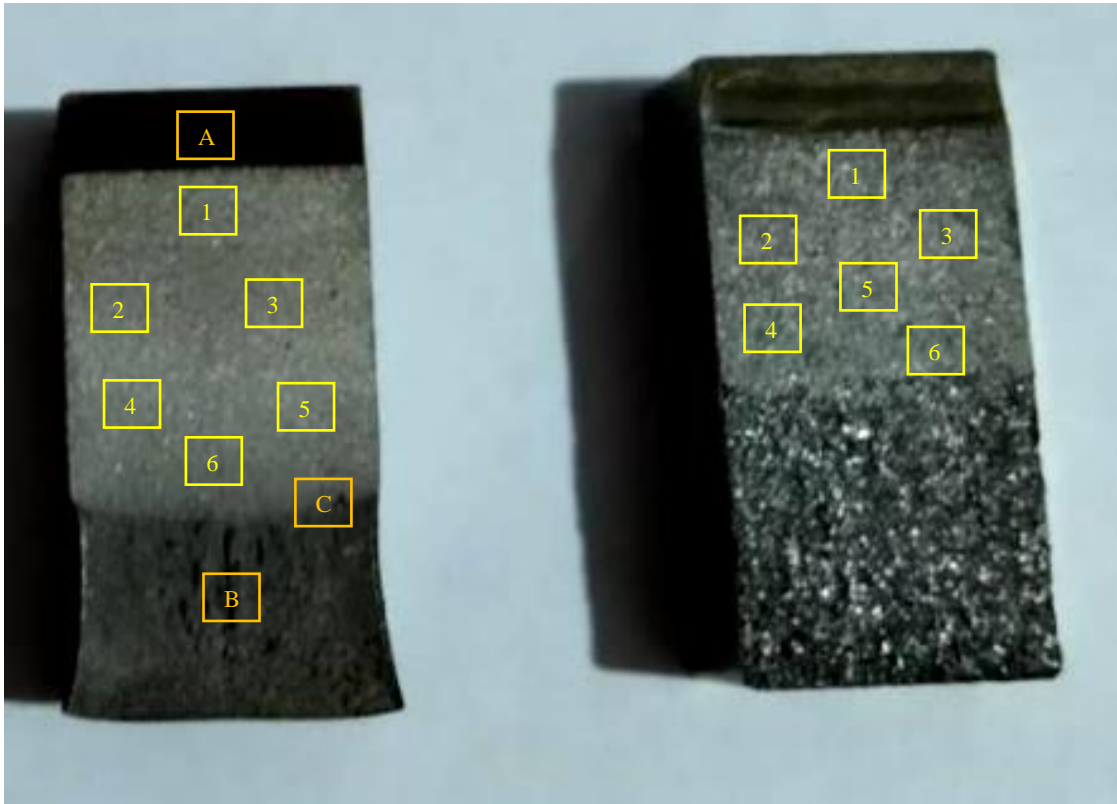


Figure 187. The area was observed by LCSM of Hadfield Manganese steel sample 8 and R260 rail steel sample 1.

Due to the limited time to use the equipment, this technique was employed to evaluate the feasibility of using 3D measurements to analyse the fractured surface further supporting the experimental results. The surface roughness of the fatigued fracture surfaces of the samples can be confirmed using 3D confocal imaging in each area. Figures 188-189 show isometric views of the fatigue surface together with cross-section profiles for both samples.

R260 rail steel sample 1



|  | Position 1 | Position 2 | Position 3 |



|  | Position 4 | Position 5 | Position 6 |
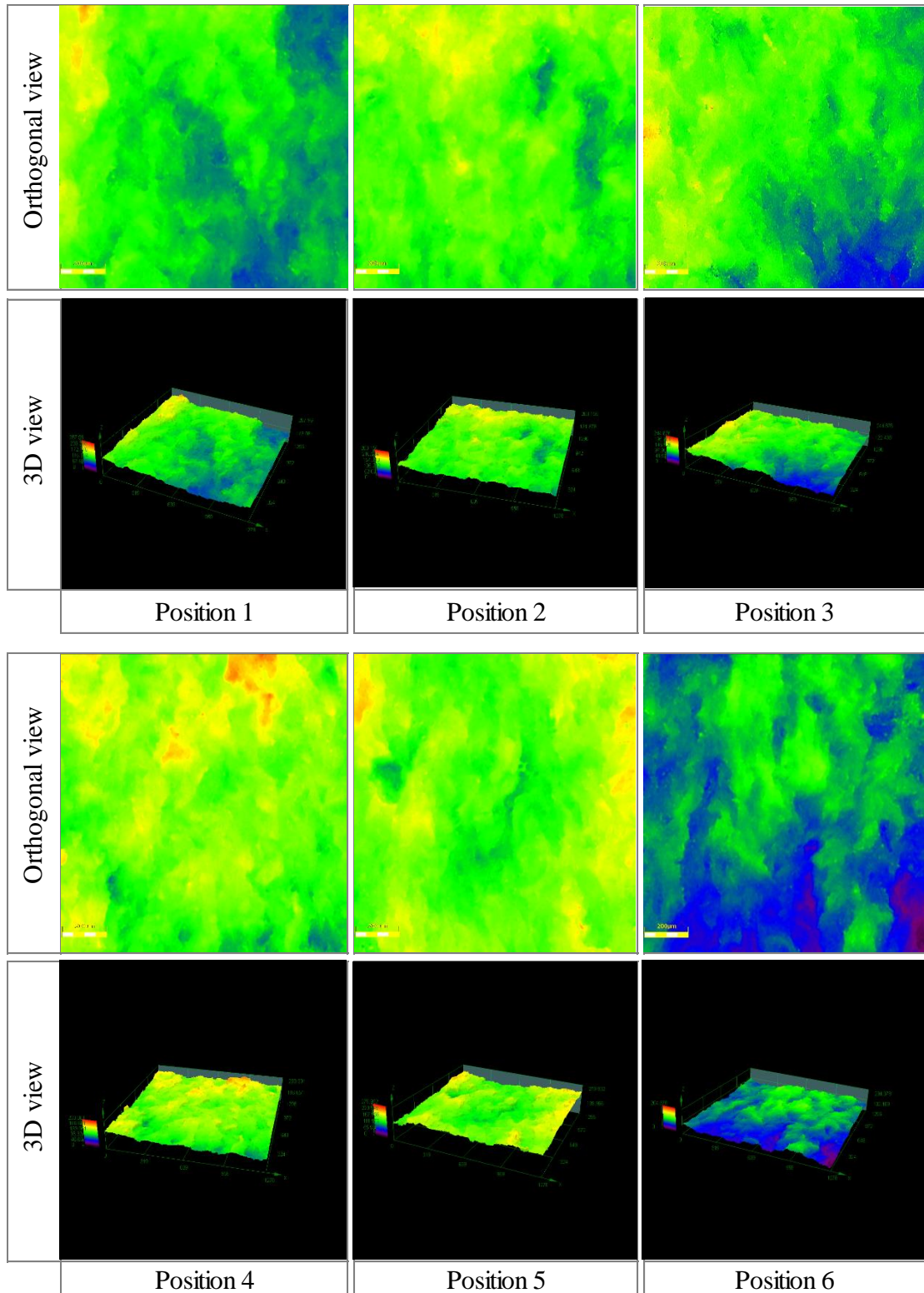
Figure 188. LCSM 3D isometric of the fatigue surfaces with cross-section profile for the R260 rail steel sample fatigue testing of the imaging process in a confocal microscope.

Hadfield manganese steel sample 8



| Position 1 | Position 2 | Position 3 |



| Position 4 | Position 5 | Position 6 |
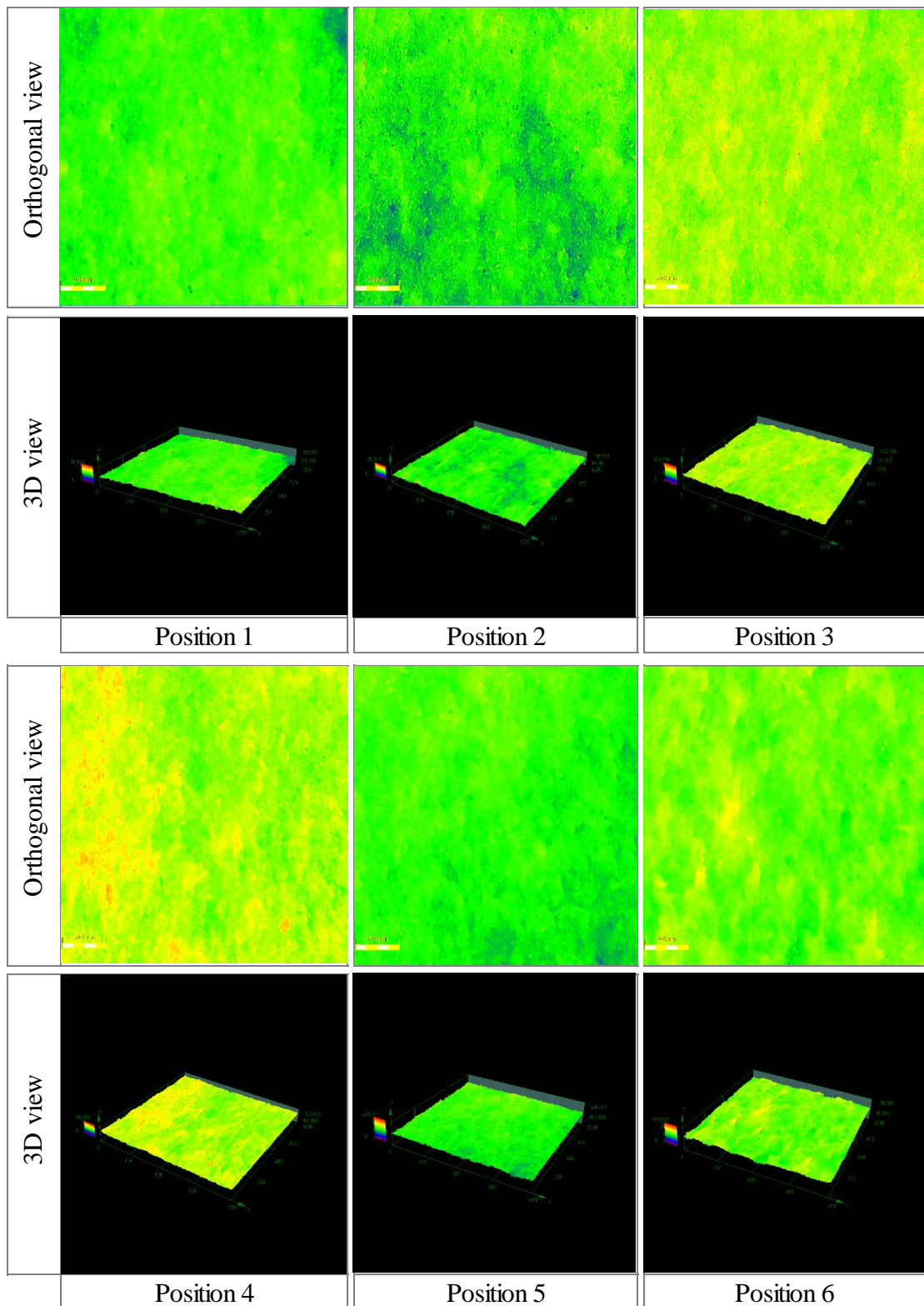
Figure 189. LCSM 3D isometric of the fatigue surfaces with cross-section profile for the Hadfield manganese steel sample fatigue testing of the imaging process in a confocal microscope.

Figure 190 is the area examined for differences in levels the tool can detect and measure to guide a future test.



| 3D view | Position A | Position B | Position C |
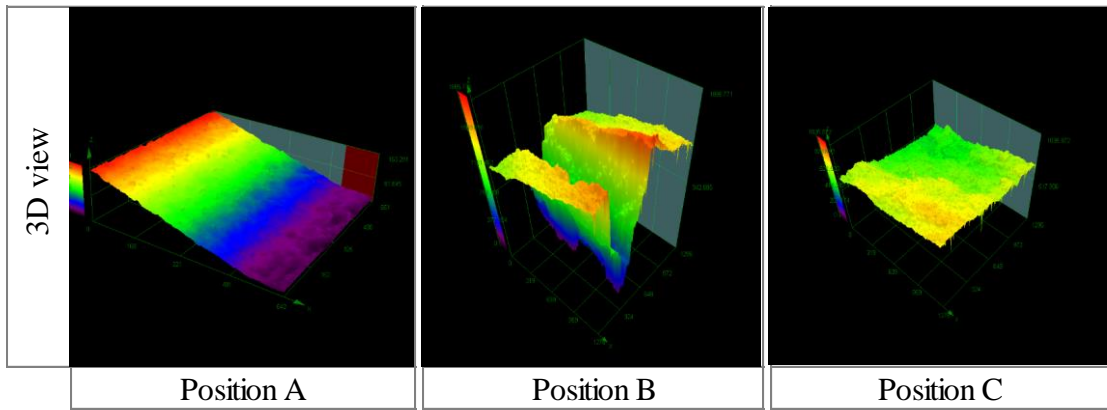
Figure 190. LCSM 3D isometric of the Hadfield manganese steel samples. The slope of notch area (A), at the middles of fast fracture surface area (B), and the interface between fatigue and fracture areas (C).

As described in 7.3.1, R260 rail steel contains many inclusions, resulting in the appearance of the crack surface found in the inclusion zone to have features corresponding to both cleavage fracture mechanism and microvoid coalescence mode.
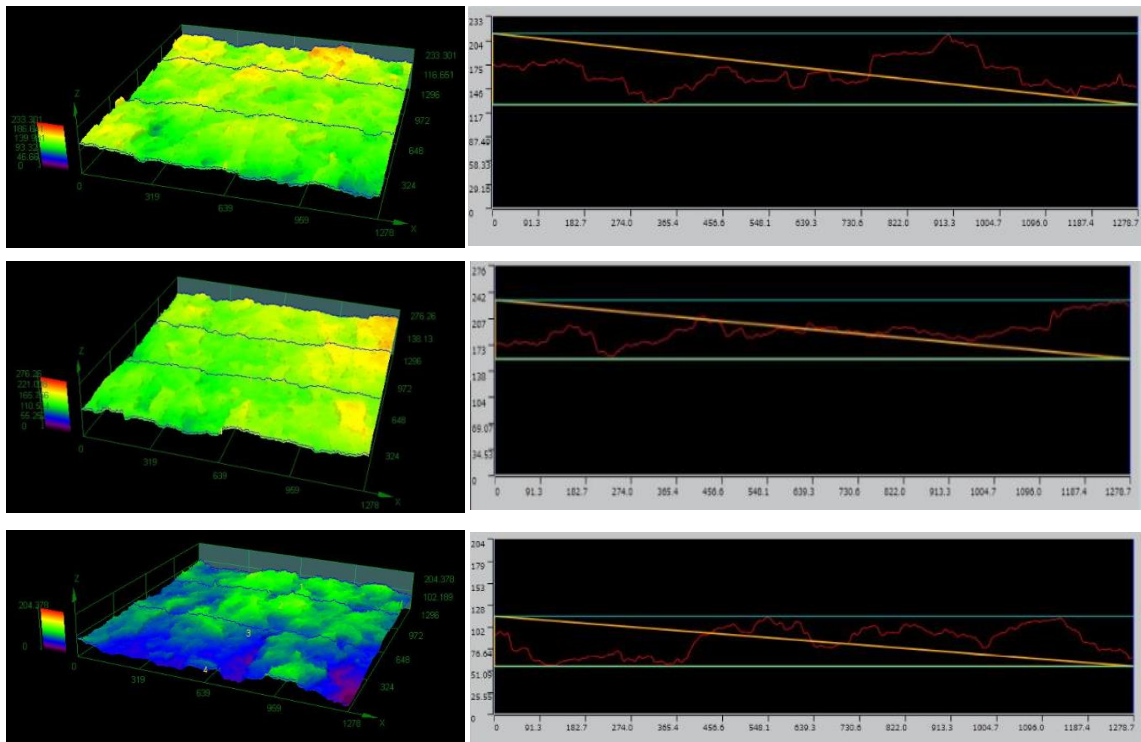


Figure 191. R260 rail steel profiles corresponding to positions 4, 5, and 6.

Unlike the Hadfield manganese steel, which has fewer inclusions, most fractures occur along the grain boundary. This makes the difference in the degree of surface change of the sample almost invisible.
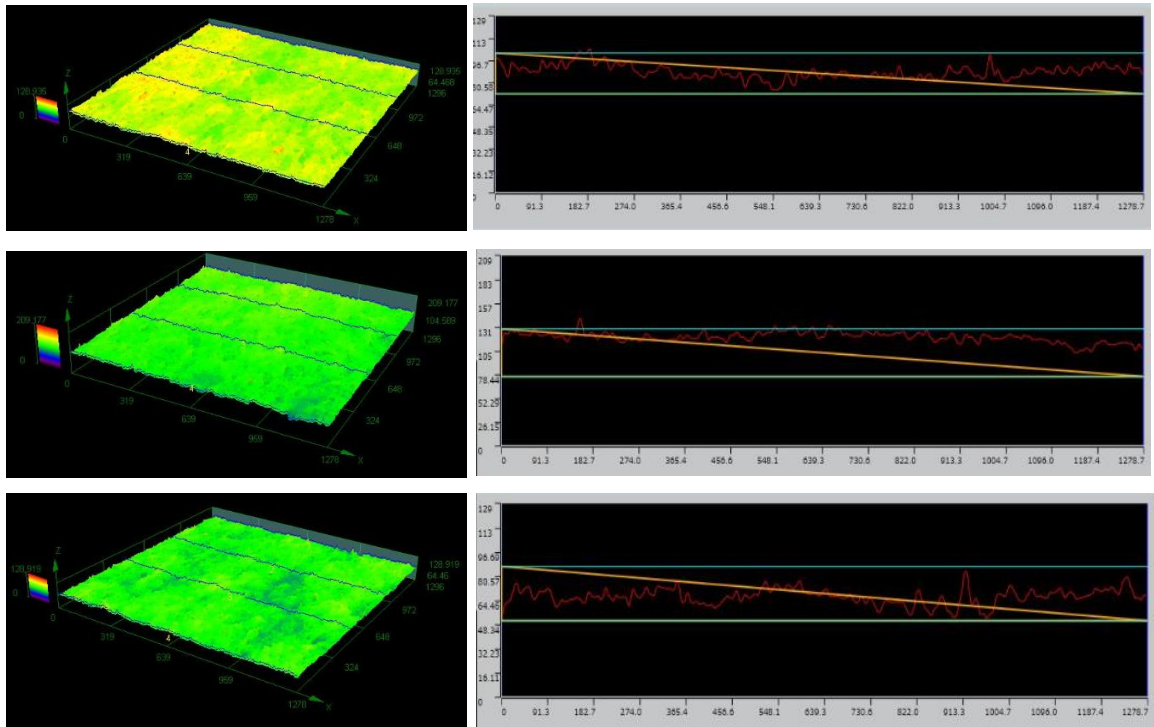


Figure 192. Hadfield manganese steel profiles corresponding to positions 2, 4, and 5.

The combination of LCSM and SEM research enables the high resolution and analytical capabilities of SEM to be combined with the three-dimensional information provided by LCSM. The ability to obtain three-dimension information, the rapidity with which data is acquired, and the potential of quantitative analysis contribute to LCSM competitiveness. Its flexibility makes it suitable for a variety of fractographical investigations, while its intrinsic productivity makes it well-suited for quality control applications. LCSM seems to have a wide range of potential applications in fractography and materials basic science since it bridges the gap between conventional optical microscopy and 3D confocal microscopy, SEM, and AFM. Considering that acquiring a single LCSM image takes only 1–3 minutes and no vacuum or other specimen preparation

is required; this technique is particularly fast compared to others [178]. It can be noted that LCSM may serve as an excellent alternative to SEM for a wide range of fractographic analysis purposes. For example, SEM images can offer a significantly higher resolution of the same fracture surface. However, SEM cannot obtain the height data produced with LCSM. Furthermore, LCSM provides the best representation of the global structure, resulting in a more detailed image; The grooves are more pronounced, and there are apparent depth variations between them. As a result, LCSM and SEM may be thought of as complementary methods.

# CHAPTER 8

# CONCLUSION AND FUTURE WORK

## 8.1 CONCLUSION

This research provides the knowledge of the application of AE techniques in developing reliable correlations to quantify damage propagation and guarantee that relevant information can be obtained from AE data in conventional rail steel (R220, R260) used in the manufacturing of plain rail and built-up turnout compared with Hadfield manganese steel used in one-piece cast frog turnout. Three-point fatigue bending experiments were carried out under laboratory conditions using a customised AE system developed by the University of Birmingham and a commercial AE system procured from Physical Acoustics Corporation.

The following conclusions can be drawn from this study:

- AE monitoring has proven to be a reliable method for identifying small defects during the propagation of fatigue cracks. It was particularly beneficial for detecting defects caused by rolling contact fatigue, such as subsurface cracking and delamination, as well as their propagation.

- The customized AE system developed in-house has similar capabilities as the PAC commercial system, which has found the possibility of further field testing applications.

- Rail steel grade R260 exhibited cleavage fracture during crack growth, whilst the Hadfield manganese steel and other high Mn manganese steels have been confirmed to exhibit ductile crack growth.

- In the R260 steel samples examined, captured AE signals with amplitudes more than 60 dB exist during steady crack growth. In the experiments performed, the distribution of high amplitude AE hits is more scattered. This is due to a continual brittle cleavage fracturing process during crack development.

- In the Hadfield manganese steel samples, most AE signals with amplitudes larger than 60 dB occur during the final stage of damage evolution. The maximum amplitude during the testing for all Hadfield samples is lower than for R260 rail steel due to the plasticity at the crack tip, resulting in lower AE energy levels being generated.

- For all steel grades studied, the crack growth rates were clearly correlated in each sample. Thus, the rapid increase in AE activity arising during crack growth in specific locations can be attributed to the presence of inclusions within the microstructure.

- R220 rail steel demonstrates an apparent fit between the energy rate, count rate, and amplitude rate of AE signals and ΔK. In addition, R220 rail steel generated more consistent elastic waves. Therefore, a better fit between their AE signal parameters and cracks growth parameters is feasible.

- R260 rail steel quantification is also feasible but with a larger margin of error due to data point scattering. All parameters except only the Amplitude rate have a moderate correlation.

- Hadfield manganese steel samples were no noticeable Paris trend from the recorded AE activity. This is likely due to the plasticity occurring at the tip of the fatigue fracture in the samples tested, based on hardness measurements and fractographic analyses. This is plausible because the Hadfield manganese steel samples were cut from a plate that had not been previously work-hardened, and the influence of carbides in the microstructure before fatigue testing is also a contributing factor.

- MnS, $Al_2O_3$, and $SiO_2$ are the most common inclusions observed in R260, whereas $Mn_3C$ and $(Fe, Mn)_3C$ are found near grain boundaries and inside austenite grains in Hadfield manganese steel. Each inclusion has a different shape and hardness that affects the occurrence of cracks in the workpiece, as described in Chapter 7.3.

- The significant rapid growth spikes seen by AE monitoring around these defects range from 300 µm to 600 µm, giving a significant signal while none can be seen on the DCPD. At this level, other commonly used detection methods are unable to detect crack propagation.

- LCSM method can be used for fracture surface analysis, but additional testing with samples is still required to improve the accuracy of the data analysis.

The knowledge the authors gained in the Hadfield manganese steel was very useful in further research. The limitations found in the test results caused by this material rarely exhibit elastic wave emission activity when the samples undergo crack growth due to the plasticity occurring at the tip. The phenomenon was confirmed using statistical as well as SEM fractography. The author suggests that AE data may be used for a more qualitative evaluation. However, the test with Hadfield manganese steel that has passed the work-hardened is necessary because it is unclear if AE from crack growth for in-service crossing would behave differently. If the implementation of the AE technique is unsuccessful, an alternative NDT method may be considered.

Ultimately, all these findings will greatly benefit research in the Thai Railways, where knowledge of AE applications is very new and rarely experts in this field.

## 8.2    POTENTIAL FOR FURTHER RESEARCH

The potential for further research is presented below.

- Further studies should be performed on Hadfield manganese steel samples that have been work-hardened and then be carried out using the AE monitoring techniques used in this study on the actual railway network. It will be interesting to observe if AE from crack growth for in-service crossings varies to that observed in the laboratory test.

- Study more about the usability of the LCSM as this fractographical method can analyse both qualitative and quantitative characterisation.

- Future research will study railways in Thailand using the experimental results from this thesis as a basis. Thailand environmental factors differ from the UK in terms of climatic conditions, train usage types, and other environmental factors. Therefore, the setting of various parameters requires further study.

# REFERENCES

[1] Songmuang, T. and Ocha, W. (2017) 'ASEAN Connectivity: What could high speed rail bring to Thailand?' *Apheit journal,* volume (5) [online]. Available at: http://apheit. bu. ac. th/jounal/Inter-vol5-1/p28-39-Teerarat% 20Songmuang. pdf. (Accessed: 23 February 2020)

[2] Dindar, S., Kaewunruen, S. and Sussman, J. M. J. P. e. (2017) 'Climate Change Adaptation for GeoRisks Mitigation of Railway Turnout Systems', 189, pp. 199-206.

[3] Kaewunruen, S., Freimanis, A. and Ishida, M. (2018) 'Effect of extreme climate on wheel-rail interaction over rail squats'. *The 6th European Conference on Computational Mechanics (ECCM 6)*: ECCM6.

[4] Kassa, E., Nielsen, J., Ekh, M. and Iwnicki, S. (2010) 'Geometry and stiffness optimization for switches and crossings, and simulation of material degradation', *Proceedings of the Institution of Mechanical Engineers, Part F: Journal of Rail and Rapid Transit,* 224(4), pp. 279-292.

[5] Roberts, C. and Davis, C. (2008) 'A review on non-destructive evaluation of rails: state-of-the-art and future development', *Proceedings of the Institution of Mechanical Engineers, Part F: Journal of Rail and rapid transit,* 222(4), pp. 367-384.

[6] EN, B. '13674-1: 2011+ A1: 2017 Railway applications', Track. Rail. Vignole railway rails, 46.

[7] Lv, B., Zhang, M., Zhang, F., Zheng, C., Feng, X., Qian, L. and Qin, X. (2012) 'Micro-mechanism of rolling contact fatigue in Hadfield steel crossing', *International Journal of Fatigue,* 44, pp. 273-278.

[8] Esveld, C. and Esveld, C. (2001) Modern railway track. MRT-productions

[8] Esveld, C. and Esveld, C. (2001) Modern railway track. MRT-productions Zaltbommel, Netherlands.

[9] Dindar, S. and Kaewunruen, S. (2017) 'Assessment of Turnout-Related Derailments by Various Causes'. *International Congress and Exhibition" Sustainable Civil Infrastructures: Innovative Infrastructure Geotechnology"*: Springer, pp. 27-39.

[10] Garnham, J. and Davis, C. (2009) 'Rail materials', *Wheel–Rail Interface Handbook*: Elsevier, pp. 125-171.

[11] Takeshi, M. and I. Atsushi (1995). "Fatigue crack propagation rate of austenitic high manganese steel." Structural Engineering 11: pp. 165-172

[12] Yan, W., Fang, L., Sun, K. and Xu, Y. (2007) 'Effect of surface work hardening on wear behavior of Hadfield steel', *Materials Science and Engineering: A,* 460, pp. 542-549.

[13] Ossberger, U., Eck, S. and Stocker, E. (2015) 'Performance of different materials in a frog of a turnout'. *Proceedings of the 11th International Heavy Haul Conference. Perth, Australia*, pp. 329-336.

[14] Onawoga, D. T. and Akinyemi, O. O. (2010) 'Development of equipment maintenance strategy for critical equipment', *The Pacific Journal of Science and Technology,* 11(1), pp. 328-342.

[15] Lewis, R. and Olofsson, U. (2009) 'Basic tribology of the wheel-rail contact', *Wheel–rail interface handbook*: Elsevier, pp. 34-57.

[16] Administration, F. R. (2015) 'Track Inspector Rail Defect reference manual'.

[17] Ishak, M. F., Dindar, S. and Kaewunruen, S.(2016) 'Safety-based maintenance for geometry restoration of railway turnout systems in various operational environments'. *Proceedings of The 21st National Convention on Civil Engineering. Songkhla, Thailand*.

[18] Bhattacharyya, S. (1966) 'A friction and wear study of Hadfield manganese steel', *Wear,* 9(6), pp. 451-461.

[19] Harzallah, R., Mouftiez, A., Felder, E., Hariri, S. and Maujean, J.-P. (2010) 'Rolling contact fatigue of Hadfield steel X120Mn12', *Wear,* 269(9-10), pp. 647-654.

[20] Guo, S., Sun, D., Zhang, F., Feng, X. and Qian, L. (2013) 'Damage of a Hadfield steel crossing due to wheel rolling impact passages', *Wear,* 305(1-2), pp. 267-273.

[21] Sällström, J., Dahlberg, T., Ekh, M. and Nielsen, J. (2004) 'State-of-the art study on railway turnouts–dynamics and damage', Department of Applied Mechanics, Chalmers University of Technology, Göteborg, Sweden.

[22] Casanueva, C., Doulgerakis, E., Jönsson, P.-A. and Stichel, S. (2014) 'Influence of switches and crossings on wheel profile evolution in freight vehicles', *Vehicle System Dynamics*, 52(sup1), pp. 317-337.

[23] Dollevoet, R. (2010) 'Design of an Anti Head Check profile based on stress relief', Enschede: University of Twente Host.

[24] Valehrach, J., Guziur, P., Riha, T. and Plasek, O. (2017) 'Assessment of rail long-pitch corrugation', *MS&E,* 236(1), pp. 012048.

[25] Oostermeijer, K., Hougui, Z., Weining, L. and Shuang, L. (2010) 'Review on short pitch rail corrugation studies', *Urban Rapid Rail Transit,* 23(2), pp. 6-13.

[26] Fesharaki, M. and Wang, T.-L. (2016) 'The effect of rail defects on track impact factors', *Civil Engineering Journal,* 2(9), pp. 458-473.

[27] Zerbst, U., Lundén, R., Edel, K.-O. and Smith, R. A. (2009) 'Introduction to the damage tolerance behaviour of railway rails–a review', *Engineering fracture mechanics,* 76(17), pp. 2563-2601.

[28] Kumar, S. (2006) Study of rail breaks: associated risks and maintenance strategies. Luleå tekniska universitet.

[29] Zakar, F. and Mueller, E. (2016) 'Investigation of a Columbus, Ohio train derailment caused by fractured rail', *Case Studies in Engineering Failure Analysis,* 7, pp. 41-49.

[30] RailCorp, M. (2012) 'Engineering manual track', *Rail defect handbook*.

[31] Johansson, A., Pålsson, B., Ekh, M., Nielsen, J. C., Ander, M. K., Brouzoulis, J. and Kassa, E. (2011) 'Simulation of wheel-rail contact and damage in switches & crossings', *Wear,* 271(1-2), pp. 472-481.

[32] Grossoni, I., Hughes, P., Bezin, Y., Bevan, A. and Jaiswal, J. (2020) 'Observed failures at railway turnouts: Failure analysis, possible causes and links to current and future research', *Engineering Failure Analysis,* 119, pp. 104987.

[33] Dhua, S., Ray, A., Sen, S., Prasad, M., Mishra, K. and Jha, S. (2000) 'Influence of nonmetallic inclusion characteristics on the mechanical properties of rail steel', *Journal of materials engineering and performance,* 9(6), pp. 700-709.

[34] Liu, C., Bassim, M. and Lawrence, S. S. (1993) 'Evaluation of fatigue-crack initiation at inclusions in fully pearlitic steels', *Materials Science and Engineering: A,* 167(1-2), pp. 107-113.

[35] ORY, D., DAVIS, C.L (2008). Inclusion density, content and compostition in a number of rail steels sourced internationally. Summer project – University of Birmingham

[36] British steel (2018a). *Steel grade dimensions and properties* [Online]. Available at: https://britishsteel.co.uk/media/40810/steel-grade-dimensions-and-properties.pdf (Accessed: 29 May 2018)

[37] Suresh, S. (1998b) Fatigue of materials. Cambridge university press.

[38] Fletcher, D., Franklin, F. and Kapoor, A. (2009) 'Rail surface fatigue and wear', *Wheel–rail interface handbook*: Elsevier, pp. 280-310.

[39] Christodoulou, P., Kermanidis, A. and Haidemenopoulos, G. (2016) 'Fatigue and fracture behavior of pearlitic Grade 900A steel used in railway applications', *Theoretical and Applied Fracture Mechanics,* 83, pp. 51-59.

[40] Suresh, S. (1998a) Fatigue of materials. Cambridge university press.

[41] Carroll, R. and Beynon, J. (2006) 'Decarburisation and rolling contact fatigue of a rail steel', *Wear,* 260(4-5), pp. 523-537.

[42] Beynon, J., Garnham, J. and Sawley, K. (1996) 'Rolling contact fatigue of three pearlitic rail steels', *Wear,* 192(1-2), pp. 94-111.

[43] Smallman, R. E. (2016) *Modern physical metallurgy.* Elsevier.

[44] Stock, R. and Pippan, R. (2011) 'RCF and wear in theory and practice—the influence of rail grade on wear and RCF', *Wear,* 271(1-2), pp. 125-133.

[45] Jack, I. (2001) *The crash that stopped Britain.* Granta Books.

[46] Ekberg, A., Åkesson, B. and Kabo, E. (2014) 'Wheel/rail rolling contact fatigue–Probe, predict, prevent', *Wear,* 314(1-2), pp. 2-12.

[47] Dhar, S., Danielsen, H. K., Fæster, S., Rasmussen, C. J. and Jensen, D. J. (2019b) '2D and 3D characterization of rolling contact fatigue cracks in manganese steel wing rails from a crossing', *Wear,* 436, pp. 202959.

[48] Garnham, J. E. and Davis, C. L. (2008) 'The role of deformed rail microstructure on rolling contact fatigue initiation', *Wear,* 265(9-10), pp. 1363-1372.

[49] Franklin, F., Garnham, J., Fletcher, D., Davis, C. and Kapoor, A. (2008) 'Modelling rail steel microstructure and its effect on crack initiation', *Wear,* 265(9-10), pp. 1332-1341.

[50] Ringsberg, J. W. and Bergkvist, A. (2003) 'On propagation of short rolling contact fatigue cracks', *Fatigue & Fracture of Engineering Materials & Structures,* 26(10), pp. 969-983.

[51] Wood, W. (1955) 'Fine slip in fatigue', *JOURNAL OF THE INSTITUTE OF METALS,* 84(1), pp. 5-6.

[52] Bernabei, M., Allegrucci, L. and Amura, M. (2016) 'Fatigue failures of aeronautical items: Trainer aircraft canopy lever reverse, rescue helicopter main rotor blade and fighter-bomber aircraft ground-attack main wheel', *Handbook of Materials Failure Analysis with Case Studies from the Aerospace and Automotive Industries*: Elsevier, pp. 87-116.

[53] Fletcher, D. and Beynon, J. (2000) 'The effect of contact load reduction on the fatigue life of pearlitic rail steel in lubricated rolling–sliding contact', *Fatigue & Fracture of Engineering Materials & Structures,* 23(8), pp. 639-650.

[54] Drouillard, T. (1996) 'A history of acoustic emission', *Journal of acoustic emission,* 14(1), pp. 1-34.

[55] Tensi, H. M. (2004) 'The Kaiser-effect and its scientific background', *Journal of Acoustic Emission,* 22, pp. s1-s16.

[56] Meo, M. (2014) 'Acoustic emission sensors for assessing and monitoring civil infrastructures', *Sensor Technologies for Civil Infrastructures*: Elsevier, pp. 159-178.

[57] Unnþórsson, R. (2013) 'Hit detection and determination in AE bursts', *Acoustic emission-research and applications*, pp. 1-20.

[58] Máthis, K. and Chmelík, F. (2012) 'Exploring plastic deformation of metallic materials by the acoustic emission technique', *Acoustic emission*, pp. 23-48.

[59] Shull, P. J. (2002) 'Nondestructive evaluation: theory, techniques, and applications'. CRC press.

[60] Price, E., Lees, A. and Friswell, M. (2005) 'Detection of severe sliding and pitting fatigue wear regimes through the use of broadband acoustic emission', *Proceedings of the Institution of Mechanical Engineers, Part J: Journal of Engineering Tribology,* 219(2), pp. 85-98.

[61] Fowler, T. J., Blessing, J. A., Conlisk, P. J. and Swanson, T. L. (1989) 'The MONPAC system', *Journal of acoustic emission,* 8(3), pp. 1-8.

[62] Ono, K. (2005) 'Current understanding of mechanisms of acoustic emission', *The Journal of Strain Analysis for Engineering Design,* 40(1), pp. 1-15.

[63] Heiple, C. and Carpenter, S. (1987) 'Acoustic emission produced by deformation of metals and alloys. II', *Journal of acoustic emission,* 6, pp. 215-237.

[64] Schmid, E. and Wassermann, G. (1929) 'Über die Textur gezogener Magnesium-und Zinkdrähte', *Naturwissenschaften,* 17(18-19), pp. 312-314.

[65] Miller, R. and McIntire, P. (2005) 'Acoustic Emission Testing. NDT Handbook', *Volume,* 5, pp. 652.

[67] Roman, I., Teoh, H. and Ono, K. (1984) 'Thermal Restoration of Burst Emissions in A 533 B Steel', *J. Acoust. Emiss.,* 3(1), pp. 19-26.

[68] Anastasopoulos, A., Kourousis, D. and Cole, P. (2008) 'Acoustic emission inspection of spherical metallic pressure vessels'. *2nd International Conference on Technical Inspection and NDT, Tehran, Iran*.

[69] Grosse, C. U. and Ohtsu, M. (2008) 'Acoustic emission testing'. Springer Science & Business Media.

[70] Marfo, A., Luo, Y. and Zhong-an, C. (2013) 'Quantitative acoustic emission fatigue crack characterization in structural steel and weld', *Advances in Civil Engineering,* 2013.

[71] Roberts, T. and Talebzadeh, M. (2003) 'Acoustic emission monitoring of fatigue crack propagation', *Journal of Constructional Steel Research,* 59(6), pp. 695-712.

[72] Lindley, T., Palmer, I. and Richards, C. (1978) 'Acoustic emission monitoring of fatigue crack growth', *Materials Science and Engineering,* 32(1), pp. 1-15.

[73] Bassim, M., Lawrence, S. S. and Liu, C. (1994) 'Detection of the onset of fatigue crack growth in rail steels using acoustic emission', *Engineering Fracture Mechanics,* 47(2), pp. 207-214.

[74] Yu, Z. z. and Clapp, P. C. (1987) 'Quantitative analysis of acoustic emission signals', *Journal of applied physics,* 62(6), pp. 2212-2220.

[75] Yoneda, K. and Ye, J. (2006) 'Crack propagation and acoustic emission behavior of silver-added Dy123 bulk superconductor', *Physica C: Superconductivity and its applications,* 445, pp. 371-374.

[76] Aggelis, D., Kordatos, E. and Matikas, T. (2011) 'Acoustic emission for fatigue damage characterization in metal plates', *Mechanics Research Communications,* 38(2), pp. 106-110.

[77] Shi, S., Han, Z., Liu, Z., Vallely, P., Soua, S., Kaewunruen, S. and Papaelias, M. (2018) 'Quantitative monitoring of brittle fatigue crack growth in railway steel using acoustic emission', *Proceedings of the Institution of Mechanical Engineers, Part F: Journal of Rail and Rapid Transit,* 232(4), pp. 1211-1224.

[78] Mindrila, D. and Balentyne, P. (2017) 'Scatterplots and correlation', *Retrieved from.*

[79] Taylor, R. (1990) 'Interpretation of the correlation coefficient: a basic review', *Journal of diagnostic medical sonography,* 6(1), pp. 35-39.

[80] Schober, P., Boer, C. and Schwarte, L. A. (2018) 'Correlation coefficients: appropriate use and interpretation', *Anesthesia & Analgesia,* 126(5), pp. 1763-1768.

[81] Montgomery, D. C., Peck, E. A. and Vining, G. G. (2021) *Introduction to linear regression analysis.* John Wiley & Sons.

[82] Kenderian, S., Green, R. E. and Djordjevic, B. B. (2007) 'Ultrasonic monitoring of dislocations during fatigue of pearlitic rail steel', *Materials evaluation,* 65(5).

[83] Magel, E., Mutton, P., Ekberg, A. and Kapoor, A. (2016) 'Rolling contact fatigue, wear and broken rail derailments', *Wear,* 366, pp. 249-257.

[85] Papaelias, M. P., Roberts, C. and Davis, C. L. (2008) 'A review on non-destructive evaluation of rails: state-of-the-art and future development', *Proceedings of the Institution of Mechanical Engineers Part F-Journal of Rail and Rapid Transit,* 222(4), pp. 367-384.

[86] Koranne, A. J., Kachare, J. A. and Jadhav, S. A. (2017) 'Fatigue crack analysis using acoustic emission', *International Research Journal of Engineering and Technology,* 4(1), pp. 1177-1180.

[87] Zhu, Y. and Olofsson, U. (2014) 'An adhesion model for wheel-rail contact at the micro level using measured 3d surfaces', *Wear,* 314(1-2), pp. 162-170.

[88] Danyuk, A., Rastegaev, I., Pomponi, E., Linderov, M., Merson, D. and Vinogradov, A. (2017) 'Improving of acoustic emission signal detection for fatigue fracture monitoring', *Procedia Engineering,* 176, pp. 284-290.

[89] Wang, P. (2015) 'Design of high-speed railway turnouts: theory and applications'. Academic Press.

[90] Coulter, J. E., Robertson, M. O. and Stevens, D. M. (1996). 'Acoustic emission for detection of corrosion under insulation'. Google Patents.

[91] Wadley, H. and Mehrabian, R. (1984) 'Acoustic emission for materials processing: a review', *Materials Science and Engineering,* 65(2), pp. 245-263.

[92] Wadley, H. and Scruby, C. (1991) 'Cooling rate effects on acoustic emission-microstructure relationships in ferritic steels', *Journal of materials science,* 26(21), pp. 5777-5792.

[93] Takeda, R., Kaneko, Y. and Vinogradov, A. (2013) 'Cluster analysis of acoustic emissions measured during deformation of duplex stainless steels', *Materials Transactions,* 54(4), pp. 532-539.

[94] Light, G. (2008) 'Nondestructive evaluation technologies for monitoring corrosion', *Techniques for Corrosion Monitoring*: Elsevier, pp. 293-312.

[95] Murav'ev, M. and Murav'ev, T. (2008) 'The possibilities of acoustic emission testing of rails during exploitation', *Russian Journal of Nondestructive Testing,* 44(1), pp. 33-40.

[96] Bollas, K., Papasalouros, D., Kourousis, D. and Anastasopoulos, A. (2010) 'ACOUSTIC EMISSION INSPECTION OF RAIL WHEELS', *Journal of Acoustic Emission,* 28.

[97] Bruzelius, K. and Mba, D. (2004) 'An initial investigation on the potential applicability of Acoustic Emission to rail track fault detection', *NDT & E International,* 37(7), pp. 507-516.

[98] Zhang, J., Ma, H., Yan, W. and Li, Z. (2016) 'Defect detection and location in switch rails by acoustic emission and Lamb wave analysis: A feasibility study', *Applied Acoustics,* 105, pp. 67-74.

[99] Vallen, H. (2002) 'AE testing fundamentals, equipment, applications', *Journal of Nondestructive Testing(Germany),* 7(9), pp. 1-30.

[100] Vallely, P. (2015). 'A Holistic Approach to Remote Condition Monitoring for the Accurate Evaluation of Railway Infrastructure and Rolling Stock'. University of Birmingham.

[101] Tilley, R. J. (2008) *Defects in solids.* John Wiley & Sons.

[102] Tec-science (2018) [Online]. Available at: https://www.tec-science.com/material-science/structure-of-metals/crystallographic-defects (Accessed: 20 December 2019)

[103] Smallman, R. E. and Bishop, R. J. (1999) *Modern physical metallurgy and materials engineering.* Butterworth-Heinemann.

[104] Merckling, C. (2018) 'Monolithic integration of InGaAs on Si (001) substrate for logic devices', *High Mobility Materials for CMOS Applications*: Elsevier, pp. 71-114.

[105] Sedmak, A. S., Rakin, M., Medjo, B. and Younise, B. (2019) 'Micromechanical modelling of ductile fracture–local approach', *Metallurgical and Materials Engineering,* 25(04), pp. 263-286.

[106] Mouritz, A. P. (2012) *Introduction to aerospace materials.* Elsevier.

[107] Callister, W. D. and Rethwisch, D. (2007) 'The structure of crystalline solids', Materials science and engineering: an introduction. New York: John Wiley & Sons, Inc, pp. 38-79.

[108] Epp, J. (2016) 'X-ray diffraction (XRD) techniques for materials characterization', Materials characterization using nondestructive evaluation (NDE) methods: Elsevier, pp. 81-124.

[109] Taguchi, T. (2006) 'A new position sensitive area detector for high-speed and high-sensitivity X-ray diffraction analysis', *Powder diffraction,* 21(2), pp. 97-101.

[110] Courtney, T. H. (2005) *Mechanical behavior of materials.* Waveland Press.

[111] Spectrographic Limited (1999) [Online image]. Available at : https://spectrographic.co.uk /products/mitutoyo-mvk-h1 (Accessed: 15 December 2019)

[112] Hetzner, D. W. (2003) 'Microindentation hardness testing of materials using ASTM e384', *Microscopy and Microanalysis,* 9(S02), pp. 708-709.

[113] ANIOŁEK, K., HERIAN, J. and CIEŚLA, M. (2014) 'Influence of hot rolling and isothermal annealing on microstructure and mechanical properties of high carbon steel', *Inżynieria Materiałowa,* 35(2), pp. 72--74.

[114] Lee, K. M. and Polycarpou, A. A. (2005) 'Wear of conventional pearlitic and improved bainitic rail steels', *Wear,* 259(1-6), pp. 391-399.

[115] Kiraga, K., Szychta, E. and Szychta, L.(2012) 'Determination of rail steel's phase composition by means of X-ray diffraction analysis'. *2012 ELEKTRO*: IEEE, pp. 316-318.

[116] Kelton, K. and Greer, A. L. (2010) *Nucleation in condensed matter: applications in materials and biology.* Elsevier.

[117] Zambrano, O., Tressia, G. and Souza, R. (2020) 'Failure analysis of a crossing rail made of Hadfield steel after severe plastic deformation induced by wheel-rail interaction', *Engineering Failure Analysis,* 115, pp. 104621.

[118] Jost, N. and Schmidt, I. (1986) 'Friction-induced martensitic transformation in austenitic manganese steels', *Wear,* 111(4), pp. 377-389.

[119] Kim, T. and Bourdillon, A. (1992) 'Influence of carbon on development of deformation microstructures in Hadfield steels', *Materials science and technology,* 8(11), pp. 1011-1022.

[120] Chen, C., Lv, B., Feng, X., Zhang, F. and Beladi, H. (2018) 'Strain hardening and nanocrystallization behaviors in Hadfield steel subjected to surface severe plastic deformation', *Materials Science and Engineering: A,* 729, pp. 178-184.

[121] Feng, X., Zhang, F., Yang, Z. and Zhang, M. (2013) 'Wear behaviour of nanocrystallised Hadfield steel', *Wear,* 305(1-2), pp. 299-304.

[122] Yan, W., Fang, L., Sun, K. and Xu, Y. (2007) 'Effect of surface work hardening on wear behavior of Hadfield steel', *Materials Science and Engineering: A,* 460, pp. 542-549.

[123] Petrov, Y. N., Gavriljuk, V. G., Berns, H. and Schmalt, F. (2006) 'Surface structure of stainless and Hadfield steel after impact wear', *Wear,* 260(6), pp. 687-691.

[124] Machado, P., Pereira, J., Penagos, J., Yonamine, T. and Sinatora, A. (2017) 'The effect of in-service work hardening and crystallographic orientation on the micro-scratch wear of Hadfield steel', *Wear,* 376, pp. 1064-1073.

[125] Shariff, S., Pal, T., Padmanabham, G. and Joshi, S. (2011) 'Comparative study on dry sliding wear behavior of various railroad steels', *Journal of tribology,* 133(2).

[126] Wen, Y., Peng, H., Si, H., Xiong, R. and Raabe, D. (2014) 'A novel high manganese austenitic steel with higher work hardening capacity and much lower impact deformation than Hadfield manganese steel', *Materials & Design,* 55, pp. 798-804.

[127] Kovács, T., Völgyi, B. and Sikari-Nágl, I. (2014) 'Hadfield steel hardening by explosion'. *Materials Science Forum*: Trans Tech Publ, pp. 93-97.

[128] Zhang, F., Chen, C., Lv, B., Ma, H., Farabi, E. and Beladi, H. (2019) 'Effect of pre-deformation mode on the microstructures and mechanical properties of Hadfield steel', *Materials Science and Engineering: A,* 743, pp. 251-258.

[129] Schindelin, J., Arganda-Carreras, I., Frise, E., Kaynig, V., Longair, M., Pietzsch, T., Preibisch, S., Rueden, C., Saalfeld, S. and Schmid, B. (2012) 'Fiji: an open-source platform for biological-image analysis', *Nature methods,* 9(7), pp. 676.

[131] Moore, P. L. and Booth, G. (2014) *The welding engineer's guide to fracture and fatigue.* Elsevier.

[132] Paris, P. and Erdogan, F. J. J. o. b. e. (1963) 'A critical analysis of crack propagation laws', 85(4), pp. 528-533.

[134] ASTM, E. (2011) '647: Standard test method for measurement of fatigue crack growth rates', *Annual book of ASTM standards,* 3, pp. 591-630.

[135] Černý, I. J. E. F. M. (2004) 'The use of DCPD method for measurement of growth of cracks in large components at normal and elevated temperatures', 71(4-6), pp. 837-848.

[136] Johnson, H. J. M. R. and Standards (1965) 'Calibrating the electric potential method for studying slow crack growth', 5(1), pp. 442-445.

[137] Bunsell, A. R., Joannès, S. and Marcellan, A. (2018) 'Testing and characterization of fibers', *Handbook of properties of textile and technical fibres*: Elsevier, pp. 21-55.

[138] Paddock, S. W. (1999) 'Confocal laser scanning microscopy', *Biotechniques,* 27(5), pp. 992-1004.

[139] Hovis, D. and Heuer, A. (2010) 'The use of laser scanning confocal microscopy (LSCM) in materials science', *Journal of microscopy,* 240(3), pp. 173-180.

[140] Merson, E., Kudrya, A., Trachenko, V., Merson, D., Danilov, V. and Vinogradov, A. (2016) 'The Use of Confocal Laser Scanning Microscopy for the 3D Quantitative Characterization of Fracture Surfaces and Cleavage Facets', *Procedia Structural Integrity,* 2, pp. 533-540.

[141] Merson, E., Danilov, V., Linderov, M., Myagkikh, P., Merson, D. and Vinogradov, A. (2018) 'Assessing Fracture Surface Ductility by Confocal Laser Scanning Microscopy', *Procedia Structural Integrity,* 13, pp. 2152-2157.

[142] Bastidas-Rodriguez, M., Prieto-Ortiz, F. and Espejo, E. (2016) 'Fractographic classification in metallic materials by using computer vision', *Engineering Failure Analysis,* 59, pp. 237-252.

[143] Hsu, N. and FR, B. (1981) 'Characterization and calibration of acoustic emission sensors'.

[144] Culwick, R. (2018). 'Effective evaluation of the structural health of rails using acoustic emission techniques', LH Materials Research Project. University of Birmingham. Unpublished report.

[145] Karjalainen, L., Taulavuori, T., Sellman, M. and Kyröläinen, A. (2008) 'Some strengthening methods for austenitic stainless steels', *steel research international,* 79(6), pp. 404-412.

[146] Dastur, Y. N. and Leslie, W. (1981) 'Mechanism of work hardening in Hadfield manganese steel', *Metallurgical transactions A,* 12(5), pp. 749-759.

[147] Remy, L. (1981) 'The interaction between slip and twinning systems and the influence of twinning on the mechanical behavior of fcc metals and alloys', Metallurgical Transactions A, 12(3), pp. 387-408.

[149] Shiekhelsouk, M., Favier, V., Inal, K. and Cherkaoui, M. (2009) 'Modelling the behaviour of polycrystalline austenitic steel with twinning-induced plasticity effect', International Journal of Plasticity, 25(1), pp. 105-133.

[150] Peixoto, D. and Ferreira, L. A. (2013) 'Fatigue crack propagation behavior in railway steels', International Journal of Structural Integrity.

[151] Toronchuk, J. (1977) 'ACOUSTIC EMISSION DURING TWINNING OF ZINC SINGLE CRYSTALS'.

[154] E/EM-11, A. (2011) 'Standard Practice for Acoustic Emission Examination of Fiberglass Reinforced Plastic Resin (FRP) Tanks/Vessels', American Standard for Testing and Materials, pp. 1-15.

[157] Hadfield, R. A. (1888) Manganese-steel: I. Manganese in its application to metallurgy: II. Some newly-discovered properties of iron and manganese. Institution.

[158] Capacity4rail (2017) *Novel rail freight vehicles* [Online]. Available at: http://www.capacity4rail.eu/IMG/pdf/c4r-d2.2.2_novel_rail_freight_vehicles_final_.pdf (Accessed: 25 December 2019)

[159] Wiest, M., Daves, W., Fischer, F. and Ossberger, H. (2008) 'Deformation and damage of a crossing nose due to wheel passages', *Wear,* 265(9-10), pp. 1431-1438.

[160] Schilke, M., Larijani, N. and Persson, C. (2014) 'Interaction between cracks and microstructure in three dimensions for rolling contact fatigue in railway rails', *Fatigue & Fracture of Engineering Materials & Structures,* 37(3), pp. 280-289.

[161] Ekberg, A. (1997) 'Rolling contact fatigue of railway wheels—a parametric study', *Wear,* 211(2), pp. 280-288.

[162] Dhar, S., Danielsen, H. K., Fæster, S., Rasmussen, C., Zhang, Y. and Jensen, D. J. (2019) 'Crack formation within a Hadfield manganese steel crossing nose', *Wear*, 438, pp. 203049.

[163] Hodgson, W. (1993) 'Rail metallurgy and processing', Rail Quality and Maintenance for Modern Railway Operation: Springer, pp. 29-39.

[164] Kittel, C. and McEuen, P. (1976a) Introduction to solid state physics. Wiley New York.

[165] Matmatch (2018) [Online image] Available at: https://matmatch.com/learn/ process/hardness-comparison (Accessed: 15 December 2019)

[166] Nejad, R. M., Shariati, M. and Farhangdoost, K. (2019) 'Prediction of fatigue crack propagation and fractography of rail steel', Theoretical and Applied Fracture Mechanics, 101, pp. 320-331.

[167] Wang, W.-F. and Wu, M.-J. (2006) 'Effect of silicon content and aging time on density, hardness, toughness and corrosion resistance of sintered 303LSC–Si stainless steels', *Materials Science and Engineering: A,* 425(1-2), pp. 167-171.

[168] Papirov, I., Karpov, E., Palatnik, M. and Mileshkin, M. (1984) 'Acoustic emission during plastic and superplastic deformation of a Zn− 0.4% Al alloy', *Metal Science and Heat Treatment,* 26(12), pp. 887-891.

[169] Physical Acoustics Corporation. Acoustic Emission Technology (2010) [online] Available at: http://www.pacndt.com/index.aspx?go=technologies&focus=acoustic%20 emission.htm (Accessed: 20 November 2018)

[170] Abbasi, M., Kheirandish, S., Kharrazi, Y. and Hejazi, J. (2009) 'The fracture and plastic deformation of aluminum alloyed Hadfield steels', *Materials Science and Engineering: A,* 513, pp. 72-76.

[171] Draeger, D. J. and Case, E. (2003) 'Engineering the surface texture and shape of channels in ceramic substrates', Materials Science and Engineering: B, 97(1), pp. 94-105.

[172] López-Cepero, J., Cancapa, J. Q., Fernández, J. M. and de Arellano López, A. (2005) 'Análisis fractográfico de fibras de circona y de zafiro mediante microscopía óptica confocal', Bol. Soc. Esp. Ceram, 44, pp. 4.

[173] McLaskey, G. C. and Glaser, S. D. (2012) 'Acoustic emission sensor calibration for absolute source measurements', Journal of Nondestructive Evaluation, 31(2), pp. 157-168.

[174] ASTM E 647 (1995). Standard test method for measurement of fatigue crack growth rates.

[175] Liu C. D., Bassim M. N., Stlawrence, S. (1993) 'Evaluation of fatigue crack growth initiation at inclusions in fully pearlitic steels' *Materials Science and Engineering A Structural Materials Properties Microstructure and Processing*, 167, pp. 107-113

[176] Kiessling, R. (1989) 'Non-Metallic Inclusions in Steel. V', The Institute of Metals, 1989, pp. 194.

[177] Thompson, A. W. and Chesnutt, J. C. (1979) 'Identification of a fracture mode: the tearing topography surface', Metallurgical Transactions A, 10(8), pp. 1193-1196.

[178] Merson, E., Danilov, V., Merson, D. and Vinogradov, A. (2017) 'Confocal laser scanning microscopy: The technique for quantitative fractographic analysis', Engineering Fracture Mechanics, 183, pp. 147-158.

[179 ] Pineau, A., Benzerga, A. A. and Pardoen, T. (2016) 'Failure of metals I: Brittle and ductile fracture', *Acta Materialia,* 107, pp. 424-483.

[180] Unnþórsson, R. (2013) 'Hit detection and determination in AE bursts', Acoustic emission-research and applications, pp. 1-20.

[181] Lavakumar, A. (2017) 'Concepts in physical metallurgy', Morgan & Claypool Publishers, pp. 4-1-4-9

[182] Standardization, I. O. f. (2002) Metallic Materials: Fatigue Testing: Fatigue Crack Growth Method. ISO 12108. ISO.